

**VOLCANIC RIFT-ZONES AND FLANK INSTABILITY:
AN EVALUATION OF GROUND DEFORMATION MONITORING TECHNIQUES**

Jane Louise Moss

**A thesis submitted to Cheltenham and Gloucester College of Higher Education in
accordance with the requirements of the degree of Doctor of Philosophy in the
Faculty of Environment and Leisure.**

January 1999



IMAGING SERVICES NORTH

Boston Spa, Wetherby
West Yorkshire, LS23 7BQ
www.bl.uk

BEST COPY AVAILABLE.

VARIABLE PRINT QUALITY

ABSTRACT

Collapse is part of the growth cycle of volcanoes with active rift-zones. As the volcano develops and grows disequilibrium between the strength of the edifice and the applied stresses, produce instability within the edifice which can potentially lead to catastrophic lateral collapse. The intra-eruptive periods on persistently active volcanoes are often short-lived. The recent intra-eruptive windows at Piton de la Fournaise, Réunion Island (1994-1996), Etna, Sicily (1994-1997) and the less-frequently-active Cumbre Vieja ridge on La Palma (1994-1998), have provided a valuable opportunity in which to compare the background deformation (which can indicate whether the edifice is stable between eruptions). Influences such as gravitational loading, tectonic activity, creep or the intrusion of fresh magma would cause coherent deformation patterns, and even small movements within the estimated errors of the measuring techniques are assessed over time to identify patterns. For each site the background seismicity has remained low and no flank eruptions were recorded during the monitoring program.

The results suggest that each site is stable between eruptions. Etna has shown increasing activity since 1995 reflected by a general pattern of inflation. This inflation and a small isolated pocket of inflation on the SW flank are attributed to the intrusion of magma in 1995. A coherent pattern of very minor deformation was observed spanning the 1949 fault of the Cumbre Vieja from 1994 to 1997, however, this was not sustained in 1998. Piton de la Fournaise remained stable during the monitoring program and then erupted at the end of the study in 1998. This inter-eruptive period also provides an optimal time for the transition from one technique to another. On each site the existing EDM (Electronic Distance Measurement) networks were re-occupied using GPS (Global Positioning System), the comparison of individual vectors indicated that the accuracy was approximately 5-12mm, which was less than the expected error between EDM surveys. The networks at all sites have been expanded during the quiescent period and the use of GPS has permitted the optimal positioning of survey stations in order to assess future ground deformation.

AUTHOR'S DECLARATION

This work is solely that of the author. The views expressed within are those of the author and not of Cheltenham and Gloucester College of Higher Education.

ACKNOWLEDGEMENTS

First, I would like to thank my supervisor Bill McGuire for his continued help and encouragement throughout my research. Bill opened many opportunities and enthusiastically discussed ideas and suggestions to develop and expand the research. I would also like to thank my other supervisors Hugh Rollinson and Claudio Vita-Finzi, and my advisor Andy Pullen who explained finite element modelling to me with great patience. This research was undertaken with financial assistance from a number of sources including; the Commission of the European Communities, DG XII Environment Programme, Climatology and Natural Hazards Unit, in the framework of the contract EV5V-CT92-0170, The Benfield Grieg Hazard Research Centre & The British Council. Cheltenham and Gloucester College of Higher Education has supported my research and I would like to express my thanks to the staff of the College and the (old) Geography and Geology Dept. especially Phil Gravestock who has acted as an unofficial, invaluable mentor. Acknowledgement must also go to the Environmental Science Department of the University of Plymouth, where I took my first degree. I owe my first visit to Etna to Dr. Stuart Scott from the University of Plymouth who introduced me to Volcanology and Dr. John Murray. John gave me the opportunity to assist him in his work on Etna and got me interested in ground deformation.

I am indebted to Steve Saunders for showing me round the Etna and Piton de la Fournaise networks (& helping to set up the Cumbre Vieja network), teaching me how to use the EDM and for cheerfully helping out with many fieldtrips. I would like to thank the many other people who have helped out with my data collection through rain, snow, hail, scorching heat and high winds, especially Ashley Morrel, Bill McGuire, Paul Rollin, Jane Wilcocks, Rob Rees, Delia Page, Tiziana Busà, Sergio Vinciguerra (& friends), Vicky Buck, Phil Gravestock, Steve Cooke, Paul Everill, Rachel Rogers and Jo Gilman. I would like to thank Professor Richard Howarth from the University College London for help on Etna and for checking all my statistical calculations.

I would like to mention everyone from the Institut du Physique de Globe du Paris who made working on Piton de la Fournaise such a wonderful experience, in particular Pierre Briole, Partick Bachèlery and Phillipe Sabauroult. I would like to thank Juan-Carlos Carracedo his hospitality and assistance on La Palma and also to Simon Day for many serious discussions about the research for all of the field sites. My work on Etna was supported by many people, I would like to acknowledge and thank the International Institute of Volcanology in Catania for discussion about the research program and to the University of Catania for the occasional loan of the Jeep. The research would not have been possible without the loan of equipment and support from many organisations, I am grateful to all those who lent me GPS equipment: International Institute of Volcanology in Catania; Institut du Physique de Globe Du Paris; University College London, Newcastle University and Leica UK.

Much thanks and affection must go to my peers at Cheltenham and in the Volcanological community without whose support I would have had a more arduous and less spirited time. I extend this gratitude to all my friends and to my family who have supported my interest in volcanoes and who have encouraged me at every step. Finally, I would like to thank Steve Cooke for his loving support and encouragement and for always believing in me.

FOR MY MOTHER

CONTENTS

<i>1. INTRODUCTION</i>	<i>1</i>
1.1 Background	1
1.2 Aims and objectives of the study	6
1.3 The structure of the thesis	8
1.4 Development and growth of selected volcanoes	9
1.4.1 Shallow magma transport within rift-zones	11
1.4.2 The role of the local stress regime in the operation of rift-zones	13
1.5 The role of pore fluid pressures in inducing volcano instability	15
1.6 The sources of ground deformation on active volcanoes	17
1.7 The identification and classification of edifice failure	21
1.8 Summary	26
<i>2. DEFORMATION MONITORING AT ACTIVE VOLCANOES</i>	<i>27</i>
2.1 Ground deformation monitoring techniques	27
2.1.1 Tiltmetry	28
2.1.2 Precise Levelling	29
2.1.3 Strain gauges	30
2.1.4 Electronic Distance Measurement	30
2.2 Non-terrestrial ground deformation monitoring	31
2.2.1 The Global Positioning System	32
2.3 Choice of methods for this study	33
2.4 The establishment of a ground deformation survey network	34
2.4.1 Measurement errors	37
2.5 Total Station: Electronic Distance Measurement & theodolite	39
2.6 The Global Positioning System	41
2.6.1 Basic principles	42
2.6.2 Processing GPS data	46
2.6.3 Network adjustment	51
2.6.4 Biases	52
2.7 Observation procedures	54
2.8 Critical discussion of techniques & problematic issues	55
2.9 Summary	56
<i>3. DATA REDUCTIONS AND ANALYSIS</i>	<i>58</i>
3.1 The ground deformation data	58
3.2 Sources of ground deformation	59
3.3 Data collection, reduction and analysis	61
3.3.1 EDM data processing and resolution	63

3.4 Statistical Tests _____	65
3.5 Numerical modelling _____	67
3.5.1 Preliminary modelling tests _____	74
3.6 Summary & conclusions _____	82
4. <i>MT. ETNA, PART ONE: THE GEOLOGICAL CONTEXT</i> _____	84
4.1 The eruptive history of Etna _____	85
4.2 Structural framework of the Etna region _____	88
4.2.1 The Rift-Zones _____	92
4.2.2 The Lower Eastern Flank Faults _____	96
4.3 The relationship between the volcano plumbing system and regional tectonics _____	98
4.4 Monitoring ground deformation and gravity on Etna _____	102
4.5 The 1991-93 eruption: magma transport and storage and the prevailing stress conditions. _____	109
4.6 Finite element modelling of the 1983 and 1989 dyke emplacements _____	111
4.6.1 The 1983 dyke emplacement _____	113
4.6.2 The 1991 dyke emplacement. _____	116
4.7 Activity at Etna between September 1994 and December 1997 _____	119
4.8 Conclusions _____	121
5. <i>MT. ETNA, PART TWO: MEASUREMENT & MODELLING</i> _____	122
5.1. Evaluating the ground deformation networks _____	122
5.2. The Upper South-Eastern Flank Network: location and purpose _____	124
5.3. The Lower Eastern Flank Networks _____	126
5.4. Additional intermediate survey stations installed in the network _____	129
5.5. Upper and Lower Flank survey reports: 1994-97 _____	130
5.6. GPS survey reports: 1995-7 _____	133
5.6.1. July 1995 _____	133
5.6.2. June 1996 _____	135
5.6.3. July 1997 _____	138
5.7. The results of the Upper South-Eastern Flank Network _____	138
5.7.1. The 1994 co-ordinate positions _____	139
5.7.2. The 1995 co-ordinate positions _____	140
5.7.3. 1994 to 1995: line length and vectors changes _____	140
5.7.4. The 1996 co-ordinate position _____	145
5.7.5. 1995 to 1996: line length and vector changes _____	145
5.7.6. 1997: co-ordinate position _____	149
5.7.7. 1996 to 1997: line length and vector changes _____	149
5.8. Modelling the significant 1996-7 data _____	154
5.9. The results of the Lower Eastern Flank Networks _____	160

5.10. The implications of the recorded ground deformation between 1994-97	166
5.10.1. The Upper South-Eastern Flank Network	166
5.10.2. The Lower Eastern Flank Networks	170
5.10.3. Summary of principal conclusions	171
5.11. Discussion of models to examine the relationship between regional tectonic faults and the rift-zones .	172
6. <i>PITON DE LA FOURNAISE</i>	175
6.1 Introduction	176
6.2 Geological structure of Piton de la Fournaise	179
6.2.1 The active rift-zones	180
6.3 Historic activity	181
6.4 Previous models for the stability of the volcanic edifice	183
6.5 The ground deformation monitoring of the volcano	187
6.5.1 Total station field campaign: 1993-4	189
6.5.2 The GPS field campaign: January 1995	189
6.6 The results of the NE and SE Rift-Zone Networks	192
6.6.1 1993 to 1994; Line length and vector changes.	192
6.6.2 1994 to 1995; line length and vector changes.	194
6.6.3 1993 to 1995; EDM vs. GPS & total vector displacement within the study	196
6.7 Discussion of results	198
6.8 The ground deformation results of the March 1998 eruption	199
6.9 Implications of the ground deformation data to edifice instability.	200
6.10 Summary	203
7. <i>LA PALMA</i>	204
7.1 Introduction	205
7.2 The geology of La Palma	207
7.3 The Cumbre Vieja Volcano	209
7.4 The historical activity of the Cumbre Vieja volcano	210
7.5 The objectives of the baseline ground deformation network	214
7.5.1 Stage One: The ridge network	216
7.5.2 Stage Two: The Western Flank Network	219
7.6 Measuring the ridge network (using the Total Station and GPS)1994-97	221
7.7 The GPS network, 1997	224
7.8 Results and interpretation	226
7.8.1 Additional data: the 1998 re-occupation	229
7.9 Modelling magma intrusion	231

7.10 A model for the structural evolution of La Palma	234
7.10.1 Surmised eruption scenarios	239
7.11 Conclusions and Summary	240
8. CONCLUSIONS	242
8.1 An evaluation of the methodology	242
8.2 The principal findings of the study	245
8.3 Are the relationships between gravitational, magmatic and tectonic stresses similar for all the case-study sites ?	246
8.4 How do the different edifice morphologies affect deformation patterns?	249
8.5 Further research	250
<i>APPENDIX</i>	
A Kilauea Volcano, Hawaii	252
B Ground deformation data	256
C Station descriptions	266
Bibliography	277

FIGURES

Figure 1-1 Cumulative year versus number of summit and flank eruptions for Etna, Piton de la Fournaise and Cumbre Vieja. The data is compiled from Chester et al. (1985) and Stieltjes & Moutou (1989), after Lénat (1989a, p317).	6
Figure 1-2 The relationship between stress orientation and magma intrusion on Mt. Etna, after McGuire and Pullen (1989).	14
Figure 1-3 The inflation and deflation cycle; A schematic diagram illustrating the cyclical process of magma ascent into the summit storage areas, transport into the rift-zones and eruption.	18
Figure 2-1 Geometric network polygons, the triangle represents the reference point, the circles represent the survey stations and the thick grey lines represent a rift-zone or a fault. Polygon a is an ideal network with an evenly spaced polygon shape, while b represents a more realistic, irregular network.	34
Figure 2-2 An example of a station description from Mt. Etna showing the to-reach description and approximate co-ordinates.	37
Figure 2-3 The GPS constellation, showing the rough satellite orbits around the earth. Each satellite in the diagram represents a number of satellites; between three and four travelling along the orbit.	43
Figure 2-4 Receiver tracking the satellites (S1 and S2) as they move along their orbital planes.	44
Figure 2-5 Relative positioning using reference and rover receivers and four satellites (S1-S4).	49
Figure 3-1 Flow diagram illustrating EDM data reduction; green = field collection of data, blue = initial data reduction, red = data processing and adjustment; yellow = output of co-ordinates.	62
Figure 3-2 Mogi's buried sphere model; a = radius of sphere, f = depth to sphere for the surface, d = changes in horizontal deformation of the 'ground surface', x = the point on the 'ground surface' above the buried sphere.	68
Figure 3-3, (a) The results of Test1b showing the pattern of surface displacement across a flat ground surface above a newly emplaced dyke. (b) The graph shows a cross-section along the top surface of the host block, U_x = horizontal displacement, U_y = vertical displacement.	76
Figure 3-4 (a) Geometry of Test1c showing a 1000m step containing a vertical dyke, the dashed line along the upper top surface of the host box (above the step) is illustrated in (b) as vertical displacement along the cross section.	78
Figure 3-5 The model (Test1e) indicates (a) the displacement vectors associated with an extensional dyke adjacent to a 1000m step (b) with the horizontal and vertical surface displacement.	79
Figure 3-6 Test 1h showing (a) displacement vectors and (b) surface displacement associated with the emplacement of a dyke dipping at 70° .	81
Figure 3-7 The simulation of the normal fault.	82
Figure 4-1 Stratigraphy of the eruptive centres of Etna and their temporal distribution. After Chester et al., (1985) and Calvari et al., (1996). Information from: ¹ Condomines et al., 1982; ² Chester & Duncan, 1982; ³ McGuire, 1982; ⁴ Guest et al., 1984; ⁵ McGuire <i>pers com</i> ; ⁶ Gillot et al., 1994 ⁷ Calvari et al., 1996.	87
Figure 4-2 The structural framework of the Etnean region showing the regional tectonic features.	89
Figure 4-3 The relationship between the eastern flank mobile sector and the summit 'rift-zones'.	92
Figure 4-4 Opening of the rift-zones to initiate associated shear displacement of the opposite rift-zone (after McGuire et al., 1996).	94

Figure 4-5 The Lower East Flank Faults showing the position of the Praiola embayment and the large towns. _____	97
Figure 4-6 The Upper South-Eastern Flank of Etna (section taken from Figure 4-7) divided into the shallow blocks proposed by McGuire and Pullen (1989), the circles represent ground deformation survey stations that are now included in this study. _	106
Figure 4-7 The Southern Rift-Zone of Etna indicating the principal areas and dyke swarms. _____	112
Figure 4-8 The dyke emplaced adjacent to the cliff causing the 'rock' close to the cliff edge to rotate (dyke length = 100m). _____	114
Figure 4-9 (a) The Mohr stress (S_m) & horizontal stress (S_x) and (b) the horizontal and vertical displacement (U_x & U_y) acting upon the top of the cross-section (west to east) illustrated in Figure 4-10. _____	115
Figure 4-10 The vector displacements over the west-east cross-section, and the dipping dyke. _____	116
Figure 4-11 a. The topographic cross-section, showing the 1991 dyke, b. surface displacements, c. Mohr stress values. _____	118
Figure 5-1 The ground deformation networks of the Eastern Flank of Etna included in this monitoring program, Matera (included as an inset) was used as a _____	123
Figure 5-2 The Upper South-Eastern Flank Network _____	125
Figure 5-3 The difference between baseline measurements between 1994 and 1995 using EDM. _____	141
Figure 5-4 The relationship between strain and altitude, 1994-5 _____	142
Figure 5-5 Horizontal vector displacements between 1994-95 including the disparate shallow blocks, see test for explanation. For the general location see Figure 5-1& Figure 5-2. The large displacement vectors are determined by eye to represent the general trend of displacement. _____	143
Figure 5-6 Upper South-Eastern Flank Network indicating survey stations and principal shallow blocks (divided sectors). _____	144
Figure 5-7 Baseline repeatability between 1995-5 _____	146
Figure 5-8 Relationship between strain and altitude, 1995-6. _____	147
Figure 5-9 Vector displacements between 1995-96, indicating general displacement orientations. _____	148
Figure 5-10 Line length changes between 1996-97 _____	150
Figure 5-11 Relationship between strain and altitude, 1996-7. _____	151
Figure 5-12 Vector changes between 1996-97. _____	152
Figure 5-13 Height changes between 1996-7, for survey station numbers see Figure 5-2. _____	153
Figure 5-14 Vector displacements between 1994-97, indicating general displacement orientations. _____	154
Figure 5-15 The transect of the southern wall of the Valle del Bove; a, the cross-section of the ground surface (with survey stations), b, the geometry of the model showing the mesh and the orientation of the dyke (2km long). _____	156
Figure 5-16 The 1996-7 ground surface changes depicting the difference between modelled and measured deformation; a, vertical deformation b, horizontal deformation. The Figures are combined together with the ground surface of Etna in Figure 5-17. _____	157
Figure 5-17 Modelled and measured data from 1996-7. _____	158
Figure 5-18 Failure criteria for the finite element model _____	160
Figure 5-19 Line length changes on the Lower Eastern Flank Networks compared to the 10mm +3ppm error estimate of the techniques. _____	162
Figure 5-20 The Carruba network showing line length changes (survey station c4 was destroyed in 1995). The data refers to movements from the first measurement of	

each survey station to the latest, newer survey stations such as c6 and c7 only reflect the displacement over a two year period.	162
Figure 5-21 Vector changes on the Lower Eastern Flank between 1995 and 1997, for the locations see the area map (Figure 5-1).	165
Figure 5-22 The low levels of deformation have provided an opportunity to examine i), the smaller strain relationships between the shallow surface blocks examined in Section 4.2.1 and ii) the accuracy and suitability of the techniques to measure continuous ground deformation. (additional data supplied by McGuire)	167
Figure 6-1 Réunion Island, 1. Cirque de Mafate, 2. Cirque de Salazie, 3. Cirque de Cilaos, 4. Rivière de L'Est, 5. Rivière des Ramparts, 6. Rempart des Sables, 7. North-West Rift-zone, 8. North-East Rift-zone, 9. South-East Rift-zone, 10. l'Enclos Fouqué, central craters, 11. Plaine des Osmondes, 12. Grand Brûlé (the scarp is the Grandes Pentes).	177
Figure 6-2 The lavas from the March 1998 eruption showing the path of the lava flow and the names of the prominent cones near the flow (From Staudacher, 1998).	183
Figure 6-3 The NE, SE and IPGP Ground Deformation Networks in l'Enclos Fouqué, (contour intervals = 100m, the central cone contour = 2500m).	188
Figure 6-4 The areas covered by the Rift-Zone networks and the survey stations of the Coastal Networks including the principal French GPS benchmarks.	191
Figure 6-5 Variations in the measurement of lines between survey stations from 1993 to 1994	193
Figure 6-6 Vector displacements from 1993 to 1994 (for key and station numbers see Figure 6-3).	194
Figure 6-7 The different measurement of lines between survey stations from 1994 to 1995 (excluding 2M25).	195
Figure 6-8 Vector displacements from 1994 to 1995 (for key and station numbers see Figure 6-3).	196
Figure 6-9 Vector displacements between 1993-1995 (for key and station numbers see Figure 6-3).	197
Figure 6-10 Horizontal ground deformation vectors (GPS) from the March 1998 eruption of Piton de la Fournaise, the filled circles represent (EDM & GPS) survey stations (from Staudacher, 1998). For the location of the eruption see Figure 6-2 and for the survey stations refer to Figure 6-3.	199
Figure 7-1 Location map of the Canary Islands in the Atlantic ocean, 200km west of Africa.	205
Figure 7-2 Sketch to illustrate the evolution of the island of La Palma, after Staudigel and Schmincke (1984); Carracedo et al. (1997c) & Ancochea et al. (1994).	207
Figure 7-3 A simplified sketchmap of the historic eruption sites	211
Figure 7-4 The ridge network established in 1994 showing the proximity to the features of the 1949 eruption.	217
Figure 7-5 The Western Flank Network showing the survey stations and principal towns.	220
Figure 7-6 The changes in line length plotted against the 5mm ± 3ppm error estimate; all the data-sets are obtained using EDM.	221
Figure 7-7 Vector changes between 1994 and 1996, with approximate height contours.	223
Figure 7-8 Line length differences between 1996 EDM data and 1997 GPS data.	225
Figure 7-9 The vector differences between 1996 and 1997 with approximate height contours.	226
Figure 7-10 Vector changes between 1994 and 1997 showing the position of the 1949 fault.	228
Figure 7-11 Co-ordinate velocity between 1997-8 with an approximate contour outline showing the locations of the survey stations.	230
Figure 7-12 The basic geometric model of the southern part of the island of La Palma	232

Figure 7-13 The Mohr stress value of the start of the dyke emplacement into the N-S riftzone. _____	232
Figure 7-14 The Mohr stress field around the dyke as it propagates towards the surface. _____	233
Figure 7-15 The displacement of the edifice due to the dyke reaching the surface. _____	233
Figure 7-16 A sketch combining separate volcanoes onto the same base to show the role of buttressing on the creation of unstable rift-zone-bounded sectors; the grey dashed lines represent the rift-zones. _____	237
Figure 7-17 The Mohr stress values for a simplistic triple-rift array undergoing N-S compression (where N-S is down the page), the dark areas indicate increased strain and the arrows illustrate the compressive stresses. _____	238
Figure 7-18 The hazard potential from landslides on the Cumbre Vieja volcano, after Carracedo et al. (1997b). _____	240
Figure A-1 The Big Island of Hawaii showing the relative surface areas of the volcanoes; the central vents of Mauna Loa and Kilauea are indicated by a white circle and the shaded areas are their active rift-zones. _____	253
Figure C-1 Location maps for the Lower Eastern Flank Networks: a, Vena, b, Macchia, c, Carruba, d, Trecastagni. _____	276

EQUATIONS

Equation 1-1 Magma overpressure required to propagate the dyke	12
Equation 1-2 Brittle strength of material containing a pressurised pore fluid, the derivation of the values used the equations, are explained by Day (1996).	15
Equation 2-1 The standard deviation error (s) for the levelling transect.	29
Equation 2-2 The calculation of the distance measured by infra-red Electronic Distance Measurement.	40
Equation 2-3 Single differencing formulae and key	48
Equation 2-4 Double differencing	48
Equation 2-5 Triple differencing	49
Equation 2-6 Baseline vector between two survey stations	50
Equation 3-1 The determination of strain using Equation 3-1	63
Equation 3-2 Baseline differences between two surveys using one or two different methods e.g. EDM and GPS.	65
Equation 3-3 Network precision (σ) taking into account survey errors.	65
Equation 3-4 Calculation of the Pearson product moment coefficient (r).	66
Equation 3-5 Horizontal change on the surface of the elastic halfspace as a result of the intrusion of a buried source (Dieterich & Decker, 1975).	69
Equation 3-6 Vertical change on the surface of the elastic halfspace as a result of the intrusion of a buried source, for definition of variables see Equation 3-5, (Dieterich & Decker, 1975).	69

TABLES

Table 1-1 Potential causes of slope failure that may occur on Etna in response to changes in the internal properties of the edifice and changes in the external applied stresses (After Guest et al., 1984).	20
Table 1-2 Classification of landslide mechanisms, after Dikau et al. (1996)	23
Table 1-3 Emplacement and deposition variations between recognised deposits of volcanic debris avalanches and slumps 1 Piton de la Fournaise, Réunion (Lénat et al., 1989), 2 Hilina Pali, Hawaii, (Moore et al., 1989), 3 Alike Landslides, Hawaii, (Moore et al., 1994), 4 Mount St. Helens, 1980 eruption, (Voight et al., 1981), 5 Cumbre Vieja Volcano, (Carracedo, 1996) 6 El Hierro, Canary islands, (Day et al., 1997)	24
Table 2-1 Advantages and disadvantages of using tiltmetry to monitor ground deformation.	28
Table 2-2 The advantages and disadvantages of using the tilt monitoring methods. ¹ Defined by the International Geodetic Association (1912) cited in (Murray et al., 1996).	30
Table 2-3 The advantages and disadvantages of using the EDM method.	31
Table 2-4 Remote-based ground deformation monitoring techniques. ¹ Massonnet et al., 1995.	32
Table 2-5 Advantages and Disadvantages of the application of the Global Positioning System to ground deformation monitoring. (¹ Dzurisin, 1989)	33
Table 2-6 The range of errors experienced the Sokkia Set3c Total Station used in this study. (After Uren & Price, 1994)	41
Table 2-7 GPS processing steps (after Hofmann-Wellenhof, et al., 1997, page 170)	51
Table 2-8 Estimate of total GPS precision taking into account user and equipment errors.	52
Table 2-9 Potential biases in GPS data from the satellite, signal and the receiver.	52
Table 3-1 The baseline between 8 and 10 on Etna, 1995-6 EDM and GPS data	63
Table 3-2 Mechanical properties used in the finite element models. ¹ Wahab Khair (1989), ² Birch (1966), ³ Encyclopaedia Britannica (Vol. 15, P954). Bold = The value used in the model	72
Table 4-1 A summary of observations during the first stages of the 1991-93 eruption.	111
Table 5-1 Ground deformation networks on the Upper and Lower Eastern Flank of Etna, ¹ established or modified during the course of the research.	122
Table 5-2 Network occupations, techniques & new stations: a, 1994; b, 1995; c, 1996; d, 1997.	133
Table 5-3 Geodetic co-ordinates of Matera in WGS84	135
Table 5-4 EDM and GPS comparisons on the Lower Eastern Flank (EDM measurements were not recorded in 1997)	164
Table 7-1 Physical parameters for the finite element model illustrated in Figure 7-12	231

1. INTRODUCTION

Monitoring active volcanoes during eruptive events enables the scientist to record and categorise the current eruptive status of the volcanic edifice. The observations can be used to formulate an eruption model to anticipate on-going or predict future events, and to hypothesise on the sources and causes of the eruptive phase. During inter-eruptive periods, however the monitoring of active volcanoes allows the physical status of the edifice and the background levels of measurable quantities such as ground deformation and seismicity to be ascertained. These background levels or *baseline data* enable changes occurring as a result of the very first indicators of fresh magma ascent or on-going edifice instability from gravitational loading, to be clearly identified. The scope of this thesis focuses on monitoring the ground deformation of three predominately basaltic, active volcanoes with established intra-volcanic rift-zones; specific attention is applied to the relationship between the rift-zones and edifice development. Existing ground deformation networks are evaluated and developed and one complete new network is established. The monitoring techniques are carefully evaluated as the measurements during the inter-eruptive periods are small (<10cm).

1.1 Background

Large, long-lived volcanic constructs are often characterised by the development of rift zones. These constitute linear extensional features, along which persistent magma emplacement has taken place over a long period of time (tens to hundreds of thousands of years). Rift-zones are defined as areas characterised by tightly packed intrusive bodies where the ratio of the intrusive complex to the country rock is greater than 40%. Typically such features are represented by extensive fault and fissure systems which permit shallow magma transport, and reasonably pronounced topographic highs (depending, amongst other factors, on age). At central-vent volcanoes, rift zones usually propagate outwards from beneath active summit crater systems. A rift-zone undergoes measurable deformation in response to each magma intrusion episode due to mechanical and thermal

pressures. Accommodation of the magmatic stresses associated with these events partly involves the elastic deformation of the upper levels of the edifice. Stress values that exceed the strength of the host rock result in brittle fracture. This leads to the lateral displacement of large volumes of volcanic material adjacent to the rift zones and possibly flank failure (Swanson *et al.*, 1976). As shown at Mount Etna in recent years (McGuire *et al.*, 1990; 1991), such displacements can exceed five metres over periods as short as ten years. This can lead to a significant increase in slope instability and promote structural failure of the edifice on a range of scales from rockfall to major lateral collapse.

The widespread instability of volcanic constructs with recognised rift-zones has recently become evident from the imaging of the sea-floor off-shore from coastal and island volcanoes (Moore *et al.*, 1994; Holcomb & Searle, 1991; Lénat *et al.*, 1989a). The sea-floor scans have found large debris avalanche and slump deposits that have originated from rift-zone bounded areas of adjacent volcanic edifices. The most studied volcanoes are; Hawaii (Moore *et al.*, 1994), the Canary Islands (Holcomb & Searle, 1991; Carracedo, 1994) and Piton de la Fournaise (Lénat *et al.*, 1989a), the landslides that emplaced these deposits are large-scale lateral collapses with volumes in excess of six million cubic metres.

Debate continues contesting the importance of rift-zones in the instigation of collapse. Hirn (*pers com*) argues that in some cases (e.g. Piton de la Fournaise) the rift-zones are a superficial feature of the eruptive process and do not actively aid in flank collapse (even where there is evidence of past failure). Hirn maintains that as published seismic data for Piton de la Fournaise do not identify a *signature* for the rift-zones during eruptive events and these seismic data should not be considered important in edifice evolution (Nercessian *et al.*, 1996).

Given such arguments, the development of an understanding of the nature and operation of rift-zone growth and rifting mechanisms, during and between eruptive events, is crucial to assessing their involvement in generating instability-related volcanic hazards ranging from instantaneous debris avalanches to slow-

moving creep and sector slumping. The author argues that, where present on any developing edifice, rift-zones play a crucial role in the on-going stability of the volcanic edifice. In order to determine the nature of the relationship between rift-zone development and edifice instability, the characteristics and evolution of rift-zones are examined at currently-active volcanoes, through investigation of the interaction of stresses generated by regional tectonics, gravitational effects, and the persistent, high-level, emplacement of magma bodies (McGuire & Pullen, 1989).

The relationship between rifting, edifice instability, and structural failure is assessed through the collection of ground deformation data, using a combination of geodetic monitoring techniques (Murray, 1990; Murray *et al.*, 1994; Nunnari & Puglisi, 1994) and a critical review of the appropriate, contemporary literature. Data based conceptual models are constructed using computer finite-element modelling methods, firstly, to ascertain the validity of the models and secondly to determine the linear source parameters of observed deformation.

The study focuses on a number of volcanoes characterised by active rift-zone systems that show evidence of measurable, contemporary or recent ground deformation and display a range of topographic and structural features. The case-study volcanoes are Mount Etna (Sicily), Cumbre Vieja volcano on La Palma (Canary Islands), and Piton de la Fournaise (Réunion Island). Rift-zone structure and operation at each of these three volcanoes is different.

At Etna, recent structural and geodetic studies suggest a relationship between current rifting and contemporary co-and a-seismic fault displacements at lower altitudes (Chester *et al.*, 1985; Stewart *et al.*, 1993). This relationship appears also to be in some way linked to flank instability and lateral collapse, as revealed by (i) the existence of the Valle del Bove flank depression located between two of the most active rift-zones (McGuire, 1982; Guest *et al.*, 1984), and (ii) the long-standing mobility of a large sector of the eastern flank of the volcano (Kieffer, 1985; Lo Giudice & Rasa, 1992). The combined use of geodetic monitoring and

data modelling is designed to reveal the broad pattern of rift-related deformation. This strategy determines the relative roles of regional tectonic stresses, magma pressures and gravity-related downslope movements in triggering rifting events and in dissipating rifting-induced stresses.

The Piton de la Fournaise volcano is characterised by a similar rift-zone system to that of Etna, but with three rift-zones converging on the summit. Evidence for past summit collapse takes the form of the Grand Brûlé landslide scar which is bounded by the two most active rift-zones and the sea (Duffield *et al.*, 1982). Lénat and Bachèlery (1990) suggest that this feature confirms that dyke emplacement at Piton de la Fournaise has caused the asymmetric growth of the central cone and the over steepening of the eastern flanks. They also proposed that the mechanical strains associated with edifice growth are dissipated through the activation and resultant extension of the rift-zones at the apex of the eastern part of the volcano, leading to the seaward movement of the entire eastern flank. Here, as at Etna, edifice instability and collapse appears to be confined to the poorly buttressed seaward flank. The rift-zone systems at Piton de la Fournaise do, however, differ from those at Etna, in that the rift-zones intersect within the collapse scar itself rather than on the stable part of the edifice. Furthermore, there are no major controlling tectonic strains within the region or tectonically-related faults along which co- or a-seismic displacements may either expedite magma intrusion or dissipate strains from rifting events. Accumulating strains may only be relieved by seaward dilation of the rift-zones or periodic edifice failure on the unbuttressed seaward flank.

In contrast to Etna and Piton de la Fournaise, the Cumbre Vieja volcano has a single, active rift-zone and no central vent complex; the volcano takes the form of a steep topographic ridge bisecting the southern part of the island. The rift-zone abuts to the north against an older collapsed rift system (The Taburiente-Cumbre Nueva). Recent eruptions (1949 and 1971) have been characterised by both explosive and effusive activity, and have occurred at widely spaced locations on the rift-zone and from fractures in the western flank (See Figure 7.3). The strong

topographic expression of the ridge can be expected to promote and constrain parallel dyke emplacement within the N-S oriented ridge, however the absence of a central magma conduit makes the determination of magma transport and storage problematic. As at Piton de la Fournaise, the Cumbre Vieja edifice is under no obvious regional tectonic influence and given this situation, the collapse structures associated with the older Taburiente volcano in the north of the island, which is bisected by numerous dykes, argue for persistent rift accommodation by flank collapse. During the 1949 eruption a 2km long system of faults and fractures developed along the crest of the northern Cumbre Vieja. The normal faults were downthrown by up to 4m westwards and are considered to represent an aborted flank collapse (Carracedo *pers com*). The relationship between flank stability and eruptive events is unknown, and precise geodetic monitoring during the current inter-eruptive period is designed to reveal if any gravitational sliding is occurring in the absence of magmatic influences.

Figure 1-1 shows the eruptive frequency of the three volcanoes monitored within this research. Etna and Piton de la Fournaise have a very high eruption rate with summit eruptions almost every year coupled with large flank eruptions every three to five years. The eruptive similarities between the two edifices is clearly seen. It is difficult to enumerate the flank eruptions from Piton de la Fournaise as the records do not distinguish the partial propagation of fissures into the rift-zones during summit eruptions with distinct flank eruptions (Stieltjes & Moutou, 1989). The Cumbre Vieja Volcano has however, only erupted twice this century, there is no central vent area and both eruptions occurred along the prominent north-south rift-zone.

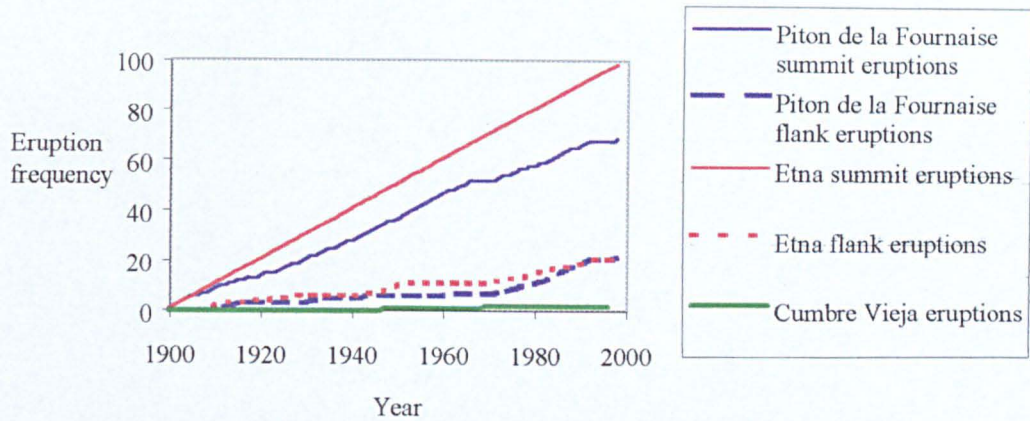


Figure 1-1 Cumulative year versus number of summit and flank eruptions for Etna, Piton de la Fournaise and Cumbre Vieja. The data is compiled from Chester *et al.* (1985) and Stieltjes & Moutou (1989), after Lénat (1989a, p317).

1.2 Aims and objectives of the study

The broad aims of the study are to (i) establish the current deformation status of the edifices and to (ii) develop an understanding of the nature and contemporary operation of the rift-zone systems of the selected volcanoes and their role in edifice instability. Furthermore, the aims seek to distinguish the relative influences of magmatic-, gravitational- and tectonic-stresses and to critically evaluate their roles in edifice development and evolution. As it could not be known whether any of the case-study volcanoes would erupt during the course of the monitoring programme, the aims are designed to address the different causes of deformation that could be detected during differing states of activity. The level of ground deformation is measured relative to a baseline data-set collected during an inter-eruptive period. Therefore the study seeks to detect the following;

- (i) magma-related deformation in the event of an intrusion
- (ii) tectonically-related displacements occurring during co-seismic events (either magma-related or non-magmatic)
- (iii) inter-eruptive (aseismic) deformation occurring as a result of gravitational instability or deep magma transport.

- (i) A comprehensive and critical review of relevant contemporary geological, deformation and seismic data from the selected volcanoes.
- (ii) Establishment of ground deformation networks over the rift-zones and adjacent tectonically active faults and appropriate extension of existing networks.
- (iii) Periodic measurement of the (new and existing) networks to ascertain survey station velocities over time.
- (iv) Analysis of the station velocities for coherent patterns of displacement
- (v) Modelling of deformation using the finite element method to constrain potential deformation sources.
- (vi) Evaluation of the application of the Global Positioning System (GPS) for periodic deformation monitoring

In determining the current eruptive status of the selected volcanoes, the successful achievement of the aims has permitted the following critical questions to be answered:

- (i) What are the relative contributions of regional tectonics, magma emplacement and gravity-induced displacement in the current operation of the plumbing system of Mt. Etna?
- (ii) What is the relationship between magma emplacement and gravity induced displacement at Piton de la Fournaise, and is the seaward flank of the volcano currently stable at shallow depths?
- (iii) Is the steep-sided rift-zone of the Cumbre Vieja volcano on La Palma stable during the current inter-eruptive period, and what is the likely outcome of a fresh dyke emplacement event?
- (iv) Are the relationships between gravitational, magmatic and tectonic stresses similar for all the selected volcanoes and how do the different morphologies and eruptive patterns affect deformation patterns?

1.3 The structure of the thesis

This chapter defines the principal focus of the thesis and outlines the broader context of the investigation. The aims are listed as are the objectives through which these aims have been fulfilled. Case-study volcanoes are briefly introduced and specific investigative questions relating to each site are stated. The principal volcanological concepts examined in the thesis are defined and discussed.

Chapter two investigates the types of ground deformation monitoring that have been used within the monitoring program, explaining in some detail the working of the two principal methods; *Infra-red Electronic Distance Measurement* and *the Global Positioning System*. Chapter three describes the various ways in which ground deformation data are recorded, analysed and modelled.

Chapters four and five focus on Mt. Etna, the principal volcano examined in this thesis. Chapter four forms a comprehensive and critical survey of the literature relating to Etna and the surrounding region, drawing particularly upon recently published work to provide a picture of the regional stress regime, the current eruptive status of the volcano and the stability of the edifice. Chapter five focuses on the monitoring procedures, data collection, and the growth and development of the networks. Data acquired on Etna are analysed using methods outlined in chapter three and the results are discussed.

Chapters, six and seven, are devoted respectively to deformation studies on Piton de la Fournaise (Réunion Island) and the Cumbre Vieja (La Palma). Background discussion of the geological settings of the volcanoes, are succeeded by details of the establishment and measurement of the ground deformation networks and data collection and analysis. In both cases the data are discussed in light of the current status of the volcanoes.

Chapter eight evaluates the methodologies used, outlines the conclusions of the study and provides recommendations for future work. The principal findings of

the thesis examine the role of magma in forming coherent (if negligible) patterns of deformation that directly reflect tectonic and gravitational stresses in the edifice.

1.4 Development and growth of selected volcanoes

The three case-study volcanoes are all young, predominantly basaltic volcanoes. Although they each exhibit different morphologies and eruptive rates, they share common characteristics such as the continued emplacement of dykes into rift-zones and pre-historic indications of flank collapse from rift-zone bounded flanks.

A basaltic volcano develops from frequent eruptions of fluid basaltic lava emitted from central or rift eruptions. The edifice develops as a shield, cone or ridge, made up of overlapping predominantly effusive or intrusive products, and a smaller percentage of explosive products. The latter comprise pyroclastic fall products of limited dispersion such as vent scoria or spatter and deposits produced by lava-fountaining and phreatic or phreatomagmatic explosions. More silica- or gas- rich explosive magmas arise from the storage and subsequent fractionation of magma in shallow reservoirs. Basaltic shields develop as broad shallow-sloped edifices, although the development of rift-zones may cause the edifice to grow asymmetrically forming steeper slopes on one side or another. The rift zone itself represents the surface expression of a feeder-dyke complex, and is usually characterised by surface cracks, grabens and fissures which are a direct result of sub-surface magma intrusion. The persistent intrusion of magma within an edifice leads to the clustering of dykes into the rift-zones due to the formation of internal discontinuities (Walker, 1990). The intrusive bodies display a high degree of parallelism, since for dykes to propagate within the intrusive complex at a collective level there must be a common impetus, of acting internal and/or external forces.

The supply of magma into an edifice is controlled by a number of factors such as plate movement and magma plume proximity. The rate of development of a volcanic edifice is controlled by the ascent of fresh magma into the volcano. The plumbing system controls the transport and storage of magma prior to eruption and *neutral buoyancy* primarily determines the vertical ascent of magma into the rift-zone. The different rock types are stratified according to density, such that the least dense material ascends until the densities of each rock type are in equilibrium (Ryan 1987; Walker 1992). If magma is the least dense material, it ascends until there is a surface eruption; if however it meets a stratum of a lower density, then the magma no longer rises allowing formation of a magma reservoir. The lower density area may be a result of the existence of a plexus of shallow fractures or an unconsolidated area (such as thick ash deposits). The storage of magma beneath the surface within the rift-zone is termed the *neutral buoyancy zone* (NBZ) or the level of neutral buoyancy (LNB). Within the NBZ the in-situ density of magma is the same as the density of the host country rock. The vertical resistance is higher than the horizontal resistance so the magma body spreads laterally as horizontal sills propagating just below the lower density zone. As the magma propagates and cools, the density of the zone rises due to an increase in the relative proportion of dykes to country rock. This is indicated by geophysical investigations that have detected a high P -wave velocity depicting a high density zone beneath the NBZ in Kilauea (Walker 1992).

Additional geophysical studies by Lénat and Aubert (1982) determined high-amplitude magnetic anomalies under the rift-zones of Piton de la Fournaise. These may be explained by the surface load increases, where by successive eruptions add material changing the in-situ density of the upper-most rock which consequently alters both the confining pressure and the pore fluid pressures. This is termed *contractancy*, and can be simply defined as the increased reduction in pore fluid pressure and pore space as a function of depth and confining pressure. As the density increases the dykes propagate at an increasingly higher level, raising the NBZ and thus the magma storage area in the growing edifice. A constant magma supply sustains the NBZ and the resultant rift zone, however

asymmetric loading could cause a lateral migration of the centre of activity and the disproportionate development of the edifice.

The lack of a shallow storage area may be due to the following factors; (i) the rate of magma supply is rapid and the magma is ascending under pressure, forcing the magma to the surface beyond any lower density zone, (ii) the rate of magma supply into the shallow area is insufficient to sustain a substantial shallow storage area, (iii) there is no lower density area beneath the surface that acts to trap the magma. The intrusion of magma creates a self-perpetuating rift-zone system that functions due to the continued ascent of magma in the stress regime of the rift-zone. The magma ascends due to either magma pressure or positive buoyancy to the NBZ. As magma pressure builds up and eventually exceeds the tensile rock strength and the local minimum compressive stresses ($P_m > \text{tensile rock strength} + \sigma_3$), dykes are emplaced. Repeated dyking events in the same orientation, form a wedge that forces the distension of the rift zone, which in turn leads to lateral displacement and maybe collapse. Fresh eruptive products and fracturing above the NBZ then raise the lower density zone (Walker, 1992; Head, 1996). This cyclical pattern may vary due to changes in the magma supply rate. Summit eruptions occur as a result of the rapid emplacement of a strongly enriched magma with a high volatile content. An increase in magma viscosity may affect the prevalent storage and eruption pattern within the edifice as a viscous magma is less sensitive to variations in the density and pressure of the surrounding rock and therefore ascends in a diapiric manner.

1.4.1 Shallow magma transport within rift-zones

Once magma is at shallow depths within an edifice it is either transported passively along an existing fracture, or actively, forcefully propagating to the surface within a pressurised planar crack. The magma is driven by fluid injection which ruptures the surrounding rock in the direction least resistance. Lister and Kerr (1991) outline the relationship of forces responsible for the propagation of a magmatic intrusion such as; (i) the internal propelling forces of buoyancy, (ii)

fluid mechanics (iii) the resisting influences of elastic forces of the host rock on the propagating tip. Magma over pressure required to propagate the dyke is the internal pressure against the tectonic stress, and is illustrated in Equation 1-1. The values are irrespective of units used (Lister & Kerr 1991). The strength of the host rock is termed the uniaxial tensile strength. The lithostatic pressure value depends on the rock type; in Kilauea, Hawaii the magma density is on average 2600kg m^{-3} with the values at the top of the rift-zone being 2900kg m^{-3} and 2300kg m^{-3} at the deepest part (Lister and Kerr, 1991). This indicates that the difference in pressure is around 300kg m^{-3} . The lithostatic pressure changes with depth depending upon magma body pressure, gravity and height.

$$\Delta P_o = \Delta P_i - \sigma$$

ΔP_o = The difference in magma overpressure

ΔP_i = The difference in internal magma pressure

σ = The acting tectonic stress

Equation 1-1 Magma overpressure required to propagate the dyke

The elastic response of the host rock to applied stresses is determined by the elastic parameters, *shear modulus* (μ) and *Poisson's Ratio* (ν). From undertaking laboratory experiments Griggs *et al.* (1960) and Birch (1966) determined the approximate shear modulus of basalt to be 25-35 and the Poisson's Ratio to be 0.22-0.28. Variations in the fractured nature of an entire volcanic edifice due to dyke emplacement, graben formation and contractancy, however, means that such values can fluctuate with depth. Once a dyke is emplaced it will continue to propagate if the magma pressure inside the fracture continues to exceed the strength of the host rock. The internal pressure is indicated by the viscous pressure drop (VPD), which is the velocity of the flow within an intruding body. Lister and Kerr (1991) suggest that the VPD value is approximately 100Pa. Since the propagation rate depends upon the flow within the dyke tip, the viscous pressure drop towards the tip of the dyke reduces the driving force available for continued propagation.

1.4.2 The role of the local stress regime in the operation of rift-zones

The tensile stress of the country rock immediately around the intrusion determines the characteristics of an intrusive episode. Walker (1992) suggests four different scenarios which produce either dykes or sills. Dykes are intruded where the rift either is (i) free to expand laterally, or (ii) a fast spreading ridge. Sills are intruded where the rift is either; (i) buttressed; or (ii,) anchored. While the magma pressure, the density and tensile strength of the host rock determine the characteristics of the magma propagation, the local stress conditions control the orientation of the intrusion. A dyke propagates in a direction perpendicular to the minimum principal strength (whether compressive or tensile). In order for vertical dykes to form in a volcanic cone the minimum compressive stress must be uniform and tangential to the topographic contours of the edifice. Anomalies in the stress regime redirect the dykes into clusters away from the radial norm. These anomalies result in deviatoric stress caused by for example gravitational loading, underlying tectonic stresses and topographic features. Deviatoric stress is the regional lithospheric stress modified by loading, tectonic and creeping influences. Dykes are intruded in the plane perpendicular to the direction of deviatoric tension, confirming that the deviatoric tension must be the minimum compressive stress.

The emplacement of magmatic intrusions is affected by the regional and local stress regimes. McGuire and Pullen (1989) maintain that different intrusive episodes on Etna characterised by the differing orientation of intrusions, are facilitated by alternating stress regimes, see Figure 1-2.

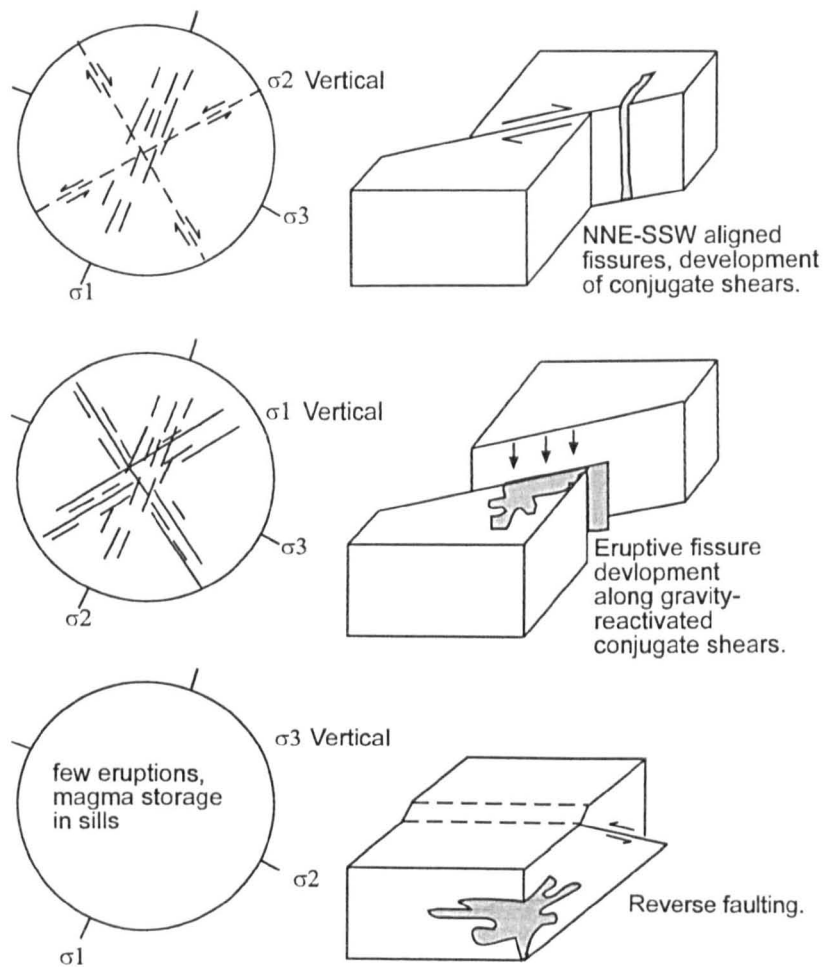


Figure 1-2 The relationship between stress orientation and magma intrusion on Mt. Etna, after McGuire and Pullen (1989).

The authors propose that the dominant NNE-SSW eruptive fissures and tectonic lineament trends on Etna developed when the maximum and minimum compressive stresses were both horizontal, facilitating the development of conjugate shears. When the maximum compressive stress switched to become vertical (most likely due to the increase in magma pressure at depth), the conjugate shears were activated as normal faults facilitating fissure development and surface eruption. Finally, at times when the least compressive stress is vertical, there is no active eruption or intrusion and the magma is stored laterally most likely as sills.

1.5 The role of pore fluid pressures in inducing volcano instability

Magma intrusion causes thermal and mechanical changes that may induce instability within an edifice. Hydrothermal fluids transported within the edifice can change the material properties of porous permeable rocks and unconsolidated debris, weakening the rock by reducing the tensile strength (Day, 1996). The presence of hydrothermal fluids in pores and fractures prior to collapse is realised by the presence of hydrothermally altered material in collapse deposits such as mud rich debris flows. Prior to collapse the presence of fluids may be observed through an increase in the hydrothermal discharge from summit and flank fumaroles. Day (1996) addresses the importance of pore fluid pressures in relation to host rock strength, friction and stress orientation. Changes in pore pressure and the acting stresses affect the host rock changing the critical shear stress required in induce brittle failure, Equation 1-2.

$$\tau_c = \tau_o + (1 - \lambda)\mu s$$

τ_c	= Critical shear stress required to cause slip in fractures or faults
τ_o	= Cohesive rock strength (very small or 0)
λ	= Pore pressure as a fracture of lithostatic load
μ	= Effective coefficient of friction
s	= Stress normal to plane of fracture

Equation 1-2 Brittle strength of material containing a pressurised pore fluid, the derivation of the values used the equations, are explained by Day (1996).

Cohesive rock strength (τ_c) is determined through laboratory experiments on rock samples. This method is sufficient but can not be accurately applied to large bodies of rock, as they would have a smaller value due to internal fracturing. Massive rock has a cohesive rock strength of between 10 and 40MPa while shales have a lower range of 5 and 20Mpa (Day, 1996). Highly fractured rocks are inherently weaker. The effective coefficient of friction (μ) value for immature unlined fault surfaces is around 0.6. This is reduced by hydrothermal alteration, which increases the percentage of clay minerals within fault zones. The value of

pore pressure, as a fraction of lithostatic load (λ) effecting strength, is between 0.001 and 0.4 (but varies with changes in temperature and pressure). If the ratio of pore pressure to entire lithostatic load is less than 1 then this is regarded as over-pressure, (Day, 1996). The actual changes in temperature and pressure that alter the pore pressure and consequently the strength of the rock, arise from the heating of pore fluids by the emplacement of magma bodies into adjacent water-rich sediments. The dissipation of magma-induced temperature and pressure changes is determined by the type and permeability of the surrounding rock. Volcano degassing also increases pore pressure as more fluids are released within the system. If the pore fluids are discharged under pressure from great depths then the *in-situ* fluids are heated by the new hot gases. In addition, the fluids from emplaced magma bodies may be injected into pressurised fault zones, causing the fluid migration seismicity (giving a measurable seismic signature). This may weaken the rocks within the fault zone promoting further intrusions and the development of higher pore fluid pressures, thus sustaining elevated pore fluid pressures within the edifice (Day, 1996).

A high pore pressure as a fraction of the lithostatic load (λ) allows considerable fluid migration and facilitates the dissolution of minerals from the edifice. Where a low permeability zone overlies a high permeability zone the accumulating pore pressures can be released via fractures through fumaroles at the surface. To summarise, a high λ (where $\lambda=1$) eliminates all residual tensile or cohesive strength thus prompting catastrophic failure (Day 1996). Equation 1-2 does not take into account however, the rheology of the host rock or the fault geology, which would be specific to each volcano. As well as the thermal changes discussed above, mechanical changes due to the physical environment of the magma filled fracture can cause displacement of adjacent material. This dilation must be accommodated in the surrounding rock often inducing failure.

1.6 The sources of ground deformation on active volcanoes

Magma-related deformation produces distinct, coherent, displacements reflecting the characteristics of the ascending magma source. As magma rises from depth the overlying rock is placed under increasing stress and typically deforms elastically above the rising body. This was first recognised at Usu, Japan, through precise levelling when inflation occurred just before an eruption (Mogi, 1958). Subsequent studies (on old data-sets) found that concentric inflation was observed during a period of unrest prior to the 1914 eruption of Sakurazima, Japan. Mogi found that the exact pattern of deformation could be used to anticipate the shape of the sub-surface body and analytical models were developed to constrain the actual size and depth of the magma reservoir.

Mogi (1958) also noted (from analysis of Usu and Sakurazima) that there were two distinct zones of deformation; (i) a broad (>5km) zone of concentric inflation that occurred for a period of time prior to the eruption; and (ii,) a smaller zone close to the crater (1-5km), where deformation of several metres (~5m) occurred accompanying the eruptive event. Mogi interpreted the broad deformation in terms of changes in pressure and strain within the crust. The deformation recorded in 1914 took the form of a cycle of inflation, reflecting the ascent of fresh magma and subsequent deflation of the ground surface, due to the fall in pressure caused by magma loss during the eruption. Several metres of deformation were observed in a circular pattern, 60km wide similar to the deformation patterns observed at Kilauea between 1967-8 (Monthly reports at Hawaiian Volcano Observatory¹); due to regular inflation and deflation cycles accompanied by increases and subsequent falls of magma pressure (Appendix A). In this case however the magma was funnelled into the Eastern Rift-Zone through a valve-type system and the material was subsequently erupted (See Figure 1-3) The total deformation observed at Kilauea between 1965 and 1970 amounted to only 80cm, distributed in a near circular pattern over the main summit area of the

¹ Information is from an unpublished report 'Ground deformation recorded on Kilauea from 1970-1980' prepared by the author during 1994 when working as a USGS volunteer at the Hawaiian Volcano Observatory.

volcano. The deformation on the Eastern Rift-Zone was characterised by however, an extension of 2.5m due to the opening of fractures above dyke emplacement (Monthly reports).

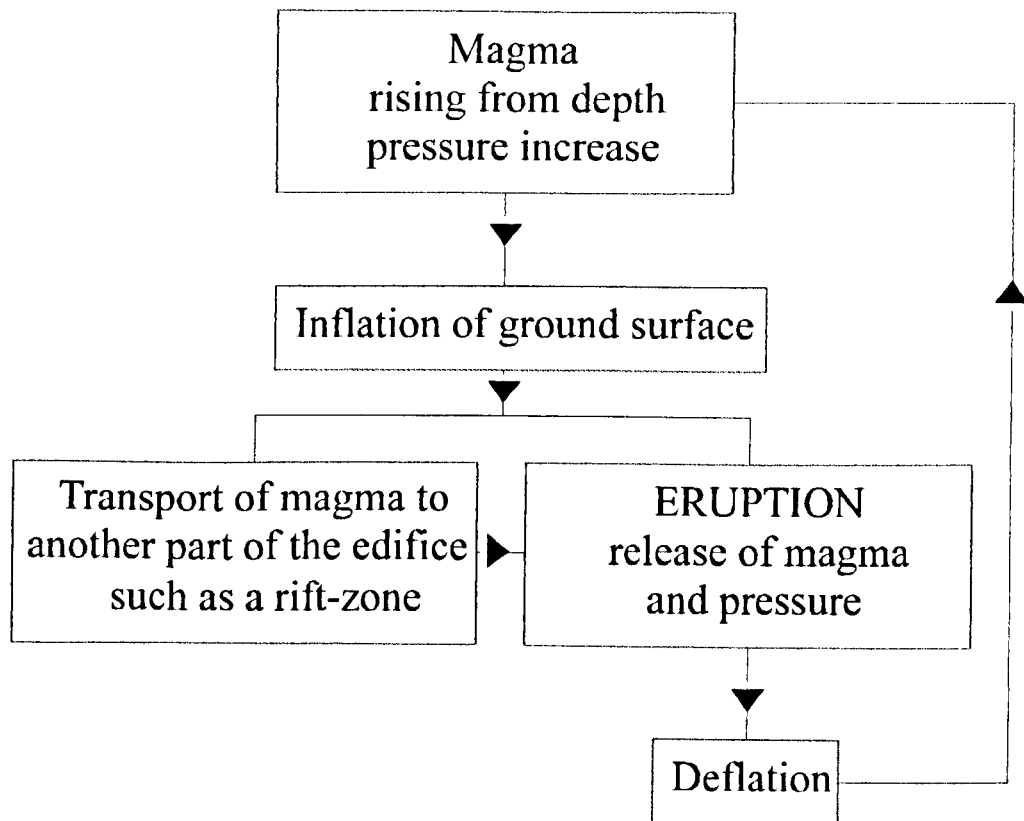


Figure 1-3 The inflation and deflation cycle; A schematic diagram illustrating the cyclical process of magma ascent into the summit storage areas, transport into the rift-zones and eruption.

The more localised deformation observed by Mogi (1958) occurred close to the vent and is explained in terms of the shallow storage of magma in a central conduit system. The deformation reflects the abrupt changes in pressure accompanying the discharge of material during eruption. Deformation observed during the 1983 eruption of Piton de la Fournaise (Lénat *et al.*, 1989a) conforms to the patterns of deformation termed by Mogi (1958) as *upheavals* which were observed close to the centres of Usu and Sakurazima volcanoes.

There was no precursory deformation measured 5km beyond the central conduits and deformation surveys close to the central conduits measured little movement leading up to the initial phase of the eruption. At the onset of activity however, rapid deformation was recorded, taking the form of the edges of the crater tilting

inwards, reflecting shallow magma movements and pressure release in the central conduit system. The intrusion of magma is not always assisted by elastic compensation. If the magma pressure exceeds the tensile strength of the rock, brittle fracturing occurs, forming fractures which propagate along the lines of weakness. The volcanic unrest at Campi Phlegrei during 1968-72 and 1982-84 manifest predominately as radial inflation and subsequent radial deflation. However at the end of each episode some permanent deformation remained, (150cm in 1972 and 100cm in 1984) due to rock fracturing (Barberi & Carpezza, 1996). In-elastic deformation also occurs where the shallow sub-surface is strongly fractured. In such cases the relative displacement of faults and block-bounded areas relieves the accumulating pressures during magma emplacement. During the 1974 eruption of Kilauea for example a series of *en echelon* fissures facilitated the eruption of magma from the Southwest Rift-Zone. At the north-east end of the fissure array, compressive features such as thrust faults and buckles were observed (Swanson *et al.*, 1976). The types of fault observed at the surface provide an indication of the local stress regime under which the eruption is occurring. During the dome-building episode on Mt. St. Helens in December 1980, thrust faults were observed on the crater floor accommodating the intrusion of magma, some extending to around 5 metres seven months prior to the eruption and lateral collapse (Brantley & Topinka, 1984; Iwatsubo & Swanson, 1992).

The 1983 and 1985 eruptions of Etna, both produced surface fissures with associated measured displacements of between 50 and 300cm for adjacent survey stations (Murray & Pullen, 1984; McGuire *et al.*, 1990). The 1991-93 eruption of Etna was preceded by the formation of surface fissures in 1989, overlying a sub-surface fracture extending from the SE Crater for 7km to the south-south-east. Maximum height changes associated with this event were <10cm (Rymer *et al.*, 1993), and the horizontal displacement in total was over 2m (McGuire *et al.*, 1996). The types of brittle deformation associated with these fissure systems represents un-recovered extensional strain. In addition to intrusion-related ground deformation on Etna, Murray (1988) identified localised surface deformation resulting from the weight of lavas down-warping and buckling the ground

beneath. Such deformation recorded using precise levelling methods is particularly obvious in the form of cracks in buildings adjacent to the 1983 lava flow field.

Major ground deformation also occurs as a result of slope failure (which may be indirectly associated with magma movements or eruption). The relationship between the applied shear stresses and the strength of the rock determines the likelihood of slope failure (due to increased external shear stresses or reduced internal shear strengths). Table 1-1 summarises magma-related ground deformation and possible sources of instability that might occur on Etna. These circumstances are not exclusive to Etna and may apply equally to similar volcanic edifices.

Cause	Possible situation
Increased external shear stress	overloading of slope by lavas, especially if erupted continually from the same source vent over a long time
	excess weight at the top of the slope because of the build up of a large cone, or a large area of summit lavas
	lack of seaward support for the slope sometimes due to the presence of an active fault
	a rift-zone, which is being dilated by dyke intrusions
	earthquakes acting as a trigger and dislodging otherwise stable slopes
	faulting increasing angle of slope
	removal of support through phreatomagmatic explosions on the flanks
	caldera collapse or sector graben
Low or reduced internal shear strength	breaching of summit lake in large crater or caldera
	ash layer dipping down slope, overlain by lava. A similar situation would occur when old lava surfaces containing soils were overlain by new flows
	shear strength of ashes covered by lavas reduced by waterlogging and mobilisation by earthquake trigger mechanisms
	increase in pore water pressure, aquifers being trapped behind dykes.

Table 1-1 Potential causes of slope failure that may occur on Etna in response to changes in the internal properties of the edifice and changes in the external applied stresses (After Guest et al., 1984).

1.7 The identification and classification of edifice failure

Gravitational loading may also induce slope instability resulting in creep, slumps and debris avalanches (McGuire 1996). The balance of stresses on an edifice determines the stability of the volcano. Over steepened slopes and fault bounded cliffs can become unstable due to changes in physical properties such as pore-fluid pressure, increased seismicity, or aseismic tectonic displacements. Many volcanoes, including Stromboli (Kokelaar & Romagnoli, 1995), Piton de la Fournaise (Labazuy, 1996), the Hawaiian Islands (Moore *et al.*, 1994), the Canary Islands (Carracedo *et al.*, 1996), and Fogo (Cape Verde) (Day 1998) exhibit scars that indicate previous large scale lateral collapse.

Lateral collapse is a normal part of the growth cycle of volcanoes. As the volcanic edifice grows, the layering of lava flows with hyaloclastic and pyroclastic deposits can form inherent weaknesses. The morphology and the internal stress regime associated with magma-related inflation undergo periodic change. This disequilibrium between the strength of the edifice and the applied stresses produces instability within the edifice, and potentially leads to the ultimate destruction of shield volcanoes (Elsworth & Voight, 1996).

Conceptual models have been developed that propose various influences on the growth, instability and lateral collapse. Borgia (1994) proposes that the relationship between a volcano and the strength of the basement is an important determinant of instability. He suggests that as an edifice grows on a weak basement, it deforms under the additional mass, causing it to be flattened and laterally extended. The basement deforms to produce perpetual ripples and folds at the edge of the volcano pile and the sideways spreading of material develops along a system of thrust faults. Swanson *et al.*, (1976) propose that persistent dyke emplacement within the rift-zones of Kilauea, widens the rifts and laterally displaces unbuttressed flanks, (see Appendix A). Lo Giudice *et al.* (1982, 1992) developed the concept of shallow sliding, suggesting that the increasing gravitational pressure from the growth of the edifice and the persistent magma

pressures are accommodated by brittle deformation of shallow fault structures. They maintain that this is a shallow process and not related to any deeper underlying tectonic movements.

To reiterate, the instability of a volcano is controlled by a balance between the strength of the edifice and the applied stresses. The relationship between these factors is influenced by the internal and external morphology, notably the forms and composition of the internal strata and slope steepness (Labazuy, 1996). The rate of failure types listed in Table 1-2, represent from differing circumstances of one or more types of failure that may be found at a particular volcano. Theoretically, basaltic volcanoes should be stable (relative to non-basaltic steeper, more silicic edifices), and have on average a low slope angle of around 5°-12°, which is less likely to collapse due to the influences of gravity than the very steep slopes (20°-30°) characteristic of predominately andesitic volcanoes. Furthermore the internal structure also determines the cohesive strength and the more explosive andesitic volcanoes tend to be layered with a mixture of pyroclastic layers, pyroclastic flow deposits and fewer lava flows. Pyroclastic layers are generally unconsolidated and are often hydrothermally altered, providing weak layers that act as potential slip planes as a flank becomes unstable. Basaltic volcanoes in contrast have a more homogeneous internal structure with less potential for slip planes to develop. Water causes over-saturation and variations in pore fluid pressure, reducing cohesion and friction. Seismicity also acts to downgrade the form of a slope by breaking bonds, reducing friction and destroying cohesion (Bulmer & Guest, 1996). The classifications discussed above are very general and each individual volcano needs to be assessed independently in terms of the potential for instability development and slope failure.

Name	Type of failure	Deformation and process
Fall	detachment from a single point on a failure surface	free fall, fluidisation, liquefaction, cohesionless, grain flow, thermal and chemical mechanisms.
Topple	detachment from pre-existing discontinuities or tension failure surfaces	as above
Slide (i) <i>rotational</i>	sliding on a plane, circular failure surface	toe area may bulge, override, flow or creep.
(ii) <i>non-rotational</i>	sliding on a plane, non-circular failure surface, a, listric or b, bi-planar	often develops a graben at the head
(iii) <i>translational</i>	sliding on a plane; a, planar, b, stepped, c, wedge, d, non-rotational	may develop into run-out
Spread	lateral spreading of ductile or soft material deforms as a layer beneath a hard rock surface, within a weak inter-stratified layer or a collapsible structure.	spreading, liquefaction
Flow (i) <i>debris flow</i>	debris movement of flow on an unconfined or channelled complex	may develop into run-out
(ii) <i>creep</i>	hill slope, gravitational	pre-failure or progressive creep
(iii) <i>rock flow</i>	gravitational, rotational or compound form listric biplanar	slow gravitational creep in early stages of landsliding
Complex	involving two or more of the above	

Table 1-2 Classification of landslide mechanisms, after Dikau *et al.* (1996)

The types of failure listed in Table 1-2 produce different types of ground deformation patterns, the identification of which can provide information on the timing and type of future failure. Many of the failure types produce precursory tension such as cracking around the head of the unstable body perpendicular to the direction of failure and may precede rockfall, slides or flow events. *En echelon* fracturing or shearing can occur along the lateral edges of the failure body as it becomes mobile; this is recorded at Mt. Etna in the form of the Pernicana and the Trecastagni-Mascalucia Fault Zones (Lo Giudice *et al.* 1982; Rust & Neri, 1996; McGuire & Moss 1997). Creep can occur before failure either

in the form of steady-state creep or tertiary creep, that accelerates towards the point of failure.

Failure of a specific type may often be repeated and identification of previous failure deposits may therefore provide evidence for a forthcoming failure. The two largest and most distinctive landslide types, *debris avalanches* and *slumps* have very characteristic deposits; the differences between them are defined in Table 1-3 using examples from volcanoes known or thought to have undergone lateral collapse.

Features	Debris avalanche	Slump
Morphology of source	amphitheatre source ^{1,3}	steep sided cliffs ^{2,5,6} lack of a well developed amphitheatre ²
Morphology of deposit	hummocky ^{1,3,4} talus slopes from the shore to 2km depth ³ steep marine slopes ¹	width to length ratio > 1 ² physical blocks not broken up ² scarp slope at the toe ²
Size of blocks	up to 1.5km across ^{1,3}	up to and above 1.5km across
Thickness of deposit	varies, can be <50m, distal part is thinner, fan-shaped ¹	thick (usually >10m) and steep ²
Features		slopes are cut by transverse faults ^{2,5}
Emplacement	rapid emplacement in a single episode	failure occurs in periodic events, resulting in aborted collapse scarps ^{2,6} assumed co-seismic

Table 1-3 Emplacement and deposition variations between recognised deposits of volcanic debris avalanches and slumps ¹Piton de la Fournaise, Réunion (Lénat *et al.*, 1989), ²Hilina Pali, Hawaii, (Moore *et al.*, 1989), ³Alika Landslides, Hawaii, (Moore *et al.*, 1994), ⁴Mount St. Helens, 1980 eruption, (Voight *et al.*, 1981), ⁵Cumbre Vieja Volcano, (Carracedo, 1996) ⁶El Hierro, Canary islands, (Day *et al.*, 1997)

Active slumps may creep continuously, as at Kilauea, permitting their displacement to be monitored. In Kilauea, persistent dyke emplacement and eruption of lava along the East Rift-Zone causes the increasing mass of intruded and erupted material to gravitationally load the head of the flank. Slumps may

also undergo periodic displacement. For example at the infrequently-active volcano the Cumbre Vieja Volcano, movement of a slump block caused 4m of vertical displacement during the eruption in 1949 (Moss & McGuire, 1997).

Debris avalanche deposits are significantly different from slump deposits in that they are longer, thinner, less steep, are often disconnected from the source and form a distinctive hummocky terrain (Moore *et al.*, 1989). At the source of the debris avalanche deposit there is an amphitheatre which for older deposits is often eroded away or overlain by younger volcanic deposits. Debris avalanches may be formed by lateral failure that begins as a slump and later accelerates into a debris avalanche. Mount St. Helens displayed catastrophic sector collapse in the form of a debris avalanche during the eruption in 1980; this witnessed event recorded the action and nature of the failure of a volcanic edifice enabling the comparison of the deposition conditions for similar deposits on other volcanoes.

Although slumps and debris avalanches display important differences in terms of operation, they can occur either in succession or through one evolutionary continuum into the other. Rift-related, aborted rift flank collapses are thought to have occurred on El Hierro, where the absence of pressurised fluids in the slump have caused the cessation of movement resulting in the formation of a large normal fault instead of a gigantic volcanic landslide (Day *et al.*, 1997). Piton de la Fournaise exhibits evidence of past collapse in the form of a 8km wide amphitheatre and off-shore debris deposits that originated from the edifice (Lénat *et al.*, 1989; Elsworth & Voight, 1995; Labazuy, 1996; Siebert, 1984). Evidence of both debris flows and slumps were identified by the submarine observations, on the basis of the morphological classification proposed by Moore *et al.* (1989). The submarine deposits included fan-like shapes and block slumps made up of sub-aerial material composed of three distinctive temporal elements, suggesting that they originated from numerous past landslides.

1.8 Summary

Every volcano is a unique construct, the growth of which depends upon the nature of the magmatic products from which it is constructed, the morphology and structure it develops, and the stability of the underlying terrain. Volcanic edifices may be weakened due to the presence of internal discontinuities and as a result of asymmetrical rifting, as well as being further destabilised by erosive processes. Cyclical patterns of growth and lateral failure within volcanic edifices have long been identified with failure elements usually preceded by ground deformation from a magmatic, tectonic or gravitational source, or a combination of these. The precise source determines the patterns of observed precursive deformation; careful monitoring of which needs to construct an image of the current stability of the volcano, its potential for lateral failure and its future activity.

2. DEFORMATION MONITORING AT ACTIVE VOLCANOES

In order to effectively and appropriately analyse acquired ground deformation data it is necessary to be familiar with the two techniques used in the study: Infra-red Electronic Distance Measurement (EDM) and the Global Positioning System (GPS). A detailed understanding of the techniques is particularly required in order to determine the validity of the data in the context of the limitations of the methods. This is especially important when dealing with small movements (<10mm) when the accuracy and precision of the data are crucial. Consideration of the two methods also provides the opportunity to justify; (i) data collection procedures (ii) the change in measurement techniques during the course of field campaigns and (iii) the errors encountered during observations.

2.1 Ground deformation monitoring techniques

This study examines ground deformation recorded during periods of possible volcanic or tectonic unrest on active (but not necessarily erupting) volcanoes, to identify the source and nature of the disturbance. The measurements can be undertaken using a number of different techniques, the choice of which depends upon the nature of the deformation anticipated and logistical constraints. The techniques and processing methodologies applied to measuring ground deformation determine the degree of accuracy and precision of the data gathered.

The different techniques that can be used to monitor ground deformation will all be examined to justify the use of EDM and GPS in this study. Ground deformation monitoring at active volcanoes can be divided into; terrestrial and non-terrestrial. The former category includes: tiltmetry; EDM, precise levelling and the use of strain gauges. Non-terrestrial remote sensing includes GPS and interferometry.

2.1.1 Tiltmetry

There are two principal methods of measuring ground tilt, dry tilt and electronic or water-based tilt. Dry-tilt stations may also be referred to as spirit-level tiltmeters. They normally comprise between three and five stations in an array that covers a specific area of ground surface. The inclination of the area is then carefully determined and monitored by the relative measurement of the height of each station in the array. Electronic tilt and water-based tiltmeters are single items of equipment usually located in either boreholes or lava tubes, they record the changes in inclination of the equipment over time and commonly transmit data to a central control station. The two different types of tiltmeters were installed at Kilauea in the 1950s and have been regularly monitored since (Delany *et al.*, 1993). In 1980, four dry tilt stations were set up at Piton de la Fournaise in triangular arrays with 30m bases, and in 1995 an additional water-based tiltmeter was established in a lava tube. The technique was also applied in Iceland with accuracies of between 2-10 μ rad (Rymer & Tryggvason, 1993). The method is relatively cheap and instruments are easy to construct, install, and monitor. Table 2-2 below lists the advantages and disadvantages of using tilt methods to monitor ground deformation.

Tiltmetry	accuracy depends on technique used
<p>Main advantages</p> <ul style="list-style-type: none"> ✓ Inexpensive equipment (basic tilt apparatus) ✓ Permanent measurement of radial and tangential tilt possible with fixed apparatus. 	<p>Main disadvantages</p> <ul style="list-style-type: none"> ✗ Only tilt of ground directly beneath apparatus or network measured. ✗ Local movements complicate data. ✗ Water tilt apparatus need to be housed to reduce meteorological interference. ✗ No overall amplitude and spatial extent of vertical and horizontal deformation is recorded. ✗ Resetting equipment is necessary after a large tilting event.

Table 2-1 Advantages and disadvantages of using tiltmetry to monitor ground deformation.

2.1.2 Precise Levelling

Precise levelling measures changes in the relative elevation of permanent survey stations over a period of time. A graduated rod and a level are used to measure elevation changes from one point to another situated about 30-50m apart with an accuracy of ~0.1mm being achieved in ideal conditions. A string of points with intermediate markers may be used so establish the relative heights over a long distance (normally <10km). The accuracy for a levelling transect is represented as the standard deviation (for the observed elevation), multiplied by the root of the distance of the transect. This is represented in Equation 2-1 where 0.2mm is taken as the standard deviation (Murray *et al.*, 1996). To maximise the potential accuracy levelling is usually completed in each direction along the transect.

$$\sigma(h) = 0.2mm\sqrt{\text{distance}}$$

Equation 2-1 The standard deviation error (σ) for the levelling transect.

Precise levelling has been used on active volcanoes: from 1896 at Sakurazima (Japan) and from 1923 at Yellowstone Caldera (USA). The technique was also used in combination with tide gauges to record periods of inflation at Campi Flegrei (Italy) between 1968 and 1972 and 1982 to 1984 (Barberi & Carapezza, 1996). The method is straightforward in terms of set up, measurement and data processing, with relatively low capital and running costs. Table 2-2 summarises the advantages and disadvantages of the precise levelling technique.

Levelling	Accidental $<\pm 1 \sqrt{\text{km}}$ or Systematic $<\pm 0.2 \sqrt{\text{km}}$
Main advantages	Main disadvantages
<ul style="list-style-type: none"> ✓ Most accurate method to measure relative vertical heights. ✓ Inexpensive equipment (basic level & staff), little training needed. ✓ Data reduction can be done without the use of a computer in the field. 	<ul style="list-style-type: none"> ✗ At least two people are needed for each survey. ✗ Atmospheric data needs to be recorded to reduce error to a viable accuracy. ✗ Needs to start from a known (vertical) benchmark.

Table 2-2 The advantages and disadvantages of using the tilt monitoring methods. 'Defined by the International Geodetic Association (1912) cited in (Murray *et al.*, 1996).

2.1.3 Strain gauges

Strain gauges measure the displacement between two points or between two faces of rock. A number of different types of gauge exists ranging from graded rods or wires to monitored laser beams spanning voids in the rock. The technique is very versatile and can be implemented in boreholes and fractures. Sophisticated strain gauges were used to determine ground deformation during the 1991 eruption of Hekla in Iceland (Sigmundsson, 1996).

2.1.4 Electronic Distance Measurement

Electronic Distance Measurement is designed primarily to measure distances and distance changes between fixed points. Many current systems are of the *Total Station* type combining the Infra-red EDM and theodolite. In use the instrument is set-up over a benchmark at one end of the line to be measured and a retro-reflector (which may consist of 1 to several corner-cube prisms) is located over another at the other end such that the line-of-sight is not obscured. The corner-cube prism located on the retro-reflector is an array of mirrors that reflects incoming waves directly back at the radiation source. An electromagnetic wave is transmitted from the instrument and reflected back from the other end of the line. By comparing the number of whole and partial wavelengths reflected over a

known period of time, the user may compute the distance and vertical angle of the line.

The technique was developed during World War II and has been used in ground deformation surveying since this time, with extensive trilateration networks being established in Iceland in 1966 and Hawaii in 1970. There are networks on most of the volcanoes of the developing world including Etna (McGuire *et al.*, 1990; Murray *et al.*, 1996; Bonnaccorso *et al.*, 1990); Piton de la Fournaise (Bacheléry *et al.*, 1990), Hawaii (Delany *et al.*, 1990; Denlinger & Okubo, 1995), Mt. St Helens (Iwatsubo & Swanson, 1966). Advantages and disadvantages of the method are summarised in Table 2-3.

EDM		accuracy ±3-5mm +2-5ppm
Advantages	Disadvantages	
<ul style="list-style-type: none"> ✓ Distances can be calculated in the field. ✓ Rapid data reduction ✓ EDM cheaper than GPS 	<ul style="list-style-type: none"> * Line-of-sight necessary between benchmarks. * Clear, dry weather is essential for readings. * Line lengths are measured, co-ordinates must be derived from relative positions. * At least two people are needed for each survey. 	

Table 2-3 The advantages and disadvantages of using the EDM method.

2.2 Non-terrestrial ground deformation monitoring

Remote-based techniques use non-terrestrial based equipment such as satellites to monitor ground deformation changes from an aerial perspective. Digital elevation models created from images are compared over time to identify changes in surface morphology. The most accurate technique uses differential synthetic aperture radar interferometry. Comprehensive models of the ground surface are logged and centimetric changes in the ground surface are analysed. Interferometry was first applied in Iceland in 1991 to create a digital elevation model accurate to a few metres, adequate only monitoring very large scale deformation. On Etna,

however, centimetre scale accuracies were achieved in 1992-93 during a survey undertaken during the second half of the recent eruption (Massonnet *et al.*, 1995). Although the results were acceptable, they differed from terrestrial results obtained using EDM and precise levelling and problems were encountered by seasonal snowcover (Murray *pers com*).

Interferometry		~3cm ¹
Advantages	Disadvantages	
<ul style="list-style-type: none"> ✓ No location and occupation of benchmarks on the ground is necessary. ✓ Any areas along the satellite orbit can be measured. 	<ul style="list-style-type: none"> ✗ Survey field is limited to satellite paths. ✗ Confused by impermanent (e.g. snow) or non-stationary cover (e.g. vegetation). ✗ Large movements can cause interference fringes to overlap and deem the images unusable. 	

Table 2-4 Remote-based ground deformation monitoring techniques. ¹ Massonnet *et al.*, 1995.

2.2.1 The Global Positioning System

GPS works by establishing the distances from the known position of satellites orbiting the Earth to unknown positions on the Earth's surface, through communication between ground-based receivers and satellites. The constellation of orbiting satellites is maintained from ground-based control centres who transmit information on satellite location and status. The system was originally developed for military use by the United States Government in the early 1980s and has been adapted for civilian use since 1985. GPS is gradually taking over in many situations from terrestrial surveying techniques. GPS was first used for ground deformation surveying in Iceland in 1986 when 51 survey stations were established covering most of the island (Sigmundsson, 1996). The network was especially dense in the southern part of Iceland and provided a broad framework for future work including later volcano deformation studies. Advantages and disadvantages are summarised in Table 2-5.

Global Positioning System		Δ Line length = $(0.6 \pm 0.5 \text{ mm}) + (0.1 \pm 0.1 \text{ mm km}^{-1})^1$
Advantages	Disadvantages	
<ul style="list-style-type: none"> ✓ Position co-ordinates are relative to geoid. ✓ No line-of-sight needed between benchmarks. ✓ Not reliant on clear, dry weather. ✓ Yields 3D vectors with no need to combine different techniques. ✓ Easy to set up, one operator required with little training. 	<ul style="list-style-type: none"> ✗ No accurate real-time positioning. ✗ 15° above the horizon sight-to-satellite is required. ✗ The equipment is often heavy in the field (~25kg) ✗ Complex data reduction is needed for high accuracy. ✗ Line of sight required for real-time GPS ✗ Sufficient sky view required with no obstructions such as trees or buildings 	

Table 2-5 Advantages and Disadvantages of the application of the Global Positioning System to ground deformation monitoring. (¹Hoffman-Wellenhof, 1997)

2.3 Choice of methods for this study

The most applicable techniques to use to monitor rift and fault-related ground deformation are EDM and GPS. These techniques are accepted due to the following reasons:

- (i) The data need to be as precise as possible (<20mm)
- (ii) GPS can detect height changes to a similar accuracy to precise levelling
- (iii) Sections of the GPS networks can be used as tilt array.
- (iv) EDM networks were in place already at Mt. Etna and Piton de la Fournaise over the rift-zones prior to the start of the study.
- (v) A network set up using EDM can usually be easily adapted to be measured using GPS (when it becomes available) or to be maintained within a broad GPS network.

Both EDM and GPS measure networks of survey stations, using a network of survey stations, which are periodically measured to assess the ground deformation. To establish the context for the application of the techniques, the set-up and limitations of a *network* will be examined first.

2.4 The establishment of a ground deformation survey network

The ground deformation network is designed to meet the objectives of the study, maintaining the following specific requirements;

- (i) the spatial positioning of the network must be able to meet the objectives of the study
- (ii) the level of accuracy required must be obtainable with the available hardware and software in the required time.

The measurement of a ground deformation network is designed to detect small changes in the surface (in the horizontal and vertical plane). This is undertaken by either measuring the precise absolute co-ordinates or by measuring the distance and vertical angles between survey stations. A network is designed so that the baselines form groups of triangles making up braced quadrilaterals or centre-point polygons (Figure 2-1)

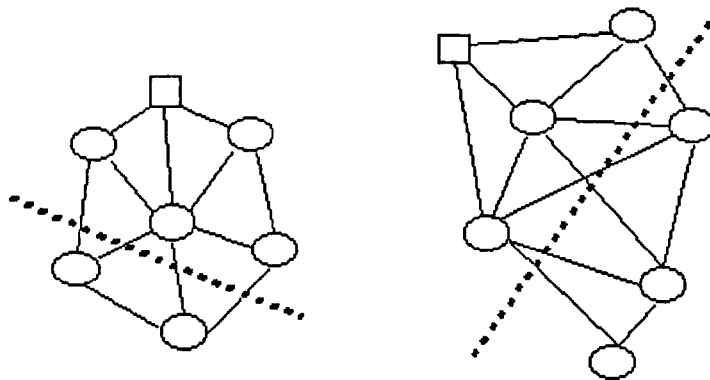


Figure 2-1 Geometric network polygons, the triangle represents the reference point, the circles represent the survey stations and the thick grey lines represent a rift-zone or a fault. Polygon a is an ideal network with an evenly spaced polygon shape, while b represents a more realistic, irregular network.

This geometry facilitates mathematical cross-checking of network data as many redundant measurements are recorded that are used to adjust the network (see section 2.5.3) and highlight major errors. Networks are designed such that no horizontal angles are less than about 20-25° while the shape and density of the benchmark distribution provides sufficient data to interpret the relative causes of

recorded deformation. Network design also depends upon the technique used to undertake the measurements, as different techniques have distinct spatial and temporal requirements. As many existing networks are designed for the EDM method they may include aspects unsuitable for GPS such as close proximity to metal objects or a restricted sky view. Network occupation is undertaken to obtain the current positions of the survey stations, quickly and accurately. At least one of the survey stations in the network is used as the *reference station* (square survey station in Figure 2-1), this is presumed stable and is held fixed between survey occupations.

Before field reconnaissance, the study area is examined on a topographic map, a geological map and where possible, aerial photographs. Geomorphological features, boundaries and access to the area can be assessed from the topographic map, and areas of geological relevance can be identified from the geological map. Analysis of both maps allows the optimum locations for the survey stations to be plotted on the base-map. Rough distances between the stations are measured, so that occupation times can be estimated. In addition, major obstacles and likely metal reflective surfaces (such as farm buildings or pylons which would make the use of GPS problematic) are noted and existing control stations located. It is also possible to identify which survey stations would be suitable for use as reference stations in terms of access, electrical supply and safety. Pre-measurement field reconnaissance affirms the suitability of survey station sites in terms of access, sustainability and line-of-sight (either to other stations or in terms of unobstructed skyview).

The type of survey marker adopted depends upon the terrain. The terrain of the selected volcanoes is mainly packed ash, scoria layers and thick lava flows, with occasional large boulders. The main form of monumentation is zinc-coated steel survey nails hammered into deep-anchored rocks. Some massive blocks from within lava flows are resistant to even steel nails and for these holes are drilled into the rock and small nails or discs are inserted and fixed with glue. In the more unconsolidated areas with no suitably-stable rocks, reinforcing rods >50cm in

length are hammered into the substrate. To an extent they remain stable and firm. Such methods of station monumentation have been tried and tested on Etna over a number of years (Murray *et al.*, 1996; Saunders 1997, un-pub thesis). It is important for any survey marker that the centre of the marker is obvious and can be located precisely for each survey. On Etna, nails are often pulled or chipped out by curious tourists and suspicious shepherds, and steps taken to cover the nails with cairns, boulders and piles of scoria do not unfortunately always deter persistent vandals. The solution in some cases where recurrent loss of survey markers occurs, is to paint vesicles in rocks (with waterproof paint). A good station description describing the precise situation of the vesicle and the centring over the paint allows accurate repeatability. On all selected volcanoes one or two stations can be expected to be either lost or destroyed each year.

When potential sites are chosen, they are located on a map and rough co-ordinates in the local system are noted (using a handheld GPS receiver). When survey stations are established the 'to reach' description is written including bearings to nearby easily recognisable features such as a peak or a volcanic cone.

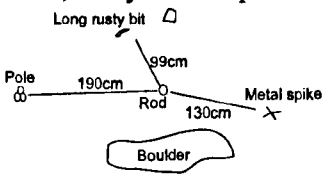
Station Code	Station name	Date Established	Height (m)
e48	Montagnola	1981 as e9, re-established 1993 as e48	2640
Location		Type	Co-ordinates
Ascend the summit road past the Piccolo Refugio, turn right heading upwards towards the top of the ski lift at the base of Montagnola. Walk up and along the ridge along to the aerials. The nail is by a large boulder.		Disc, rusty misshapen disc.  190cm from the triple pole, 99cm from the rusty spike, 130cm from the X shaped spike.	4881431.530 1308571.478 3882341.110

Figure 2-2 An example of a station description from Mt. Etna showing the to-reach description and approximate co-ordinates.

The description includes distances along roads or paths and centimetre measurements to close-by objects such as trees or distinctive rocks. If the station is not close to any clearly identifiable features then approach photographs are included and rough bearings are taken to distinctive features. An example is shown in Figure 2-2, simplified stations descriptions are listed in Appendix B.

2.4.1 Measurement errors

In order to identify and distinguish instrumental, set-up and other errors from the *real* volcanic or volcano-tectonic movements of a survey the potential causes of error are recognised for each occupation, estimated and removed. This is conducted within the post-processing software. Different types of errors result from different aspects of the survey procedure and processing. *Measurement errors* are false readings that have occurred during the observation and include inaccurate siting over survey stations, failing to account for temperature and pressure variations in the field and misreading values. Errors can be minimised by adequate reconnaissance, operator training, the accounting for tropospheric interference and adhering to a *standard operating procedure*. *Booking errors*

occur when the user enters the wrong information into the instrument or the booking form. The booking information for EDM surveying includes: tripod height, temperature, pressure, details of position and time, distance and vertical angle readings. Inaccurate input of height may add significant gross errors to the final position and this value should be measured at the start and end of the benchmark occupation. Vibration including tremors from a volcanic source or nearby heavy traffic may effect data readings and data from sustained periods of vibration should be discarded and the position re-recorded.

Gross errors are mistakes made in the measuring and recording of data. By examining the data by eye large unexpected anomalies can be highlighted. Although the survey is set up to detect large changes, gross errors will not fit the anticipated deformation patterns that would result from a *real* event. The GPS technique has the disadvantage that accurate cross-checking is not possible during survey station occupation, and therefore post-processing needs to be conducted in the field. Systematic errors exhibit a bias which will affect all the measurements in a survey, for example using an uncalibrated thermometer or reading an error in a satellite orbit for all survey stations. Since these errors follow a mathematical bias, this effect on an instrument can be calculated, accounted for and removed. Any additional bias on the equipment can be identified through field tests.

Random error includes all non-systematic errors such as set-up errors or user errors that apply to only part of the survey. When all other known errors are removed, a series of repeated measurements taken under the same conditions will still show some variation. These variations are random errors, and are the unaccountable difference between the measured value and the real value. Since the real value is never known, the mean value is used (this is the precision). The mean value of a precise network has only a small deviation from the expected mean value. Accuracy is measure of the *truth* of a value and although the precision may be good the accuracy may be poor if, for instance, the whole network is skewed by a mathematically determinable amount.

2.5 Total Station: Electronic Distance Measurement & theodolite

A brief explanation of the EDM method was given in section 2.1.4. In order to justify the accuracies obtained within this research a more detailed description of the technique is provided here. Measurements are undertaken by positioning the total station (EDM and theodolite combined) at a survey station at a high elevation. This ensures good line-of-sight to a large number of other survey stations (as the EDM requires line-of-sight between benchmarks). The set of retro-reflectors are mounted in turn on each of the visible survey stations and the lines are read. This is repeated until all the lines in the network are measured either using a survey station in the centre of the network as a reference or leap-frogging around the network, moving each set of equipment onto the next station. The Total Station is mounted on a tripod using a *tribrach*, this fixture levels the equipment on the tripod. The tripod is positioned over the survey marker and accurately positioned over the point using a tribrach with an optical plummet. Then where appropriate either the Total Station or set of reflectors are attached to the tribrach and the measurement is made. The horizontal distance and vertical angle are recorded in a notebook along with tripod height, temperature, pressure and time of reading. For each day the equipment used, date, weather and operators are noted. The EDM works by transmitting electromagnetic waves to a reflector and measuring the time it takes for the wave to return. Electromagnetic waves are the means by which electrical energy is transported through an electromagnetic field. Wavelength variation is controlled by modulating the electromagnetic fields. The distance is calculated by adding the number of whole and partial wavelengths reflected back to the instrument by comparing the phase of the generated signal with the phase of the reflected signal, see Equation 2-2. Since the signal travels to the reflector and back, the distance required is half the distance measured.

The wavelength and the cycle are determined by the electrical source producing the wave but the speed depends upon the medium through which it travels,

specifically, variations in the temperature and pressure of the air along the length of the baseline. To determine the baseline distance to the required precision the *phase angle* is also used. This is a measurement which determines a value for each part of the wavelength; the start is 0°, the middle is 180° and the end 360° (Burnside, 1991).

$$D = L + n \left(\frac{c}{f} \right) = 2r$$

D = total distance travelled by the signal

n = the integer number of wavelengths

L = the fraction of the wavelength recorded if the value is not an integer

c = speed of light in a vacuum

f = the frequency of the signal

r = the required range between the total station and the reflectors

Equation 2-2 The calculation of the distance measured by infra-red Electronic Distance Measurement.

Variations in temperature and pressure must be recorded and taken into account. Readings are taken at each end of the line and averaged to provide an estimate for the influence of the temperature and pressure variations along the baseline. A temperature difference of 1°C can affect the final distance reading by 1ppm, while a pressure variation of 3mmHg (mbar) may produce a 1ppm variation. Humidity does not effect the reading provided temperature variations along the baseline are not greater than 25°C (Burnside, 1991). Long lines with large height differences between the benchmarks can incur significant errors if the variations are not accurately estimated. Other atmospheric influences that may affect readings include heat shimmer that affects target acquisition, high winds (which increase vibration), and specific volcano related effects such as heat shimmer from lava flows and hot fissures, and dense gaseous plumes. Pointing errors involve failure of the operator to aim the instrument exactly on target and are aggravated by aforementioned environmental conditions such as heat shimmer and volcanic plumes together with rain, cloud and obstructive vegetation. Repeated measurements (at least 5) are undertaken in order to reduce the magnitude of the errors to a minimum. Experience has shown that lines over 2km experience *pointing errors*, although these can be minimised by always using the same

procedure to position the instrument cross-hairs i.e. from the left and then down to the target using the fine tuning.

Internal instrument errors are usually systematic and are checked through field tests and by the manufacturer. They include; (i) *scale error*, due to variations in the modulation frequency (this is particularly noticeable in long lines), (ii), *zero error*, caused by incorrect calibration of the mechanical, electrical, and optical centres of the instrument. Many internal systematic errors can be detected and compensated for by taking measurements from *face-left* and *face-right* (measurements using the optical sight in two different orientations) and averaging (mean) the result.

Sokkia Set3c Total Station	Type	Estimated error
Distance measurement error ¹	Random	3mm + 3ppm
Vertical angle measurement ¹	Random	±3"
Temperature 1°C variation ¹	Random	1ppm
Pressure 3mmHg variation ¹	Random	1ppm
Setting up error	Random	1-2mm
Internal instrument errors	Systematic	unknown
Prism pointing	Random	±0.5-1mm

Table 2-6 The range of errors experienced the Sokkia Set3c Total Station used in this study. (After Uren & Price, 1994)

2.6 The Global Positioning System

Transitions to GPS from EDM have been undertaken by deformation measurements on most of the closely monitored volcanoes in the world. The trilateration network on Kilauea, Hawaii established in 1970, has been measured using GPS since 1993 (Sigmundsson, 1996) while GPS was first introduced on Mount Etna, Sicily in 1988 (Nunnari & Puglisi, 1994b).

The technique provides three basic survey modes; (i) *static*, (ii) *rapid static* and (iii) *kinematic (& real time kinematic)*. Static and rapid static are used in this

study. These techniques use both *relative positioning*, often referred to as *differential GPS*, in which a stationary receiver is positioned as a reference at a known survey station and additional *rover* receivers are used to occupy unknown survey stations. Data are processed to obtain rover positions relative to the stationary reference receiver. Shorter occupation times and specialised processing techniques make rapid-static surveying quicker but less accurate than static surveying. The fast efficient application of the technique, however, makes it preferable to use in time-limiting circumstances. In kinematic GPS, a stationary receiver again acts as a reference, but in this case the rover is within line-of-sight to the satellite maintaining reception of the satellite signals at all times, thus producing a constant path of data as the rover moves around the network..

2.6.1 Basic principles

Satellites provide a means for identifying longitude, latitude and height for any point on the surface of the Earth, using long range trilateration. The position of a satellite at a given point in time (relative to the *geocentre* of the Earth) is transmitted on an encoded signal from each GPS navigation satellite orbiting the Earth. These signals are received by GPS antennae positioned on the Earth's surface. The clock in each GPS receiver is, in theory, set to exactly the same time as the satellite clock. The receiver notes the time of arrival of the signal and compares this time with a *departure time-tag* encoded onto the signal (which records when the signal was emitted). The time difference between signal transmission and reception is used to calculate the *range*. Signals from all the satellites visible to the receiver are collected. Clock differences between the receiver and the satellites however, add an additional clock bias making the calculated range just a *pseudorange*. This pseudorange is multiplied by the clock bias and the speed of light to obtain the real range. The satellite is not stationary in time and space however, and the Doppler Shift in the transmitted signal must also be accounted for (Hofmann-Wellenhof *et al.*, 1997). This is an alteration in the signal frequency, that occurs due to change in distance between the signal source (satellite) and the receiver.

The Global Positioning System is divided into three segments; (i) space, (ii) navigation and control, and (iii) user (Wells *et al.*, 1986; Blewitt, 1997). The *space segment* refers to the orbital satellites that transmit the encoded signals. At any time at least 24 satellites orbit the Earth on six orbital planes oriented at 55° to the equator at a height of 20,183km (See Figure 2-3). From any point on the Earth's surface at least four satellites (and usually between six and nine) are in orbit above an elevation of 15° . Due to orbital parameters each satellite appears in the same part of the sky four minutes earlier than the previous day causing the geometry of the visible satellite configuration overhead to vary over time from a given point.

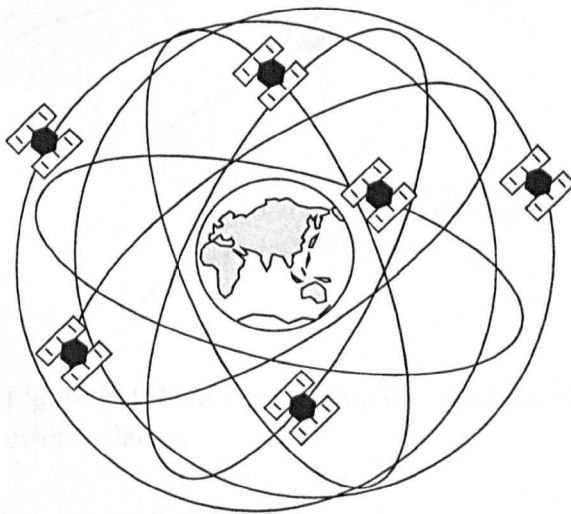


Figure 2-3 The GPS constellation, showing the rough satellite orbits around the earth. Each satellite in the diagram represents a number of satellites; between three and four travelling along the orbit.

Each satellite transmits an encoded signal, that is received by the antenna. The satellite does not however generate its own signal, the signal information and its *ephemeris* are determined by the master control station within the control segment. The ephemeris are the predicted positions of a satellite during a specific period. Orbital characteristics (*broadcast ephemeris*) are predicted through the measurement of successive ranges to the satellite. Errors do, however, occur when the satellite does not follow the orbit that has been predicted for it due for example to satellite propulsion errors or inaccurate ephemeris calculation at ground control. Because of this possibility, the precise actual satellite orbit is later calculated by the navigation segment and subsequently published (in an unrestricted NASA ftp account) as the *precise ephemeris*.

The encoded signal is transmitted at 10.23 MHz (the oscillation of the satellite's atomic clock). It is modulated onto two carrier waves (L_1 and L_2) that are multiplied by 154 and 120 respectively. The code information is included through binary-phase modulation, this is accomplished by multiplying the electrical signals by either 1 or -1 and thus inverting sections of the carrier wave. This enables the unmodulated carrier wave to be restored through multiplication by 180° . The signal is boosted by an amplifier and transmitted towards Earth as an electromagnetic wave, where it is detected up by GPS antennae, see Figure 2-4.

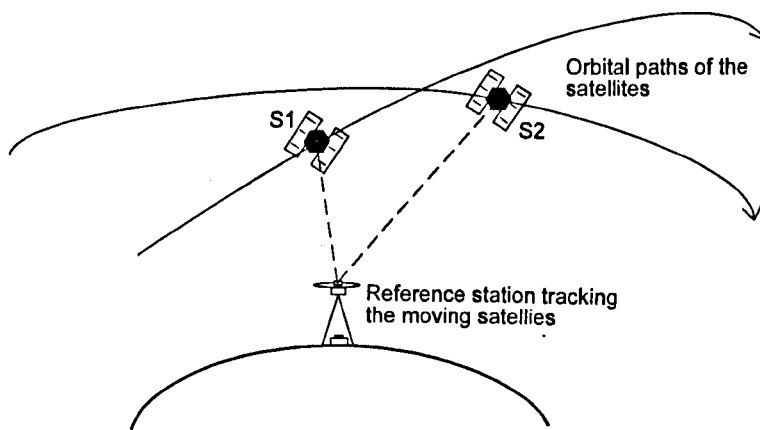


Figure 2-4 Receiver tracking the satellites (S1 and S2) as they move along their orbital planes.

L_1 is a carrier radio band transmitting at 1575.42 MHz. This wavelength is modulated by a *course* or *acquisition* code (C/A code), a *precise* code (P code) and a navigation message. C/A code comprises a *pseudo-random noise* (PRN) which acts to identify the satellite, and a repetitive binary modulation that contains the time of transmission. The P code is a further PRN repetitive binary modulation; it is changed every 267 days, and is encrypted by *anti-spoofing* and restricted by *selective availability*. L_2 is a carrier radio band transmitting at 1227.60 MHz, and is modulated by the P code. An additional navigation message is transmitted at 50 MHz, and includes information on clock corrections, satellite health status, almanac data, ionospheric conditions and the predicted satellite orbit.

The P code has a 3m wavelength and the incorporation of the code in processing facilitates accurate positioning, consequently the United States Government (that operate the Global Positioning System) denies full access to the code by non-military users. Access is denied through the application of two errors; selective availability (SA), which *dithers* the satellite clock and changes the broadcast ephemerides, can be eliminated when pseudoranges are *differenced* between two receivers or by using the correct precise ephemerides published a few days after signal receipt. Anti-spoofing (A-S) denies the use of the P code by either switching the code off or by adding an encryption. This encryption prevents any source from broadcasting a false imitation of the P code. When A-S is switched on the P code is modulated by an algorithm known to the United States military, called the *W code*; the modified P code is then referred to as the *Y code* (Hofmann-Wellenhof *et al.*, 1997). *Most importantly for this study the selective availability and anti-spoofing errors are eliminated when relative (differential) GPS surveying is undertaken.*

When a GPS receiver is occupying a survey station, the data-logger displays signal strength and the time required to obtain a position. The primary indicator of accuracy is the *geometric dilution of precision* (GDOP). This reflects the orbit geometry of the visible satellites, such that if the visible satellites are all close together then the GDOP would be high (above 8) and if they are spread evenly over the visible sky then the value would be low (around 2 or 3). If the GDOP is greater than eight then the observation is automatically rejected, although in practice for the best results, data are rejected by the user if the GDOP is greater than four.

GPS satellites obtain all their broadcast information from the *control segment*. This consists of five tracking stations positioned around the world with the main station at Colorado Springs in the United States. The functions of the control stations are to monitor the GPS signals, predict orbits, and establish the 'health' of the satellites. Three of the stations transmit signal data to the satellites updating their orbits, navigation and health status. The *navigation segment* is more closely

linked to the *user segment*, providing a civilian tracking network for reference control and the publishing of the actual satellite orbits (Wells *et al.*, 1986). Many institutions across the globe make up the navigation segment with the main organisations being the US Surface Weapons Centre (Wells *et al.*, 1986) and the International Global Positioning Service (IGS). The main objective of these bodies is to provide a support service for GPS users in the form of precise ephemerides, earth rotation parameters, the co-ordinate and velocity information for the tracking stations, satellite and receiver clock information and data on ionospheric conditions. The tracking stations and data centres collect and freely publish the data for general use.

The *user segment* is made up of civilian users and their GPS instruments. A user receives the signal and processes it to establish the position of the receiver. The type of signal processing undertaken depends upon the receiver type. Single frequency receivers only receive the L_1 carrier wave and dual frequency receivers record L_1 and L_2 . The advantage of the dual frequency receiver is that the delay of the signal by the Earth's ionosphere can be calculated through time difference in the reception of both signal frequencies. Multichannel receivers can receive the maximum number of available satellite signals and many can now process the C/A code and the P code in a combination of code and carrier phase processing.

2.6.2 Processing GPS data

The fundamental basis for signal processing is the comparison of the received satellite signal with a receiver generated duplicate signal. The receiver produces the C/A code sequence and has a duplicate PRN code for every satellite. There are two main types of processing; *code* and *phase*, and receivers use a combination of the two. *Code processing* entails the receiver issuing a code until it correlates with the satellite-generated code. The wrong PRN code will mean that the signals will not correlate. When the codes are fully correlated the start time of the satellite-generated signal is known and the time difference calculated. This value is irrespective of any clock error between the satellite clock and the

receiver clock. A distance measurement based on the correlation which has not been corrected for clock bias is the *pseudorange*. The Doppler shift and the navigation message are also retrieved. The code pseudorange from the receiver to the satellite is derived from the sum of the time difference, the range and the clock bias, each multiplied by the speed of light.

Phase processing examines the L_1 or L_2 carrier signal, looking at the number of complete and partial wavelengths received, and also taking into account clock bias. The navigation message contains information so that the satellite position and the clock bias can be computed. The satellite signal is multiplied by the receiver-generated signal giving a *beat signal*. This *carrier beat phase* is thus the difference between the satellite and receiver signals; the beat phase can be understood even when the carrier wave is modulated.

Point positioning determines the location of a receiver without reference to another position while *relative positioning* requires knowledge of the location of a secondary point. In the later case the occupied point is then processed as a known point, this maybe either a location identified by point positioning (such as a national survey benchmark) or a permanent GPS tracking site. The accuracy and precision obtainable in locating unknown survey stations varies according to the GPS mode used, so the basic principles are outlined below.

Point positioning involves the identification of an unknown site by a single receiver. There are four unknown parameters; the three site co-ordinates (x, y, z) and the receiver clock bias. If there are four satellites or an atomic clock in the receiver, then the number of *known values* is greater than the number of *unknown values* and the latter can be computed. The term *differencing* is used to describe the comparison and cancelling of two or more common elements within the signal processing. The objective of differencing is to reduce the number of unknowns. The processing algorithm differences the satellite signals and cancels out the common receiver units and systematic errors.

Single differencing is similar to point processing but the receiver variables change, such that the equation is calculated taking into account different values for two or more receivers, labelled A and B shown in Equation 2-3. Thus common systematic satellite errors and any common satellite measurements such as clock bias are cancelled out, reducing the number of unknowns.

$$\Phi_{AB}^j(t) = \frac{1}{\lambda} r_{AB}^j(t) + N_{AB}^j - f\delta_{AB}^j(t)$$

Φ = pseudorange
 t = time of observation
 λ = wavelength
 i = receiver (A and B)
 r = range
 δ = clock bias
 f = frequency
 j = satellite
 N = (integer) number of cycles

Equation 2-3 Single differencing formulae and key

Double differenced uses two or more receivers which are differenced with at least four satellites. The frequency and the clock bias is assumed to be the same for both satellites and is therefore cancelled. Equation 2-4 is the double differencing equation.

$$\Phi_{AB}^{jk}(t) = \frac{1}{\lambda} r_{AB}^{jk}(t) + N_{AB}^{jk}$$

Equation 2-4 Double differencing

For single and double differencing the calculations take place in a single time frame. In order to look at changes over time *triple differencing* is applied. Ambiguities which are common to either satellites, receivers or time are cancelled out, such as the number of cycle integers. Equation 2-5 is the phase pseudorange equation for triple differencing.

$$\Phi_{AB}^{jk}(t_{12}) = \frac{1}{\lambda} r_{AB}^{jk}(t_{12})$$

where $t_{12} = t_1 \dots t_2$ etc.

Equation 2-5 Triple differencing

Relative positioning locates an unknown site relative to a known stationary site, through the processing of the reference and rover stations together (Figure 2-5). The position of the reference station is entered manually at the start of processing and the offset between the entered position and the position calculated is applied to the rover thereby cancelling out common errors.

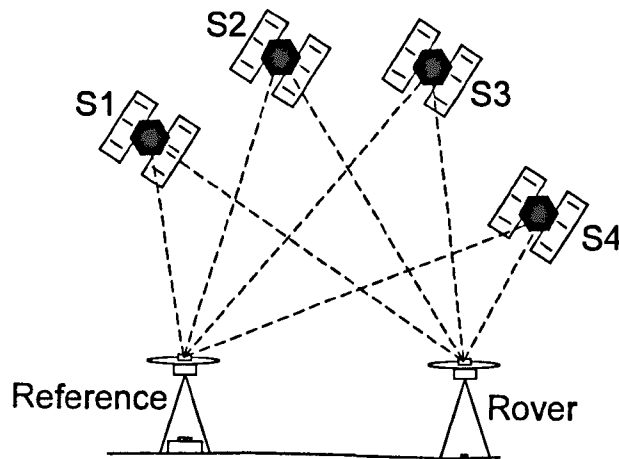


Figure 2-5 Relative positioning using reference and rover receivers and four satellites (S1-S4).

Rapid static relative surveying uses the *Fast Ambiguity Resolution Approach* (FARA). FARA is an algorithm that makes statistical assumptions about the data and reduces the set-up time required for the resolution of ambiguities. Processing uses a combination of code and phase measurements on the L_1 and L_2 carrier waves. The method is limited to receiver baselines up to 10km in length and is accurate to approximately $5\text{mm}+1\text{ppm}$. Distance and elevation change between the two stations is represented as a vector, see Equation 2-6.

\underline{b}_{AB} = Baseline vector

A = the position of the reference

B = the position of the rover

Equation 2-6 Baseline vector between two survey stations

Locations are represented as vectors \underline{X}_A and \underline{X}_B . To locate the second position, the first position is multiplied by the baseline vector. Initially, a preliminary (float) carrier phase solution is computed using double differencing. The best sets of ambiguities are selected, according to the confidence intervals of the

ambiguities. Least squares adjustment is undertaken with each set of the statistically-accepted fixed ambiguities. The solution with the smallest standard deviation and variance is further investigated. If the final fixed ambiguity is better than the original floating value then it is accepted.

Table 2-7 describes the steps performed during the individual baseline processing. Although most software processing executes multi-baseline processing this table provides a simplistic description of the various stages of processing. When processing is completed the investigation and analysis of the results is crucial in estimating the quality of the data. The main aim of the processing is to *fix* the integer ambiguities using double-differencing. The quality of this fix is depicted in the ratio between the *fixed* and the *floating* values (non-fixed ambiguities). Each estimated value is also appraised in terms of its statistical confidence, represented by the *variance co-variance matrix*. The floating values are the values calculated through the triple-differencing and the initial double-differencing. The *root mean square* (rms.) of the fixed value should be less than two or three times the original triple differenced rms. value. The ratio between these values indicates the quality of the fix. Another check is whether the ambiguity value is near to an integer in the single differencing between a satellite and each receiver. Poor ranges to specific satellites can be identified and problem satellites removed from the processing. The final check is to compare the positions with data from previous surveys.

Processing steps for Static processing	
1.	Generation of orbit files.
2.	Computation of the best fit values for the point positions from the code pseudoranges.
3.	Creation of the undifferenced phase data from the receiver carrier phase readings and satellite orbit data. Time errors may also be corrected.
4.	Creation of differenced phase data and computation of their correlations.
5.	Computation of an estimate of the vector using triple-difference processing. This method is insensitive to cycle slips but provides least accurate results.
6.	Computation of the double-difference solution solving for vector and real values of phase ambiguities.
7.	Estimation of integer values for the phase ambiguities computed in the previous step, and the decision whether to continue with fixed ambiguities.
8.	Computation of the fixed bias solution based upon best ambiguity estimates computed in the previous step.
9.	Computation of several other fixed bias solutions using integer values differing slightly (e.g. by 1) from selected values.
10.	Computation of the ratio of statistical fit between chosen solution and the next best solution. This ratio should be at least two to three, indicating that the chosen solution is at least two to three times better than the next most likely solutions.

Table 2-7 GPS processing steps (after Hofmann-Wellenhof, *et al.* 1997, page 170).

2.6.3 Network adjustment

When any bad observations and lines have been removed from the collected data, the network can be adjusted using least squares adjustment. This balances all the vectors within the network, adding small changes to the vector components to create a 'flat' geometric figure (Hofmann-Wellenhof *et al.*, 1997). Adjustment is weighted according to the *vector correlation matrix* and the standard errors. If the network has not been processed from a fixed position, then a fixed adjustment is undertaken, whereby the grid co-ordinates are transformed onto a known stable reference co-ordinate (measured during the survey as a relative position) and the network adjusted as before. Accuracy is presented in terms of the *a posteriori* loop misclosures and the error ellipse values. Errors of less than 10mm + 10ppm

at the 2σ confidence level can be classed as first order surveys (US Standards).

Table 2.3 indicates the estimate of precision using the rapid static method.

Source	Error
GPS manufacturers estimate (broadcast ephemeris)	5mm + 1ppm
Set up errors	4mm
Unaccounted for tropospheric variation	2ppm
Total	6mm + 3ppm

Table 2-8 Estimate of total GPS precision taking into account user and equipment errors.

Processed data are presented in the global co-ordinate datum *WGS84*. The surface height is relative to the centre of the Earth (*the global geoid*). The *orthometric height* is the height from the geoid to the unknown position on the surface. Variations in the geoid can be detected by calculating the geometric height minus the orthometric height (usually <100m). The horizontal datum is the *geocentric reference ellipsoid*. The *geometric height* (*h*) is the distance from the ellipsoid to the unknown point.

2.6.4 Biases

Many potential sources of error are encountered when using GPS to determine unknown positions. *Biases* differ from errors since they represent deviations from a true value or reading due to a specific effect. Table 2-9 lists the common biases and their sources.

Source	Type
Satellite	Satellite clock bias
	Orbital bias
Signal propagation	Ionospheric refraction
	Tropospheric refraction
Receiver	Antenna phase variation
	Receiver clock bias

Table 2-9 Potential biases in GPS data from the satellite, signal and the receiver.

The effect of ionospheric refraction can be eliminated using a dual frequency receiver and thereby comparing the two carrier waves. This does not however, eliminate tropospheric bias since the carrier waves are not affected in the same way. Tropospheric refraction is modified due to varying amounts of water vapour along the signal path to the satellite. Modelling of water vapour is normally however, undertaken by using an appropriate model - often contained within the GPS software. If conditions are very different at the reference station and the rover then, wet and dry humidity and temperature readings are collected at each receiver and modelled to estimate the *wet path delay* along the *line-of-sight*.

Receiver biases reflect the quality of the receiver, the most common results from an antenna phase centre offset. This adds an error if the antenna is rotated 180° and the phase centre does not remain precisely above the survey marker and can be simply reduced by always rotating the antenna to north during signal reception. The cheaper clocks built into receivers have a bias that is calculable; atomic clocks with no bias could be used but would make receiver costs prohibitively expensive.

Random GPS errors are more complex, since they show no correlation between receivers and signals and cannot be cancelled out during double or triple differencing. They are caused by random effects and lead to unpredictable modifications to the data. The most common of these is *multipath*, a phenomenon caused by the bouncing of signals off adjacent metal objects prior to reception. This causes multiple reflections of the signal that are subsequently picked up by the receiver, causing the range of the signal to change. Multipath effects can be eliminated by ensuring that the site of the receiver is away from reflective surfaces such as wire-mesh fences, metal buildings and reflective structures. *Cycleslips* are breaks in the recording of the signal, and can occur during the measurement of the carrier beat phase. They represent a discontinuity in the counting of integer cycles in the receiver. Temporary loss of lock causes the counter to reinitialise and therefore miscount. Fortunately most processing software will mend a few cycleslips with no alteration to the result. Additional

errors may occur if, for example, the antenna phase centre changes during data collection due to unforeseen physical interference.

2.7 Observation procedures

Set up procedures aim to minimise all types of GPS error. Before a survey station is measured, all vehicles are parked at least 10m away to prevent multipath effects. The antenna is mounted on a tripod in a similar way to the Total Station using a tribrach. The height to the phase centre is read and input into the receiver with the antenna offset. At each site the date, the station name and code, the antenna height and any abnormalities are noted in the field notebook.

Prior to the commencement of the survey the receiver is pre-programmed with sampling information and survey limitations, with each receiver used in the survey being initialised to ensure that they are compatible for processing. The sampling rate is set - usually to ten seconds - to determine how often the data are stored. While the timing of sessions is synchronised between the reference receiver and the rovers. Where possible (depending on the system used) the approximate baseline distance is input into the receiver to determine the occupation time or manually calculated. This does not affect data collection and can be modified for each occupation. Due to the likelihood of unforeseen delays such as battery failure, the loss of a station or equipment failure, communication is maintained throughout by the use of two-way radios. *The GPS mode used within this study is static and rapid-static relative positioning using either single or dual frequency receivers. The choice of methods used depended upon the hardware and software available but the general survey techniques are described below.*

Static positioning requires a long occupation of survey stations (>60 minutes) by stationary receivers, while a quasi-static survey involves a periodically repeated static survey to examine changes over time. Co-ordinates of a reference point are

either determined through a long observation time at the station (<six hours) to acquire enough data to fix the location, or the network is linked to an existing stationary point which is monitored continuously and has accurate up-to-date coordinates. This latter type of survey is appropriate for volcanoes since no survey stations can be confidently assumed to be stable. From the reference point either a static or rapid static survey can be completed. Rapid static GPS works by setting-up one receiver at a known point and the rovers moving among unknown survey stations viewing common satellites for a short period of time. The occupation time for a rapid static depends upon the make of equipment and the baseline length between the rover and reference, and is usually between 5 and 20 minutes. The baseline length between the reference station and the rover station is input before measurement begins and the time needed to resolve the ambiguities is determined by the receiver software.

2.8 Critical discussion of techniques & problematic issues

The use of ground-based EDM surveying systems limits ground deformation network design in two principal ways: firstly, survey stations can only be located such that each station is visible to at least two others, secondly, station separation has a maximum measurable baseline length of <2.5km (with the Sokkia Set 3c Total Station). The integration of survey stations in distal networks would require the establishment of potentially hundreds of intermediate benchmarks. These two problems are not issues for satellite surveying systems, since inter-visible survey stations are not required and the overall accuracy is controlled by the processing of satellite signals not by measurement to adjacent survey stations. Some of the problems encountered when operating a Total Station in the field do however, apply to satellite surveying since the GPS receivers themselves are ground-based and dangerous terrain, deep snow, lightening and volcanic activity can disrupt measurements. Meteorological phenomena such as rain, snow flurries and cloud do not, however, impede GPS readings.

2.9 Summary

The transition from IR-EDM to GPS has provided an opportunity to re-define objectives and to improve the spatial quality and accuracy of ground deformation at the volcanoes in the study. On Etna and Piton de la Fournaise it has become possible to integrate distal survey stations and networks into a single, comprehensive network combining both short and long baselines. Consequently it is now possible to measure large networks within two weeks to provide a *picture* of the deformation. This has enabled, on each of the volcanoes in the study, relative movements of survey stations within the networks to be compared, in order to constrain the deformation over the rift-zones and the adjacent flanks.

Expansion of a network also permits the addition of further survey stations at strategic points in order to improve network density in areas known to be sensitive to minor movements or to act as relatively stable reference points. If the survey stations were established originally to form a trilateration network, consisting of inter-visible points, then most of the survey stations are located on elevated positions.

To ensure a satisfactory transition from EDM to GPS, it is recommended here that one of the following three procedures should be followed;

- (i) reject the existing EDM network and design and establish a new GPS network as undertaken on Etna by Nunnari & Puglisi (1996)
- (ii) maintain the original and re-measure for at least one year using EDM and GPS as undertaken on the Cumbre Vieja and the Lower Eastern Flank Network of Etna within this study
- (iii) re-measure the network using only GPS if the volcano is within a sustained period of quiescence or if only one set of equipment is available as undertaken at Piton de la Fournaise within this study.

The choice of transition method depends upon the activity of the volcano and the resources available. In order to maintain a long term record of measurement of a

sensitive network, it is however, necessary to re-occupy the original survey stations using GPS. Gradual adjustments to the network and the removal of redundant survey stations can be conducted when the successful transition is complete.

3. DATA REDUCTION AND ANALYSIS

As previously mentioned deformation at the ground surface of active volcanoes can occur as a result of many different factors. The aim of this study is to separate the various deformation sources and influences in order to determine the causes of the observed displacement and their potential effects. In this context, reduction and analysis of the acquired data are crucial.

Deformation data acquired during this study are compared where possible with an existing baseline data-set. This baseline data-set is a set of co-ordinate measurements taken during an inter-eruptive period when no major volcanic or volcano-tectonic event has occurred. On Etna the baseline data-set since the end of the last eruption in 1993 was obtained by Saunders & McGuire (1995) and on Piton de la Fournaise the original measurement of the network was undertaken in 1993 by Saunders (*unpub-data*). There is no network established on the Cumbre Vieja Volcano. Where possible data-set comparisons identify differences between the new and existing data-sets that may be due to errors or *real* movements. When sources of error have been removed any *significant* data remaining is analysed and numerically simulated to construct conceptual models that attempt to explain the current eruptive status (and stability) of each volcano.

3.1 The ground deformation data

The *true* positions of a network are determined through an initial baseline survey. A baseline survey involves the comprehensive measurement of the physical and chemical characteristics of the non-erupting volcano. This is typically undertaken as part of a comprehensive monitoring program that includes deformation and seismic monitoring to establish background levels, and also normally encompasses the measurement of background gas & fluid geochemistry together with the thermal signatures of fumaroles and well water. This thesis focuses entirely on the ground deformation element of such a baseline survey. Interaction

of acquired deformation data with that obtained using other geophysical techniques such as measurement of micro-gravity or seismicity has however been used to improve the interpretation of the results. Deformation monitoring provides a crucial tool for detecting pre-eruptive tumescence and fracturing and is vital to any eruption early-warning system. The baseline monitoring strategy should be established ensuring that the monitoring is feasible and sustainable during long periods of volcanic repose.

An initial baseline deformation study typically utilises a few survey stations forming a network covering a small area that is known to have actively deformed prior to previous eruptive events. When significant ground deformation or other indicators of impending activity occur, the area under investigation is widened. Baseline deformation network occupation has three principal functions to determine; (i) background 'noise' in the form of small changes which might occur for example due to long-term slow deformation (explained further in section 3.1.2), (ii) the operating error (accuracy) of the measurement method or (see Sections 2.3.2; 2.5.4) and, (iii) the absolute locations of the survey stations in other words, the initial station co-ordinates from which all future displacements are determined.

When baseline observations show mean changes *below* the expected level of accuracy then the volcano can be considered for the moment quiescent and stable. Changes in the position of survey stations during such periods are typically very small, between 4 and 10mm. The first signs of an impending eruption may taken the form of a slight rise in background 'noise', although this may be difficult to detect at volcanoes such as Etna that display high background deformation 'noise' levels for example due to continuous degassing, deep magma transport and local structural instabilities.

3.2 Sources of ground deformation

When a volcano is constantly degassing from open vents the background deformation levels often creep above the margin of expected errors and since the increases may be pre-cursive to a future eruption such changes although small maybe significant and must be carefully considered. Although large changes (>10cm) accompanying shallow intrusions of magma are easily observed, the smaller changes (<5cm) associated with an increase in degassing, deep magma transport or even tectonic activity may indicate a change in the internal plumbing of a volcano in advance of an actual eruption.

It must be stressed here that the ground deformation surveys undertaken as part of this study do not focus specifically on eruption forecasting, rather they seek to identify flank movements associated with instability, and as such must continue to monitor the flanks in the event of minor summit activity such as at Etna between 1995-1997. The commencement of a summit eruption or a deep intrusion may not be the climax of the eruption episode and a *current* baseline state must be quickly ascertained, in order to detect changes in behaviour which may indicate further larger eruptions or flank instability. The detection of *real* movement initially results from the identification of *outliers* in the data-sets. These are single values that indicate a change in co-ordinate position beyond the error margins of the technique are most likely (in individual cases) to be due to instrumental or set-up errors. Real movements on the other hand are attributable to physical changes in the volcano within the confines of the ground deformation network, and may range from a few millimetres to tens of centimetres or metres. A sufficiently dense network spanning a large enough area will detect such real movements at more than one station and will be able to distinguish a coherent deformation pattern for the area. As previously mentioned most volcanoes inflate prior to eruption in response to increased pressure due to magma emplacement at shallow depths. Observed fluctuations in the data at such volcanoes represent the actual changes in the position of the ground surface in response to fresh magma intrusion, but complications in the data-set may also arise due to variations in the elasticity of the sub-surface. Magma intrusion within a volcano may lead to

elastic inflation of the surface. This may be due either to forceful intrusion by the magma or to the release of hydrothermal fluids or pore fluid pressure changes accompanying magma emplacement. Where intrusive forces exceed the elastic limits of the host rock brittle failure occurs, often leaving permanent surface fractures. Intrusion may occur through opening of existing fractures and fissures creating relatively minor surface deformation. This will, however, be identifiable due to its coherent pattern (i.e. points each side of the fracture moving apart in opposite directions). Surface deformation also occurs after an eruptive event, typically as a consequence of deflation following the eruption or withdrawal of magma, the compaction of eruption products and increased surface loading. It is crucial that such effects are taken into account when baseline deformation monitoring is initiated shortly after an eruption.

Ground deformation on active volcanoes may also occur due to non-magmatic sources. For example, tectonic activity in the form of earthquakes or micro-seismicity may occur due to the presence of major fault beneath or adjacent to the volcano, unconnected with volcanic activity. Slow (sporadic or continuous) deformation may also occur in the vicinity of steep slopes. In such situations pore pressure changes from water saturation causing loss of cohesion and reduced friction may cause escalation of such creep-like behaviour, leading to mass wasting in the form of rockfalls, debris avalanches and mud slides.

3.3 Data collection, reduction and analysis

The data are represented as either changes in measured line length between survey stations or a shift in the co-ordinate location of the survey stations. Observation may either be of individual stations within a specific area, for example in the vicinity of an active fracture or vent, or they may be combined in a network to form a picture of deformation over a wider area. The co-ordinate shift of a survey station is termed the *station velocity*, which determines vertical or horizontal linear motion over a period of time. The velocity vector is

calculated from a least squares estimate, using the co-ordinates and the variance covariance matrices. Figure 3-1 illustrates stages in the acquisition and analysis of EDM data from field observations to derivation of the final co-ordinate. The step after the production of the co-ordinates is the comparisons between different data-sets.

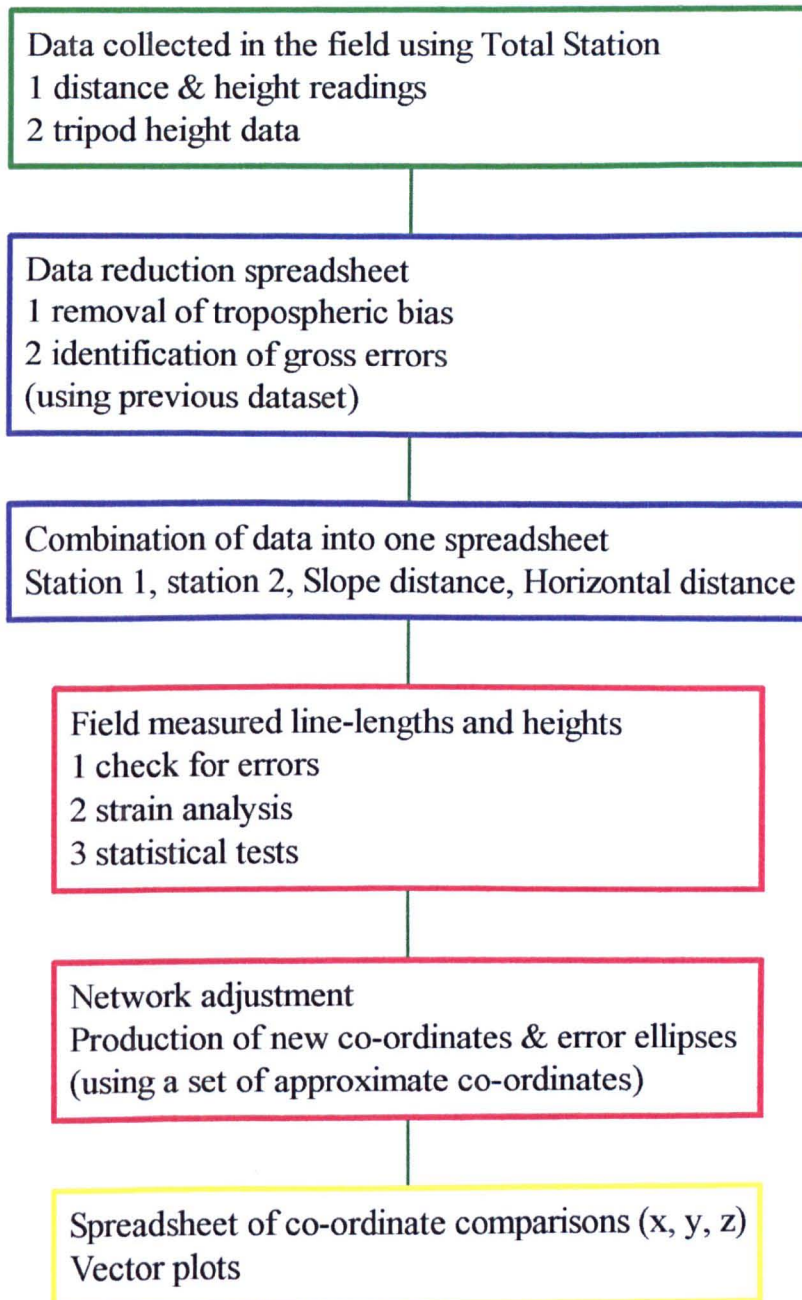


Figure 3-1 Flow diagram illustrating EDM data reduction; green (top, 1) = field collection of data, blue (2,3) = initial data reduction, red (4,5) = data processing and adjustment; yellow (bottom, 6) = output of co-ordinates.

3.3.1 EDM data processing and resolution

Data collected from the Total Station is recorded onto spreadsheets to easily remove the bias resulting from the pressure and temperature differences at each end of the measured line (Section 2.4). Data from the notebooks is entered into a spreadsheet to determine the exact horizontal and vertical distances between two survey stations. At this stage, gross errors are identified if the value is very different the measurement from a previous occupation (if available), such erroneous line lengths can then be re-measured during the same survey to verify the result. The data are then ready for analysis. For each survey station changes in line-length, strain, and station velocity are initially compared with data collected during previous occupations. As the EDM data commonly reveals a part per million (ppm) error then the actual change in line-length may be skewed by the length of the line which is measured. Statistical tests undertaken on the data from Etna (see Section 5.7) confirm that there is a - largely unsurprising - statistical correlation between long line lengths and larger errors. Because of this, when analysing EDM data the strain value (see below) is generally used in preference to the line length change in millimetres, unless the repeatability of the technique is being assessed.

Strain is determined by examining the change in line length relative to the length of the baseline it is measured in ppm. error, Table 3-1 and Equation 3-1 exemplify the procedure.

Baseline	1995	1996	Change (m)	Strain (ppm)
8-10	778.049	778.052	0.003	3.86

Table 3-1 The baseline between 8 and 10 on Etna, 1995-6 EDM and GPS data.

$$(778.052-778.049)/778.049 \times 1000000$$

$$[(\text{new line-length} - \text{old line length})/\text{new line-length} \times (1 \times 10^6)]$$

Equation 3-1 The determination of strain using Table 3-1.

In order for three dimensional co-ordinate displacements from successive occupations to be compared the data must be transformed from line lengths to co-ordinates. Two programs are used in this study to undertake this task: AG3D (Ruegg & Bougault, 1992) and LSXY (Crook, 1983). In this study, both programs undertake a new approach in network adjustment, as the new co-ordinates are defined using an approximate set of GPS co-ordinates to outline the spatial distribution of the survey stations. Both programs both follow the same basic principal; within a network the azimuth of one vector and the height of one survey station is held fixed. A least squares estimate is then applied to fit the measured vectors to a set of vectors calculated from an approximate set of co-ordinates. The estimates of error for each co-ordinate are represented by a standard a posteriori error in parts per million and an error ellipse. If the network appears to be rotated around a particular survey station then the data are corrected using a spreadsheet-formula (Pullen *pers com*) to rotate back until no element of rotation remains.

To reveal the real displacements within a data-set the expected error must be determined. Since this includes both random error and survey specific systematic errors, calculations and estimates for the levels of error must be made for each survey and this is done by assessing repeatability. To measure repeatability, distances between pairs of benchmarks in a trilateration network are measured in consecutive surveys. Although it has already been observed that using the strain values is preferable to comparing line lengths, only the latter is used in determining repeatability. In order to evaluate the measurements and the measuring methods (EDM vs. GPS) fully the strain and the line length changes must be compared. The following method compares line lengths and identifies the error *for each survey* in millimetres and ppm of line lengths, thus allowing comparison of the values obtained and the methods used. The distances measured in one survey subtracted from those measured in a successive survey, are plotted as a function of distance for each baseline in the network. The systematic bias and variation between measurements of distance L can be represented by a linear

relation, shown in Equation 3-2 (Nunnari & Puglisi, 1995; Uren & Price, 1994; Savage, 1997).

$$dL = L_{EDM} - L_{GPS}$$

dL is plotted against the baseline, error bars represent 1 standard deviation.

Equation 3-2 Baseline differences between two surveys using one or two different methods e.g. EDM and GPS.

In order to assess repeatability between two data sets Nunnari and Puglisi (1996) use the plot of baseline length versus line length change. To estimate the 'error' or precision as a function of line-length increase. This is represented by the linear expression in Equation 3-3.

$$\sigma = \alpha + \beta L.$$

L = baseline length, α = (random + systematic) error and β = error (ppm) of the baseline length.

Equation 3-3 Network precision (sigma) taking into account survey errors.

The linear expression represented in Equation 3-3 (σ) represents the maximum expected error (systematic + random) for a survey. Measurements beneath σ are close to the mean and beneath the level of expected change, while measurements between σ and 2σ indicate either large random error or minor *significant* real movements. Measurements $>3\sigma$ indicate gross errors, very large random errors and major *significant* real movements. The term significant is used in this study with reference to data in excess of 2σ .

3.4 Statistical Tests

Statistical tests can determine trends and relationships between and within data-sets. They are used in this study in order to statistically determine the significance of any trend within a data set or between two data sets that might either skew the data or reflect a change in time. Very large errors skew the normal distribution

curve and must be removed if any statistical analyses is to be carried out. These arise from large random errors such as unaccounted temperature and pressure variations over long baseline lengths and from real movements such as flank eruptions or dyke emplacements. Large errors identified here will be the same as those identified in the repeatability test to be $>2\sigma$ or 3σ . Any benchmarks that do not fit the curve are noted and removed from the test. When all major significant movements and gross errors have been removed the resulting list of differences can be presented as a normal distribution curve. If the data set of differences fits a normal distribution curve then the following assumptions can be made;

1. Small errors occur frequently and are more probable.
2. Large errors occur less frequently and are less probable.
3. Positive and negative errors of the same size are equally probable.

To undertake the statistical correlations a *parametric* test is used. This was chosen because exact numerical values are to be correlated and the data follows a normal distribution with an even variability of values. The *Pearson product moment coefficient* (r) was used as a measure of the amount of linear dependency between two variables which make up a suspected trend within the data sets.

$$r = \frac{\{nS_{xy} - S_x S_y\}}{\{[nS_x^2 - 9S_x]^2 - (S_y)^2\}}^{0.5}$$

Equation 3-4 Calculation of the Pearson product moment coefficient (r).

The result, r reflects the amount of correlation of a number between -1 and +1. -1 reveals a perfect negative correlation, where a low value for one variable corresponds with a high value for the other variable and 0 indicates no correlation while +1 is a perfect positive correlation such that a high value correlates with another high value in the other set of variables. The observed value of r is compared with a standard statistical table which lists the magnitude of the absolute value of r which must be exceeded if one is to reject the null hypotheses. The null hypothesis in this case states that no correlation exists between the pair of variables under consideration as a function of the degrees of freedom ($v = n - 2$, where n = number of pairs of observations) and the level of risk.

Once the real movements have been identified and their reliability statistically proven, they are analysed to deduce their meaning and significance. The first step is qualitative speculation, for instance the elevation of survey stations may indicate that there is magma ascending beneath, or the recognition of groups of coherently moving stations may indicate differential movement of shallow blocks. Although qualitative speculation is a valuable tool, quantitative analysis through numerical modelling serves two functions; (i) to better constrain the most likely deformation sources and (ii) to quantitatively define specific physical parameters such as the dimensions of an intrusion responsible for a deformation event.

3.5 Numerical modelling

Numerical modelling is the mathematical representation of areas (two dimensional) or objects using known and assumed physical values to create a conceptual model which will respond as realistically as possible to simulated events. Such events for example the emplacement of a dyke, are imitated by the adjustment of the physical parameters of the model.

Mogi (1958) devised one of the first volcano-related mathematical models in order to explain ground deformation above an inflating magma reservoir, specifically with uplift associated with activity of the Sakurazima volcano (Japan) in 1914 (see Section 1.5). The model assumes a small buried sphere of varying pressure, within a larger block (elastic halfspace where the elastic Lamé coefficients are equal). Mogi varied the pressure of the sphere and analysed the vertical and horizontal deformation on the top surface of the larger elastic halfspace (representing the ground surface). The model data were compared to observed deformations, measured on the volcano by precise levelling and triangulation. The main limitation of the model is that the radius of the sphere must be less than the depth to the surface, making it less useful for shallow or unspherical bodies. Furthermore the observed deformation on real volcanoes

depends more upon changes in the hydro-static pressure within the sphere than other factors such as the size or depth of the sphere.

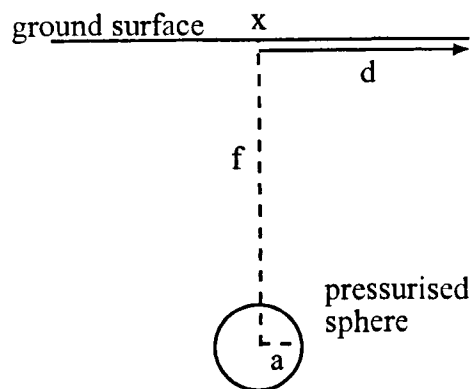


Figure 3-2 Mogi's buried sphere model; a = radius of sphere, f = depth to sphere for the surface, d = changes in horizontal deformation of the 'ground surface', x = the point on the 'ground surface' above the buried sphere.

When using a Mogi type model an assumption is made that the material properties and boundary conditions used within the model to achieve the displacement values detected by observed displacements at a particular volcano, are constant for that volcano (at the present time). This allows further simulations to be run where one or more of the parameters are absent. For example, if the surface displacements are known from observation, then excess magma pressure in the reservoir can be determined.

The Mogi model assumes that the point on the surface above the buried sphere divided by the radial distance on the surface from x (See Figure 3-2) is less than or equal to 1. Further numerical modelling has however shown that even where the value is equal to 0.5 the surface deformation only deviates slightly from the original model (Dieterich and Decker, 1975). Equation 3-5 and Equation 3-6 outline the mathematical formulae used to devise the horizontal and vertical changes in the surface of the elastic half space.

$$\Delta d = \frac{3a^3 p}{4\mu} \frac{d}{(f^2 + d^2)^{\frac{3}{2}}}$$

- x = point on the surface above the buried sphere
 d = radial distance on the surface from A
 f = depth of the centre of the sphere from the surface
 a = radius of the sphere with the hydrostatic pressure
 p = change of the hydro-static pressure in the sphere
 μ = Lamé's constant
 Δd = horizontal (or radial) displacement on the surface
 Δh = vertical displacement on the surface

Equation 3-5 Horizontal change on the surface of the elastic halfspace as a result of the intrusion of a buried source (Dieterich & Decker, 1975).

$$\Delta h = \frac{3a^2 p}{4\mu} \frac{f}{(f^2 + d^2)^{\frac{3}{2}}}$$

Equation 3-6 Vertical change on the surface of the elastic halfspace as a result of the intrusion of a buried source, for definition of variables see Equation 3-5, (Dieterich & Decker, 1975).

A further limitation with the Mogi model lies in the fact that it is only applicable for a *point source dilation*, and as a consequence represents only uniform pressure change for the expansion of a spherical reservoir. Observations of the eroded remnants of ancient volcanic edifices reveal, however, that the formation of small spherical magma reservoirs is unlikely. Such drawbacks led Dieterich & Decker (1975) to simulate surface deformation patterns from other shapes. The models developed by Dieterich & Decker use simple geometry to model dykes of different thickness', they assume elasticity throughout, and incorporate a range of dips and their ensuing surface deformation patterns. They firstly applied their models to dyking events on Kilauea, finding a close correlation between observed and simulated values. One outcome of this work was the recognition that gravity-related horizontal stresses in the Kilauea rift-zones were also important - in addition to magma pressure in rift-zone dilation. Dieterich & Decker's models for deformation associated with dykes has since been applied to Etna (Sections 4.6 & 5.8) and many other volcanoes.

In recent years computer-based, graphic-input, finite element modelling had become increasingly important in modelling and visualising volcano deformation data. The FEM software used in this study is Quickfield™, in addition to examining the ground deformation data the study also investigates the usefulness of this package to study volcano-related deformation. FEM uses known parameters to estimate unknown ones, and is able - in the context of volcano deformation - to quantify stress and strain relationships through the simulation of an internal pressure source within a host block, with the gross properties of a volcanic edifice. FEM is a reductionist technique in which the engineering properties in terms of stress and strain, of the structure under investigation, are realised by dividing the object of interest into smaller, simpler units. These smaller, defined units or *elements*, are finite in size and have properties pre-determined to define their *simulated physical identity*. When changes are included in all the discrete elements of the model, for example by means of an applied stress, the effects on each element are resolved individually forming a new object.

Known data are input and modelled to determine unknown parameters, the model parameters can then be modified and the further surface displacement compared to observed measured ground deformation data. FE models can provide much visible information for example areas of a model showing the largest strains with the least displacement can be determined and may indicate areas susceptible to future brittle failure and, therefore possible sites for future dyke emplacement. Models can be developed in series, for example incorporating propagating fractures within a defined geometry, thereby shedding light on dykes emplacement and rift-zone processes.

A FE model contains three components;

- (i) geometric parameters such as dyke dip and topography,
- (ii) physical parameters such as magma pressure and Young's Modulus
- (iii) geological structures such as faults and fissures.

A FE model is a two-dimensional construct with pre-determined material properties positioned in an elastic half-space. Horizontal and vertical forces can then be applied to the geometric shape or *block* to simulate *real* forces such as gravity or extensional and compressional tectonic stresses. By designing a model in which there are smaller blocks within larger blocks, buried objects can be simulated. The model is limited to two dimensions, thus inhibiting a true 3-dimensional model and time is also excluded as a possible contributing factor within each 'run' of a model. In order to establish the individual affects of a force or property a series of steps are undertaken to simulate each in turn until all the acting pressures are applied.

The FE model can be of either the *plane stress* or the *plane strain* type, depending on the theoretical thickness of the out-of-plane dimension. Since the dyke-model requires thick out-of-plane dimension (the dyke blade) the plane strain is chosen. The precision of the processing can also be selected as either high or normal, tests show within this study, that although high precision processing gives marginally better results, the time taken to process did not merit the degree of improvement required at least during early tests of the method. The geometry of the problem can use the x and y axis or a radial (asymmetrical) axis. Finally the model of the geometry is designed simplifying the shape along lines of symmetry.

The geometry of the problem to be investigated is input through the positioning of vertices onto a grid. Edges are drawn between the vertices, either straight, or curved to simulate arcuate fractures. Surface fissures can be illustrated with the top end of a defined fracture left 'open' at the surface of the larger block to portray an extensional crack. A topographically arcuate cross-section can be incorporated using topographic maps and benchmarks. Modelled vector translations can then compared to observed horizontal and vertical displacements.

A *mesh* is constructed in the blocks formed by joined edges. This is essentially a web constructed between nodes, and which consists of triangular elements. The

number and spacing of the nodes can be user-defined, allowing the density and regularity of the mesh to be specified. The mesh is made more dense in areas of particular complexity or importance such at the ground surface or dyke margins. Applied forces act on each node of the mesh thereby deforming the entire model.

Hooke's law states that a stressed body deforms to a degree proportional to the force applied. The defined blocks in the model are given elastic properties through the application of the relevant *Young's Modulus* and *Poisson's Ratio*. The Young's Modulus is a number, characteristic of a particular rock type, that indicates the amount of strain caused by a pre-determined application of stress. It is a numerical constant describing the elastic properties of a material undergoing tension or compression (a measure of the ability of a material to withstand changes in length when under stress, where stress is given in *Mpa*, and strain is dimensionless). Values for the Young's Modulus are derived from samples of rock tested in laboratories (Birch, 1966). The real, in-situ, gross values for an entire basaltic volcano can only however be estimated from these, see Table 3-2.

Rock type	Young's Modulus (E)	Poisson's Ratio (ν)
Tuff ¹	$2 \times 10^{10} \text{ Nm}^{-2}$	
Basalt ¹	$8.7 \times 10^{10} \text{ Nm}^{-2}$	
All rock types ²	0.5×10^{11} to $1.5 \times 10^{11} \text{ Nm}^{-2}$	< 0.5
Sandstone ³	$5.7 \times 10^{10} \text{ Nm}^{-2}$	0.221
Basalt ²	$8-12 \times 10^{10} \text{ Nm}^{-2}$	
Granite ²	$0.3-0.6 \times 10^{11} \text{ Nm}^{-2}$	
Basalt ³	$7.6 \times 10^{10} \text{ Nm}^{-2}$	0.235
Molten Basalt ³	$6 \times 10^9 \text{ Nm}^{-2}$	0.49
Granite ²	$2.94 \times 10^{10} \text{ Nm}^{-2}$	
Shallow fractured basalt	$5 \times 10^{10} \text{ Nm}^{-2}$	0.25

Table 3-2 Mechanical properties used in the finite element models. ¹Wahab Khair (1989), ³Birch (1966), ²Encyclopaedia Britannia (Vol. 15, P954). **Bold** = The value used in the model

The model assumes that the material behaves in an elastic manner and has no internal discontinuities. The shallow surface of the volcano is, however, behaves in a brittle manner to a considerable degree, and contains numerous

discontinuities such as fractures and cracks as evidence of this. This effectively reduces the real elastic parameters of the rock to values less than those determined in a laboratory (from complete unfractured samples). Consequently it proved necessary to reduce the Young's modulus and to experiment with various values. For the initial tests the value of $5 \times 10^{10} \text{ Nm}^{-2}$ for E was decided using the range of values listed in Table 3-2. An extensional fracture is defined solely by the forces applied to the *edges* of the defined shapes, so the Young's Modulus for the cavity block is irrelevant and input as neutral. The Poisson's Ratio is the ratio of the amount of contraction per unit dimension of a block of rock to its elongation per unit length, when subjected to a tensile stress. The volume is conserved but the material is compressed and the value is always less than 0.5.

In the context of the modelling a force is a pressure which alters a geometrical plane upon its application, while pressure is a vector with a particular magnitude and an angle of approach to the plane. An example of such a force is gravity, which acts vertically at $6.67 \times 10^{10} \text{ Nm}^{-2} \text{ kg}^{-2}$. More than one force can act upon a plane at a given moment as vectors can be combined, some producing resistance, such as friction, can reduce the magnitude of an acting force. The material properties of the block under stress and the size of the plane under pressure also determine the modification in form that the block undergoes. A stress acting directly onto a plane at an angle of 90° , is the normal stress, and a stress acting across the plane is either tensile or compressional.

The edges of the defined blocks may be used to simulate principal stresses as forces acting onto the elastic block, here, in the FEM context it is termed the *bodyforce*. For the software used, it is necessary to fix a certain proportion of the edges so that they are not able to move when under stress. This may add *edge effects* to the surface of the host block so the scale must be used to minimise this, placing the modelled forms in the middle of a larger block beyond the reaches of the edge effects.

3.5.1 Preliminary modelling tests

The preliminary tests comprised a series designed to model the opening of various realistic fractures and dykes within an elastic half-space having the estimated material properties and boundary conditions of a basaltic or semi-basaltic volcano such as Etna, Kilauea, or Piton de la Fournaise. *Mohr Stress* values around the stressed fracture or dyke are examined to constrain stress accumulation and release during fracture and dyke formation on active volcanoes.

The series of tests focused in particular on assessing the roles of the material and structural properties of the defined blocks and the pressures acting on the edges of the block boundaries. The impact of dyke dimensions on surface deformation were also evaluated using data from the 1991 dyke intrusion as a standard for Etna (Murray, 1994). The finished model is a topographically accurate, two-dimensional, cross-section through the upper Southern Flank of Etna, hosting a realistic dyke intrusion that generates observed surface deformations. For each parameter input into the model a series of tests are run to check the realism of the value.

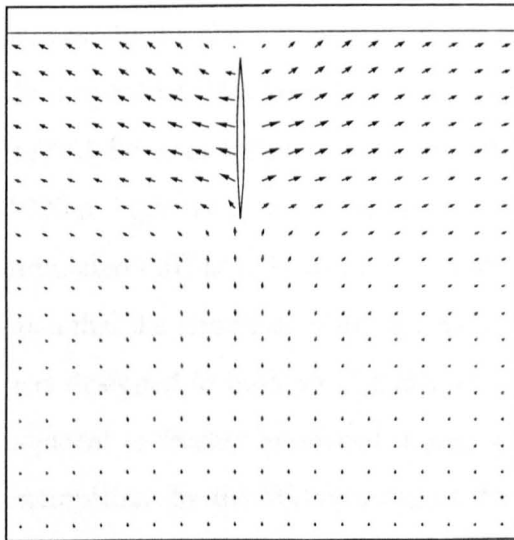
Test 1a

The tests are run with the aim of examining the way the software package creates and processes input parameters. Test1a, a block was defined as a square box of 10000m by 10000m dimensions, and a mesh created with a dense spacing. The block was given a Young's Modulus of $5 \times 10^{10} \text{ Nm}^{-2}$ and a Poisson's ratio of 0.25 (as explained in Section 3.5.1). As expected (with no forces being applied) the block showed no change during processing. The next stage was to apply a vertical negative force (or -30000 Nm^{-2}) to the model to simulate gravity. When such a force is applied the package does not allow all the sides to be free, although it is possible to fix the left and right sides of the box to move in just the y axis and the bottom edge in only the x axis, the top surface remains free at all times. When gravity is applied to the model the defined block sinks, as the sides of the block are fixed they do not move causing a distortion in the displacement. The

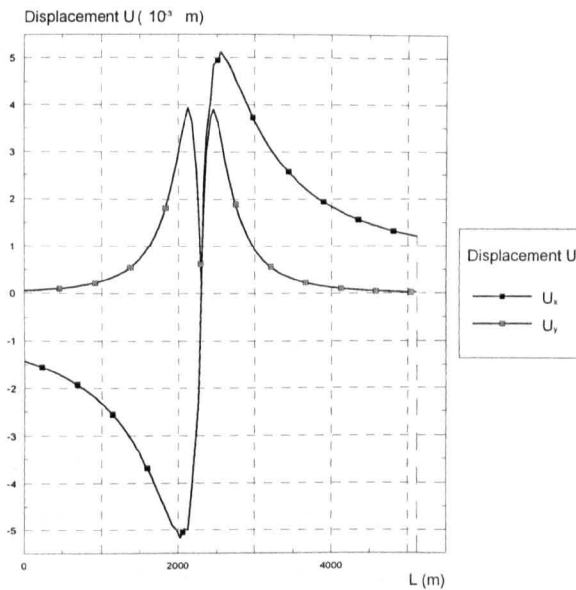
conclusion of this test was that the block is assumed to be already ‘under the influence of gravity’ and as such it is not necessary to simulate gravity during the experiments. As the experiments are designed to be progressive the reliable parameters are carried over from each experiment to the next.

Test1b

Test1b used the same 1000m x 1000m square box but with another block positioned within it to simulate a vertical dyke. The dyke was formed by two vertices, the first 50m from the surface and the second at 350m, two edges were defined between the vertices with a slight arc, forming a narrow tapering crack with a maximum width of 2 metres. At each edge a differential force of $2 \times 10^{10} \text{ Nm}^{-2}$ was applied acting into the host block, this caused the buried dyke to produce the characteristic double peak surface deformation pattern characteristic of vertical dykes. Vertical displacements of a few centimetres are of the order of magnitude observed in the field, see Figure 3-3. All diagrams are close-up images of the geometric shape, the whole model is too large to be displayed in full.



a,



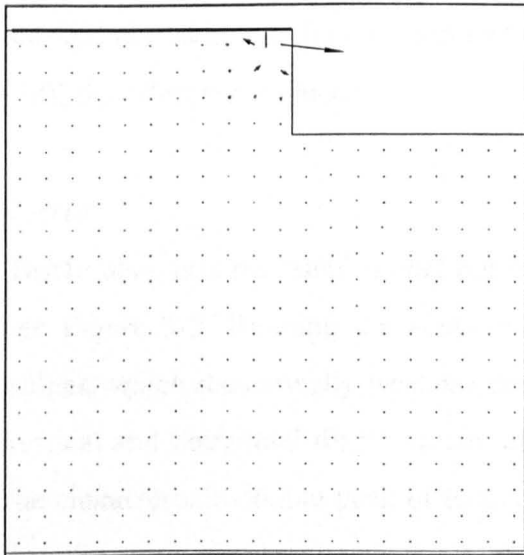
b,

Figure 3-3, (a) The results of Test1b showing the pattern of surface displacement across a flat ground surface above a newly emplaced dyke. (b) The graph shows a cross-section along the top surface of the host block, U_x = horizontal displacement, U_y = vertical displacement.

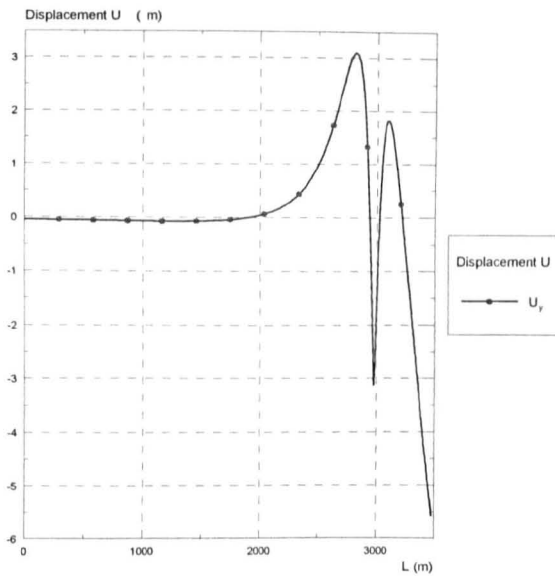
Test1c

In Test 1c the flat top surface of the host block was modified in order to assess the impact of variations in local topography on surface deformation associated with dyke emplacement. The surface of the model was modified to include a 1000m high step, with the dyke positioned 50m away from the top of the simulated cliff at a depth of 50m and a height of 300m. The step was positioned such that the simulated cliff edge was located in the top middle of the box. Test1c was designed to look specifically at the potential instability of steep topography adjacent to freshly emplaced dykes; a common situation in active rift-zones. As exemplified by the Western rim of the Valle del Bove at Mount Etna, extension of the simulated dyke provides information on where the steep surface is most likely to fail. When the simulation was run the opening dyke deformed the simulated cliff face in preference to the greater bulk of material on the other side of the dyke. Positive vertical surface deformation in the order of a few metres was still observed each side of the dyke with extensive horizontal displacement of the area adjacent to the cliff.

Vertical displacements continue to show the distinctive double peak from, although unlike the situation with a flat surface (Test1b, Figure 3-3). The peaks are no longer equal in height or scale, instead increased horizontal displacement towards the cliff-face has reduced the degree of vertical deformation between the dyke and the edge. An additional point to note is that dyke opening in this situation ‘drags’ material from the lower left side of the dyke up and towards the cliff-edge. The elastic nature of the host block prevents true instability from being accurately simulated. Although for example, the model indicates elastic horizontal displacements of the simulated cliff-edge this does not take into account the brittle strength of the material and it is not therefore possible to simulate the failure event. The simulation does, however, define those areas prone to the greatest stress accumulation and therefore provides a semi-quantitative measure of the spatial distribution of failure susceptibility.



a,



b,

Figure 3-4 (a) Geometry of Test1c showing a 1000m step containing a vertical dyke, the dashed line along the upper top surface of the host box (above the step) is illustrated in (b) as vertical displacement along the cross section.

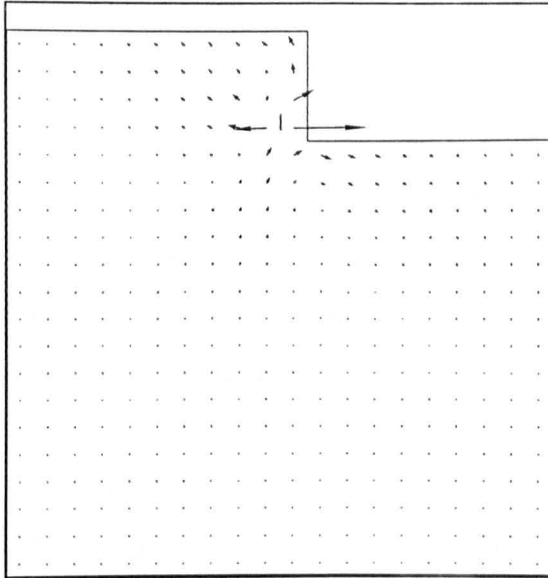
Test1d

Test1d was designed to examine the importance of the proximity of the dyke to the cliff to do this the dyke was simulated further from the cliff. The results showed that although the displacement was still effected by the proximity of the cliff, the effect was reduced.

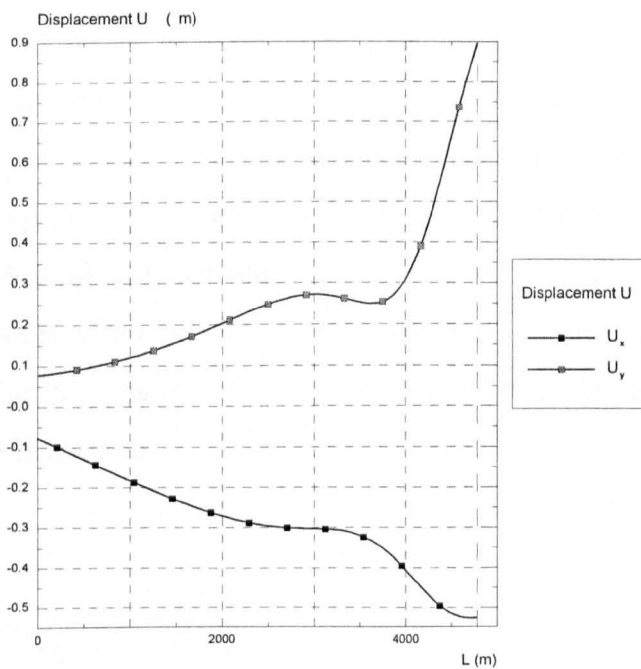
Test1e

Test1e also uses the 'step' model but here the depth to the dyke top is -1500m, see Figure 3-5. Running the simulation shows that the base of the cliff-face bulges, which theoretically weakens the whole edge. The top surface still shows vertical and horizontal displacement although the pattern has now changed and the characteristic double peak of tests 1b and 1c bulges are no longer observed. This has important implications for deformation monitoring. Simulated stations defined on the surface of this model would not show the expected displacements associated with intrusion of a dyke of these dimensions, and if a simulated baseline measured between the edge of the cliff and the left edge of the model surface then the baseline would be shown to have contracted rather than

extended. Mohr stress values express the failure potential for Test 1c, indicating the relationship between the accumulated stresses and observed displacements thereby providing an estimate of topographic failure positions.



a,



b,

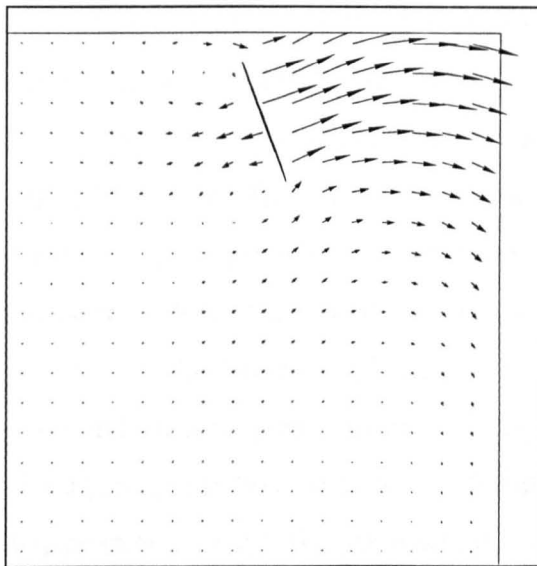
Figure 3-5 The model (Test1e) indicates (a) the displacement vectors associated with an extensional dyke adjacent to a 1000m step (b) with the horizontal and vertical surface displacement.

In addition to examining different geometries other input parameters were also tested. Using the geometric model 1c, the influence of changing the mesh spacing

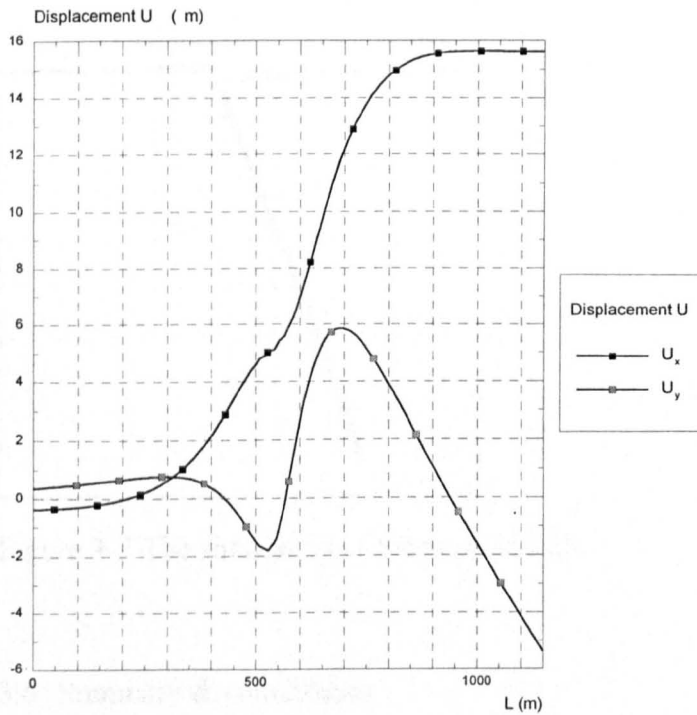
was examined, in order to determine if this significantly modified the results of the simulations. The geometry of test1c was chosen to typify the complexity of a more realistic model and three meshes were tested with spacings of 1000, 300 and 33 (unitless parameters within the software). The simulations were run and the values for three different co-ordinates were compared, for displacement along the x and the y axis. The maximum range of values over the three mesh sizes was 6mm along the x axis and 10mm along the y axis, between the largest and the smallest mesh size. The mesh spacing was changed to be as precise as feasible in areas where the displacement was expected (200) and where a graphic plot of displacement was required.

Test 1f-k

Tests 1f-k were devised to simulate differences in surface displacement associated with emplacement of vertical and dipping dykes, as undertaken by Dieterich & Decker (1975). The basic geometry from Test1c (Figure 3-4) was used but the dyke set, respectively, to dip at 70° , 45° and 0° . The results (Figure 3-6) indicated that surface displacements are sensitive to the dip of the dyke. For a vertical dyke vertical displacements were greater in the side of the dyke since opposite the simulated cliff, horizontal displacements were much larger on the cliff-side. on the other side of the dyke. A dipping dyke creates much larger lateral displacements between the dyke and the simulated cliff edge, suggesting that the potential for inducing slope instability and structural failure would be much greater.



a,



b,

Figure 3-6 Test 1h showing (a) displacement vectors and (b) surface displacement associated with the emplacement of a dyke dipping at 70°.

Test2a

Test2a was devised to examine the effects of incorporating simulated faults into the FE models. A straight-sided crack that had a surface gap was simulated.

The data were entered such that a pre-determined displacement occurred on each side of the fault. Thereby effectively defining a normal fault. It should be stresses however that since the displacement was fixed the fault was not generated by an applied force, but from a pre-set co-ordinate change. To achieve an input force pressure was applied as a bodyforce, with the left side of the fault given bodyforce values of $x=-1 \times 10^{12}$ and $y=+1 \times 10^{12}$, and the right side, $x=+1 \times 10^{12}$ and $y=-1 \times 10^{12}$. These fixed displacements of bodyforce act upon the crack generating a normal displacement. Although, the displacement values prove too large, consequently the bodyforce was reduced to 2×10^7 , in order to generate realistic displacements of 0.5-1m. Arcuate fault sides were also modelled, with a surface opening of 0.0004m, producing similar results.

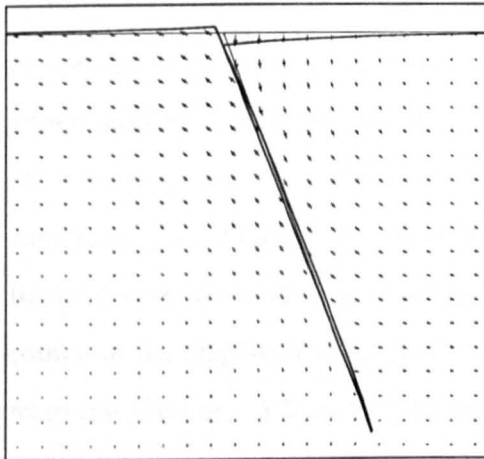


Figure 3-7 The simulation of the normal fault.

3.6 Summary & conclusions

All the tests were undertaken were designed to define the limits of Quickfield™ in order to ensure the realism of simulated surface displacements in response to the input of special parameters. The series of tests illustrate the characteristics of surface deformation associated with the opening of a dyke. In a range of environments and orientations simulating vertical and horizontal displacements reveal the ability of the surrounding material to accommodate the resulting stresses. In addition, they show how the geometry and the mechanical parameters,

in terms of differing host block, reservoir shape and the elastic properties affect the resulting pattern of surface displacements. Dieterich and Decker (1975) determined that it is difficult to derive a reliable estimate of reservoir geometry and depth using vertical displacement data alone. Particularly, since the models can only produce surface deformation from a known buried source, rather than extrapolate the source from input observations of real displacements.

This chapter examines the construction of a baseline ground deformation network; and the subsequent collection and analysis of data. From the original baseline positions of the survey stations, displacements can be attributed to magmatic, non-magmatic and error sources. A detailed chronology of the procedure for processing the data, explains the methods used to distinguish between real movements and errors. The analysis is undertaken through mathematical, graphical and statistical analysis. The data, which may display either significant and insignificant displacements is checked for coherent patterns of movement. The validity of any perceived patterns are investigated using statistical tests. Significant data which exhibit patterns are then modelled using finite element modelling in order to graphically represent the data and discern the source of the displacements. Structural and mechanical unknowns may be derived from the models, such as magma pressure or dyke dip. The FE modelling using Quickfield™ has produced the following important findings;

- (i) The Young's modulus for the shallow fractured surface of Etna is approximately $5 \times 10^{10} \text{Nm}^{-2}$
- (ii) The modelled vertical dyke is characterised by a double peak surface deformation pattern that may be modified by the dip of the dyke.
- (iii) The dyke emplaced adjacent to a simulated cliff deforms the material between the dyke and the cliff, rotating it away from the dyke towards the 'cliff' suggesting that the dip of a dyke may be modified by an adjacent cliff.
- (iv) The surface deformation associated with the dykes emplaced next to the cliff (see (iii)) reveals that a baseline measured between the cliff edge and the opposite edge of the model will appear to have contracted despite the intrusion.

4. MT. ETNA, PART ONE: THE GEOLOGICAL CONTEXT

Mt. Etna is the largest volcano in Europe, it is approximately 3250m high and 30km across. It has a central feeder conduit with four active craters, constant degassing occurs (at the time of writing) from one or more of the vents. The edifice has three distinct trends of magma emplacement aligned NNE-SSW, ENE-WSW and SSE-NNW, with the most active segments defining the NE, NNE and SE Rift-Zones. There is a fourth topographically-influenced sigmoidal rift referred to as the Southern Rift-Zone which will be examined in detail later.

In addition to the main aims of the study, the investigation of Etna specifically addressed the questions listed in Section 1.2 that ask: *What are the relative contributions of regional tectonics, magma emplacement and gravity-induced displacement in the current operation of Mt. Etna?* In order to answer this question and to fulfil the broader aims of the thesis (Section 1.2), ground deformation data was collected and analysed from the SE and Southern Rift-Zones. The results from this chapter have been presented at conferences and published in reports¹

A ground deformation network established in the summit area in 1971 (Wadge, 1976) was extended in 1982 (McGuire *et al.*, 1991) and again in 1992 (Saunders *unpub-data*) to span the area comprising the SE and Southern Rift-Zones. This network together with a number of small networks established over the Lower

¹ Moss J. L., Saunders S. J., & McGuire W. J. (1995) The monitoring and interpretation of recent ground movements on active volcanoes. *Poster. Volcanoes in the Quaternary*, The Geological Society of London.

Moss J. L. (1996) Recent horizontal ground deformation at Mount Etna, Sicily. In: Gravestock P. and McGuire W.J. (Eds.) *Etna 15 years on*, p. 64-66. Cheltenham: Cheltenham and Gloucester College of Higher Education

McGuire W. J., Moss J. L., Saunders S. J. Stewart I. S. (1996) Dyke-induced rifting and edifice instability at Mount Etna. In: Gravestock P. and McGuire W.J. (Eds.) *Etna 15 years on*, pp. 64-66. Cheltenham: Cheltenham and Gloucester College of Higher Education

Moss J. L. & McGuire W. J. (1997) Ground deformation monitoring at Mount Etna: the transition from IR-EDM to GPS. *VSG-Minsoc 1997 Conference Proceedings*, Cambridge.

Eastern Flank (Stewart *et al.*, 1993), have been combined into one network and systematically re-occupied in order to examine magma-, gravitational and tectonic-related displacement. This field work has been supplemented by a critical evaluation of relevant literature and scientific data. This study is in two parts; this chapter examines the geological context of Etna and the recent eruptive history, and chapter five describes the occupation of the networks, discussing the results and presenting the conclusions.

4.1 The eruptive history of Etna

Volcanic activity in the Etna region began in the Pleistocene with fissure fed eruptions of alkali olivine basalts and tholeiitic basalts near the contemporary coastline at Paterno, Acitrezza and Acicastello (Rittman, 1973; Chester *et al.*, 1985). The first Etnean lavas (tholeiitic) are situated on the clay units of the Gela Nappe that overlie Middle Pleistocene marine clays (Cristofolini *et al.*, 1982; Lentini, 1982). The Etna edifice developed a succession of central vent edifices that underlie the current *Mongibello*. Earliest products from this immediately locale are dated from 95ka B.P. (Chester *et al.*, 1985), these are exposed in the Valle del Bove and mark the start the alkalic series (which continues until present time). The Valle del Bove is a large depression feature in the eastern flank of Etna, most likely formed as a result of piece-meal (and maybe occasional catastrophic) collapse. Material removed from the depression forms a fluvial fan called the Chiancone that protrudes along the eastern coastline (McGuire 1983; Guest *et al.* 1984; Calvari *et al.*, 1996). Figure 4-1 illustrates the evolution of Etnean volcanism. The periodic change in the eruptive style from the effusion to explosive phreatomagmatic events is thought to be a result of the available water in the edifice (McGuire 1982).

Historic activity is focused on the central craters and the rift-zones and this has led to the production of numerous cinder cones on the flanks of the volcano. From Figure 4-1 it can be seen that there have been no major events during the

activity of the present centre, the last caldera collapse occurred from the 'Il Piano' centre probably just after the philosopher Empedocles was believed to have died on Etna. Historic accounts do record major eruptions and collapses during this time, but destructive, systematic collapses similar to the ones that may have formed the Valle del Bove, have not been described (Chester *et al.*, 1985). The biggest historic eruption of Etna was in 1669 when a fissure opened from Monte Frumento Supino just below the summit of Etna, extending 12km to the town of Nicolosi. Early stages of this eruption were accompanied by a large collapse at the summit vents and the formation of a cinder cone near Nicolosi that produced a long lava flow that eventually reached the sea and destroyed a large part of the city of Catania.

The volcanic plumbing system of Etna consists of the feeder conduits and deep storage areas directly beneath the edifice. Wadge (1976) concluded from ground deformation data that magma was stored in 'open vertical cylindrical reservoirs' below the Chasm and the North East Crater, but unlike Kilauea (Hawaii), there is no evidence for sub-rift storage areas. Petrochemical studies (e.g. Rittmann, 1973; Guest & Duncan, 1981; Armienti, 1989) suggest that there is no large shallow magma reservoir underneath Etna. Guest and Duncan (1981) agree that magma ascends without high level storage since patterns of independent activity are observed from the summit craters suggesting that they are not connected at least at shallow depths. Wadge's model proposes that the plumbing system incorporates a central cylindrical storage area which is nearly-constantly fed by ascending magma. Hydraulic fracturing of the walls of the storage area causes radial fracturing. This is triggered by the E-W extensional tectonism which increases magma supply, permitting the short term high-level storage of magma (Wadge, 1976; Murray & Guest, 1982). It is widely accepted, that mass high-level storage occurs in the short term (a few weeks). The petrological evidence (from the presence of plagioclase) indicates that the crystallisation pressures are medium to low (Guest & Duncan, 1981).

Stratigraphic unit	Volcanic centre	Events	Products	Age
recent Mongibello	Present centre	1669 summit collapse ⁵	hawaiites thick massive flows	1669 AD
	Il Piano	caldera collapse		490 AD
		<i>possible creation of the Valle del Bove</i> ⁴		
Ancient Mongibello	Leone	caldera collapse	hawaiites, basic mugearites	14.5ka ¹ B.P.
	Ellittico	<i>possible creation of Valle del Bove</i> ⁷		
	Belvedere		hawaiites, basic mugearites	
	Vavleri	caldera collapse		
Trifoglietto II	Trifoglietto	phreatomagmatic <i>possible creation of Valle del Bove</i> ³	basic mugearites and hawaiites	65.8k ¹ B.P. 80ka ⁶ B.P.
Pre-Trifoglietto	Calanna	caldera collapse	hawaiites	95ka ⁴ B.P.
Paterno			alkali olivine basalt, sub-aerial and sub-marine tholeiitic basalts	210ka ² B.P. 300ka ⁴ B.P.
	no centre identified			

Figure 4-1 Stratigraphy of the eruptive centres of Etna and their temporal distribution. After Chester *et al.*, (1985) and Calvari *et al.*, (1996). Information from: ¹Condomines *et al.*, 1982; ²Chester & Duncan, 1982; ³McGuire, 1982; ⁴Guest *et al.*, 1984; ⁵McGuire *pers com*; ⁶Gillot *et al.*, 1994 ⁷Calvari *et al.*, 1996.

Contrary to the common belief that there is no permanent shallow storage area beneath Etna, Sharpe *et al.* (1980) identified a low velocity zone beneath the edifice using seismic data. Their model established a 16-24km deep, oval matrix of partially molten dykes and sills. Crystal fractionation occurs in this magma reservoir and the differentiated magma ascends via fractures. Sharpe *et al.* (1980) attributed the alignment of fractures 'along the lines of tectonic dislocation'. They identified the principal influences on the system to be (i) the tectonic structural features and (ii) magmatic surges. The existence of distinct inflation and deflation cycles on Etna, implies a temporary shallow storage system is argued for by

Massonnet *et al.*, (1996) and Murray *et al.* (1997) from the interpretation of interferometry and levelling data, but it has not been identified by GPS measurements (Nunnari & Puglisi, 1994a).

Continuous de-gassing at the summit craters and flank fumeroles suggests that Etna has an open conduit system. This open system causes differentiation of the magma due to the cooling of the upper parts and by the back-fall of the products from Strombolian eruptions into the open vent. This causes the non-Newtonian rather than elastic behaviour of magma near the surface. Due to this continuous degassing, Etna is regarded at the present time to be active. At the time of writing the summit of Etna comprises four active craters: the North-East Crater, the Bocca Nuova, the Chasm (La Voragine) and the South-East Crater. Most activity originates in and is centred at, the summit craters, although flank eruptions occur every few years along the rift-zones. Etnean eruptions currently occur every few years from the summit craters and every three to five years from the rift-zones. Eruption types are primarily Strombolian and effusive, although the start of an eruption from the central craters is often accompanied by vulcanian or ultra-vulcanian activity exploding lithic blocks and producing large ash clouds. Strombolian eruptions occur from both the summit and flank vents ejecting blocks hundreds of meters into the air. Often the activity is vigorous and continuous enough to be termed 'lava or fire fountaining'.

4.2 Structural framework of the Etna region

Etna resides within the Calabrian Arc, this is an arc-trench system that formed during the Miocene as a result of the subduction of the African plate (in a NW-SE direction) under the European plate, (Forgione *et al.*, 1989). The geometric disparity between the opposing plates, causes the overthrust of the European plate and the disjuncting of the African continental margin into a system of micro-plates. The foredeep of one micro-plate collision is situated a few kilometres

south of the current location of Etna, encompassing the Iblean mountains and Hyblean plateau.

Etna is situated on the *Gela Nappe*, an overthrust fault within the thrust belt of the Appennian-Maghenhian chain generated by this collision of the Iblean foreland micro-plate and the Calabrian Arc (Butler *et al.*, 1992), see Figure 4-2.

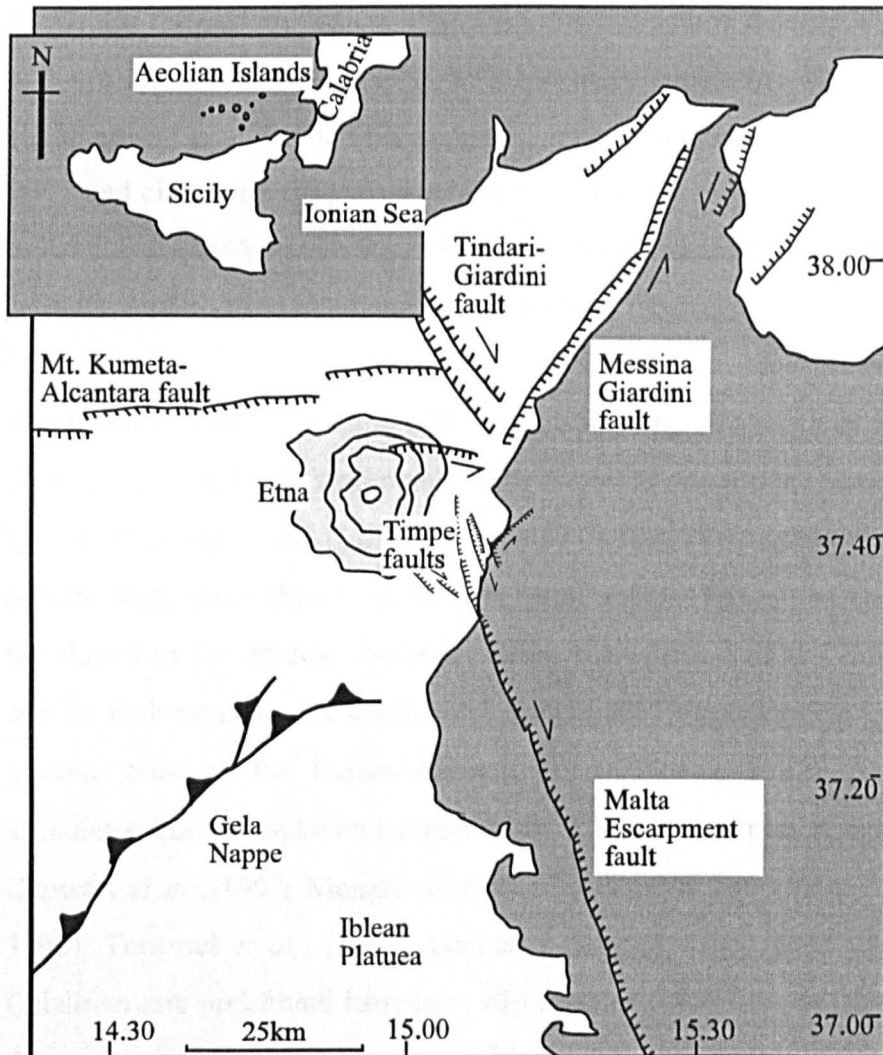


Figure 4-2 The structural framework of the Etnean region showing the regional tectonic features (After Lo Giudice *et al.* 1982).

Etna should not be considered an isolated volcano but is closely related - temporally and geographically with volcanism in the Iblean mountains further south. The Iblean volcanism occurred during the late Miocene and early

Pleistocene producing submarine and subaerial tholeiitic lavas and alkaline basalts, similar to those from Etna (Labaume *et al.*, 1990).

As mentioned above, Etna developed on the Gela Nappe, however, prior to this volcanic loading the clays of the Gela Nappe were sliding eastward as a result of lateral gravitational instability due to either (i) sliding down a buried 'ramp' (of unknown material) or (ii) the adjacent Malta Escarpment fault (Labaume *et al.*, 1990). On the eastern flank of Etna the pre-Etnean clays outcrop at Vena at 750m and are also found co-mingled with the early submarine lavas at Acicastello (Labaume *et al.*, 1990). This suggests; (i) contemporaneous deposition of the lavas and clays, and (ii) subsequent uplift. Uplift rates for this area are estimated to be 0.8-1.4mm/y (Grindley, 1973), these are equated to the Holocene rates recently derived from emergent coastal features (Stewart *et al.*, 1993).

The eastern flank of the Etna edifice is bisected by two regional tectonic trends (Figure 4-2), the Malta escarpment from the south and the Messina-Giardini fault system from the north (Lo Giudice *et al.*, 1982). The Malta escarpment is a normal fault, down-thrown to the east (with a slight left-lateral component) that developed in the Middle Jurassic, during the opening of the Ionian Sea. This normal fault separates the continental crust of the Pelagonian Sea from the Paleooceanic crust of the Ionian Abyssal Plain (Tinetti, 1982). It has been speculated that the faults on the eastern flank of Etna are part of the Calabrian arc (Stewart *et al.*, 1997; Monaco in press; Forgione *et al.*, 1989; Tortorici *et al.*, 1995). Tortorici *et al.*, (1995) examined the faults associated with the 180km Calabrian Arc and found long-term slip rates of 0.8-1.1mm/yr, the extension on the outer edge of the arc can be used to explain the E-W extension prevalent in the Etnean region (Forgione *et al.*, 1989). Evidence from the investigation of raised marine shorelines and the dating of invertebrate marine fauna gives uplift rates of around 1.1-1.8mm/yr Stewart *et al.* (1997), these data suggest that the large emergent features (raised marine shorelines) are most likely a result of abrupt co-seismic movements along the faults. The absence of a recent major seismic event in the southern part of the arc ominously places the north-eastern

coast of Sicily into a 'seismic gap' period, suggesting that a destructive earthquake is imminent.

The broad stress regime of Etna (Lo Giudice, 1982; McGuire & Pullen, 1989) is compressive, with the maximum compressive stress trending predominantly NNE-SSW and the minimum compressive stress acting perpendicular to this. The Appenninian-Magrebian mountain chain north of Etna is a compressive feature, reflecting the NNE-SSW maximum compressive stress orientation of the whole region (Lo Giudice *et al.*, 1982). The approximate N-S contraction is confirmed by geodetic measurements (Nunnari & Puglisi, 1994) that measured strain of $-3.8 \pm 0.5 \mu$ per year. The volcanic activity south of Etna suggests that there has been WNW-ESE extension in the past in this part of Sicily, the extensional regime therefore appears to be migrating northwards to its current location under Etna (Labaume *et al.*, 1990; Stewart *et al.*, 1993).

Although Etna has developed as a central vent volcano, structural lineaments crossing the edifice are not radial as would be expected for a predominantly symmetrical cone controlled purely by gravitational stresses (Fiske & Jackson, 1972; McGuire & Pullen, 1989) nor are they parallel to the NNE-SSW compressive regime. This confirms that there are more complex regional tectonic influences controlling the development of the volcano.

The compressive stress regime and the E-W extension have resulted in the opening of conjugate shear faults under the edifice oriented ENE and NW (Figure 4-3). Conjugate fault sets that act as preferential pathways for magma ascent are characterised by persistent dyke emplacement and flank eruptions. The nature and development of these active rift-zones will be examined further in Section 4.2.1. Stewart *et al.* (1993) found that there is no actual through-going major seismogenic fault cutting the volcanic pile, however, seismic activity along the portion of the Malta Escarpment which enters Sicily at Santa Tecla correlates statistically with activity at the summit of Etna (Latora *et al.*, 1996).

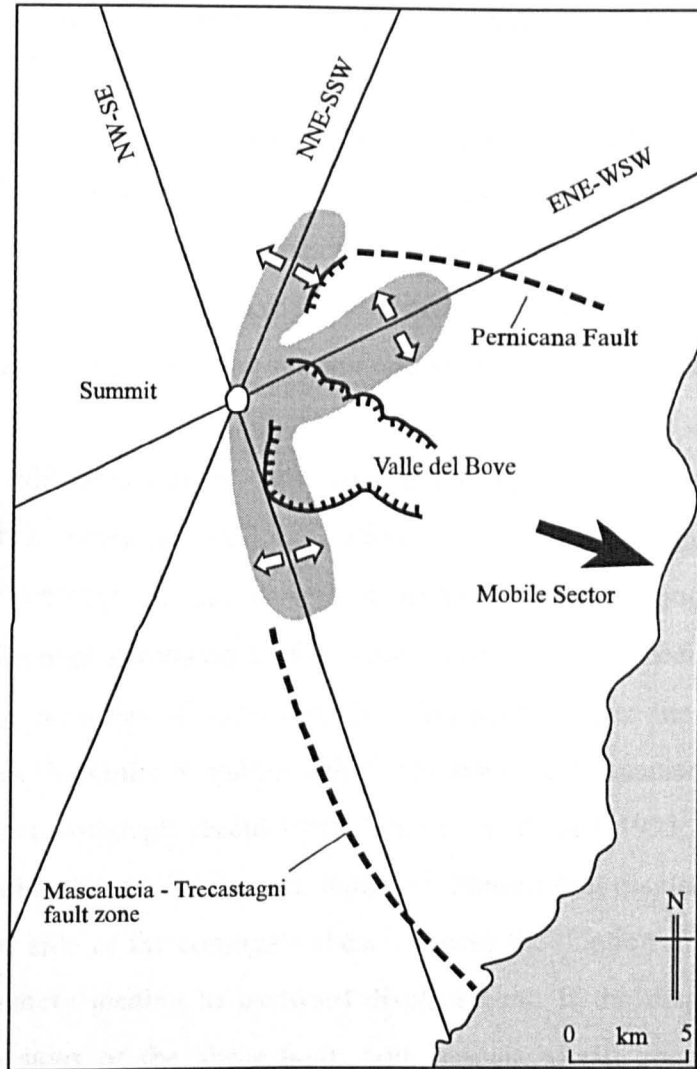


Figure 4-3 The relationship between the eastern flank mobile sector and the summit 'rift-zones' (After Moss, 1996)

This critical observation suggests that there is either a shallow link between the opening of the rift-zones and the mechanical transfer of stress to faults lower down the flank or (contrary to Stewart *et al.*, 1993) a deep seated tectonic link, this argument will be developed further in Section 5.11.

4.2.1 The Rift-Zones

Rift-zones are areas characterised by the persistent transport of magma away from the central conduit in either temporary fissures or as permanent distended fractures. On Etna they are identified by clustering of fissure eruptions on the

flanks the volcano (Frazetta & Villari, 1981; Lo Giudice *et al.*, 1982). There are three distinct trends aligned NNE-SSW, ENE-WSW and SSE-NNW and a less perceptible sigmoidal rift. The sigmoidal clustering of dyke trends reflects the influences of the localised stress regime created by the adjacent 2km high cliff of the Valle del Bove. The stress regime created by this adjacent cliff modifies the SSE rift as it approaches the edge, causing the fractures to run parallel to the cliff edge (Fiske & Jackson, 1992; McGuire & Pullen, 1989). The positions of the rift-zones relative to the summit craters are shown in Figure 4-3.

The edifice is situated on a tilted basement and is buttressed in the west. These factors, aided by gravity, facilitate the preferential extension and transcurrent displacement of the eastern segments of the conjugate shear zones. The preferential activation of the eastern sector of the shear system has led to the active positions of the rift trends being referred to as the NE, ENE and SE Rift-Zones (McGuire & Pullen 1989). The opening mechanisms for the rift zones are unclear, although recent work (Ferruci & Patané 1993; McGuire *et al.*, 1996) explains the mechanisms in terms of transcurrent displacement occurring along either side of the conjugate shear to cause the dilation in the complimentary set, ultimately leading to eastward displacement. If the displacement occurs along both sides of the shear fault, both associated rift zones open simultaneously causing eastward movement, see Figure 4-4.

Seismicity associated with the 1991-3 eruption from the Southern Rift-Zone indicated that transcurrent displacement had occurred along the NNE-SSW rift, (displacing the Pernicana Fault by a few centimetres). The sinistral displacement of the Pernicana fault released the accumulated strains within the rift, facilitating the rift eruption from the Southern Rift-Zone. The dissipation of strains is also proposed to occur as aseismic creep through the Timpe faults (McGuire *et al.*, 1996).

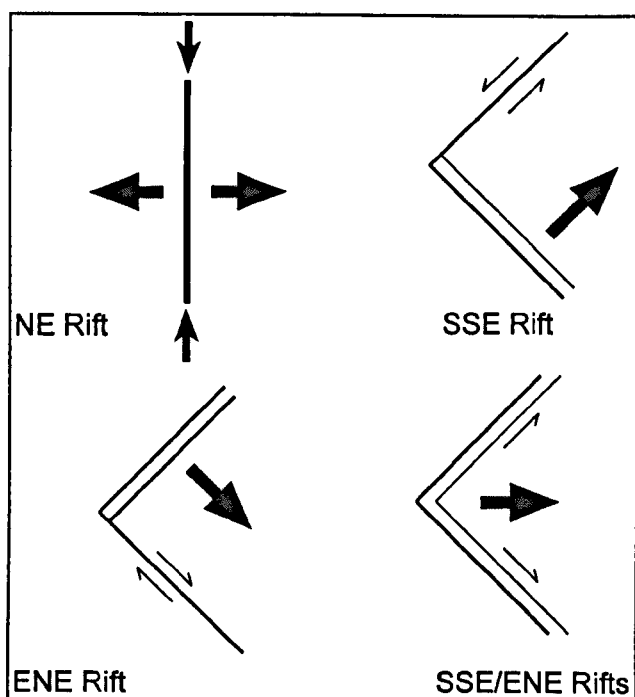


Figure 4-4 Opening of the rift-zones to initiate associated shear displacement of the opposite rift-zone (after McGuire *et al.*, 1996).

The SE, ENE and Southern Rift-Zones on Etna are indistinct above 1750m (the NE rift will be discussed later). At this elevation the surface expressions of fissures radiate away from the central conduits suggesting a gravity dominated stress regime where the minimum principal stress facilitates the emplacement of dykes tangential to the slope contours. Below 1750m the propagation of fractures has been governed by two factors; (i) the topographic features of the edifice and (ii) the regional trends in the underlying basement. Although the distribution of eruptive fissures coincides with the major structural features of the area, the local stress regime predominantly influences the direction of propagation of shallow dykes. This local stress regime is controlled by gravity, surface morphology and active shallow faults. These features facilitate the distribution of the fissures into the established rift-zones but do not appear to be directly linked to the underlying structural features (McGuire & Pullen, 1989). McGuire and Pullen (1989) used gelatine modelling to interpret the peculiar track of the SSE rift zone (now recognised at the Southern Rift-Zone), which appeared to divert to the south as it neared the Valle del Bove. The modelling results indicated that the cliff edge of the Valle del Bove re-orientates the local stress regime such that the least-effort

path is parallel to the rim. The bulk of La Montagnola further down slope is also thought to re-orientate the stress regime further, diverting the fractures around its margins. These topographic influences have modified the tectonically-controlled SSE Rift-Zone into the morphologically-controlled Southern Rift-Zone, thus explaining the sigmoidal pattern identified by Frazzetta & Villari (1981).

Further experiments undertaken using gelatine modelling, (Fiske & Jackson, 1972; McGuire & Pullen, 1989) show that dye injected into the axis of the ridge, propagated along the axis of the ridge (Fiske and Jackson, 1972). In this way, the magma is transported down a ridge (such as the NE Rift-Zone), where it either solidifies without reaching the surface or it erupts either via a fracture or a vent. The build-up of material in this way, re-enforces the structure and morphology of the ridge, facilitating preferential magma transport for the next batch of magma. Fiske and Jackson (1972) termed these phenomena 'self-perpetuating' ridges. The ridge of the NE Rift-Zone is formed from lava flows and layers of pyroclastic deposits. As the ridge developed, topographic gravitational influences have overridden the regional tectonic influences (of the underlying NNE fault). The developed morphology has maintained the topographic stress influences even above 1750m. Further down the ridge where the topography is less defined, the dykes appear to fan out in a radial pattern, Borgia *et al.* (1994) noted that these faults and dykes trend NNE and NE and extend and join the *en echelon* tract of the Pernicana fault.

Tectonic lineaments underlying the volcano controlled the early growth of the edifice, during the fourteenth century low altitude flank eruptions were attributed to the underlying basement stresses (Chester *et al.*, 1985). Eruptions that occurred due to the regional stress regime led to the creation of prominent ridges and dyke swarms that have been 'inherited' and have consequently altered the local stress regime (McGuire & Pullen, 1989). This will be discussed further in Section 4.3.

4.2.2 The Lower Eastern Flank Faults

The Timpe is the local name for the inland cliffs exposed on the eastern flank of Etna. The cliffs mark the positions of the NNE oriented faults, they are characterised by scarps up to 200m high, most of which are down-thrown to the east although some are down-thrown to the west forming localised graben features, see Figure 4-2.

The north part of the Moscarello Fault at Macchia has a scarp over 100m and has generated two seismic events in the last century (Lanzafame *et al.*, 1996). The San Leonardello Fault has shown recent dextral displacement, in 1989 there was 30cm dip slip and 2cm dextral displacement associated with the Codavolpe earthquake (Azzaro *et al.*, 1989 In: Stewart *et al.*, 1993). Both the Santa Tecla and San Leonardello Faults are thought to undergo episodic co-seismic slip and continuous aseismic creep of about 10-20mm/yr (Stewart *et al.*, 1993). The Mascalucia-Trecastagni Fault Zone trends NW-SE and is undergoing right-lateral displacement and normal faulting evident by ground cracking and topographic features (Stewart *et al.*, 1993). There is currently insufficient evidence to determine whether or not the movement is aseismic or co-seismic. The current activity of the Timpe faults is apparent from the shifts of ephemeral stream paths (Stewart *et al.*, 1993).

The faults cross the 'Chiancone' exposed on the Lower Eastern Flank, this is a pile of fanglomerates thought to originate from the opening of the Valle del Bove (Guest *et al.*, 1984; Calvari *et al.* 1996). Within the Chiancone deposit, the fault patterns change from single to multiple strands, possibly due to gravity induced deformation on the weaker Chiancone units (Lanzafame *et al.*, 1996). Further branches of the Malta Escarpment appear onshore at Praiola north of Acireale, where the fault intersects the Messina-Giardini Fault creating a wedge-type structure.

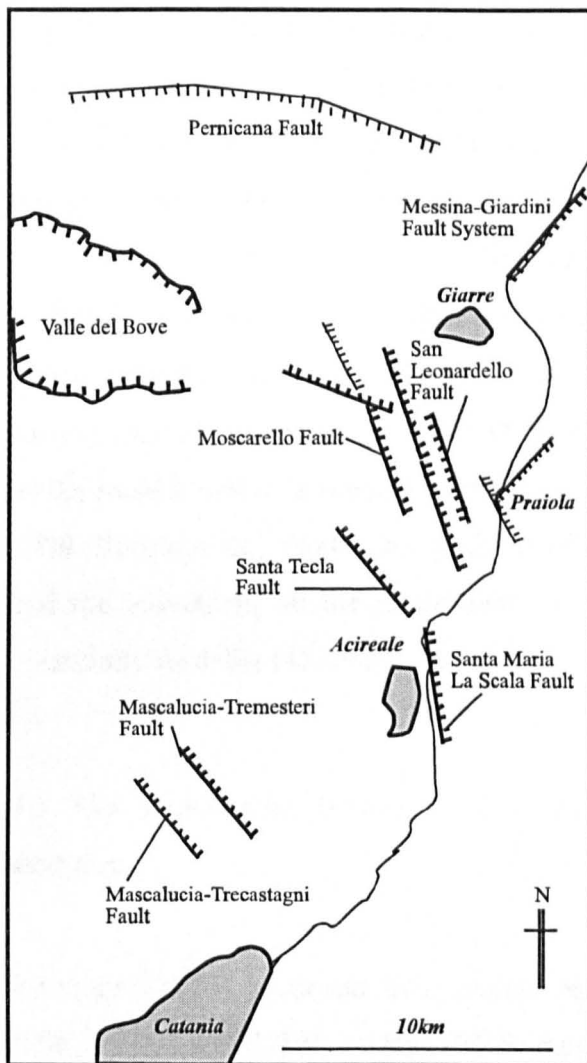


Figure 4-5 The Lower East Flank Faults showing the position of the Praiola embayment and the large towns (After Calvari & Groppelli, 1996; McGuire *et al.*, 1996 and Lanzafame *et al.*, 1996)

The Praiola embayment (Figure 4-5) is a 40m high cutting formed due to marine erosion rather than tectonic displacement. The easterly displacement of this wedge is facilitated by the strike-slip displacement of either fault, this situation mimics the junction of the SE and NE rift zones at the summit (Lanzafame *et al.*, 1996). The Pernicana Fault (Figure 4-5) is on the upper NE flank of the volcano, it undergoes left-lateral oblique-slip normal displacements (Rasà *et al.*, 1996). The fault system shows discontinuous creep in the form of: (i) *en echelon* soil cracks up to 1m wide (where the NE rift joins the Fault), (ii) coseismic surface faulting (normal and sinistral components); (iii) aseismic left-lateral movements,

3cm from 1992-1995, 40cm from 1972-1995 (using markers on buildings)². The Pernicana Fault marks the northern boundary of the mobile sector of the eastern flank, the Southern boundary is the Mascalucia-Trecastagni fault system that is thought to be extensions of the main structural trends of the region (McGuire *et al.*, 1996; Stewart *et al.*, 1993). Lanzafame *et al.* (1996) and Forgione *et al.* (1989) disagree, placing the southern boundary at the Ragalna Fault further south. These faults trend up to meet the rift-zones on the upper flanks creating a 'mobile' eastern sector bounded by the active faults and the rift zones. In this way the apex of the mobile sector is formed by the SE and NE rift zones (McGuire & Pullen, 1989 ;Borgia *et al.*, 1994). Due to the uplift of the substrate, the input of magma and the movement on the faults over the eastern flank the area is considered potentially unstable (McGuire *et al.*, 1996).

4.3 The relationship between the volcano plumbing system and regional tectonics

Rittmann (1973) proposed that magma ascends along the intersection of the NNE-SSW, ENE-WSW and SSE-NNW fault systems, noting that the distribution of the eruptive vents reflect the underlying regional tectonic stress regime. He did not, however, link the persistent activity of Etna to the tectonic setting but instead attributed it to chemical interactions within the magma storage system, and the external pressure of magma loading. Tanguy and Kieffer (1976) recognised the importance of the regional tectonic stress regime, proposing high-level storage in dykes where the eruptions are triggered by tectonic activity. Their hypothesis was backed-up by the increased levels of seismicity accompanying eruptions and from petrological evidence (examining magma crystallinity) and differentiation. They also noted a crude connection between the rift-zones and the structural features around Etna and were puzzled by the flank eruptions along the ENE orientation, a tract now recognised as a rift-zone (Lo Giudice *et al.* 1982). They attributed the

² The left-lateral aseismic creep is observed within the Vena network

persistence activity of Etna to the 'general distensive character of the region'. Guest and Duncan (1981) agreed that the eruptions are controlled by regional tectonics.

Statistical analysis has revealed a correlation between the onset and continuation of eruptions at Etna and seismicity around the summit and flanks of the volcano (Latora *et al.*, 1996). McGuire *et al.* (1996) speculated that rifting and dyke emplacement are consistent with movements on selected faults on the eastern flank implying that the deformation associated with both structures is related. Through geodetic monitoring, vertical and horizontal displacement were measured in the 1980s to compare current rifting rates with the displacement rates estimated for the Timpe faults (McGuire *et al.* 1989). Rifting rates on the Southern Rift-Zone are 1.5 to 2m per rifting event, if this is compared to the rifting rate determined from analysis of the dykes in the Valle del Bove wall it suggests an annual rifting rate of 2-13mm (McGuire, 1996). On the NE Rift-Zone the net dilation over the least few thousand years gives a rifting rate of 6-18mm/yr. (Borgia *et al.* 1994). These values agree with the rifting rates determined for the regional tectonic structures, approximately 5-23mm per year (Stewart *et al.* 1993; Rasà *et al.*, 1996) on the Santa Tecla and San Leonardello Faults and approximately 10mm per year on the Pernicana (Borgia *et al.*, 1993; Rasà *et al.* 1996).

In order to assess the relationships between the volcano and the faults on the Eastern Flank in more detail, the seismic data are investigated. Sharpe *et al.* (1980) noted that flank eruptions are preceded by earthquakes. Prior to the 1984 eruption strong shallow earthquakes (unspecified magnitude) were recorded 10 km from the summit along both the Pernicana and Santa Tecla Faults. One interpretation from this correlation is that there is a tectonic trigger inducing both the eruption (rather than the magmatic surge) and the seismic activity. This is corroborated by McGuire *et al.* (1996) who suggest that the 1984 seismic event is a 'reactivation of the deeper fault zones' that leads to a flank eruption. The

magma of the 1984 eruption does, indeed, appear to come from a deep source and was not stored in any high level reservoir (Tanguy & Clocchiatti, 1984).

The link between volcanic activity at the edifice and tectonic activity on the Eastern Flank Faults is not wholly accepted. Although, during the 1991-3 eruption a positive mathematical correlation was found between summit eruptive events and seismic activity on the Timpe (Latora *et al.*, 1996), many authors do not consider that there is a relationship (Rasà *et al.*, 1996). The large number of small seismic events and the near persistent activity at the summit confuse the relationship between regional tectonics and volcanic events. McGuire *et al.* (1996) and Moss (1996) proposed that the creep and slip along the Timpe faults represents dissipation of rift-related stresses accumulated within the rift zones. The Eastern Flank is characterised by the strike-slip faults thought to be moving seaward, either as a single block sliding on the underlying clay (Lo Giudice & Rasà 1986; McGuire & Pullen 1989), or more conceivably as a number of fault bounded smaller blocks facilitated by the aforementioned uplifted tilted substrate (Lo Giudice *et al.*, 1982; McGuire *et al.*, 1990).

Montalto *et al.* (1996) examined the role of seismicity in the de-stabilising of the unbuttressed eastern flank. They identified the most seismo-tectonically active part of Etna to be the Timpe faults in the area between Acireale and Giarre (Figure 5.1), this area experienced a high frequency of earthquakes and ground fractures and displayed morphological features denoting fault systems such as graben horst features between Macchia and Carruba and high scarps such as Santa Maria La Scala and the northern part of the Moscarello fault. Montalto and co-workers (1996) examine seismic events ($m \geq 2$) between April 1989 and December 1991, including the significant episode in June 1989 of 14 clustered events ($m \geq 3$) on the Santa Tecla Fault. They concluded that the deep hypocentres recorded at Santa Tecla corresponded with shallow hypocentres at San Leonardello. Latora *et al.* (1996) examine the two main fault systems of the Timpe; the Santa Tecla and the San Leonardello Faults. The authors examined the spatial and temporal relationship between microseismic events ($m < 1$) on the

Timpe using the time correlation methods (Kendell & Stuart, 1965; Levitich, 1971) and fractal analysis (Smalley, 1987). Results showed a similar dynamic mechanism between the major seismic swarms at Santa Tecla and San Leonardello and the 1989 dyke emplacement in the Southern Rift-Zone. The activity on the Santa Tecla Fault showed deep seismicity at the early stage of the eruption, thought to cause a modification of the local stress field at depth leading to the displacement of the San Leonardello Fault. This secondary movement occurred after a delay of about 100 days and was accompanied by shallow seismicity suggesting that it may be attributed to the accommodation of the displacement of the Santa Tecla Fault (Latora *et al.*, 1996). The seismic stations of Santa Venerina and Acireale did not correlate to eruptive events but had a similar distribution cluster of seismic events interpreted to be derived from regional tectonic activity (Latora *et al.*, 1996).

McGuire *et al.* (1996) proposed that the relationship between the tectonic regime and volcanic activity is controlled by magma, such that the reorganisation of crustal stresses accompanying magmatic inflation triggers fault movements and seismicity. Nercessain *et al.* (1996) reiterates the suggestion that magma is the trigger and, more specifically that magmatic inflation under the thin crust of Etna swells under the mounting magma pressure at depth. The uprising of magma controlling the tectonic stress regime at Etna is also proposed by Shaw (1980), Wilson & Head (1981) and Cristofolini (1982).

McGuire *et al.*, (1996) suggest that the persistent activity along the rift zones is maintained through a feedback mechanism, such that the opening of the rifts promotes the sliding of the eastern flank, which in turn facilitates the opening of the rifts. The key to this theory is *uplift*, Stewart *et al.* (1993) noted that Holocene uplift was accommodated in episodic co-seismic displacements along SSE trending faults coinciding with the SSE Rift-Zone. This observation suggests that as the edifice grows, the bulk slides under gravitational forces along the basal clay boundary. The tectonic activity of the Timpe however indicate that the accommodation is more complex. The Timpe are divided into; (i) 'tectonic faults'

that have deep earthquakes, and (ii) 'creeping faults' that accommodate the tectonic movements (Latora *et al.*, 1996). This concept of stress accommodation was suggested by Lo Giudice and Rasà (1992) to occur within a thin layer of faulted volcanic material overlying the basement rocks and tectonic faults. This faulted layer would undergo aseismic creep when instigated by the deeper tectonic faults. For example, the San Leonardello Fault is formed in the shallow faulted layer and is activated by the application of tectonic stresses from the deeper Santa Tecla Fault. Additional activation of these faults may also occur as a result of the gravitational sliding of the eastern sector along shallow décollement structures, due to frictional de-coupling Montalto *et al.* (1996). This is demonstrated by the shallow earthquakes along the de-coupling zone.

From this discussion it was evident that there is a link between regional tectonic, volcanic activity and the stability of the edifice. In detail however, the relationship remains unclear, and requires further investigation through the analysis of ground deformation over both the upper rift-zones and the faults of the Lower Eastern Flank simultaneously in order to quantify their relationship.

4.4 Monitoring ground deformation and gravity on Etna

Ground surface changes occur as a result of the relationship between sub-surface transport and storage of magma and the strength and elasticity of the surface. Ground deformation occurs across the upper flanks of the volcano as a result of the build up of pressure caused by the confinement of magma within the central conduit. This pressurisation is a result of either an obstruction of magma and gases within the central conduits or due to the non-Newtonian behaviour of the magma near the surface (Murray & Pullen, 1984). Regulation of the pressure build-up in the central conduits means that any associated ground deformation can be readily alleviated and as a consequence is usually short-lived.

Ground deformation monitoring of The Upper South-Eastern Flank began in 1975, this section investigates the results from occupations undertaken prior to the present study. From 1975, Murray and co workers established and commenced; (i) the bi-annual occupation of an 11 km levelling traverse across the summit of Etna, and (ii) the measurement of a 32-station dry-tilt network located in a radial pattern around the (1000-2000m) flank of Etna (Wadge 1976; Murray *et al.*, 1977; Murray & Guest 1982). Repeated levelling and dry tilt measurements between 1975 and 1980 detected little vertical deformation over the area, except (unsurprisingly) across fresh lava flows. From their pioneering work, no major inflation and deflation cycles were recognised, however, two distinct types of minor deformation were documented. Firstly a vertical downward movement of survey points on fresh flows (thought to be caused compaction and consolidation) and secondly, small isolated pockets of inflation and deflation. The small pockets of inflation were due to the transport of magma beneath the flank, notably between Cisternazza and La Montagnola, where benchmarks exhibited a 4cm rise over the two year period before the small 1978 flank eruption. The levelling traverse of Murray and Guest (1982) is however limited by three factors, (i) all the measurements are relative to the Piccolo Rifugio a site in the centre of the active Southern Rift-Zone whose stability is questionable (the 1983 eruption occurred very close to this site), (ii) data are interpolated for eruption sites not crossed by the traverse, and (iii) the traverse is not closed, although a series of closed rings within the traverse are used to validate the estimates of precision, the accuracy of the whole traverse is not assured.

In 1972, Wadge established an EDM network around the summit craters, this ground deformation data enabled the identification of the summit storage areas as the main receptacle of ascending magma (Wadge, 1976). As the magma enters and fills the reservoirs the magma pressure increases, until the pressure becomes greater than the tensile strength of the rock and the minimum compressive stress. At this point the walls fracture and magma filled fissures propagate outward along the least-effort path causing sub-terminal dyke fed eruptions. Wadge (1976) attributed the source of larger flank eruptions to a deeper second reservoir near

the base of the volcanic pile. This connection is upheld by the certainty that the ground deformation caused by the magma stored in the central conduits does not correlate with the total amount of magma emitted, for example in 1979 the inflation suggested a volume of $8 \times 10^4 \text{ m}^3$ compared to the estimated output of $12 \pm 10^6 \text{ m}^3$ (Wadge, 1976).

Sanderson (1982) set up a high precision gravity network on Etna in September-October 1979 to examine high-level transport and storage. Sanderson proposed that magma rises passively via vertical fissures thus entering a void rather than actively intruding into consolidated rock. The precursive deformation (as in 1978) attributed to the changing levels of magma in the central conduit rather than a reflection of the total volume in the system. By closely examining the micro-gravity changes related to the March 1981 eruption, Sanderson challenges the model that there is a single cylindrical storage area on Etna which feeds every eruption (Section 4.1), proposing instead that the eruption of 1981 was fed from a deep source that had previously been stored in a high-level dyke for 6-12 months. The possible dimensions of the central conduits are unknown, however ground deformation data from Saunders (*unpub-data*) and Murray (1990) indicate that the precursive 'sinking' of the summit region may reflect the size of the vent. Saunders (*unpub-data*) examined the problem, using finite element modelling and found that the retreat of magma in the central column causes the upper flanks adjacent to the summit to deflate and the outer rim of the vent to tilt inwards. This model also concludes that when the magma level is high a conical plug is formed and the greater weight and breadth at the rim causes the upper flanks to sink and the outer rim of the conduit to be pushed apart. Murray (1990) suggests that the 'sinking' may be due to the steep topography of the area and the extra loading by lavas causing the top to slump or tectonic extension caused by east-west extension. After the start of the ground deformation monitoring program on Etna in 1975 to 1980, the eruptive pattern was of continuous summit eruptions, apart from a passive flank eruption in 1978 during which no major associated ground deformation was recorded. This flank eruption was thought to occur from a dyke

emplaced prior to 1975 (Murray & Guest, 1982), or from a dry fissure utilised by a sudden magma surge.

In 1980 a large scale seismic swarm was recorded in the Mascalucia-Tremestieri Fault Zone resulting in a surface rupture. After this event flank eruptions became more common. This may be explained by two different interpretations; either, prior to the earthquake, rifting-related strain had not been accumulated in the Timpe fault system thus ceasing the eruption of the rift-zones. Else, the activation of a deep SE Fault 'opened' the magma system facilitating the deep transport of magma into the summit area and the rift-zones (i.e. not via the summit).

Since 1981, the flank eruptions that have occurred in 1981, 1983, 1985, 1986, 1987, 1989 and 1991 can be divided into two groups (Murray, 1990). Murray distinguished two broad patterns of behaviour, firstly, prior to a flank eruption (two to three years), sections of the summit area experienced progressive deflation. This was seen prior to the events of 1983, 1985 and 1986-7, where it was interpreted that loading resulting from the filling of the central conduit with magma, caused the summit area to deflate and the adjacent flanks to inflate (Murray, 1984). This pressure produces strain on the summit flanks deforming the upper flanks to exceed the yield strength, leading to radial fracturing, facilitating dyke intrusion. The second behavioural pattern is of little or no precursory deformation before an eruption. This is most likely due to sudden magma ascent, which causes brittle fracturing of the conduit due to the rapid stress build up, the fractures open radially from the conduit, but close instantly the magma pressure is released. This produces short-lived eruptive events such as in 1978-79 and 1981. However, in December 1985 after a years deformation a dyke was intruded ESE from the central conduits, the eruption only lasted six days. This event does not fit with the theories put forward, since either the eruption should have been (according to the Murray's theories) long and large in volume, oriented towards the rift-zones or short and with no percussive deformation. This event seems to be a mixture of the two types proposed, the magma ascended from depth slowly, was stored and caused local deformation in

the form of the inflation of the ground above the storage area. This intrusion was slow and stresses were gradually accommodated, since the expected timescale for an intrusion to be formed is around two years, the premature eruption indicates that the situation changed. One interpretation is that a new rapidly ascending pulse of magma arrived in the system causing the sudden fracturing of the storage area in a radial form. This would explain the off-rift path and vent of the 1985 dyke and the fact the erupted material contained stored and fresh magma mixed (Clocchiatti *et al.*, 1988). After the fleeting pulse of magma, the system continues to fill and the inflation continued and the complete flank eruption occurred in 1986.

McGuire and Pullen (1989) distinguished shallow blocks in the Upper South-Eastern Flank of Etna by analysing horizontal vector displacements for the period 1981 to 1987, including the dyke emplacements of 1983 and 1985, see Figure 4-6.

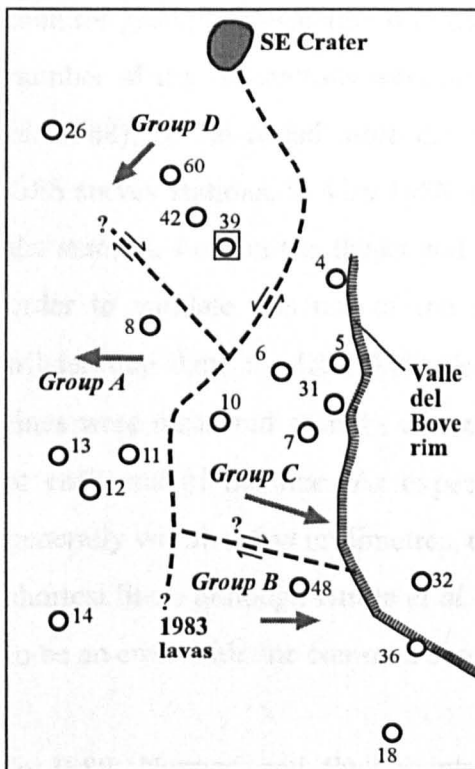


Figure 4-6 The Upper South-Eastern Flank of Etna (section taken from Figure 4-7) divided into the shallow blocks proposed by McGuire and Pullen (1989), the circles represent ground deformation survey stations that are now included in this study.

The shallow blocks were divided into four groups; the eastern groups showed an eastern displacement and the western groups showed western displacement. Data indicated that the area adjacent to the Valle del Bove was being displaced eastwards, the horizontal ground deformation (measured using EDM) detected 5m lateral displacement in 10 years.

In the late 1980s the Global Positioning System was introduced to be tested against existing surveying methods already established on Etna (Briole *et al.*, 1990). The strategy was, to use GPS as a universal method, such that if it proved viable it would take over as the alternative to levelling, Infra-red-Electronic Distance Measurement and dry tilt. GPS had already been tested extensively in Iceland (Fougler, 1987) and Hawaii (Okamura, 1996) to gradually take over the ground deformation monitoring of the active volcanoes. Briole *et al.* (1990) completed the first systematic study of the use of the GPS static method to monitor ground deformation on Etna, using a combination of GPS and dry tilt. A number of dry tilt stations were already established (Wadge, 1976; Bousquet *et al.* 1988), Briole added more dry tilt stations, strategically located near to the GPS survey stations. In May 1988, nine GPS benchmarks were installed, three on the summit, four on the flanks and two in the Peloritan-Nebroden mountains. In order to validate this use of the method the GPS data were compared with trilateration data; the IR-EDM trilateration data were collected with great care, lines were measured at night where possible, with meteorological data collected at each end of the line. As expected the EDM data and the GPS data were generally within a few millimetres, the greater differences were observed over the shortest lines, although Briole *et al.* (1992) determined the probable cause of this to be an error with one common survey station.

In 1989, Nunneri and Puglisi introduced GPS as part of the comprehensive monitoring strategy of Etna, (Nunnari & Puglisi, 1994b). They did not seek to combine the two techniques, instead choosing to discontinue monitoring the EDM network and establish a new GPS network since the removal of the limiting factors of EDM provided more opportunities for strategic benchmark

positioning. The first surveys occupied networks of nine new benchmarks and consisted of 18 strategic baselines (the longest was 25km long). From 1989-1991, the network was enlarged to 36 benchmarks (some of which were also part of a precise levelling network), network design allowed repeatable systematic surveys over the whole of Etna. The data were collected in a 'minimum-effort strategy' such that, the factors limiting the precision of the data were observed, only in so far as to provide data of an acceptable precision (Nunnari & Puglisi, 1994b). The surveys are undertaken using the minimum data collection time, a mixture of receivers, a standard data processing package and the broadcast ephemeris.

The 1989-91 surveys the networks were adjusted as a minimally constrained network, such that no absolute control-point co-ordinates (fiducial points) were added. Nunnari and Puglisi (1995) introduce an evaluation method for GPS baseline solutions, See Section 3.2. For the comparison between 1990-1992 the data were found beneath the sigma line (see explanation in Section 3.4), except where the baselines included a height difference of >800m as these outliers are thought to be a result of tropospheric effects. The GPS data collected (Nunnari & Puglisi, 1995) between 1989 and 1990 shows significant movements (>10mm) over the Southern Rift-Zone where large displacements occurred related to the dyke emplacement. The network was too spatially diverse over the effected area to undertake precise interpretation. Distance changes reveal a broadscale stress regime defined by a N-S compression associated with E-W extension (Lo Giudice and Rasà, 1986). The vertical element was not considered since the geodetic components of azimuth and ellipsoid height are affected by un-specified bias factors and atmospheric conditions. The results of the 1991-92 survey was that the data were satisfactory in terms of precision and that a general pattern of contraction was observed reflecting the N-S compressive regime except over the Upper Summit area where there were no coherent patterns.

During the same period, Bruyninx and Warnant (1995) also undertook a GPS survey, spread over three campaigns, in the autumn of 1992, 1993 and 1994. They used the same locations for their survey stations as Nunnari and Puglisi

(1994), although it is unclear if they used the same markers. A mixture of single and dual frequency receivers were used; the dual frequency receivers primarily fixed the network to a distant absolute co-ordinate (Noto, Southern Sicily), and were then used in combination with the single frequency models to complete the four hour static sessions on Etna. The greatest errors in ppm were observed for short baselines with large height differences, this was justified to be due to the different micro-climates in the Etna region and the tropospheric variance. The data were analysed through baseline length repeatability. The results showed that negligible deformation occurred during this period, (although an unexplained displacement of >4cm occurred at a survey station at an altitude of 2800m on the SE flank). The effectiveness of the troposphere was estimated by the application of the zenith path delay over a long baseline (28km) with a large height difference (1.8km), the application of the delay altered the height by around 11cm, although the effect on the baseline length was smaller (0.5cm), (Bruyninx & Warnant, 1995).

In 1994 Murray (Sergeant & Murray, 1994) incorporated GPS to use alongside and potentially take-over from levelling and trilateration networks. Murray monitored an area extending from the summit down to the NE ridge, the network has approximately 48 benchmarks. For the application of the GPS technique, three survey stations installed by Puglisi, were used in the survey. The results were good, with an estimated repeatability of <10mm (subsequent annual surveys had a repeatability in the order of 10-20mm, Murray (*pers com*)).

4.5 The 1991-93 eruption: magma transport and storage and the prevailing stress conditions.

Seismic swarms resulting from the sub-surface transport of magma were recorded during the end of the 1989 summit eruption. The fractures propagated from the summit craters across the upper SE flank of the volcano, where they erupted to feed a 12-day flank eruption (Alparone *et al.*, 1994). The opening of the 1989

fault at depth facilitated the transport of magma to the surface. Bonaccorso *et al.* (1996) and Cocina *et al.* (1995) recognised a change in the deep extensional regime characterised by the switching of σ_1 to vertical facilitating dip-slip movements and the emplacement of the magma in the feeder dyke. Given the data available it is not possible to determine a definite cause of the stress inversion, although the most likely cause is the transfer of magma into the low confining pressures of the shallow sub-surface causing the switch of σ_1 back to horizontal. All groups monitoring the stress field noticed the distinct change in the local stress field two months before the onset of the 1991 eruption which allowed the magma to ascend into the fracture system. Cocina *et al.* (1995) recorded that most of the abundant seismic activity in the year preceding the December 1991 eruption occurred either at shallow depths (<10km) in the western part of Etna or at depths of 15-30km in the east. They also determined the maximum compressive stress to have a strike of 351° , and the minimum compressive stress (EW) 83° .

With hindsight, Patanè *et al.* (1994) considered that the level of seismic activity was relatively small compared to the amount of material emitted by the eruption and the strain levels recorded during the event. From this observation he concluded that the amount of seismic energy released did not relate to the total magma quantity (Patanè *et al.*, 1994). During the first three months of the flank eruption, microgravity data confirmed that the intrusion of magma was coming directly up from depth rather than from the summit (Rymer *et al.* 1995). The possible implications of this will be examined subsequently. The microgravity results showed that between June and November 1989, stations south-east of the summit recorded a gravity increase of up to $100\mu\text{Gal}$ in a distinct trend oriented south-south-east from the summit craters. Despite a brief decrease in microgravity between November 1989 and June 1990, the area showed a cumulative increase leading up to the eruptive event. This data identified a magma filled fracture propagating SSE from the summit area. The intrusion of magma was essentially aseismic and the slight deformation could be modelled elastically, see Section 4.6.2. In total increases of over $100\mu\text{Gal}$ were observed. No

accompanying seismic activity was recorded which suggests that a passive intrusion through the 'pre-strained' low stress path of the fractures that propagated during the last stages of the 1989 eruption. Data collected during the 1991-93 eruption highlight the rapidly changing stress conditions that occurred as magma was emplaced into the pre-existing fracture on the south-eastern flank (see Table 4-1).

Date	Summary of data analysis
August 1990 - September 1991	maximum compressive stress was aligned N-S at a low angled dip (Cocina <i>et al.</i> , 1995).
January 1991	the epicentre depth was around 3km, the σ_1 was trending NE-SW. Bonaccorso <i>et al.</i> (1996)
July 1991	NE-SW ruptures on oriented fault planes of depths from 3-20km, with reduced levels of seismicity from July to October. Patanè <i>et al.</i> (1994)
October 1991	σ_1 reoriented to NNW-SSE, Bonaccorso <i>et al.</i> (1996), seismicity resumed at depth, culminating in a dip-slip tensile opening of the NNW-SSE structural trend thought to be the northern branch of the Malta Escarpment. Bonaccorso <i>et al.</i> (1996)
December 1991	σ_1 switched back to horizontal tending SW-NE (Bonaccorso <i>et al.</i> , 1996), at 120° (Cocina <i>et al.</i> , 1995).

Table 4-1 A summary of observations during the first stages of the 1991-93 eruption.

4.6 Finite element modelling of the 1983 and 1989 dyke emplacements

In Section 3.5, a series of tests were completed to examine the use of finite element modelling in analysing ground deformation. In order to prepare for the modelling of the significant ground deformation data on Etna, the physical and mechanical properties of the sub-surface can be devised in advance. Known dyke parameters and surface ground deformation (Murray & Pullen, 1984) from the dyke emplacement in 1983, were input into *new models* in order to estimate the unknown parameters of magma pressure and the host rock's physical properties. The data were then further tested (using ground deformation data, (Saunders, *unpub-data*; Murray, 1990) on the emplacement event of 1989/91. This pre-

emptive approach allows typical deformation patterns to be identified and for the influence of common features (which may effect subsequent data) such as an existing fissure or a typical dyke trends to be understood. The Upper South-Eastern Flank of Etna has hosted numerous dyke emplacements and fissure openings in the last decade alone. The principal dyke swarm follows a trend from the Torre del Filosofo down to the Piccolo Rifugio, see Figure 4-7.

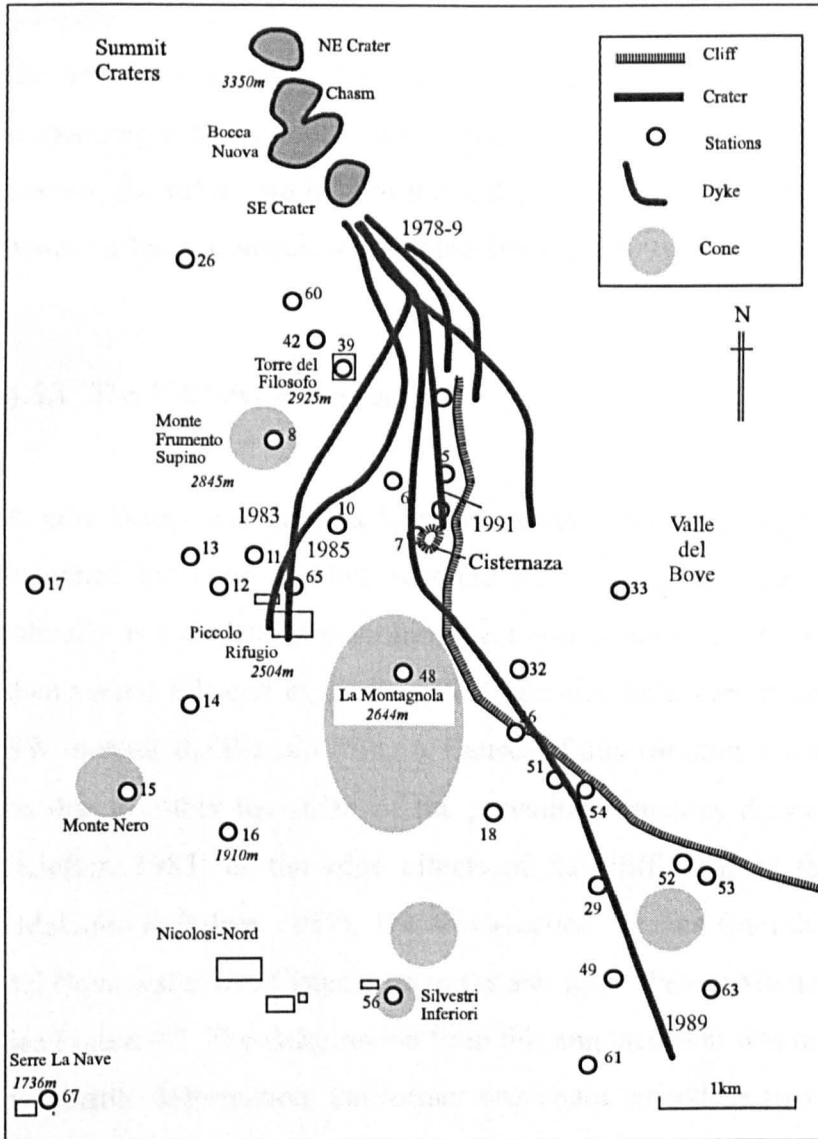


Figure 4-7 The Southern Rift-Zone of Etna indicating the principal areas and dyke swarms (After McGuire *et al.* 1996)

Although the dip, depth and opening pressure of dykes being transported along this weak zone, may vary it is assumed that the physical properties and the ratio

of brittle and elastic failure will remain similar. It is therefore beneficial to model the recent dykes emplacements on Etna in the central zone of the flank (1983) and the area adjacent to the rim of the Valle del Bove (1989/1991).

The value for the Young's Modulus was chosen to reflect the fractured nature of the shallow surface, to be $5 \times 10^{10} \text{ Nm}^{-2}$. The magma overpressure applied into the host block from the dyke is the differential pressure between the lithostatic pressure and the magma pressure. The relationship between these two values is the same irrespective of the actual values, since the force applied causes a responding deformation. Unless a real value for the pressure or the elasticity is known, the values are held to the realistic ratio. The dyke pressure and Young's Modulus have been balanced for the 1983 and 1991 examples.

4.6.1 The 1983 dyke emplacement

A new model was devised to simulate the 1983 dyke emplacement. The dyke breached the main conduit near the SE crater at a depth of 1km, extending laterally as a bladed dyke, striking SE towards Belvedere for about 1km, where it then veered SW east of the Torre del Filosofo, from here it turned S, then finally SW towards the Piccolo Rifugio. Causes of this variation on strike are thought to be due to either the strike of the prevailing fractures dissecting the upper rift (Kieffer, 1983) or the edge effects of the cliff edge of the Valle del Bove (McGuire & Pullen, 1989). The cross-section is taken from the edge of the Valle del Bove just above Cisternazza to the ash slopes below Monte Frumento Supino, see Figure 4-7. The deformation from this emplacement was in the form of elastic and brittle deformation, the former was characterised by two raised areas 18cm and 40cm high either side of a central trough. This elastic deformation preceded the brittle failure, which created a graben 1-1.4m deep in the surface above the dyke tip (Murray & Pullen, 1984). This indicated the breach of the yield strength.

Data indicates that the dyke propagated from the central conduit vertically, measuring 950m high at a depth of about 600m, the dyke dip increased as it propagated down the Southern Rift-Zone, this was most likely due to the edge effects of the Valle del Bove. It was found during the preliminary tests that the proximity of the cliff edge to the dyke changes the host rock deformation associated with the opening dyke, this can be seen in Test1c (Section 3.5.2), where the dyke displacement seems to cause a rotation of the material towards the cliff see Figure 4-8.

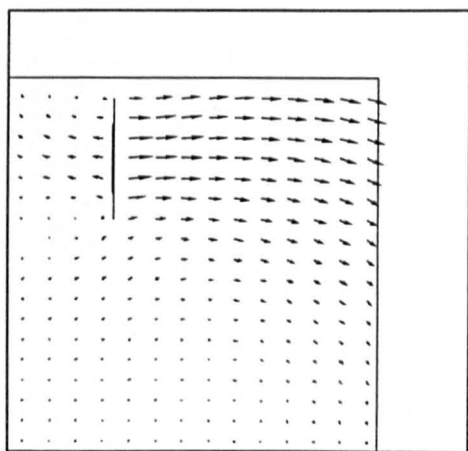


Figure 4-8 The dyke emplaced adjacent to the cliff causing the 'rock' close to the cliff edge to rotate (dyke length = 100m).

This rotation changes the dip of the dyke as it propagates through the Southern Rift-Zone. The observed surface displacement above the strongly fractured area between the Torre del Filosifo and the Cisternazza is inelastic and represents the brittle block movement (McGuire *et al.*, 1991), the areas above and below this show elastic behaviour.

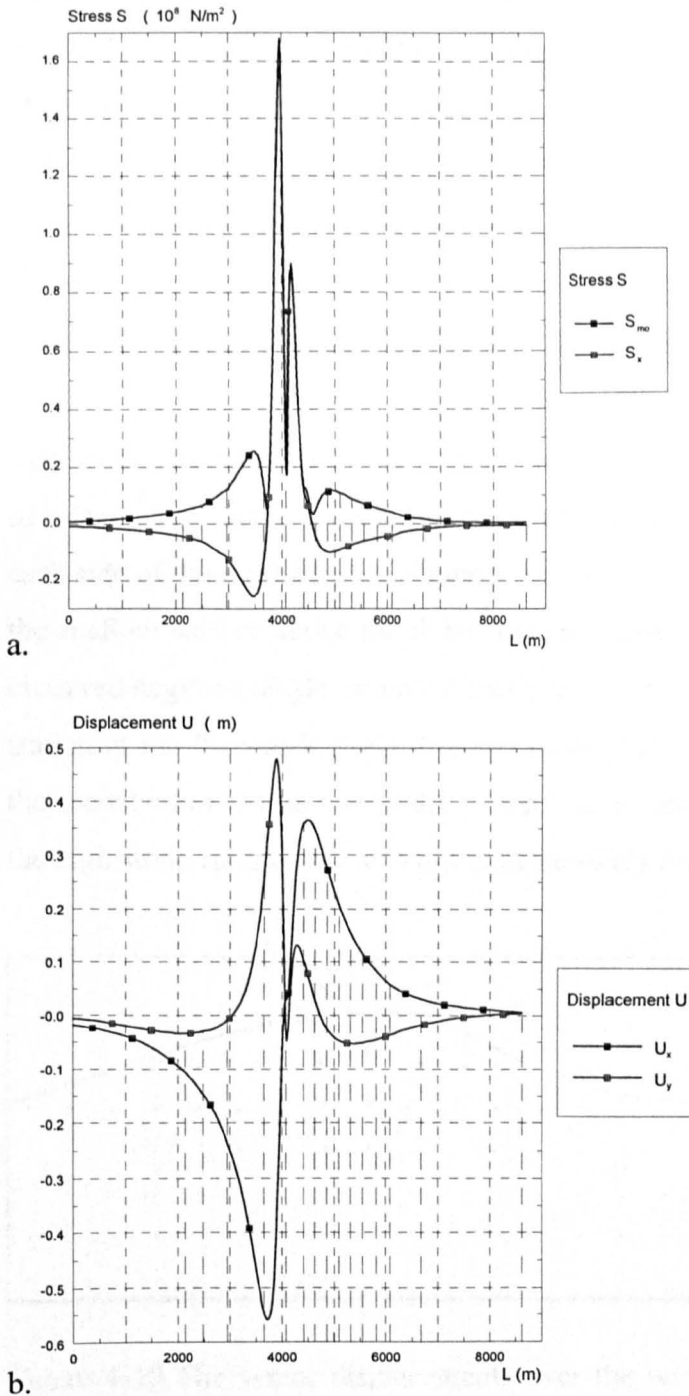


Figure 4-9 (a) The Mohr stress (S_{mo}) & horizontal stress (S_x) and (b) the horizontal and vertical displacement (U_x & U_y) acting upon the top of the cross-section (west to east) illustrated in Figure 4-10.

Dip and depth of the 1983 dyke for the line of the cross-section were taken from Murray (1990). The dip is assumed to be 75° west, with a depth of 240m, and a height of 320m. It is difficult to create accurate fault geometry for the dyke since the fracture through which the dyke was emplaced reaches to a depth of 1km

(Murray & Pullen, 1984). An opening pressure of $2 \times 10^9 \text{ Nm}^{-2}$ was assumed for the dyke, this was calculated by estimating the magma pressure and the strength of the host rock. The 1983 simulation emphasises the caution required when inferring elastic deformation in a partially brittle area. The upper shallow surface of the volcano must be modelled as an elastic material. The area is, however, strongly fractured and acts as a brittle material, shallow and deep fractures traverse the area and cause irregular deformation when under pressure.

The results are good, showing that the model fits the observed data, with a peak of +45cm to +50cm representing the elastic deformation on the ground surface each side of the intrusion, see Figure 4-9 and Figure 4-10. The fractured nature of the shallow surface above the dyke was not included in the model and the large observed negative displacements directly above the dyke were not simulated. The station at the Piccolo Rifugio dropped more than 1m, this was not identified in the model since it was due to the unpredictable brittle nature of the surface, but the high strain rates at this area did indicate likely brittle failure.

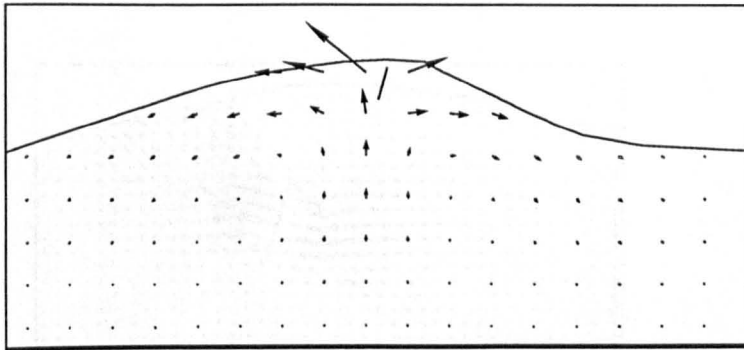
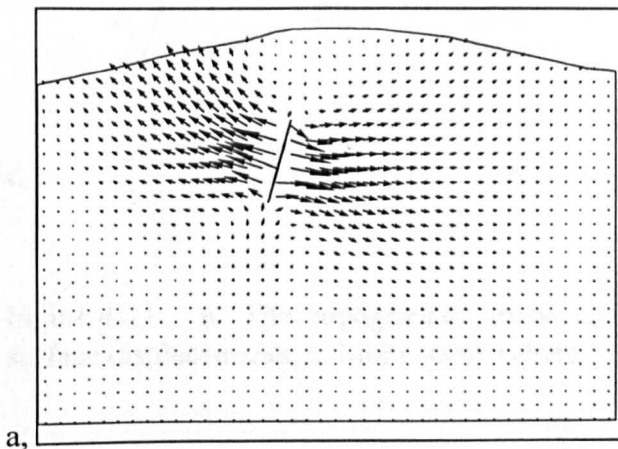


Figure 4-10 The vector displacements over the west-east cross-section, and the dipping dyke.

4.6.2 The 1991 dyke emplacement.

The horizontal and vertical displacement data observed during the filling of the 1989 fracture with magma was collected by Murray and Saunders (Murray, 1994; Saunders, *unpub-data*). Murray derived the dyke dip and depth from visual

comparisons between his data and the models by Dieterich and Decker (1975), by superimposing observed data onto the models (by eye) A magma overpressure of $2 \times 10^8 \text{ Nm}^{-2}$ produced parameters similar to the observed values, so the ground surface co-ordinates were then added to shape the surface topography to match the actual topography of Etna. The surface geometry was taken from a topographic map, using spot heights from the survey stations to enable precise vector displacements. The cross-section stretches from the southern ash slopes up to Monte Frumento Supino across to Belvedere and beyond to the NE. The topography varies by 400m over the 4000m long section. The dyke is 600m in breadth and dips 75° to the east, the top of the dyke is 450m below the surface, under Belvedere. The data from Murray is presented as vectors of vertical or horizontal movement along the section with direct vertical changes for each station during the period of dyke emplacement. Saunders presents the horizontal displacement data for the half of the section between Belvedere and the ash slopes beneath Monte Frumento Supino. The model data reveal results very similar to the recorded data, showing a broad pattern of up-lift associated with the intrusive dyke, see Figure 4-11a.



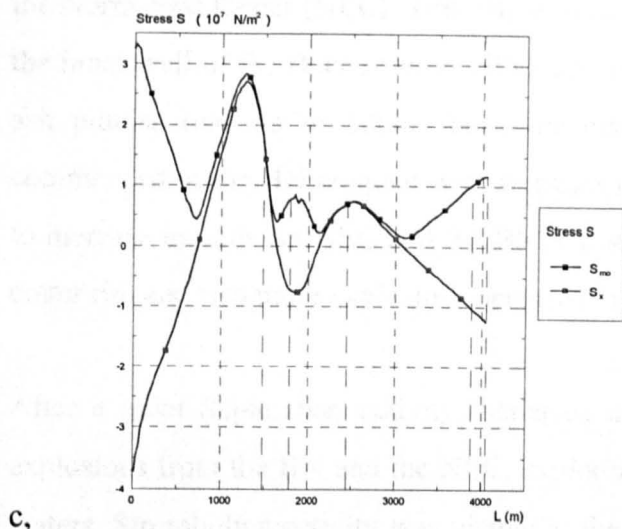
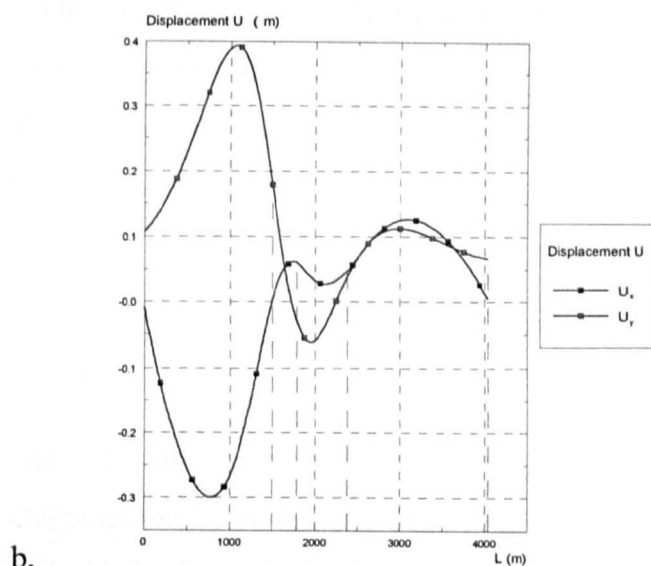


Figure 4-11 a. The topographic cross-section, showing the 1991 dyke, b. surface displacements, c. Mohr stress values.

The Mohr stress pattern indicates the relationship between the displacement and the stress build up. In Figure 4-11a and b, it is seen that the stress values correspond to the displacement values, there is however an disparate peak in the Mohr stress at Belvedere. From the east the displacement value is high corresponding to the high Mohr stress value and the increasing horizontal stress. As the displacement is reduced and the Mohr stress increases, the potential for

brittle failure increases. The Belvedere area underwent a disparately high degree of brittle displacement not predicted by the model. The recorded values for Belvedere show a displacement of over -20cm. *This value is much higher than anticipated due to the strongly fractured shallow surface area.*

4.7 Activity at Etna between September 1994 and December 1997

After the end of the 1991-1993 eruption, the volcano entered a quiet period; characterised by continuous degassing of from the summit craters and fumerole activity. In May 1995, the activity began to increase with non-juvenile ash observed within summit plumes, and on the 23rd lithic blocks were ejected from the North-East Crater (NEC). This renewed activity was thought to be a result of the inner wall of the Bocca Nuova (BN) collapsing (Coltelli, 1995). By July 25th, ash plumes rose up to 100m above the crater rim and Strombolian activity commenced at the BN coupled with frequent gas explosions. Activity continued to increase in both the NEC and the BN. On August 2nd, lava jets rose above the crater rim and two more explosions occurred later in the month.

After a quiet September, activity increased in October with renewed frequent explosions from the BN and the NEC, exploding juvenile bombs 200m from the craters. Strombolian activity was visible at the bottom of the craters and the gas plumes were notably denser, this was accompanied by loud explosions and a roaring noise like a jet engine. By the end of November activity continued and seismic tremor was recorded; a powerful explosion occurred on December 23rd which produced a tall eruption column which deposited ash on the volcano flanks (Coltelli, 1995).

Activity continued into 1996 with two episodes of lava fountaining from the NEC and the BN producing scoria fallout 2km from the summit. After a few quieter months explosive activity returned at the end of May and a lava pond was visible at the bottom of the BN. During the 1996 field campaign in June, a visit by the

author to the summit on June 10th confirmed the continuing activity, two strongly glowing vents were observed in the BN and a single vent in the Chasm (CII) and weak strombolian explosions occurred every 5-10 seconds. On the approaching the NEC, the ground was notably hot underfoot and the gas emissions were very strong. The crater was full of fresh material from which gas and water vapour escaped, there was no Strombolian activity. A few days after the visit, the crater exploded producing a tall ash plume. At the end of June there were strong explosions and 30m *fire fountains*. The Strombolian activity continued and by the end of July a lava flow emerged from the NEC. Flows continued for another month until the 17-18th when the flow descended into the Valle del Bove (it then stopped). For the rest of the year degassing and Strombolian activity continued from the NEC and the BN, weak Strombolian eruptions occurred from the South-east crater (SEC) in December (Smithsonian, 1996).

In January 1997, there was periodic Strombolian activity from the BN and the NEC, with one hour of observed activity from the SEC. The activity continued into February with continuous ash emission from the BN and NEC with weak degassing from the CH and a small cinder cone began growing in the SEC. Activity increased again producing a cinder cone in the BN and activity in all craters although it was restricted to within the crater rims (Coltelli, 1997). Mild Strombolian activity was again observed in the SEC, producing lava flows by the end of the month; Strombolian activity from the other craters was observed nightly. Through May and June activity continued, a magma pond was formed in the BN; activity at the NEC lessened (Coltelli, 1997). For the rest of the summer of 1997, spasmodic Strombolian activity continued and explosions could be seen at night from Catania. Lava filled the craters, spilling out producing lava flows. There was no indication of a dykes emplacement or flank fracture.

4.8 Conclusions

Etna is situated in a complex regional tectonic area, and the relationship between volcanic and the tectonic activity is contested. Recent monitoring of the faults during the 1991-93 eruption produced divided opinion on a correlation between eruptive activity and displacement of the Timpe Faults (Latora *et al.*, 1996; Rasà *et al.*, 1996). If the seismic data from the last eruption (and others from the last decade) is accepted then it can be argued that long-lasting flank eruptions may be fed by deep faults on the SE flank. The implications of this are that regional tectonic activity triggers flank eruptions rather than just the pressure of the ascending magma.

Finite element modelling was successfully used to simulate the 1983 and 1991 magma intrusions, it also revealed an interesting edge effect of the Valle del Bove. When a dyke is simulated adjacent to the cliff edge the prevailing stresses are directed towards the cliff effectively re-orienting the dyke, thus explaining the shallow dip of the dykes that propagate into the Southern Rift-Zone. The ground deformation network established by McGuire and Pullen (1989) spanning the Southern Rift-Zone is ideally located to examine magma-related deformation (from summit eruptions or dykes emplacement in the SSE & S rifts). Furthermore, the local deformation effects caused by the adjacent steep cliff of the Valle del Bove provide data on slow gravitational deformation. This network combined with the Lower Eastern Flank networks provides a comprehensive network that will examine the individual and combined roles of magma-, gravitational and tectonic-related deformation. This discussion is continued in light of the ground deformation data in Section 5.11.

5. MT. ETNA, PART TWO: MEASUREMENT & MODELLING

In order to detect ground deformation over the south-eastern and eastern flanks of Etna, data were collected from a combination of established and newly installed networks; two techniques were used Electronic Distance Measurement and the Global Positioning System (the methodologies are described in chapters two and three). The data are analysed for coherent patterns and small but mathematically significant patterns of data are modelled. The interpretation of the results leads to the presentation of new conceptual models to explain the ground deformation.

5.1. Evaluating the ground deformation networks

The ground deformation networks can be divided into two parts: the Upper South-Eastern Flank and the Lower Eastern Flank Networks. Table 5-1 lists the different networks indicating their location, size and date of establishment.

General area	Specific region	Survey stations	Date established	Group
Upper south-eastern flank	Southern Rift-Zone	~35 ¹	1971, extended in 1982 & 1992	Wadge (1976), McGuire <i>et al.</i> , (1991), Saunders (<i>unpub-data</i>)
	Serre la Nave	1	1995	Istituto Internazionale de Vulcanologia
	Milo	1 ¹	1996	Moss
Lower eastern flank	Macchia	6 ¹	1992	Stewart <i>et al.</i> , (1993)
	Carruba	5 ¹	1992	Stewart <i>et al.</i> , (1993)
	Vena	6 ¹	1994	Moss
	Trecastagni	4 ¹	1994	Moss
	Catania	1	1995	Istituto Internazionale de Vulcanologia
	Fondacello	1 ¹	1996	Moss
	Piedimonte	1 ¹	1996	Moss

Table 5-1 Ground deformation networks on the Upper and Lower Eastern Flank of Etna, ¹established or modified during the course of the research.

Most of the networks were already established by previous scientists who examined eruption pre-cursors and flank deformation (Wadge, 1976; Murray & Guest 1982; McGuire & Pullen 1989; Stewart *et al.*, 1993). The combination of these networks provides a valuable opportunity to examine the relationship of deformation in the upper south-east flank of the volcano with displacement of the coastal tectonic faults. This allows direct comparison between displacements due to regional tectonic activity, magma emplacement and other deformation sources (Section 1.5). Figure 5-1 Illustrates the location of the survey stations on the Eastern Flank relative to the summit craters and the principal tectonic faults.

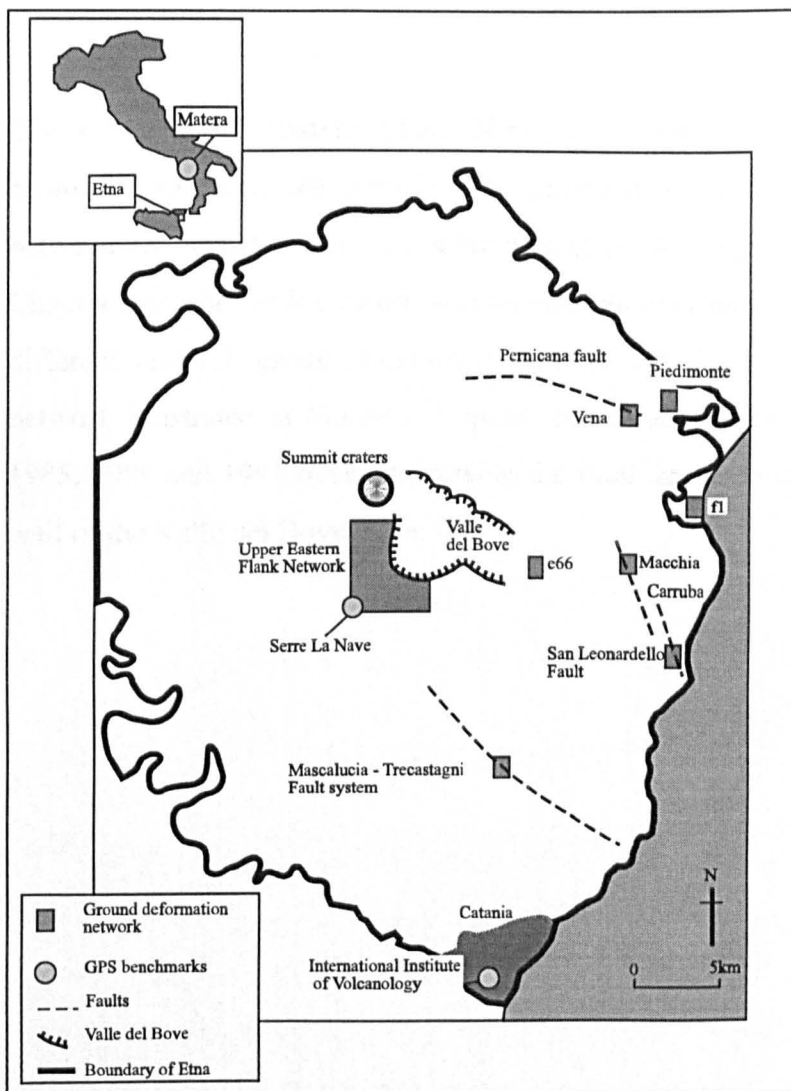


Figure 5-1 The ground deformation networks of the Eastern Flank of Etna included in this monitoring program, Matera (included as an inset) was used as a reference station in 1995. The Lower Eastern Flank faults are illustrated in more detail in Figure 4.5. (Modified after Rasà *et al.* 1981)

During the study period between 1994 and 1997, there was no large summit eruption, dyke emplacement or major seismicity on the flank faults. The monitoring of this time period (with no major magmatic flank eruption) thus facilitates the examination of the gravitational stability of the Upper South-Eastern Flank. The networks will be described in turn and analysed first separately and then as a single comprehensive network. The station descriptions for all the survey stations in the Etna study are listed in Appendix C.

5.2. The Upper South-Eastern Flank Network: location and purpose

The Upper South-Eastern Flank Network (approx. N37° 44' E15° 0') was positioned to detect the intrusion of shallow dykes in the Southern Rift-Zone between Nicolosi-Nord and the summit craters, see Figure 5-1. As discussed in Chapter four, the flank network was established over many years by a number of different research groups examining summit and rift-related deformation. The network illustrated in Figure 5-2 spans the surface traces of the 1978-9, 1983, 1985, 1989 and 1991 dykes, traversing the flank and extending over the western wall of the Valle del Bove to the floor.

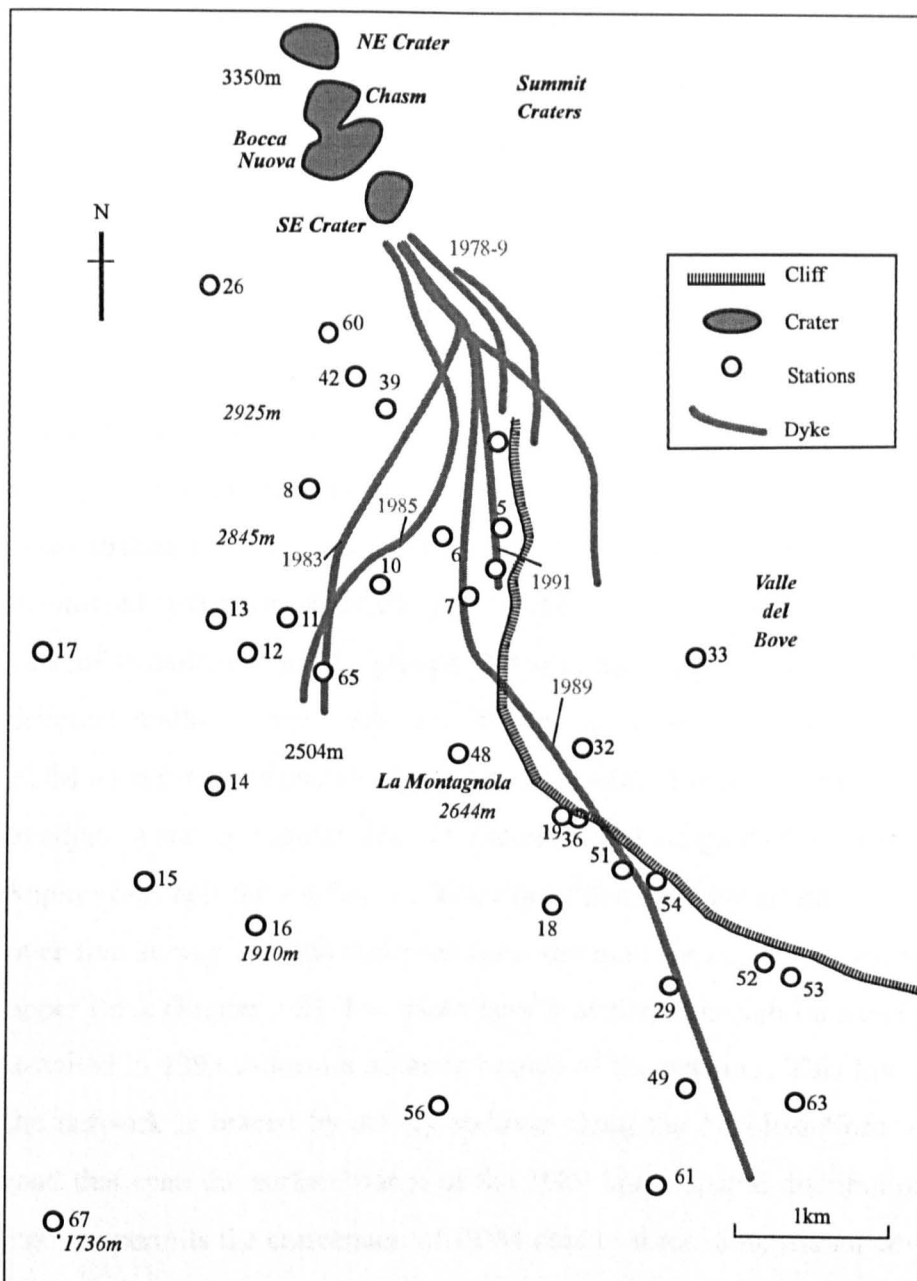


Figure 5-2 The Upper South-Eastern Flank Network

The specific research questions outlined in Chapter four asked *What are the relative contributions of regional tectonics, magma emplacement and gravity-induced displacement in the current operation of Mt. Etna?* The deformation monitoring specifically addresses these questions through the identification of:

- (i) dyke emplacement and propagation
- (ii) coherent movements of survey stations in the Upper South-Eastern Flank Network that would suggest the existence of discrete blocks

- (iii) creep of the shallow surface particularly the area adjacent to the Valle del Bove cliff and the Lower Eastern Flank Networks
- (iv) deformation directly related to regional tectonic activity

Further sources of magma-related deformation that may be observed are summarised in Table 1.1 (Chapter 1).

Three different types of survey station marker were measured on Etna; (i) steel survey nails hammered into stable rock or boulders, (ii) green discs glued into holes drilled into the rock or boulders, (iii) reinforcing rods (50-100cm long) hammered into loose material. The marker used depends upon the site and the year of installation (as the groups that originally established the networks used different markers), see Table 5-1. The network was originally measured using EDM so survey stations are located at sites with at least two vectors measurable to adjacent survey stations. Survey stations La Montagnola (e9), Monte Frumento Supino (e8) and the roof of the Torre del Filosofo (e39) all have line-of-sight to over five survey stations and thus form the main brace of the network over the upper flank (Figure 5-2). The lower survey stations beneath La Montagnola were installed in 1993 to form a separate branch of the network. This lower section of the network is braced by survey stations along the Nicolosi-Nord to Zafferana road that span the surface traces of the 1989 fault. Spatial distribution of survey stations permits the conversion of EDM data to three dimensional co-ordinates if all possible vectors are measured (the absence of any measurements can prevent the formation of co-ordinates).

5.3. The Lower Eastern Flank Networks

The Lower Eastern Flank Networks were initially established in June 1992 to measure displacement along tectonic fault strands (Stewart *et al.* 1993). The purpose of this was to establish the relationship between the activity of the volcano and tectonic displacement (see Section 4.3). Specifically to attempt to

identify if magma-related deformation at the summit was in some measurable way accommodated in the Lower Eastern Flank faults. The small levels of movement associated with the accommodation of either magmatic or tectonic stresses are not easily discernible. In order to recognise coherent displacement behind the 'background noise' of error the network must be measured for a number of years. The time constraints of this study did not favour the establishment of new networks to look for small creep movements, thus the monitoring of the existing networks with three year data-sets was therefore *taken-over* to maintain the data-sets and provide a link between the Upper South-Eastern Flank Network and the regional tectonic stress regime.

Networks were located at Macchia, San Leonardello and Carruba, in 1993, the networks were monitored by Saunders (*unpub-data*) and an additional network was established crossing the Pernicana fault (Provenzana-Pernicana network). Problems sustaining the Lower Eastern Flank Networks increase every year, as they are situated in a fairly densely populated area that includes numerous villages, roads and intensive agricultural land-use. This leads to many obstructions such as buildings, citrus groves and migrating rubbish tips, that have hampered the establishment and monitoring of the networks. Many of the Timpe fault scarps are very high and abundantly vegetated, reading lines from the top of a cliff face to the bottom is difficult due to this vegetation and using GPS at the bottom of the cliff is hampered by the proximity of the cliff-face. Other logistical problems including road resurfacing and urban change have lead to the loss of many of the original survey stations and have restricted the number of optimum survey stations (for EDM or GPS) locations. From the outset the San Leonardello and the Provenzana-Pernicana networks were abandoned, this was due to the loss of survey stations due to road resurfacing.

Carruba (N37°40' E 15°10')

The network at Carruba comprises five survey stations crossing the San Leonardello Fault, the layout of the network is illustrated in Appendix C. The surface trace of the fault is discernible as a dip and ground cracking in the road,

which suggests recent displacement. The network was evaluated in 1994 for its suitability to be combined into the flank-wide network. The results found that; (i) two survey stations were situated near growing vegetation and could soon be obscured, and (ii) another survey stations was located on a five metre concrete wall composed of large concrete blocks separated by a polystyrene in-fill. This is not ideal as the displacement of this part of the wall could be influenced by the cushioning of movements by the soft in-fill. In September 1994, one nail was lost due to road re-surfacing and a 'sight' across some lemon groves was obscured due to abundant foliage. In July 1995 two extra survey station were added, one new station was installed on the wall adjacent to another existing station on the opposite side of the fault (to test the affects of deformation along the wall). One other station was located further up the road. The long-term maintenance of this network may be problematic due to vegetation growth. However, it was decided that given the recent ground cracking and the proximity of the network to the Santa Tecla fault (major regional tectonic fault), to continue measuring the network for the time being. It is necessary to stress here that it was attempted to install a new network around the Santa Tecla fault but no suitable site (for long-term monitoring) was found.

Macchia (N37°43' E15°9')

The network was set-up crossing a two hundred metre high fault scarp, the layout of the network is illustrated in Appendix C. Vectors are measured between two survey stations situated on the top of the scarp along the edge of a road and four survey stations at the base; one by the side of a lemon grove, and three at the edge of roads in the town. Nails by the roads are situated such that they should not be affected by road resurfacing, but urban expansion may effect the long-term stability of the network.

Vena (N37°47' E15°7')

The Pernicana fault can be clearly seen deforming the Fornazzo-Linguaglossa road north of Vena. This new network was set-up as a triangular network with a survey station at its centre bracing the network, the layout is illustrated in

Appendix C. Due to copious oak trees around the network the maintenance of line-of-sight over time may prove problematic but no better site exists in the area. The survey stations were installed at the edge of the road close to the boundary walls and in outcrops of lava each side of the road. The white line in the centre of the road was examined closely, photographed and the 'existing displacement' was measured using a tape measure. The network was extended in 1996 to incorporate fault strands further down the road, these were marked by cracks and dips in the road; an additional station were added and two stations were abandoned (as they were unsuitable to be measured using GPS). The white line was re-painted in 1996 and was subsequently re-measured and photographed.

Trecastagni

The Mascalucia-Trecastagni faults form the southern boundary of the 'mobile sector' (Figure 4.5). They are oriented 130° , similar to the Santa Tecla fault which forms the recognised onshore extension of the Malta Escarpment further to the NE oriented at 140° (Lo Giudice *et al.*, 1982). The faults in Trecastagni have a dextral oblique slip, the movement is clearly seen in a deformed wall and beyond through a religious retreat. It was not possible to establish the network in the retreat so the network was set up along a road next to the deformed wall which clearly displayed cracking. Four survey stations were installed forming a braced quadrilateral, the nails were installed at the edge of the road where the tarmac had not recently been replaced; the layout of the network is illustrated in Appendix C.

5.4. Additional intermediate survey stations installed in the network

For the 1995 survey two survey stations were added from the Italian GPS network. Static Trimble™ GPS was made available from the International Instituto de Volcanologia, to measure the Lower Eastern Flank Networks. These survey stations were used as reference stations while the third GPS set occupied existing stations. The new survey stations (see Figure 5-1) were 9523 at Serre la Nave the astrophysical observatory a few kilometres below Nicolosi-Nord and

9598 located on the roof the headquarters of the International Instituto de Volcanologia in Catania.

In 1996, two Leica™ 300 series GPS sets were used to measure the network. The use of GPS enabled the summit and the Lower Eastern Flank Networks to be measured simultaneously, relative common assumed stable points. To ensure this link between the networks an extra new survey station was installed midway between the summit networks and the flank networks, a few kilometres north of Milo (e66) (It was intended to use the Open University Survey station in Milo however, it could not be located). One survey station was installed at the coast beyond the most easterly fault on the flank (f1), this was to monitor total flank movements to see if this is different in any way to the displacement of survey stations adjacent to faults. A further survey station was installed beyond the Pernicana fault to the north to act as a control to the mobile sector movements (f2).

5.5. Upper and Lower Flank survey reports: 1994-97

This section recounts the collection of data from the field campaigns undertaken on Etna between June 1994 and June 1995 using the EDM and GPS techniques. It is unnecessary to describe each EDM campaign in detail as the principal methodology is described in Chapter two. This section will however, report any deviations and adaptations of the standard operating procedure which may affect the quality of the results. All the results from this section are listed in Section 5.7 and discussed in Sections 5.10 and 5.11.

When the network is measured using EDM a stable location (e17) that is assumed to be stationary, is used as a fixed point (see Figure 5-2). The measurement of the network using EDM and a theodolite takes about two weeks depending on the weather, summit activity and organisational logistics. The order of survey station occupation is controlled by the weather and availability of transport. The use of a vehicle in 1994 and 1995 permitted the network to be measured rapidly as the lengthy time taken to walk between each survey station was reduced. Between 6-

10 vectors can be measured in a single day depending on the terrain and the position of the survey stations. Two stations in the Valle del Bove are very difficult to measure. The path to reach the second station was destroyed by the 1991-1993 lava flows, which are very sharp and unstable underfoot, so that hundred metres takes about one hour to cross. Using GPS would still require each site to be occupied at least twice, but as this does not require line of sight to an adjacent station, time can be used more efficiently and planned in advance without having to take into account the weather. In September 1994 and 1995 a partial occupation of the network was undertaken to determine if any magmatic or non-magmatic displacements had occurred. This partial survey is important as it is used to assess if any significant deformation detected in the annual survey, occurred due to cumulative slow strain or from a sudden event.

The initial evaluation of the network and the technique (EDM and combined theodolite) concluded that the technique was very weather dependant and the failure to measure key-line (to link sections of the network) hindered satisfactory network analysis. To improve the network the actual three dimensional positions of each survey station would have to be determined independently of adjacent survey stations. This is not a problem when using GPS as a fixed point off the volcano can be used. Table 5.1 below lists the measurements undertaken between July 1994 and June 1997; the full tables of data are found in Appendix B.

1994	Network	Lines measured	Changes	Method
July	summit	50	replaced e41 by e60	EDM
Sept.	summit (partial)	12		EDM
	Carruba	4	Lost 1 nail, 1 view obscured	EDM
	Macchia	5		EDM
	Trecastagni	4	new	EDM
	Vena	6	new	EDM

a, The network was occupied in 1994 with Saunders (*unpub-data*); it was the transitional occupation between his study and the research contained within this thesis.

1995	Network	Lines measured	Changes	Method
July	summit	69	lost e58, e36 new e61, e62,	EDM
	Macchia	7 (2 GPS)		EDM & GPS
	Carruba	7 (2 GPS)	new c7, c8	EDM & GPS
	Trecastagni	4		EDM
	9523 Serre la Nave	1	new e67	GPS
	9598 IIV	1	new 9598	GPS
Sept.	Summit (Partial)	12	e7, damaged but repaired	EDM

b,

1996	Network	Co-ordinates measured	Changes	Method
June	summit	33	old 'e19' measured by mistake (to be used as e19 from now on), new e63, e64, e65, e66	GPS
	Macchia	5 (2 GPS)	old station found	EDM & GPS
	Vena	2	renumbering new v5	GPS
	Carruba	8 (2 GPS)	renumbered	EDM & GPS
	flank stations	2	new f1, f2	GPS
	9523 Serre la Nave	1		GPS

c,

1997	Network	Co-ordinates measured	Changes	Method
May & June	summit	31	new e68, e69	GPS
	Macchia	2		GPS
	Vena	2		GPS
	Carruba	6		GPS
	Flank	1, no fix on f2		GPS

d,

Table 5-2 Network occupations, techniques & new stations: a, 1994; b, 1995; c, 1996; d, 1997.

5.6. GPS survey reports: 1995-7

This section examines the methodologies of the GPS field campaigns in greater detail than the EDM campaigns since; (i) EDM site occupation closely follows the methodology outlined in Section 2.4 and no further details are considered necessary; (ii) two different types of GPS equipment were used involving slightly different methods (1995 Trimble™; and 1996 & 1997 Leica™); (iii) two different data collection and processing methods were applied (static and rapid static); (iv) introduction of GPS modified the campaign objectives, therefore these are listed in each section (where applicable). The results are recorded, analysed and discussed in further sections 5.10 and 5.11.

5.6.1. July 1995

Three single frequency receivers were borrowed for three days from the Volcanological Institute in Catania. The objectives of this campaign were to; (i) position two established survey stations (9598 & e67) as reference survey stations, (ii) occupy the networks using GPS whenever appropriate and, in the event that GPS is unsuitable then EDM is used with at least one point tied into the GPS network.

The EDM surveys were undertaken simultaneously, the survey details are listed in Section 5.1 and the results are listed in Appendix B. To achieve the first objective, two receivers were installed as static references, one on the roof of the Volcanological institute in Catania (9598) and the second on a pillar at Serre la Nave (e67) and astronomical observatory on the Southern Flank of Etna. Using the static GPS surveying method (see Section 2.7), the receivers were programmed to operate for two, sessions of three hours each after which the data from each is downloaded for processing.

An initial reconnaissance was conducted to assess the suitability of each of the survey stations for use with GPS. This determined that one station of the Vena network and two stations of each of the Macchia and Carruba networks were the most appropriate sites to occupy using the GPS, within the time constraints. For each network, survey stations on each side of the fault were used so that any fault displacement would be detected. The survey stations were occupied using GPS and the baselines were also measured by EDM to provide a comparison of both line-lengths and co-ordinates. During each session three survey stations were occupied; the two reference survey stations (9593, e67) and one flank survey station. The continued re-occupation of the 9593 to e67 baseline provided a test of the repeatability, this line was checked everyday to see if there were any external (satellite) errors. The data were processed using the method outlined in Section 2.6. Because the receivers were single frequency the bias from the ionospheric delay could not be automatically removed, however as the baselines were relatively short (<20km) the ionospheric disturbance was minimal. In order for the data to be loaded into the software (GPSurvey, Trimble™) they had to be converted to the Receiver Independent Exchange Format (RINEX), this was due to incompatibility between the old receiver and the latest software package.

All the baselines were processed from a fiducial point; this was obtained by processing the days occupation of the survey station 9598 with the nearest fixed reference point at Matera, Italy (see Figure 5-1). The Matera benchmark is a permanent GPS station maintained by the Italian Space agency. Its location is checked with data collected using Satellite Laser Ranging (SLR) and Very Long Baseline Interferometry (VLBI), (see Table 5-3). RINEX files were downloaded for each day and were processed simultaneously with the RINEX files from survey station 9598 to obtain a fixed position.

Matera (June 1995) Tygeonet Nel Sistema ITRF92
40° 38' 56.8659'' N
16° 42' 16.0419'' E
535.656 m

Table 5-3 Geodetic co-ordinates of Matera in WGS84

5.6.2. June 1996

The June 1996 re-occupation of the Upper South-Eastern Flank Network and Lower Eastern Flank Networks was undertaken using a combination of the GPS and EDM techniques. The EDM network was measured using the GPS in order to compare the 1996 GPS data-set with the existing EDM data-sets (Saunders, *unpub-data*). It is necessary to consider the methods used in June 1996 in more detail than those of the 1995 survey because of the greater versatility of the Leica™ 300 series GPS receivers used as compared to the Trimble™ 2000 series used in 1995. The following tasks were carried out in order to successfully collect sufficient accurate ground deformation data: (i) re-occupation of all Upper South-Eastern Flank Network survey stations and (where possible) Lower Eastern Flank survey stations using GPS, (ii) re-occupation of remaining survey stations using the EDM technique (where at least 1 survey station in a network was measured using GPS), (iii) addition of new stations beyond line-of-sight to improve coverage over the Upper South-Eastern Flank and Lower Eastern Flank, at the coast beyond the Timpe faults and beyond the boundaries of the mobile sliding flank. In order to identify any systematic or random bias associated with the EDM or GPS that might effect the long term trends, careful checks and mathematical comparisons were undertaken, (see Section 2.3.2).

At each site, the input parameters were checked (often with EDM data) to see that the baseline distance, the station ID, antenna height and the antenna offset were correct. A hardcopy of all the input details was recorded at each station, this facilitated cross-checking if gross errors were observed during processing. As each rover station was occupied it could then be used as a reference survey station. This so-called 'leap-frog method', ensures that all the survey stations are occupied at least twice with difference reference stations. Choice of reference station was determined by accessibility, safety and radio contact. Between 6-8 stations were occupied in a single day, sites on the flank networks which have overhead obstructions, such as trees, were measured using EDM, in such cases at least one station on the EDM network was measured using GPS.

GPS data were collected using the differential rapid static technique running two receivers simultaneously as described in Section 2.6. Parameters were specified to collect compacted data every 10 seconds from a minimum of four satellites at an elevation of no less than 15, with a maximum acceptable GDOP of 8. An estimate of the baseline length to be measured was used to judge the occupation time needed to collect sufficient data at each station. Leica 339™ uses the Fast Ambiguity Resolution Approach (FARA algorithm) to process the rapid static data. This algorithm makes a statistical assumption on the positioning of the satellites thus reducing the time required for each resolution, but with the disadvantage that it limits the maximum static baselines length 23km and the maximum rapid static baseline 10km. This limit was over come by positioning intermediate survey stations between the summit and the flank stations. When the rover receiver occupies a survey station the percentage of data collected is counted, when sufficient data has resolved ambiguities (150% confidence) the rover is then moved to the next station. Use of two-way radios ensures that the rover remains in position for a sufficient time even if the GDOP of the reference receiver increases (Section 2.6), common satellites are less than 4 or a battery is changed.

The initial starting point for the reference was chosen to be e56. This point is easily accessible by the road located about 5km from the summit, see Figure 5-2. Data collected for over six hours were processed as a single point position. The rover occupied four adjacent survey stations and was processed with the obtained fixed position (from the single point position). The first day's work provided two functions: firstly, to locate the approximate co-ordinates for a single point location so that it could be used as a reference; and secondly, to assess the time needed to collect sufficient data to resolve ambiguities during post-processing. A baseline of five kilometres required approximately five minutes occupation and 10km required approximately eight minutes. It took a further three days for a single occupation of the summit area to be completed. E56 was used as a base station for the first three days and e18 was then used, this enabled radio contact to be maintained with the rover which was now moving among the higher survey

stations on the Piano del Lago. In these first four days 17 stations were occupied, five of these twice. Using the data from the reference receiver on e56 single point calculations were computed and then averaged to obtain a starting reference for the processing (the data already collected were then re-processed using this more precise fix).

When connecting the Lower Eastern Flank Networks to the Upper South-Eastern Flank Network, e49 was used as a reference to 'fix' an intermediate station (e66), this was then used as the reference to 'fix' the Lower Eastern Flank Networks. To survey the Lower Eastern Flank Networks two survey stations were occupied from each network (twice), except at Trecastagni which was unsuitable for GPS due to metal fences adjacent to the network. A further survey station (f1) was installed at the coast, east of any normal or strike slip faulting on land. This was then used as a reference for another new survey station situated beyond the northern boundary of the mobile sector at Piedimonte Etnea (f2). The summit network was then re-occupied using different reference survey stations to those used during the first occupation.

The objectives of the post processing were to process data to an acceptable degree of precision and determine absolute WGS84 datum co-ordinates relative to e67 with error ellipses of less than 15mm. Precision is checked from the sigma a posteriori, error ellipses and standard deviations. Results of the processing algorithms include the final un-adjusted co-ordinates and slope distances, they are presented in Cartesian and geodetic format with standard deviations and error ellipses, the results are listed in Appendix B. The data confirms the adjustment reliability by comparing the number of degrees of freedom with the resultant sigma a posteriori. Large residuals indicate 'bad' baselines that have a large disparity with the rest of the network geometry; if there are just one or two they can be removed and the network re-adjusted without losing the redundancy of the network. Processed data from the entire network was adjusted to the absolute co-ordinate of e67 (Serre la Nave) fixed during the 1995 occupation. Current

stability of the survey station is confirmed by the Italian volcanologists who use this survey station as part of the edifice wide network (Puglisi *pers com*).

5.6.3. July 1997

The July GPS occupation was undertaken using the same methodology and equipment as June 1996 and will therefore not be outlined in detail. The only difference was that the fixed survey station e67, was occupied by a permanent Italian receiver; so e56 (which had been fixed in 1996) was fixed from 1996. This was not ideal but the data does not indicate any distortion of the network that would indicate that this station had been significantly displaced. Survey station e66 which acts as a reference for the flank network, was fixed using two stations of the summit network to obtain a more accurate co-ordinate position.

5.7. The results of the Upper South-Eastern Flank Network

The data results which are outlined in this section can be found in full in Appendix B.2. Results are listed year by year examining: (i) inter-year patterns, and (ii) long-term patterns and trends, through mathematical analysis and graphical interpretation. The implications of the results will be raised in this section and discussed later in Section 5.10.1. and 5.11. The results discussed here are the measured line lengths and the calculated co-ordinates, the largest outliers, caused by gross errors, are removed from the data-set. These anomalous values are stored to compare with the next years data to see if any of the extreme changes are repeated or if, more predictably, a counteracting change is recorded. The removal of anomalous measurements assures that the data fits a normal distribution (for the statistical analysis) and that the errors do not bias the analysis and the identification of trends.

Two statistical tests are undertaken on the data-sets to identify if there is a correlation between the strain of a baseline and the baseline length or the altitude of the (mid-point) baseline. The first test (vs. baseline length) aims to identify any

significant correlation between the distance between the survey stations and the repeatability of the data. The purpose of this is to identify poor repeatability caused by tropospheric differences between the survey stations influencing the equipment signal. The second test (vs. altitude) identifies any pattern in the results which could have come from real volcanic or tectonic activity either adjacent to the summit craters or lower on the flank.

5.7.1. The 1994 co-ordinate positions

Co-ordinates were determined using the EDM slope distances and vertical differences. The approximate set of co-ordinates used to determine these co-ordinates were derived using the 1996 and 1997 grid co-ordinates obtained using GPS. The data were checked for gross errors and then whole network was adjusted, the network is fixed to e39. The co-ordinate transformation software (LSXY) does not allow manual inputting of a fixed station but instead (automatically) mathematically chooses the most suitable survey station according to the geometric weighting of the network.. Appendix B.1, lists the calculated co-ordinates and their error ellipses, the fixed survey station is in italics. The error ellipses are quite large compared to the 1995 data set (see Appendix B.1) but this is not reflected in the vector changes between 1994-5 and 1994-7. The results of the partial survey undertaken in September 1994 indicate that no significant ground deformation was recorded. Co-ordinates were not calculated for the bi-annual occupation as; (i) only a few stations were occupied, and (ii) only negligible, non-significant line length changes were recorded, indicating no major change between the annual surveys.

5.7.2. The 1995 co-ordinate positions

Appendix B.1, shows the co-ordinates and their error ellipses, the values in italics are the survey stations held fixed during the network adjustment. The network was calculated in two sections as the standard error of unit weight was too large

when the network was measured as a whole. This was due to the (unavoidable) absence of data for baselines critical to the network geometry. As noted above these were not measured during the survey due to poor weather). However, by allocating two fixed points (e37 and e16) and dividing the network into two the error in parts per million per line was reduced and the error ellipses minimised. This division unfortunately reduced the redundancy of the network, but as the few key baselines were unavoidably omitted from the survey this was the only method to obtain the network co-ordinates. The results from the bi-annual survey were again negligible and insignificant. Therefore, given financial consideration it was decided to cease the bi-annual occupations.

5.7.3. 1994 to 1995: line length and vectors changes

Data revealed a lengthening of 59% of baselines measured during 1994 (full survey) and 1995 (full survey) despite the strain rates remaining small, see Appendix B.2. Since this data-set was collected in a quiet period using just the EDM technique during both campaigns these results are taken as a baseline EDM data-set with which to compare subsequent data. Figure 5-3 illustrates baseline repeatability, this examines the amount of change (positive or negative) for each baseline between the surveys plotting the difference as a measure of repeatability against baseline length (Section 3.3). There were four baselines which showed notable changes on initial analysis, these were e39-e42, e4-e5, e19-e48 and e60-e8, see Figure 5-3. Two of these baselines (e39-e42, e60-e8) are near to the summit and may indicate sub-surface transport of magma, these patches of deformation were however isolated, with one baseline showing a very large extension and another showing a smaller contraction. Unfortunately due to the network geometry the formation of accurate co-ordinate positions for some of the survey stations was not possible. These baselines will be compared with the results from the next survey.

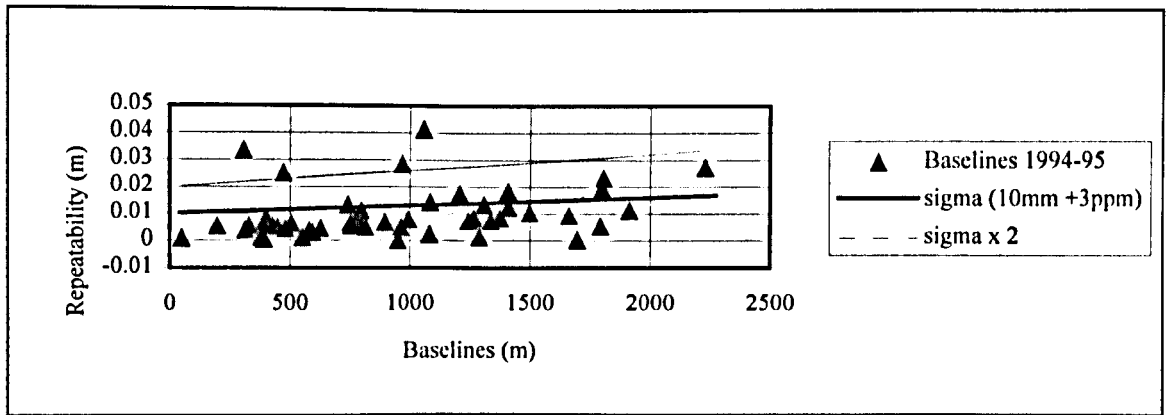


Figure 5-3 The difference between baseline measurements between 1994 and 1995 using EDM.

The statistical tests carried out on the 1994-5 data show that there is no significant statistical correlation between strain and (i) the length of the baselines and (ii) the (mid-point) altitude. Although many of the baselines extend downslope, most of these line lengths are quite short (<1km) and are thus considered to have an altitude equal to their mid-point (Figure 5-2). The data suggests that; (i) there was no volcanic or tectonic influence from any particular area of the network, and (ii) that the longer lines were measured just as accurately as the shorter lines, indicating that there was no tropospheric obstructions effecting the signals.

The data are analysed in terms of strain and line length changes. The average total strain was 4.20ppm, this is the total strain taking into account positive and negative displacements. The total positive strain was 13.97ppm and the total negative strain was -10.23ppm. This reveals that the average strain was small due to the positive and negative strains (of only a slightly larger magnitude) almost cancelling each other out. The line length data are skewed by a single high strain value of 108ppm for a single line near the summit (e39-e42), as noted above, this large strain may be due to either sub-surface magma movements under the summit conduits or an error. If this value is assumed to be anomalous, then the total strain is 2.07ppm. The strain rates are very small and do not relate to a

magmatic event, the results are discussed further in Section 5.10.1. The average line length change, taking into account positive and negative changes was 4mm.

In order to examine the relationship between strain and altitude, strain is plotted against the midway altitude of network lines. Data from 1994-5 indicated no progressive increase approaching the summit craters, see Figure 5-4. This implies that any strain associated with the replenishment of the summit conduits is either too small to be detected using the EDM technique or is confined to the immediate proximity of the vents. Small strain rates measured over the 1994-5 interval with no dyke emplacement provide background deformation values for the current phase of Etna. The strain recorded between 1995 and 1997 will be considered later.

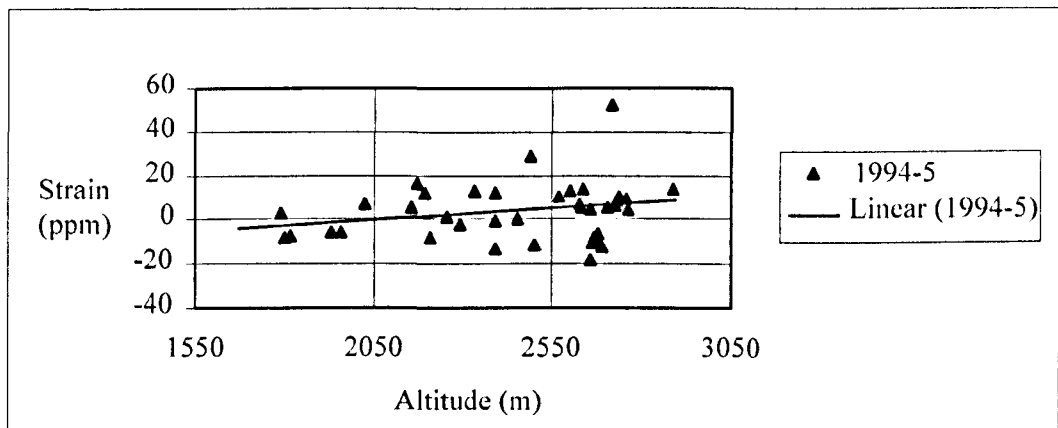


Figure 5-4 The relationship between strain and altitude, 1994-5

The co-ordinate changes between July 1994 and June 1995 show a marked displacement of most of the vectors towards the summit, See Figure 5-5.

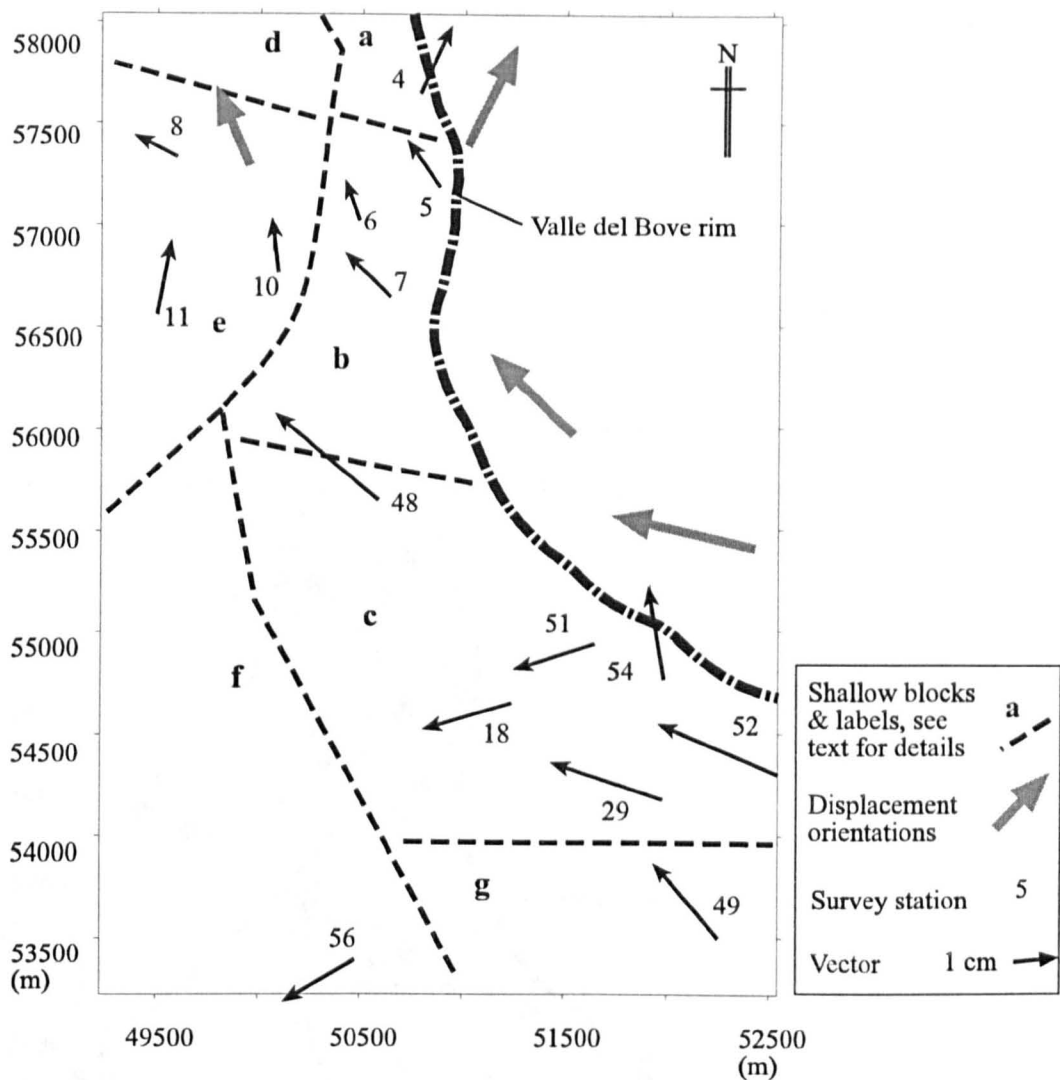


Figure 5-5 Horizontal vector displacements between 1994-95 including the disparate shallow blocks, see text for explanation. For the general location see Figure 5-1 & Figure 5-2. The large displacement vectors are determined by eye to represent the general trend of displacement.

Although the displacement is primarily to the north-west and west. Stations e54 and e4 both stand out from adjacent survey stations, indicating a more northerly displacement. The movement of e4 may indicate easterly displacement of the shallow block a, while e54 is not in a highly fractured area but does overlie the 1989 fracture. Both these survey stations will be examined closely during the next survey to see if 'counter' displacements are observed. Station e56 does not adhere to the common trend, with a south-west displacement, this is probably due to an error as this station is assumed stationary. The networks were carefully examined using the line length changes to check that the vectors were accurate and not

affected by the choice of references. The renewed activity at the end of the 1995 campaign from the summit craters suggests that this displacement pattern may typify pre-flank eruption displacement.

Shallow blocks proposed by McGuire and Pullen (1989) (see Figure 4.6) are re-determined in Figure 5-6. The stations of McGuire and Pullen's group c do not display coherent displacement in the 1994-5 or the 1995-6 results. In order to constrain the blocks more satisfactorily the data were compared using the 1994-5, 1995-6 and 1996-7 vectors; the resulting blocks are illustrated in Figure 5-6.

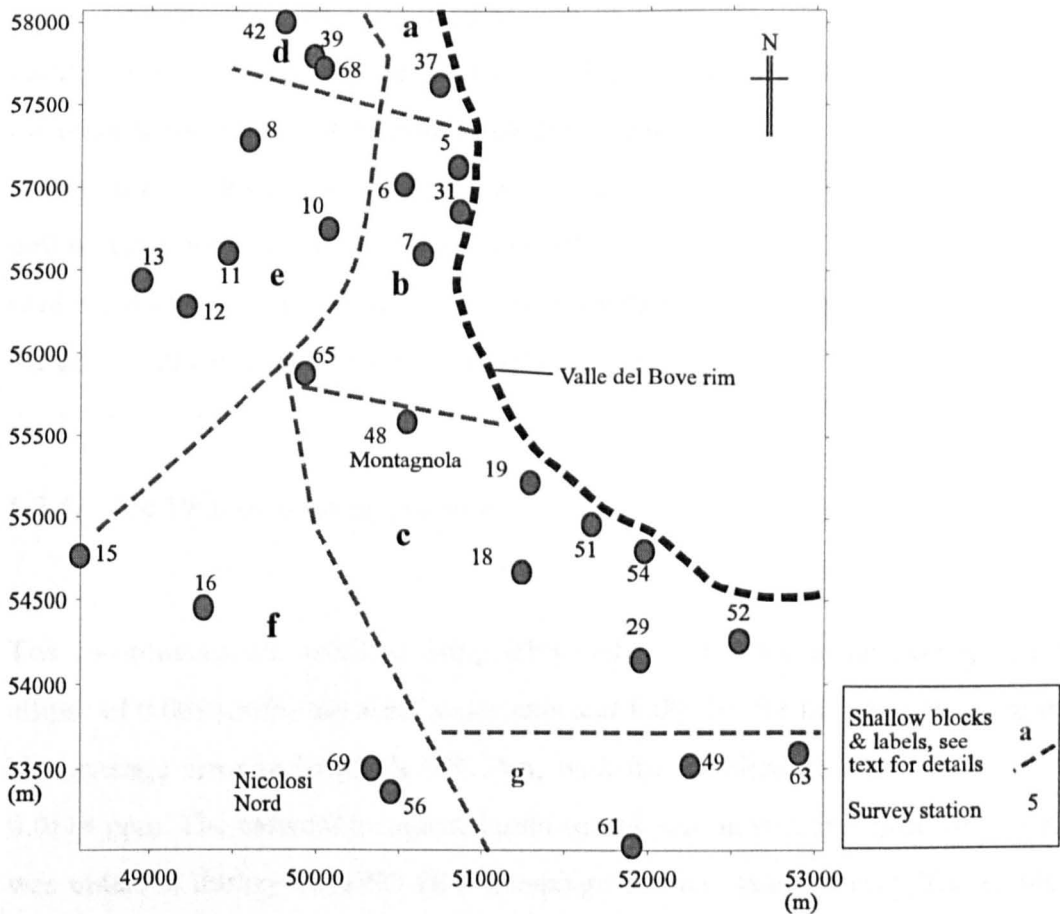


Figure 5-6 Upper South-Eastern Flank Network indicating survey stations and principal shallow blocks (divided sectors).

In examining Figure 5-3 and Figure 5-5, the EDM comparisons in 1994-5 do not reflect imminent large-scale volcanic activity or indicate a shallow fresh source of magma, since no significant decimetric movements were recorded. The summer 1995 survey was completed in the start of July and the summit activity

commenced at the end of July. The variations recorded do indicate negligible changes between two surveys, indicating either random error and/or actual displacement. If the source is actual displacement rather than error, then it is most likely to be caused by the accommodation of stresses built up from the replenishment of the summit conduits with magma. Observed strain rates are small, often falling within the acceptable error margins, indicating that although there is renewed activity (Section 4.6) and the central plumbing system is being replenished, no dyke intrusion has yet occurred within the 'Southern Rift-Zone'. This is confirmed by edifice wide monitoring by the Global positioning systems technique (Puglisi, *pers com*). Contraction of some network lines close to the summit region argues against a purely elastic response most likely reflects differential movement of individual blocks within this strongly fractured part of the volcano. Despite the magnitude of the data, the coherent pattern of deformation observed in Figure 5-5 suggests that the changes are significant and connected to the renewed activity. The measurements are useful as they reflect the deformation state of the edifice prior to the eruptive event.

5.7.4. The 1996 co-ordinate position

The co-ordinates are obtained using GPS and are accurate to an average error ellipse of 0.0098m for the semi major axis and 0.0075m for the semi minor axis. The average error in height is 0.0135m, with the standard unit error weight of 0.0114 ppm. The network is adjusted onto survey station e67, (the position of e67 was obtained during the 1995 GPS campaign on the eastern flank). The results are listed in Appendix B (sections B.1 and B.2).

5.7.5. 1995 to 1996: line length and vector changes

Data revealed a lengthening of 96% of baselines measured between 1995a and 1996. This lengthening was much greater than in 1994-5, one interpretation of

this is that it represents the inflation of the whole network (which pushes the survey stations upwards and outwards). The few lines which did not extend are most likely due to inter-block movements. An alternative interpretation of the lengthening which must be addressed is that it is an artefact produced by the change in measurement technique from EDM to GPS. If there is a systematic difference between the results of the two methods, however, it should have been also found in the results of the 1996 La Palma campaign (Section 7.8), in which line lengths were measured almost simultaneously with both techniques showing no major differences. The second hypothesis that the 1995-1996 line lengthening on Etna is an artefact can therefore be excluded.

Five significant line length changes were revealed by examining baseline repeatability in Figure 5-7 (e39-e42, e54-e52, e56-e29, e56-e49, and e51-e49). Line e39-e42 showed a large change exactly the opposite of the change between 1994-5 confirming the erroneous measurement of this line in 1995. The other conspicuous 1994-95 line length change in that area e60-e8, was not measured due to the unfortunate loss of the e60 nail. The other baselines are all interestingly in the same area, *but* not all connected to the same survey station. For, if this were so, the movements could indicate the accidental displacement of a single nail.

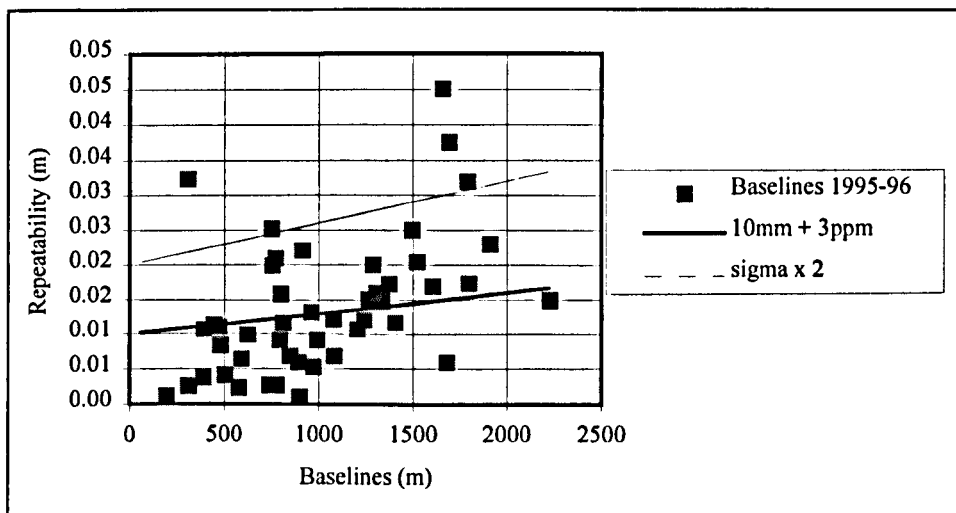


Figure 5-7 Baseline repeatability between 1995-5

The changes over the whole area are thought to be geologically significant. This statement is supported by statistical tests undertaken on the 1995-1996 that indicated a significant correlation between strain and altitude. The following statistical hypothesis were tested; null hypothesis a_0 : there is no correlation between the mid-point altitude of the baseline and the amount of strain exhibited on the baseline; alternative hypothesis a_1 : there is a statistically significant correlation between the mid-point altitude of the baseline and the amount of strain exhibited on the baseline. Figure 5-8 illustrates the relationship between strain and the mid-point altitude of the baselines. The results reflect the broad pattern of inflation over the edifice especially near the summit and on the lower part of the network (<2250m).

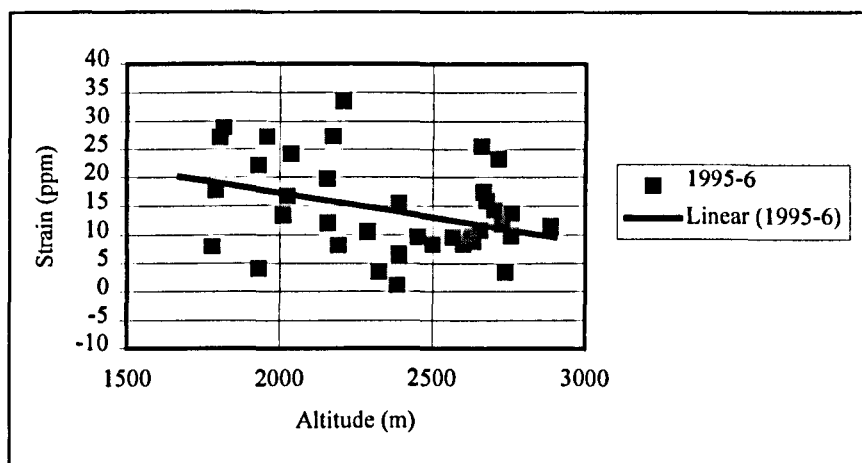


Figure 5-8 Relationship between strain and altitude, 1995-6.

The observed value for $r = -0.35$ exceeds the critical value of (-0.338) , corresponding to $v = 45$ degrees of freedom and $\alpha = 0.02$. The null hypothesis a_0 is therefore rejected, and the alternative a_1 , that there is a significant inverse correlation between the mid-point altitude of the baseline and the amount of strain exhibited on the baseline can be accepted with a risk of $[100\alpha] 2\%$ that the decision is wrong; suggesting that the largest strains are found at the lowest altitudes. The possible causes of this are examined below with further reference to the 1996-7 strain data.

The minor vector displacements of 1995-6 can be attributed to the blocks described earlier in relation to the 1994-5 changes and the work by McGuire and Pullen (1989). The 1995-6 vectors displayed coherent displacement both to the east and the west, see Figure 5-9. Block **a** containing station e37 showed NE displacement, blocks **b**, **c** and possibly **d** appear to be acting concordantly in a SE direction, this pattern is very interesting as reflects the change in dyke orientation. Dykes propagating from the summit (see Figure 4.6) divert SE or SW round La Montagnola, block **c** is being displaced coherently eastward, this will be discussed further in Section 5.10.1. and block **e** exhibits south-west displacement.

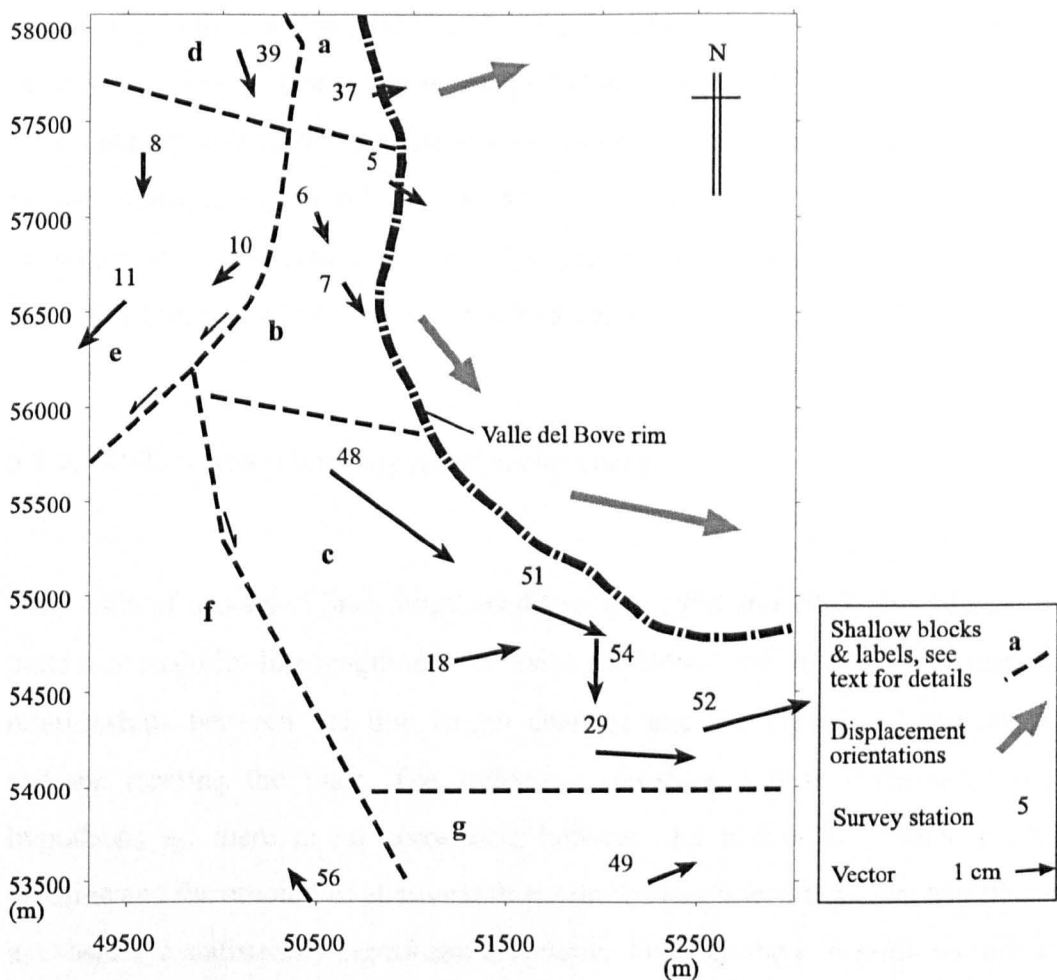


Figure 5-9 Vector displacements between 1995-96, indicating general displacement orientations.

Although blocks **f** and **g** only contain a few stations they do appear to be stable. This displacement suggests inflation of the upper flanks almost the reverse of the 1994-5 pattern (although many of the block groupings are maintained). The

direction of movement is predominately east and south east. Notably stations e56 and e54 again exhibit different behaviour to their adjacent stations. The movement of e54 confirms that the displacement of e54 between 1994-95 was erroneous due to an incorrect measurement in 1995.

5.7.6. 1997: co-ordinate position

Co-ordinate positions in 1997 were obtained using GPS. Survey station e56 was used as the initial starting position (single point process), as it was not possible to occupy e67. The network then was adjusted with e48 held fixed to marry to the 1996 data-set, this survey station was used (after comparison with other stations on the network) as it produced the results with the lowest error ellipses. The average error on the major axis is 0.01427m, 0.00998m for the semi-minor axis and 0.02122m for height, with the standard unit error weight of 0.0151ppm.

5.7.7. 1996 to 1997: line length and vector changes

Only 44% of measured lines lengthened between 1996 and 1997; this breaks the pattern of majority line length increase between 1994-1996. In order to assess the relationships between the line length changes and the altitude of the survey stations forming the lines. The following statistical test is undertaken; null hypothesis a_0 : there is no correlation between the mid-point altitude of the baseline and the amount of strain exhibited on the baseline; alternative hypothesis a_1 : there is a statistically significant correlation between the mid-point altitude of the baseline and the amount of strain exhibited on the baseline.

The observed value for $r = 0.398$ exceeds the critical value of $(-)-0.381$, corresponding to $v = 35$ degrees of freedom and $\alpha = 0.01$. The null hypothesis a_0 is therefore rejected, and the alternative a_1 , that there is a significant inverse correlation between the mid-point altitude of the baseline and the amount of strain exhibited on the baseline can be accepted with a risk of $[100\alpha]$ 1% that the

decision is wrong; suggesting that the largest strains are found at the lowest altitudes. The possible causes of this are examined in Section 5.10.1.

Figure 5-10 illustrates the repeatability of the data, it is evident that there are four prominent changes, two are from lines shortening, and two are from line length increases. The lines which exhibit the shortening are east of Montagnola in blocks c and g. The baselines which exhibit the greatest change in line length (positive or negative) are all in the area beneath Montagnola.

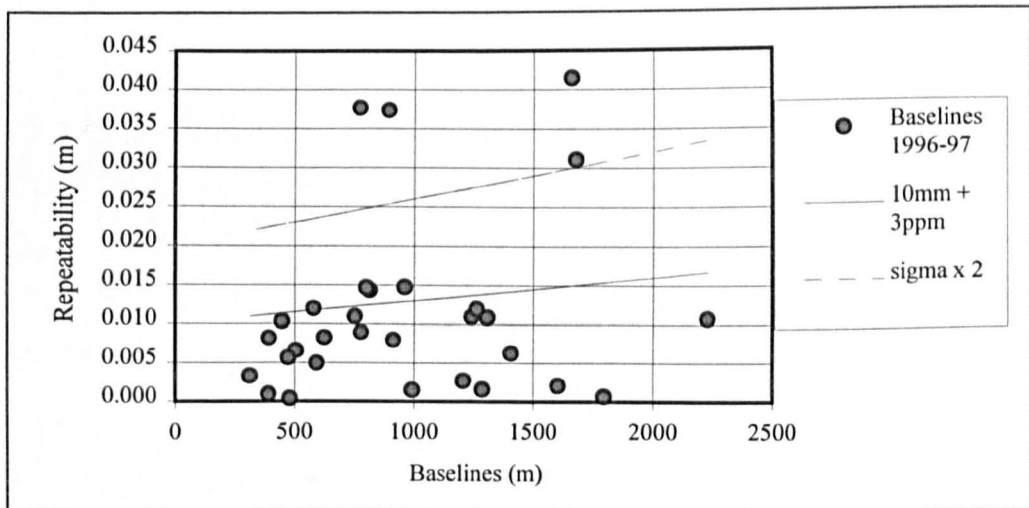


Figure 5-10 Line length changes between 1996-97

Figure 5-11 illustrates the pattern of strain from 1996 to 1997, the linear trendline suggests that the areas of highest strain are close to the summit and on the lower flanks (1750-2250m), this would suggest that the increased strain is a result of two factors; (i) magma resurgence at the summit craters, causing localised deformation near the summit, (ii) formation (or re-activation) of fractures on the lower flanks caused by either tectonic activity or deep magma resurgence.

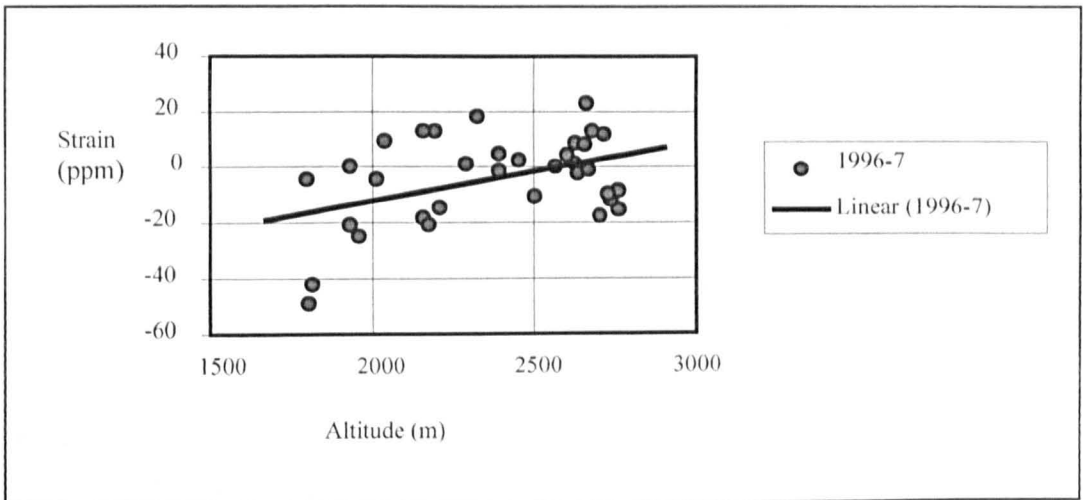


Figure 5-11 Relationship between strain and altitude, 1996-7.

Blocks **a** and **b** are grouped on the upper flank and are displaced in a NE direction. Block **c** continues to be displaced in a south-easterly direction in the same orientation as 1995-6. Groups **e**, **f** and **g** exhibit smaller less coherent displacements within the respective blocks and are interpreted as stable during this time. Blocks **c** and **g** would appear to be converging, this is confirmed by the shortening line lengths across the boundary. Block **d** contains the anomalous station e42, this station exhibits very definite south west displacement. Unfortunately there are no adjacent vectors with which to compare the deformation as e60 was destroyed. Despite this, the deformation of this particular survey station is most likely a consequence of the summit activity at this time (as outlined in Section 4.6).

Vector changes illustrated in Figure 5-12 clarify the current deformation patterns, the shallow blocks are grouped differently to how they were in 1995-6. Since 1995 much of the deformation on Etna has been centred on the area beneath Montagnola. Survey stations, e19, e51, e52, e54 and e29 all exhibit significant horizontal displacement. This displacement may be partially explained by eastward displacement due to gravitational loading, but in order to clarify this speculation, vertical deformation must also be considered.

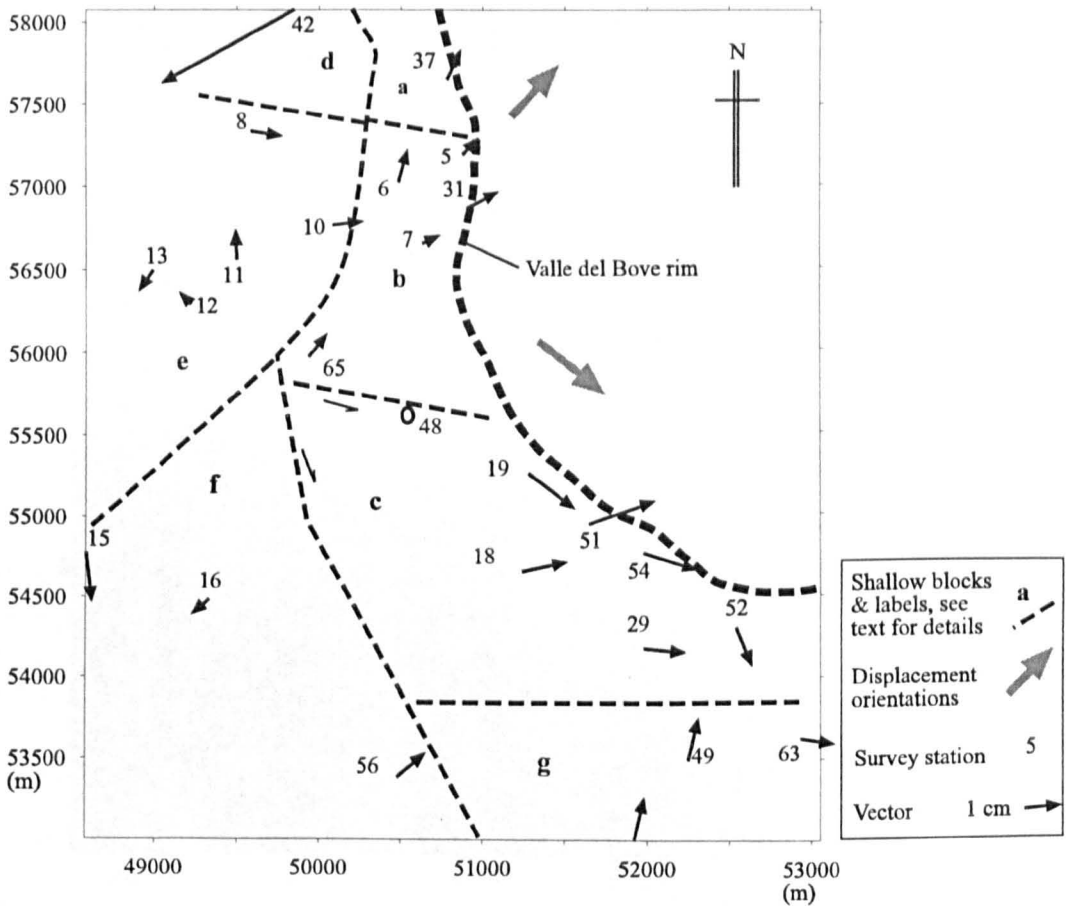


Figure 5-12 Vector changes between 1996-97.

As the co-ordinates were measured using GPS in both 1996 and 1997 it is also possible to compare vertical positions of the survey stations cover the network. Figure 5-13 illustrates vertical changes between 1996 and 1997 within a contour map of the network. The data reveals a depression in the proximity of the 1989 fracture, one interpretation is that this may be a result of the magma filling the fracture at depth then the fracture, however if this was the case then there would be other geophysical changes. Budetta & Carbone (*in press*) detected a gravity anomaly directly over the depression in 1995-6, they concluded that the source of the anomaly was either magma or hydrothermal fluids filling the crack at depth.

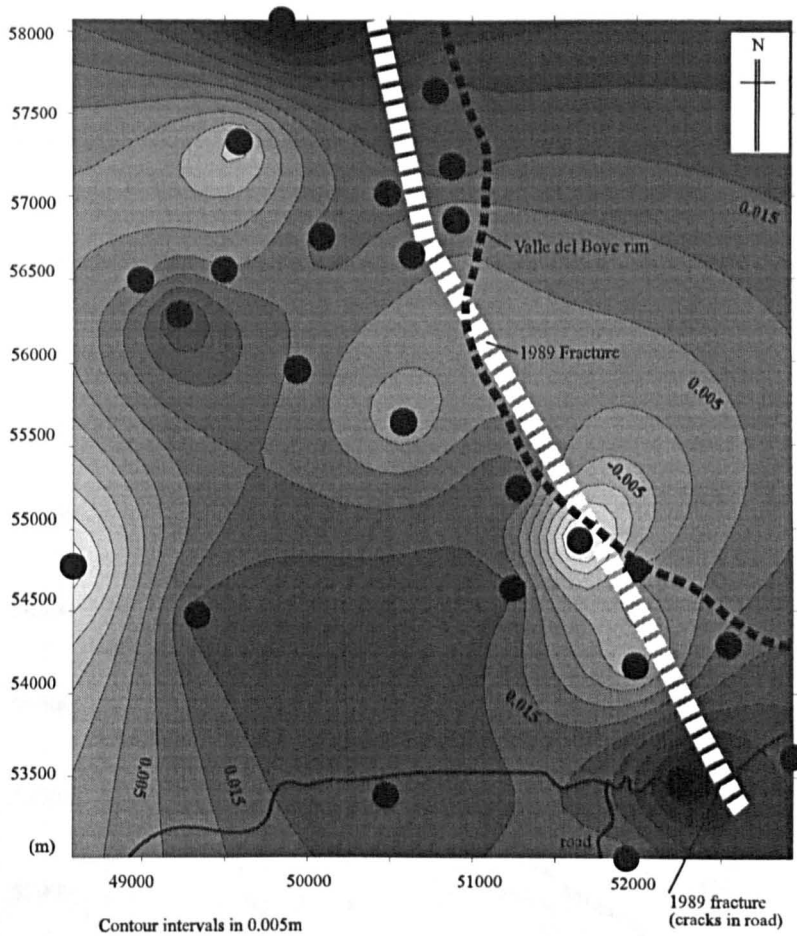


Figure 5-13 Height changes between 1996-7, for survey station numbers see Figure 5-2.

From this it can be inferred that the increased levels of ground deformation in this area are due to the re-activation of either the 1989 fracture or another fracture near-by. However, it is unlikely to be from the opening of a new fracture since there has been no recorded seismicity in the area. In order to test this hypothesis the ground deformation data are modelled using finite element modelling (in Section 5.8).

Deformation patterns observed from 1994 to 1997 (Figure 5-14). define the coherent displacement of the shallow blocks identified through the surveys. The main division of the blocks from all the vector diagrams from 1994 to 1997 (Figure 5-9, Figure 5-12, & Figure 5-14) occurs down the centre of the network, effectively dividing the eastern blocks (**a**, **b**, **c** and **g**) and the western blocks (**d**, **e** and **f**). This division is similar to the prominent dyke trend of the Southern Rift-

Zone illustrated by the recent dyke emplacement events in 1983 and 1985 (Figure 5-2). Coherent displacement of adjacent blocks does not reveal a grouping including blocks from each side of the line, it can thus be proposed that the EW division is an important structural feature and its inherent weakness provides a likely pathway for future dyke emplacements, this will be discussed further in Section 5.10.1.

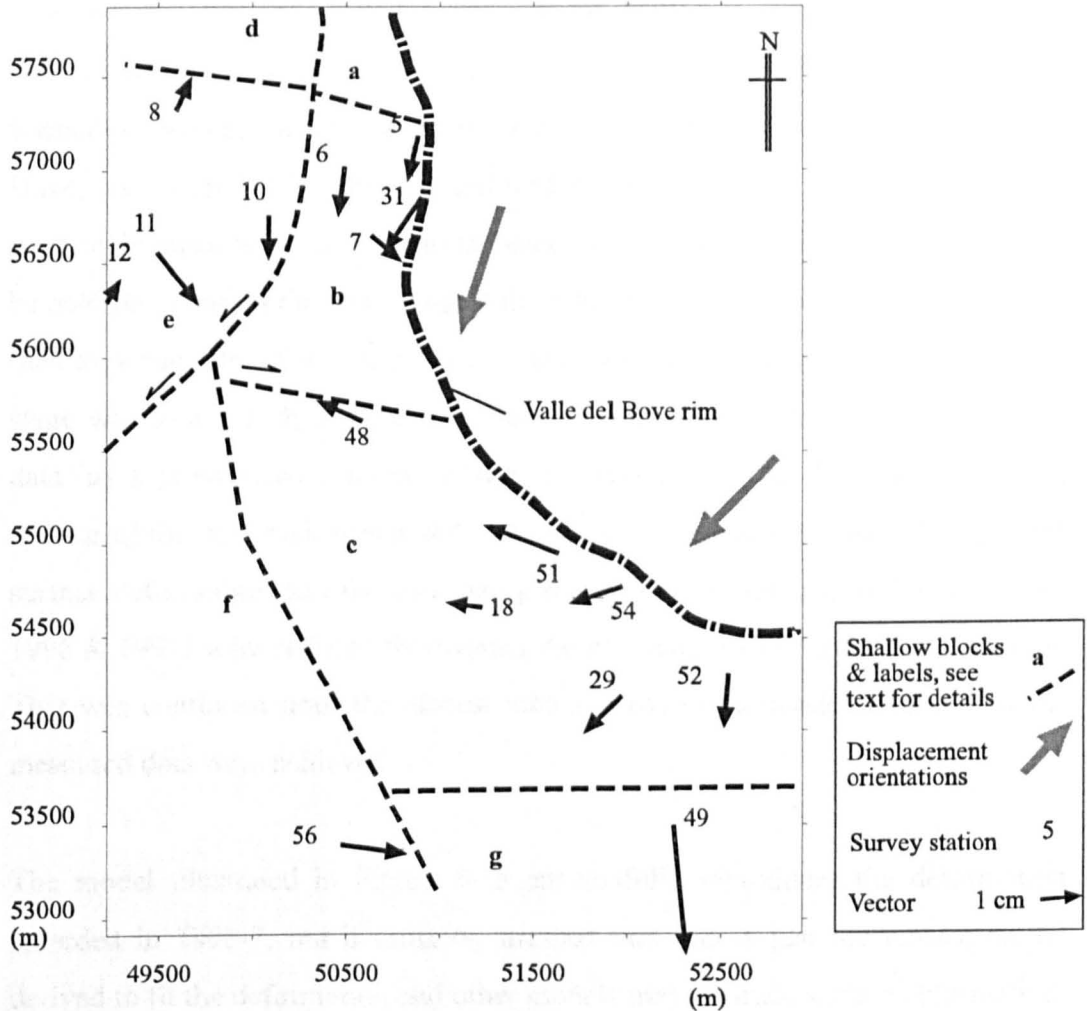


Figure 5-14 Vector displacements between 1994-97, indicating general displacement orientations.

5.8. Modelling the significant 1996-7 data

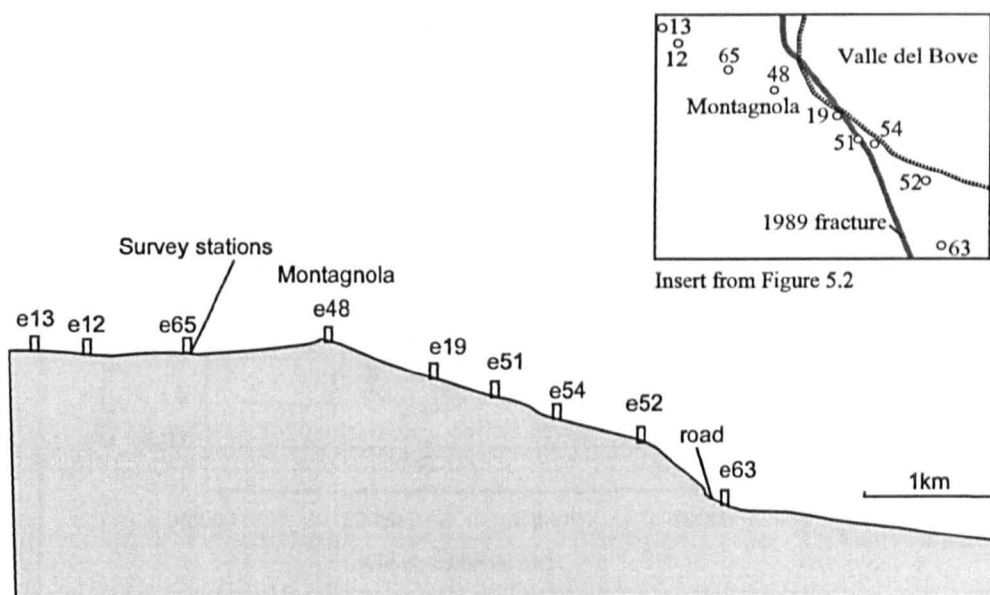
Section 4.6 explains how the generic parameters for finite element modelling on Etna were determined. A model used known dyke parameters and surface ground

deformation from the dyke emplacements in 1983 to estimate unknown parameters of magma pressure and the Etna host rock's physical properties. Data were then further tested (using ground deformation data) on the emplacement event of 1989/91. Using the parameters based on these tests a new model for the data collected in 1996-7 (from the area below Montagnola) was constructed.

The two dimensional ground surface of the host rock within the model was determined using the co-ordinates positions of a number of survey stations, these formed a transect running along the top of the southern wall of the Valle del Bove, see Figure 5-15a. The side and bottom dimensions of the host rock 'block' were maintained at the maximum distance from the surface because they have to be held fixed during the modelling; if the sides are too close to the deforming area then they can affect the results (this is explained further in Section 4.7). The first stage was to add a dyke similar to the ones modelled with the 1983 and 1991 data, as a pressurised fracture within the host rock. The deformation on the surface of the host rock was noted, the difference between this modelled ground surface deformation and the recorded ground deformation data (GPS data from 1996 & 1997) were reduced by revising the dip, length and depth of the fracture. This was continued until the closest match between the modelled data and the measured data were achieved.

The model illustrated in Figure 5-15 successfully reproduces the deformation recorded in 1996-7, but it must be stressed that this is just the closest model derived to fit the deformation and other models may produce similar deformation. The modelled fracture is 2km long, 1km deep, and almost vertical, with an opening pressure of $2 \times 10^6 \text{ Nm}^{-2}$ onto the rock with a Young's modulus value of $5 \times 10^{10} \text{ Nm}^{-2}$ the Poisson's ratio is 0.25. The model is illustrated in Figure 5-15, the mesh is illustrated in part b, these are the divisions of the 'block' (the finite elements) that are deformed by the applied stresses.

a,



b,

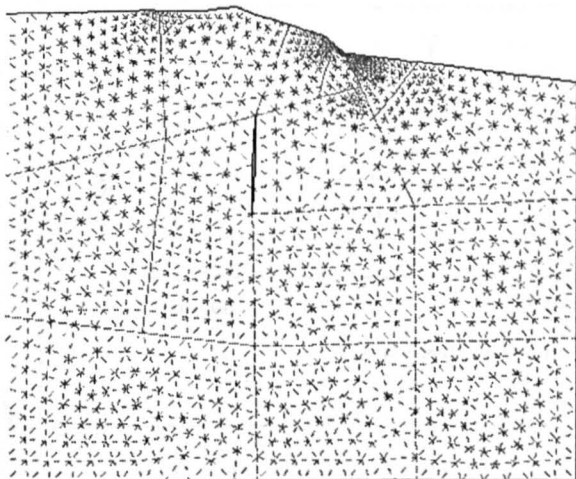


Figure 5-15 The transect of the southern wall of the Valle del Bove; a, the cross-section of the ground surface (with survey stations), b, the geometry of the model showing the mesh and the orientation of the dyke (2km long).

Deformation from this model is compared with the deformation measured using GPS in 1996 and 1997. Part a, in Figure 5-16 illustrates the modelled data compared to the measured data, the fit is good for six of the nine data points. The three points located at the following co-ordinates; 49224, 2550 (e12); 50575, 2681 (e48); and 51641, 2248 (e51) are not a good fit, this will be explained in the discussion section below. Part b, in Figure 5-16 illustrates the modelled

horizontal data. This fit is not as good as the vertical data, but the pattern is nevertheless reflected. The same few survey stations which do not follow the pattern, are the ones which did not fit the modelled estimate in part a, this pattern of discrepancies will be examined below in the discussion.

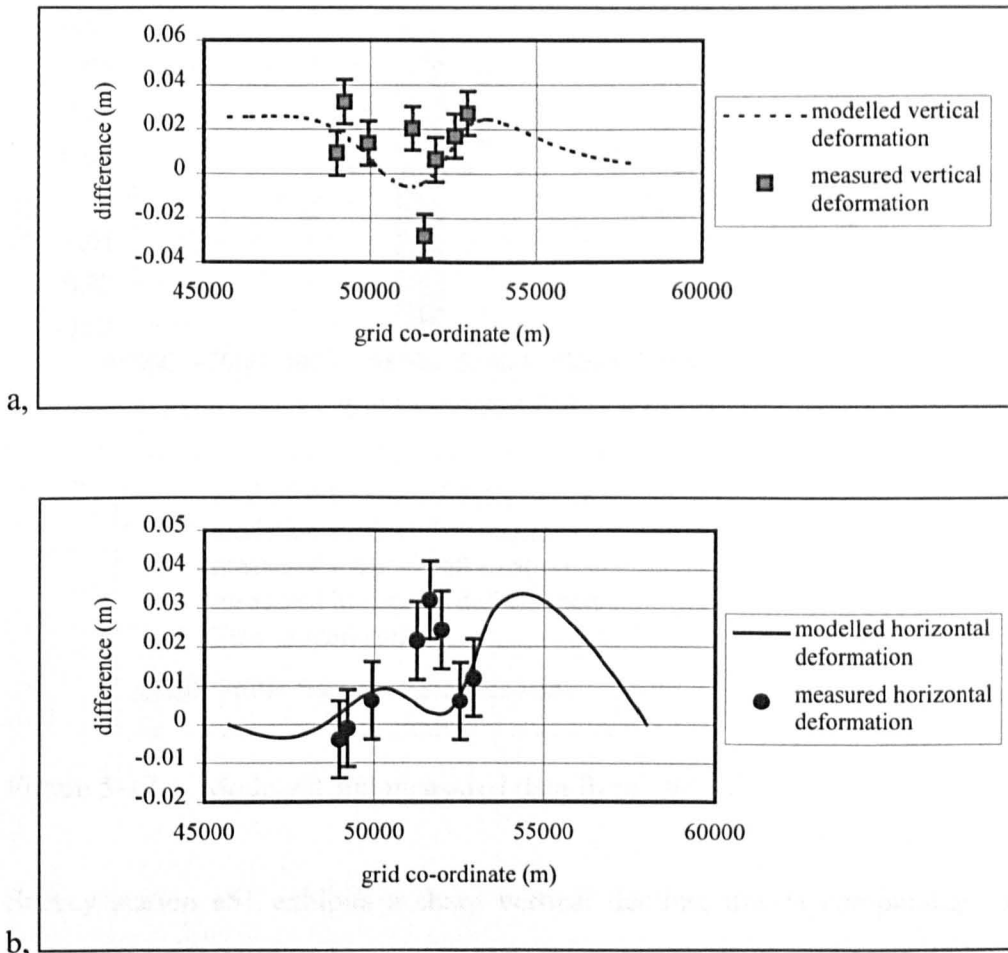


Figure 5-16 The 1996-7 ground surface changes depicting the difference between modelled and measured deformation; a, vertical deformation b, horizontal deformation. The Figures are combined together with the ground surface of Etna in Figure 5-17.

Figure 5-17 shows both the modelled and measured deformation from 1996-7, indicating the possible presence of a fracture beneath the southern flank of Etna. It can be assumed that the simulated crack in the model represents either a magma filled dyke or an opening sub-surface crack. The model only simulates elastic deformation, so the measured data which corresponds to the model is accepted as elastic deformation. The area between Montagnola (e48) and the upper part of the

southern wall (e51) does not correspond to the elastic pattern in both horizontal and vertical deformation; the reason for this is that brittle failure has occurred in the form of minor surface or sub-surface fractures and cracks.

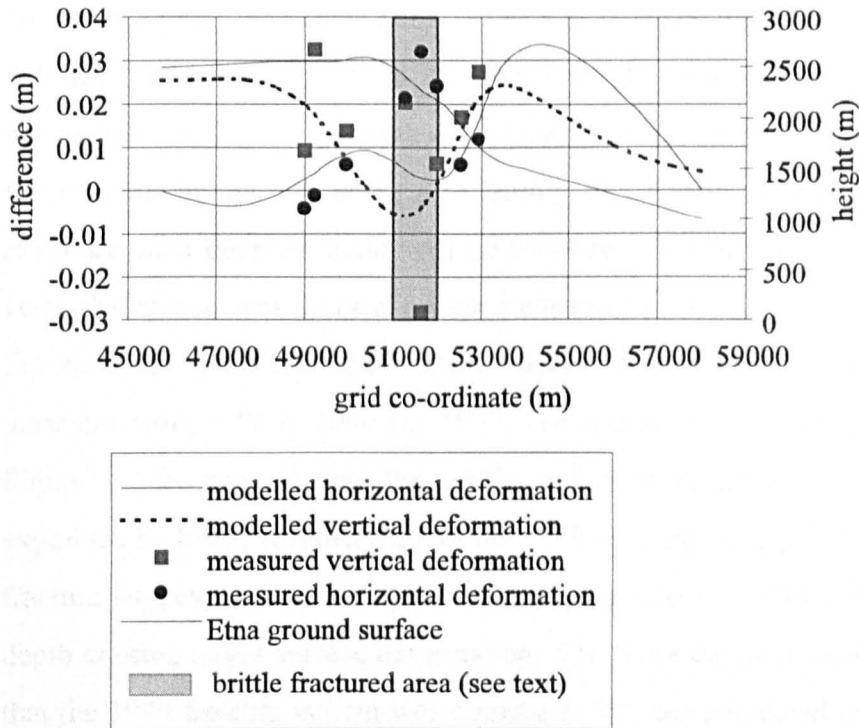


Figure 5-17 Modelled and measured data from 1996-7.

Survey station e51 exhibits a sharp vertical decline, this is comparable to the unexpected 1m drop of the Piccolo Rifugio survey station during the 1983 dyke emplacement (Murray & Pullen, 1984); this was interpreted to be a result of brittle failure associated with the intrusion of magma. Adjacent survey station, e19, shows irregular horizontal deformation which suggests similar brittle failure at this location. The survey stations in this area beneath Montagnola show much larger values of deformation than there should be for purely elastic deformation. Aside from this small area of brittle deformation the model matches the measured deformation very well; the fracture illustrated in Figure 5-15b is thus presented as a source for the 1996-7 deformation. The acceptance of a fracture as the cause of the deformation is justified below.

This isolated patch of deformation reveals that the magma supplying the fracture is from a separate source from the magma in the central conduits, this is assumed due to three factors; (i) the magma that fed the 1991 eruption was not from the central conduits (Rymer *et al.*, 1993); (ii) the SE rift-zone is a deep fracture system or fault, and although it is most likely connected to the central magma system at depth, flank vents erupt independently from the central conduits; (iii) a deformation tract leading from the summit to the area beneath Montagnola was not recorded either by the author or Murray (*Pers com*) who measured ground deformation in the Belvedere area during this period. The arguments for the existence of a deep SE fault will be justified in detail in Section 5.10.1. The vertical displacement gives a further indication of the deformation in this area, Figure 5-13 represents the vertical height differences, on a contour map, measured using GPS in 1996 and 1997. The comparisons of the contour map with Figure 5-16a, reveals that the brittle deformation above the dyke may be explained by brittle displacement of the 1989 fracture. This proximity to the 1989 fracture suggests that the magma is re-surg-ing into the 1989 fracture system at depth causing slight surface deformation. The finite element modelling indicates that the 1989 fracture system was dipping at 75°, the simulated dip was however almost vertical. This slightly modified dip may be due to the different orientation of the cross-section, however, during the preliminary tests of the finite element models it was found that the dip of the dyke is modified slightly as it propagated adjacent to a cliff edge or other influencing structure (Section 3.?) effectively rotating towards the cliff edge.

The significance of this possible magma intrusion is that there may be a flank eruption from this area, or further along the path of the fracture. The most likely area to undergo failure in the event of a fresh intrusion of magma into a dyke at shallow levels is indicated by the stress levels indicated within the software as the *Mohr stress value*. Figure 5-18 illustrates the Mohr stress values for the model; from this it can be seen that the two areas to each side and above the dyke tip that display increased stress. The right-hand side increase appears to influence the

area of the base of the slope of the southern wall, (close to the road and the 1634-38, 1792 and 1766 lava flows).

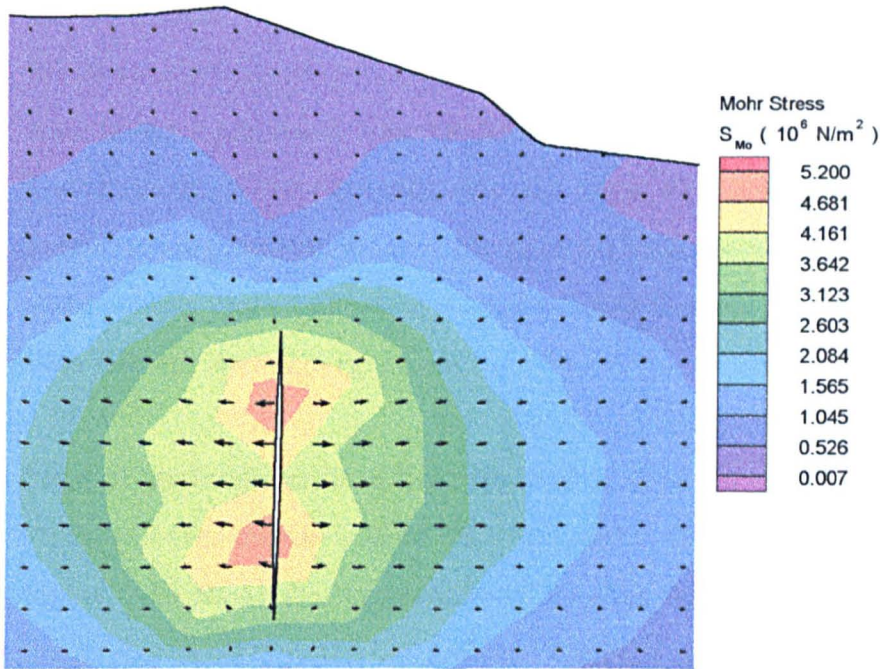


Figure 5-18 Failure criteria for the finite element model

Therefore, the results of the model would suggest that the most probable location for the next eruption would be in the area beneath Montagnola probably between stations e52 or e63 at the base of the southern wall (See Figure 5.2).

5.9. The results of the Lower Eastern Flank Networks

Results will be presented this section and discussed in context in Section 5.10.2. The Lower Eastern Flank Networks did not exhibit any particularly significant ground deformation during the period of research (1992-97). Detailed analysis of the results however, reveals minor patterns which although within the error margins of the technique, may indicate real movements which would only become apparent when examined for a longer period.

The rates of creep expected on the faults are in the order of 5-10mm per year, this is estimated from the rates of creep determined for the major tectonic features in the area (Stewart *et al.*, 1993; Borgia *et al.*, 1994; Latora *et al.*, 1996). The

interpretation of the results will report on the influence of the spatial distribution of the survey stations and of how the physical environment around the networks has affected the network changes. The networks will be analysed from the date of initial establishment even though the author only measured them from 1994. For reasons noted previously (Section 5.3), it proved difficult to obtain data from the Lower Eastern Flank Networks, this was due to two factors, firstly the difficulty in maintaining a network over time since the nails are positioned in urban areas, and secondly due to the many bogus baseline lengths, recorded due to reading lines through growing vegetation.

Most of the baselines were last measured in 1996 using EDM, although all the stations of the Carruba network were occupied in 1997 using GPS.

Figure 5-19 shows the repeatability of baseline measurements from the start of the project in 1992 to the last date that the lines were measured. The difference between the first and the last measurements records the cumulative displacement during this period; it can be seen that six of the seven baselines which fall above the line of expected background levels ($10\text{mm} \pm 3\text{ppm}$) are from the Carruba network. The other faults however do not show any movements above the background level and therefore are thought to move solely in conjunction with seismic events (none of which were recorded during the course of the monitoring programme (*Vinciguerra, per com*)).

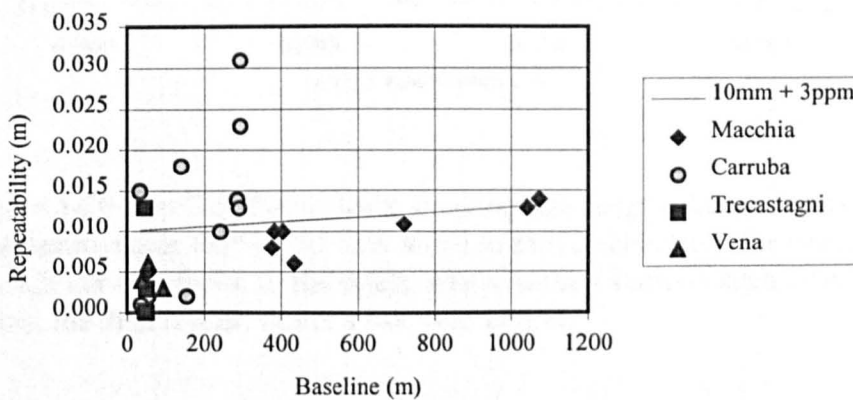


Figure 5-19 Line length changes on the Lower Eastern Flank Networks compared to the $10\text{mm} + 3\text{ppm}$ error estimate of the techniques.

Carruba

From

Figure 5-19 it can be clearly seen that the repeatability of the line length measurements at Carruba was inferior to the other networks. The significance of this phenomena can be examined by considering which sections of the network have exhibited line length changes, see Figure 5-20. Survey station c1 exhibited the most amount of displacement. The data suggest that c1 is undergoing continuous creep as a result of fault displacement, this is verified by the ground cracking adjacent to this station due to the action of the fault. The apparent lack of movement of the other two stations on the same side of the fault (c5 and c7), can be explained by their positioning on a wall. This wall has elastic filling between the blocks and it is believed that this 'filling' absorbs much of the displacement.

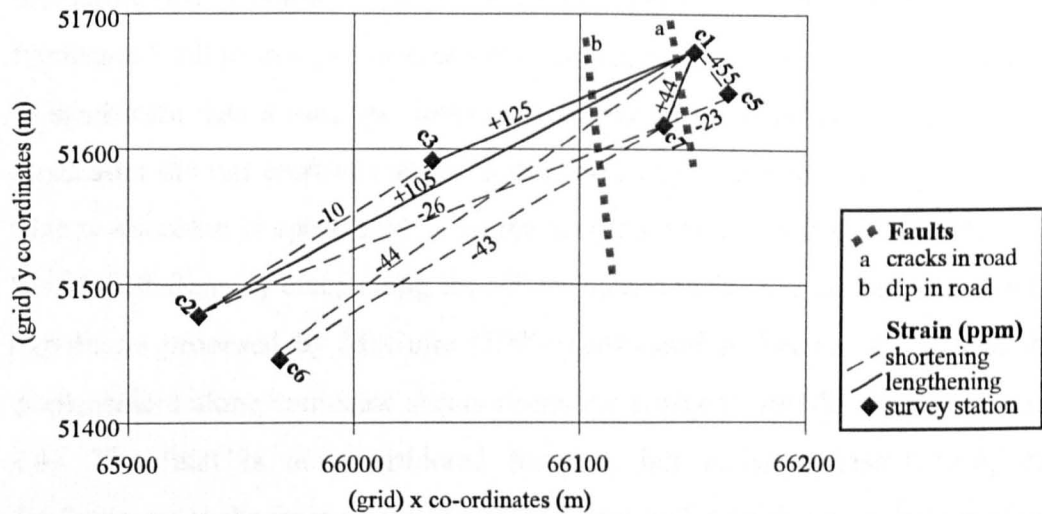


Figure 5-20 The Carruba network showing line length changes (survey station c4 was destroyed in 1995). The data refers to movements from the first measurement of each survey station to the latest, newer survey stations such as c6 and c7 only reflect the displacement over a two year period.

The results concur with the creep rates suggested by Stewart et al (1993) for the San Leonardello Fault of 1-2cm/yr horizontal and 0.3-0.6 cm/yr. vertical.

Macchia

Figure 5-19 indicates that there has been no significant deformation recorded on the Macchia network. The single baseline reading which exceeds the 10mm+3ppm mark is not considered significant as no other lines to this station recorded any change. Vegetation growth in front of station m2, reduced the repeatability of line measurements between this stations and station at the bottom of the cliff. It was possible to take readings but the final accepted value had to be determined from an average of between 8-10 readings. The fault is considered stable and not undergoing slow creep.

Vena

There was no significant deformation on the Vena network straddling the Pernicana Fault. This may be in part due to problems encountered when measuring the network. It is proposed that periodic creep occurs along the Pernicana Fault (although not necessarily co-seismic) (Section 4.2.2). The paucity of significant data during this inter-eruptive period (as opposed to the measured creep after the last eruption) suggests that the creep is related to summit activity. This relationship is speculated to be the accommodation of displacements along the SE Rift-Zone by creep along the NE Pernicana fault, thus concurring with the hypothesis proposed by McGuire (1997) (discussed in Section 4.2.1) that this displacement along conjugate shears opens the adjacent rift (illustrated in Figure 4.4). The fault is not considered inactive, but it is suggested here, that displacement in the form of either periodic creep or larger movements is confined to periods of volcanic or regional tectonic activity.

1995: East flank co-ordinate positions

In 1995 static GPS was used to locate the networks on the Lower Eastern Flank. GPS data were processed to obtain; (i) 3D co-ordinates for each survey station and (ii) baseline lengths measured during the same session. Baseline lengths for survey stations measured during different sessions are calculated using the

Cartesian co-ordinates. The precision of GPS data are determined from the repeatability of the data and the processing algorithms.

There was little difference between the data processed with the broadcast ephemeris and the precise ephemeris (satellite orbit data processed during - broadcast - and after - precise - the stations occupation by the satellite control station). However, the internal estimates of error within the software indicated smaller errors when the precise ephemeris were used. In addition, the data set processed with the precise ephemeris had a smaller range of values, so this dataset was accepted. In order to monitor vertical and horizontal displacements, the co-ordinates and baseline length changes of known survey stations between different surveys are analysed. Baseline lengths were calculated between the survey stations appropriate to be measured using EDM and GPS; Table 5-4 below shows the comparison of common baselines measured in 1995 and 1996.

Vector		1995		1996		1997
From	To	EDM	GPS Trimble	EDM	GPS Leica	GPS Leica
m2	m4	720.3497	720.379	720.341	720.3714	720.389
c1	c6	291.238	291.373	291.233	291.243	291.2254

Table 5-4 EDM and GPS comparisons on the Lower Eastern Flank (EDM measurements were not recorded in 1997)

The vector displacements in Figure 5-21, illustrate the displacements in one year. There are however large error ellipse values on the flank stations. These are a result of insufficient redundancy in the network between the summit network and the flank networks. This will be removed from future surveys by the positioning of extra intermediate survey stations between the Upper and Lower Eastern Flank Networks.

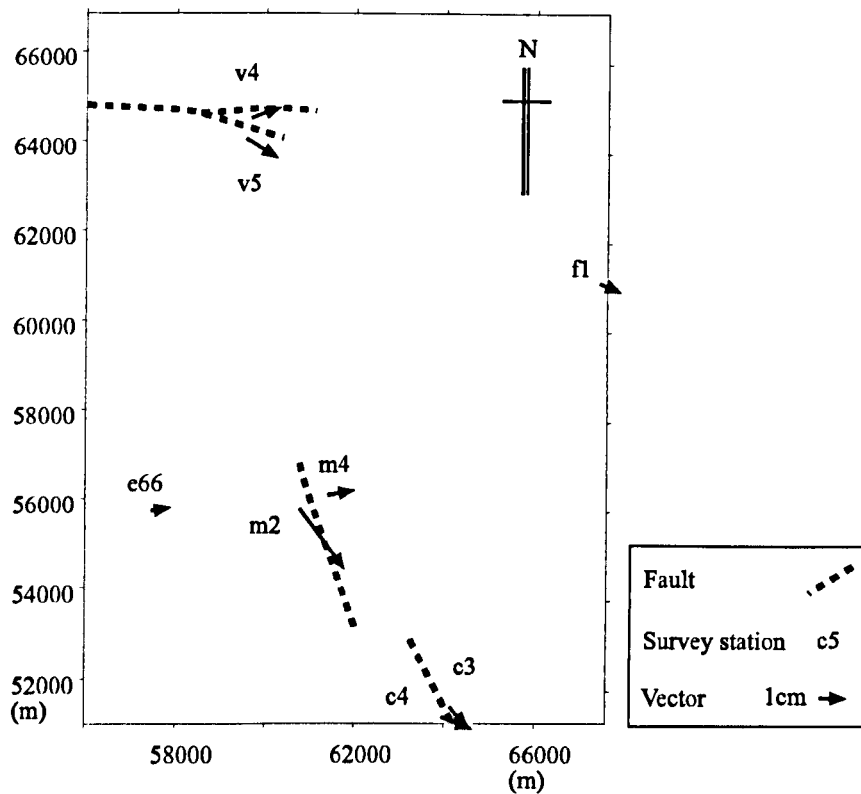


Figure 5-21 Vector changes on the Lower Eastern Flank between 1995 and 1997, for the locations see the area map (Figure 5-1).

Displacements have on average 15mm error ellipses and this must be taken into account on interpretation. Vectors do however, show a concurrent eastward displacement, but this single inter-survey occupation is insufficient to draw any conclusions on the deformation rate of the flank. The network is now in place and can be monitored in the future to determine the deformation rates. The displacement over a longer period of time will provide a more conclusive result. If this trend is maintained over future surveys then the implications are that despite any shallow displacements of the Timpe and Pernicana Faults the whole of the eastern flank is sliding. The most likely cause is the aforementioned tilted clay substrate underneath the edifice along which sliding is assumed to occur (McGuire & Pullen, 1989).

5.10. The implications of the recorded ground deformation between 1994-97

5.10.1. The Upper South-Eastern Flank Network

Renewed activity in the summer of 1995 would have been expected to have caused broad inflation of the upper summit area between 1994 and 1995 (Mogi, 1958), ground deformation data however, showed (during this time) a pattern of unexpected deflation. This is interpreted to be a consequence of either; (i) an inflated state prior to the 1995 occupation, with the deflation pattern occurring as a *relaxation* of this stressed state, or (ii) deflation occurring from a non-stressed state. The data-set from 1994 to 1997 reveals that the stations close to the summit show continuous inflation from 1995, with final levels in 1997 more elevated than the original 1994 co-ordinates. The lower stations, however, reveal a similar pattern of inflation since 1995 but to a final level still beneath the elevated 1994 levels. Therefore it is accepted that the edifice was in an inflated state prior to 1995 (see additional strain data below).

It must be remembered at this stage that the recorded deformation is minor and reflects only small but coherent patterns. The inflated state of 1994 was most likely a lasting result of the 1991-93 eruption. The data from 1995-1996 revealed a broad pattern of inflation, this is most likely due to the re-filling of the summit conduits with magma which fed the on-going sporadic summit eruptions of 1996. The irregular pattern of strain revealed an interesting pattern of higher strain both near the summit craters (>2750) and lower on the network (between 1750-2250m). One interpretation of this is that this reflects the sub-surface intrusion of magma into; (i) the summit craters, and (ii) a fracture in the area east of Montagnola. Point (i) is accepted due to the continue eruption of magma into the summit craters. The possibility of a fracture in the area east of Montagnola is discussed later.

Shallow block movements described in Section 5.7.4 show a broad easterly displacement trend in the most easterly blocks. In the 1996-97 survey (illustrated

in Figure 5-14), the general pattern is still of broad inflation (the smaller displacements indicate less noise on the data, as a result of using GPS). There is a continued easterly displacement of the eastern blocks, although blocks a and b trend NE and block c trends SE. The low level of deformation reflects the continued summit activity and the lack of a shallow intrusion. Vector displacements between each of the surveys reveal distinct horizontal deformation in the area beneath Montagnola. It is suggested that the deformation patterns reflect real movements since the area is; (i) above the 1989 fracture, and (ii) identified by Budetta & Carbone (*in press*) to show an increase in micro-gravity. In order to investigate this deformation further, a finite element model was constructed for Etna in Section 5.8; the results of the modelling show that the vertical deformation can be explained by the expansion of a fracture near to the accepted path of the 1989 fracture.

The Upper South-Eastern Flank Network survey stations are divided into two broad western and eastern groups. The western stations are those in blocks d, e, & f and the eastern stations include blocks a, b, c, & g (Figure 5-5). Figure 5-22 shows the different strain rates recorded of the western and eastern stations on the flank from 1987-97.

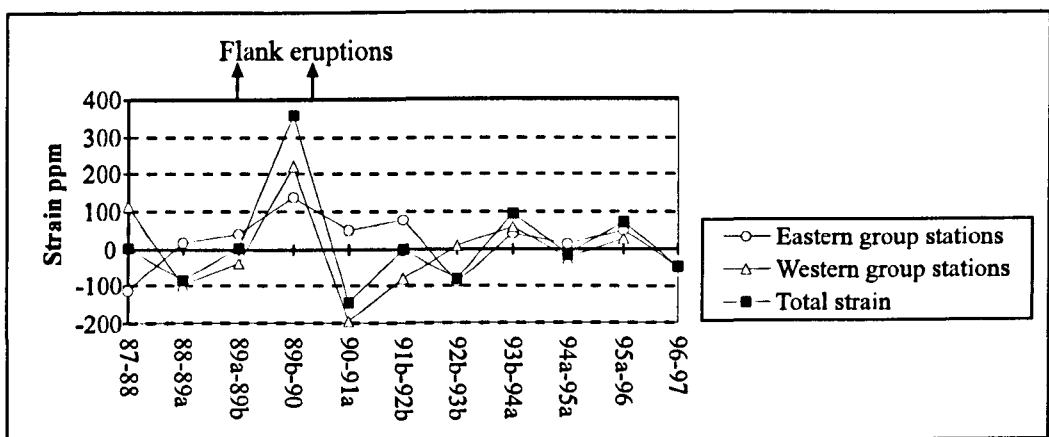


Figure 5-22 The low levels of deformation have provided an opportunity to examine i), the smaller strain relationships between the shallow surface blocks examined in Section 4.2.1 and ii) the accuracy and suitability of the techniques to measure continuous ground deformation. (additional data supplied by McGuire)

The diagram reflects the low levels of deformation recorded within the project and reaffirms the assumption made that no dyke have been emplaced since the last eruption. It also confirms the conclusion made that the upper flank was in an inflated state during 1993-4. Results from the Upper South-Eastern Flank Network from 1994 to 1997 (outlined in Section 5.3), show a continuous but small level of changing ground deformation. This pattern is reflected in comparisons between individual surveys and between the first survey in 1994 and the last in 1997. Average strain measured for each survey was; 2.2ppm (1994-5), 14.6ppm (1995-6) and 4.2ppm (1996-7), the period from 1995 to 1996 shows the highest strain, indicating time of the possible intrusion into the dyke at depth on the Eastern flank east of Montagnola. Expected strain from a single dyke emplacement would be in the order of 100ppm or more, so the data only represents either a very deep resurgence or an aseismic displacement of the fracture.

The sub-division of the Upper South-Eastern Flank into the series of shallow blocks, proposed by McGuire and Pullen (1989) is queried. The (small) ground deformation data collected during this study has permitted the further analysis of these blocks, and allows them to be re-defined into smaller coherent blocks. A major finding of this study is that they appear to behave differently in the eastern and western halves of the area. This E-W division, which has been identified throughout this research may reflect either (i) an inherited tectonic influence which has extended to the shallow surface or (ii) the edge effects of the Valle del Bove. Tectonic influences of a SE trending structural shear zone (as an extension of the Lower Eastern Flank Faults) beneath Etna are not thought to extend into the shallow surface of the volcano (McGuire and Pullen, 1989). The findings of the study have led to the proposal that the influences of the SE trending fault beneath the edifice impact upon eruptive activity and shallow block ground deformation. This argument is consistent with the two eruption types discussed in Section 4.3 by Murray & Guest (1982). They stated that long lasting flank eruptions such as the one from 1991 to 1993 occur from deep fractures in the flanks of the edifice. These fractures oriented along the SE trend coincides with

the SE trending tectonic faults on the eastern flank (including the Mascalucia-Trecastragni and Santa Tecla Faults). Thus, the EW division of the Southern Rift-Zone (and the long lasting flank eruptions) may be interpreted to be a shallow representation of a deep SE fault within the flank. Deep tectonic structure is 'inherited' through the development of the shallow blocks on the Southern Rift-Zone (from the Summit to Nicolosi-Nord).

The second interpretation of the EW divisions, is that it is a reflection of the instability of the edge of the Valle del Bove cliff first proposed by McGuire & Pullen (1989). If this hypothesis is accepted then this has important implications for the stability of the Valle del Bove scarp at the head of the depression. Continued dyke emplacement caused over five metres of extension across this divide between 1981 and 1987, McGuire and Pullen (1989) raised concerns about the continued stability of this western wall. The research undertaken in this study confirms that this area undergoes almost continued eastward displacement especially at the area known as Belvedere (e4 and e37). The wall beneath Belvedere comprises loose blocks which appear to have fallen to the Valle floor below in places. When occupying the survey station on the floor of the Valle del Bove (e33) beneath Belvedere, frequent rock falls were seen and heard descending down the slope. The area is made up of thick jointed lava flows (Belvedere series) and the eastward extension has led to periodic toppling of blocks and loose material. This evidence of continued rockfall suggests that the slope is continually readjusting to the additional stresses from eastward displacement and is unlikely to fail over the whole face unless a dyke is emplaced immediately behind it. The worst-case scenario is that this could lead to large-scale failure in the form of a small lateral blast from a 1000m collapsed wall. McGuire and Pullen (1989) proved that the dykes are diverted by the change in the stress regime close to the wall encouraging dykes to be emplaced directly behind them. This evidence of continued failure is seen along the length of the wall. The E-W pattern observed in the Upper South-Eastern Flank Network may be due to either a SE fault or a topographically controlled stress regime - or more likely a combination of both.

5.10.2. The Lower Eastern Flank Networks

Measurement of the Lower Eastern Flank Networks has been beset by measurement problems due to growing vegetation and urban development; continuous (although sporadic) monitoring has not detected any significant creep. Due to unavoidable breaks in the data-set caused by over-grown foliage and the temporary loss of nails (under dumped material), line-length change for all the stations over the long time period can not be compared.

Only the network at Carruba on the San Leonardello Fault has shown any definite signs of creep, this is aseismic and is most probably related to stress accommodation from the adjacent Santa Tecla fault (see discussion below). The absence of significant creep on the flank within a period of insignificant micro-seismicity, suggests that no gradual aseismic stress accommodation occurs between major eruptive or seismic events. The lack of deformation is in fact very important, since creep rates on the major tectonic fault strands are calculated to have a rate of approximately 10mm per year and are thought to be unrelated to seismic activity (McGuire *et al*, 1997; Tortorici, 1997). The absence of any major seismic event on the eastern flank from 1994-1997 suggests that the displacement on the faults (apart from the San Leonardello Fault) is in fact co-seismic and therefore limited to occasions of active tectonic displacement and not a function of slow deformation or creep caused by inherent instability on the eastern flank.

McGuire *et al*. (1996) speculated that the Timpe faults and the Pernicana faults relieve the stresses accumulated by persistent dyke emplacement in the active rift-zones through constant creep of the lower faults. This model of stress accommodation can not however be developed very much due to the lack of a major magmatic intrusion in the rift-zones. However information can be gained by examining taking two principal results; (i) there has been no active intrusion in the rift-zones since 1991 and (ii) the Carruba network displays slight evidence of displacement across the fault. The first point suggests that if the stresses are in fact dissipated throughout the rift-zones then it either occurs instantaneously, co-

seismically or conversely over a very long period of time at a rate less than 5mm per year (this may not have been detected during the monitoring programme). The second factor are the small movements at Carruba. During the 1991-1993 eruption Latora and co-workers (1996) noted that the San Leonardello fault undergoes shallow seismicity immediately after the Santa Tecla fault exhibits deeper seismicity; this suggests that the Carruba fault accommodates dissipated stresses, not from the summit area but from the adjacent tectonic feature. This model is discussed in more detail in section 5.11.

5.10.3. Summary of principal conclusions

Eastern Flank	No major eruptive or tectonic event between 1994 and 1997.
	Measurement of ground deformation was carried out successfully using EDM and GPS.
Upper South-Eastern Flank Network	Continuous ground deformation in the order of 10-20mm.
	The flank can be divided into shallow blocks which move independently from each other (or as joined units). Eastern-most blocks are moving eastward, leading to increasing instability in the Belvedere area (Block a) which may result in minor landsliding (toppling). Western-most blocks reveal slight westward displacement.
	Initial deflation recorded in 1994-5 was due to the inflated state prior to 1994.
	Small patch of significant ground deformation in the area east of Montagnola, attributed to re-activation (magma or hydrothermal fluids) of the 1989 fracture which runs through the area.
Lower Eastern Flank Networks	Small levels of ground deformation reveal eastward displacement, further occupations necessary to confirm pattern.
	Carruba, on the San Leonardello fault showed small amounts of aseismic deformation probably resulting from accommodation of stresses from the adjacent Santa Tecla fault.
	The Vena network indicated that there was no continuous creep on the Pernicana Fault.

5.11. Discussion of models to examine the relationship between regional tectonic faults and the rift-zones .

This section examines some of the arguments outlined in Chapter 4 and Section 5.1 concerning the structural setting of Mount Etna and the interaction between eruptive activity and active tectonic faults. The discussion takes into account the conclusions derived from the ground deformation surveys in order to redefine the nature and operation of the rift-zones on Etna.

Sicily is situated on the fold of the Calabrian Arc, the faults associated with this feature extend down through mainland Italy as far as the north-eastern coast of Sicily; here the NNE trending Messina-Giardini fault system cuts the north-east flank of Etna (see Figure 4.2 In Chapter 4). It highly probable that this array of faults has influenced the shallow faults of Etna (which maintain a similar slip component (Borgia *et al.*, 1995)). Etna is however, very complex and it is impossible to determine the exact nature of the connection. The idea that is argued here is that the fault system stops just before Etna, it is thus proposed that the fault system runs through this area as distinct surface faults (the Timpe & Pernicana Faults) which maintain a common deep seated tectonic link - the continuation of the Calabrian Arc Fault System.

The NE fault within the Praiola embayment (Figure 4.5) may be related to the Messina-Giardini fault system. It is proposed here that the NE trending faults that follow the coastline from Messina and the ENE trending Pernicana Fault are the surface representation of the deep Messina Giardini Fault system. As discussed earlier the Pernicana fault exhibits an average slip rate of 10-15mm per year (Borgia, 1995; Rasa *et al.*, 1996). This rate is higher than the rates measured for the Messina-Giardini fault system but the slip component is the same. The higher rate is most likely attributable to the proximity of fresh magma ascent within Etna and the relationship between the sets of conjugate shears (Section 4.2.1). The ground deformation results show that the Pernicana fault did not show any no evidence of continuous displacement or any recorded seismic events. It is agreed

that the displacement on the Pernicana occurs periodically rather than continuously and that it is probably co-seismic. Research by other authors undertaken on the faults on the eastern flank of Etna (as discussed in Section 4.2.2) have identified statistical correlations between eruptive events and micro-seismicity on the eastern flank (Latora, 1996). Latora and co-workers found that the microseismicity on the Santa Tecla fault and San Leonardello faults is strongly correlated with the eruptive activity at the summit. The ground deformation recorded during this research on the San Leonardello fault at Carruba and at the Moscarello Fault at Macchia have shown no co-seismic deformation.

Recent research sought to divide the faults of the eastern flank of Etna into eruptive faults and tectonic faults (Stewart *et al.*, 1993; McGuire *et al.*, 1996; Latora *et al.*, 1996; Monaco *et al.*, 1997) by examining the faults which appear to be affected by eruptive activity. McGuire *et al.* (1996) suggests that the summit stresses and the extension of the rifts is dissipated through the Santa Tecla and San Leonardello faults. This assumes that the activity on the faults is a reaction to the summit activity, but the correlation could also imply that there is a *common source*. If the faults and the eruptive activity are all part of the same system, subject to the same regional tectonic forces then the eruptive and seismic activity would correlate. The nature of this relationship can not be resolved with the data collected due to the lack of a major flank eruption during the period of this study.

In light of the arrangement of faults on the eastern flank and the associated micro-seismicity, it is proposed that the activity of Etna (particularly flank eruptions) may be related to the neotectonic faults of the Calabrian arc. This also implies that a major flank eruption could take place if a large tectonic event occurred along this end of the fault system. Tortorici *et al.* (1996) suggest that the Calabrian arc faults extend into the NE of the edifice and labelled this area as a 'seismic gap', implying that the recent lack of seismic activity in this area may indicate that an event is overdue. There was almost continuous summit and flank activity after the major earthquake in Messina in 1908 for many years (Chester *et al.*, 1985). The tectonic connection was also evident when the eruptive and

tectonic events in 1980 correspond with the Mascalucia-Tremestieri seismic swarm (The NNE-SSW conjugate shear was active). Only a small eruption occurred from the summit during 1980 but in 1981 a large flank eruption occurred from the NNW-SSE rift-zone and a different eruptive phase began (Murray & Guest 1984). Murray (1990) thought that the new phase was triggered by volcanic rather than volcano-tectonic or tectonic stresses, and that the large eruption in 1981 was the cause of the east-west opening of the main rift system (on the north-east side) due to magma entering the new storage areas. The new model proposed here reinterprets these relationships to suggest that the long term eruptions are a consequence of tectonic extension, the major eruptive events are co-seismic and produce permanent fractures concurrent with the shallow representations of the regional tectonic stress regime.

Ground deformation data from the area beneath Montagnola records aseismic deformation along the tract of the 1989 fissure. Using the model introduced above and observations during the propagation of the 1989 fracture that concluded that the 1989 fracture was fed from depth and not via the summit (Rymer *et al.*, 1994), it may be suggested that the 1989 fracture is controlled by deep tectonic stresses (combining the regional stress regime and the gravitational stress regime of the edifice) and that magma resurgence at depth is due to the passive filling of a fracture at depth rather than the transport of magma from the upper central conduit along the shallow surface of the volcano. This idea is verified by the positive correlation between high strain and low altitudes during 1996 and 1997, and by the lack of deformation recorded during the years preceding the 1995-7 deformation in this area (Saunders *unpub-data*).

6. PITON DE LA FOURNAISE

Piton de la Fournaise is situated on Réunion Island in the Indian Ocean, 700km east of Madagascar. It is one of the most active oceanic volcanoes in the world, there have been over one hundred recorded eruptions in the last three hundred years. As a result of progressive south-eastward slumping of the edifice, collapse has occurred (to the south-east) in three distinct recognised events in 250ka B.P., 65ka B.P. and 5ka B.P. (Chevallier & Bacheléry, 1981). The current eruptive centre is the l'Enclos Fouqué, consisting of a four hundred metre high edifice bisected by three distinct rift-zones, situated within a 'caldera-type' depression 8km wide. This is open towards the sea, and like the Valle del Bove on Etna, it is also thought to be formed from past collapses. Unlike Etna there are no recognised regional tectonic faults that could exert a deep influence on eruptive activity or the stability of the edifice. This study addresses the following questions listed in Section 1.2: *What is the relationship between magma emplacement and gravity induced displacement at Piton de la Fournaise, and is the shallow morphology of the seaward flank of the volcano currently stable?* In order to answer these questions data were recorded from two ground deformation networks straddling the rift-zones and a third at installed at the coast.

The results have been presented at conferences and as part of the European Laboratory Volcano project¹. This study was part of the European Laboratory

¹McGuire, W. J. & Moss, J. L. (1995) Piton de la Fournaise-European Laboratory Volcano; Contribution of the Centre for Volcanic Research, Cheltenham, UK. *Piton de la Fournaise-European Laboratory Volcano Report*.

Moss, J. L. (1996) Ground deformation monitoring of the rift zones of Piton de la Fournaise. *2nd Workshop on European Laboratory Volcanoes*. Santorini, Greece.

Briole P., Bacheléry P., McGuire B., Moss J., Ruegg J. C., Sabaurout Ph. (1996) Deformation monitoring of Piton de la Fournaise: Evolution of the monitoring techniques and knowledge acquired in the last 5 years. Abstract. *2nd Workshop on European Laboratory Volcanoes*, Santorini, Greece.

Briole P. Ruegg J-C., Chemincé J-L., Ammann J., Bacheléry P., Brefort D., Delmond J-C., Kowalski Ph., Sabaurout Ph., McGuire W. J., Moss J. L. (1997) Deformation monitoring of Piton de la Fournaise: Evolution of the monitoring techniques and knowledge acquired in the last 5 years. IAVCEI General Assembly, Puerto Rico.

Volcanoes Project 1993-1996 in collaboration with the Institut de Physique du Globe de Paris (IPGP).

6.1 Introduction

Piton de la Fournaise was chosen for detailed investigation for two reasons. Firstly the volcanology is similar to Etna, although the emission rate on Etna is twice as large. Current emissions on Piton de la Fournaise are predominately basaltic and the activity is centred around a central crater complex with active rift-zones on the flanks. These rift-zones bound the depression on the seaward flank (similar to the Valle del Bove in Etna), secondly a new ground deformation network was established in 1993 spanning the active rift-zones. During the initial installation of the network, only one set of measurements was taken, further occupations were necessary for the completion of a baseline data-set in order to examine rift-related movements. The networks were originally set-up and monitored by Saunders (unpub thesis). Periodic occupation of the broad island-wide Réunion network is undertaken by the Institut de Physique du Globe de Paris (Briole, 1996). The Rift-Zone Networks examined in this chapter were established within this broader network.

There has been no major flank eruption during the course of this monitoring programme² (1993-1996), and although this has prevented a comparison of magmatic and gravitational stresses, it has provided information on inter-eruptive deformation. A three year inter-eruptive period is a short time to classify typical ground deformation on volcanoes that do not erupt annually or bi-annually. However, on Piton de la Fournaise (and Etna) a three year interval between eruptions is rare and therefore this hiatus of activity provides a crucial window through which to observe the inter-eruptive deformation. Monitoring between eruptions is usually undertaken on a rudimentary level (1-3 seismic stations, annual ground deformation monitoring of a few key stations) until signs of impending activity are noted and the program is stepped-up. In this case the dense

² A major flank eruption began in March 1998 this will be discussed in Section 6.7.

Rift-Zone Networks were measured each year for the three years despite the inactivity and therefore provide the first detailed study of inter-eruptive deformation on this volcano.

6.1 Geology and Volcanology of Réunion Island

Réunion Island is a predominately basaltic shield volcano growing in the oceanic part of the African plate. The island is ellipsoid in shape, measuring 50 by 70 km and is oriented N120°E along an Eocene oceanic rift at the lowest part of the Mascarene basin (Lénat & Aubert, 1982; Rousset *et al.*, 1989). This rift is not considered a regional tectonic fault and has no influence on activity.

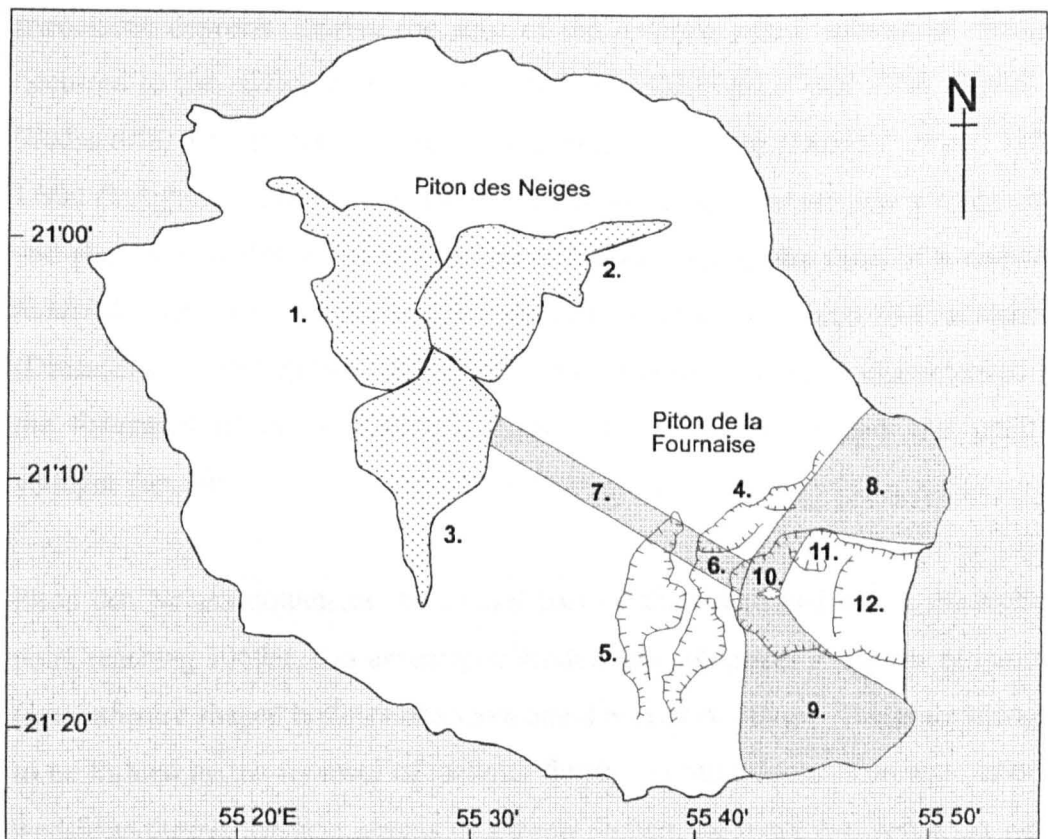


Figure 6-1 Réunion Island, 1. Cirque de Mafate, 2. Cirque de Salazie, 3. Cirque de Cilaos, 4. Rivière de L'Est, 5. Rivière des Ramparts, 6. Rempart des Sables, 7. North-West Rift-zone, 8. North-East Rift-zone, 9. South-East Rift-zone, 10. l'Enclos Fouqué, central craters, 11. Plaine des Osmondes, 12. Grand Brûlé (the scarp is the Grandes Pentes).

The current activity is most likely caused by the proximity of a magma plume that sourced the plateau basalts of the Deccan traps in India 65Ma ago (White, 1989). The oldest rocks on the island have been dated to approximately 2Ma B.P. but there are likely to be older deposits beneath these (McDougall, 1971). The island shield comprises two prominent volcanic centres; the extinct Piton des Neiges and the active Piton de la Fournaise, see Figure 6-1.

Development of the Piton des Neiges edifice can be divided into three geological phases, the first two are pre-collapse and the third is post-collapse (Duffield *et al.*, 1982). The pre-collapse stages comprise a submarine sequence of thinly bedded lavas and pyroclastic deposits covered by subaerial thinly bedded lavas and pyroclastic deposits. During the start of the *collapse phase* substantial changes occurred to the edifice in the form of 'tectonic disturbance' and uplift (Upton & Wadsworth, 1970); this culminated in a caldera collapse (Duffield *et al.*, 1982; Lénat & Aubert., 1982; Gillot, 1989). The collapse deposits are debris avalanches and slumps, and this suggests that the collapses were in the form of a *complex landslide* most likely comprising a rotational or block slide and rock avalanche (Dikau *et al.*, 1997 pp189-202). The third post-collapse stage is characterised by the formation of differentiated lavas which capped the eroded and uplifted younger deposits.

Piton des Neiges dominates the central part of the island and forms the highest point reaching 3069m, it is extensively eroded and comprises a number of cirques (amphitheatre shaped hollows of an average diameter of 10km). These are thought to be formed by the removal of material through continuous erosion and periodic landslides during the later stages of activity (when the more evolved lavas were emitted) (Upton & Wadsworth 1970). The edifices have developed and then subsequently collapsed to be covered by fresh lava flows; this pattern is typical of basaltic shield building islands. Piton des Neiges had two established rift-zones oriented 120° and 150° from the central area and a number of faults (which acted as a magma conduits) oriented 045°. Emplacement of dykes along these trends is

thought to have led to the collapses that formed the cirques. Activity ceased about 22ka B.P. and Piton des Neiges is now considered extinct (Stieltjes, *in prep*).

The active centre is now at Piton de la Fournaise, on a bearing of 120° from Piton des Neiges. Activity began at Piton de la Fournaise at the same time as the differentiated lavas were produced from Piton des Neiges approximately 350ka B.P. (McDougall, 1971). Evidence suggests that the volcanic activity migrated along the 120° orientation from Piton des Neiges to Piton de la Fournaise (Bachelery, 1981). A number of structural and morphological features along the proposed migration path (between Piton des Neiges and Piton de la Fournaise) substantiate this hypothesis, including (i) two structures interpreted as collapse calderas (McDougall, 1971, Bachelery, 1981), and (ii) a close concentration of (undated) cinder cones along the ridge following the line of activity (Bachelery, 1981). The collapse structures are defined by sets of broadly curving nested faults orientated 120°, two of these nested faults the Rempart des Sables and Rivère des Remparts are identified by McDougall (1971, p265) as headwalls of large-scale collapse events (Figure 6-1). Duffield (1982) points out that although the orientation of these scarps is not the same as the morphology of the present l'Enclos Fouqué 'caldera', they are the same as the NE and SE rift-zones of Piton de la Fournaise, see section 6.2.1. Displacement of the eruptive centre is most likely caused by the massive lateral caldera collapse that is thought to have occurred during after the uplift stages of development (as mentioned earlier). This collapse would have closed the magma system under Piton des Neiges causing the remaining magma to *differentiate*. With the current system now blocked a new least effort path developed eastward along the 120° migration axis. This created a sequence of edifices that have subsequently collapsed, the youngest eastern-most edifice is Piton de la Fournaise. This path is still volcanically active, it is recognised as the NW Rift-Zone of Piton de la Fournaise.

6.2 Geological structure of Piton de la Fournaise

Piton de la Fournaise is a young volcanic centre in the south-east of Réunion Island, see Figure 6-1. The rock series of Piton de la Fournaise is divided into pre- and post-erosional; the older pre-erosion series comprise lavas rich in either olivines or plagioclase megacrysts. The abundant olivine xenoliths are attributed to an intrusive complex under the Plaine des Sables (below the Rempart des Sables) identified from high gravimetric anomalies (Rousset *et al.*, 1989). The transition from the pre- to post-erosional products is most likely due to the caldera collapse (as discussed in Section 6.1) closing the magma conduit system and allowing the magma in the shallow storage area to evolve.

The present eruptive edifice is the l'Enclos Fouqué, a sunken caldera-type feature with a diameter of 8km bounded on three sides by the 300m high cliffs and open towards the sea (east). Chevallier & Bachelery (1981) identified differing stages in the development of the l'Enclos Fouqué each ending in collapse events, the headwalls of these collapses join to form the steep scalloped cliff walls of the l'Enclos Fouqué. The depression open in the seaward direction forms the Grand Brûlé and the Grandes Pentes (see Figure 6-1). l'Enclos Fouqué has a central cone with two summit craters, Bory and Dolomieu that have formed through successive collapse and filling (rather than from explosions). Seismic and ground deformation data suggest a plumbing system model comprising a shallow magma reservoir beneath the central summit area which is replenished from a deeper source (Lénat *et al.*, 1989a). This storage area comprises an array of dykes and sills whose irregular filling creates uneven inflation and seismicity. There are radial and concentric fissures around the cone, that form during the initial surge of magma to the surface prior to a summit eruption, they are concentrated at the north and south of the cone (Bachelery, 1990).

Magnetic and gravimetric data reveal the path of dyke sheaves radiating from the summit to the NE and SE, these clusters of dykes form the Eastern Rift-Zones: NE Rift-Zone and the SE Rift-Zone (Lénat *et al.*, 1989a). Both the Eastern Rift-Zones have produced pronounced shore-line promontories, these are illustrated in Figure 6-1.

6.2.1 The active rift-zones

The existence of rift-zones on Piton de la Fournaise is not wholly accepted, Upton and Wadsworth (1970, p. 143) initially questioned their existence because they are topographically less well pronounced than the rift-zones of Kilauea. The importance of rift-zones in the eruptive cycle and their current role and relationship to the eastern flank is unclear.

The exact orientation of the rift-zones is imprecise, the Eastern Rift-Zones as illustrated in Figure 6-1 are identified as a broad roughly aligned north-south strip curving through the summit area with the ends pointing eastwards (Lénat & Aubert, 1982). Despite the breadth of the rift-zones Duffield *et al.* (1982) proposed specific orientations of N50°, N45° and N135°. Nevertheless, the rift-zones will be henceforth referred to as the NW, NE and SE Rift-Zones. The SE Rift-Zone is characterised by many cones and surface fissures up to 2m wide and 30m long, the NE rift also has many cinder cones and extensive shelly pahoehoe flows. The less active NW rift-zone which has been referred to as an *intrusive axis* (Lénat *et al.*, 1989a) and a *saddle ridge* (Duffield *et al.*, 1982), occurs along the line of migration of activity from Piton des Neiges. It is identified by numerous cinder cones, there has been one eruption on this rift in historic time in 1820, this eruption lasted between four and six weeks erupting from two craters on the edge of the Rivière des Remparts (Stieltjes & Moutou, 1989).

6.3 Historic activity

Historical records began in 1655 when the French colonised the island and since that time there have been eruptions nearly every year. The current activity is effusive with fire fountaining during the start of the eruptions. Ninety-five percent of the recorded activity has occurred within the l'Enclos Fouqué, with the other five percent occurring outside this area (Stieltjes & Moutou, 1989). Eruptions are

predominately effusive with occasional phreatic and phreatomagmatic eruptions accompanying the draining of lava lakes. Most eruptions are predominately basaltic and typically last from approximately 24 hours to about one month. There have been in the past, long periods of sustained activity which produced the large pahoehoe fields in the l'Enclos Fouqué similar to the on-going eruption of Pu'u O'o on Kilauea, Hawaii (Rubin & Garcia, 1998). Infrequent pyroclastic deposits are attributed to phreatic or phreatomagmatic events (and may be connected to the collapse events). Since 1985 there have been over 20 eruptions, most occurred between 1985 and 1989 around the central craters of Bory and Dolomieu. Although seismic activity accompanied the eruptions, it was largely centred in an area 5km north-east of the central cone called the Plaine des Osmondes (Figure 6-2). During this period of frequent eruptive activity (1985-89), numerous 4km deep seismic shocks were recorded in this area (Delorme *et al.*, 1989). Two eruptions in recent years have occurred outside the l'Enclos Fouqué in (i) 1977, on the NE rift-zone and (ii) 1986, on the SE rift-zone (Stieltjes & Moutou 1989).

From the beginning of the study in 1993 (Saunders *pers com*) there were no signs of impending activity, until 1996 when an intrusive event was recorded. It was first identified by an increase in radon flux, background seismicity, and changes in ground tilt and EDM line-lengths of up to 10mm (Staudacher, 1998). At the end of this study, (during the final writing up of the thesis) a flank eruption occurred in the NE Rift-Zone of Piton de la Fournaise³. The eruption commenced on the 9th March at 15h00, it was predicted by the observatory who gave two days warning due to the preceding seismicity and ground deformation (tiltmeters). The eruption started with the opening of a fissure system at 2450m in the north flank of the Dolomieu crater, this propagated north and erupted at an elevation of 1950m (Figure 6-2). A lava-fountain fed lava flow proceeded north-east towards the Plaine des Osmondes at a rate of 20m³/sec, the final flow length was 4km long.

³ It was not possible to return to Piton de la Fournaise to reoccupy the network. However, the team from IPGP occupied two surviving survey stations, the full analysis is as yet unpublished but the preliminary results are discussed in Section 6.7.

Scoria cones over 50m were built up around the eruption site on the northern flank. Three days after the start of the eruption a second fissure system opened on the south-west side of the cone at 2250m, the output rate was only 5-10m³/sec and the flow only travelled 1.5km. This phase of the eruption ended on the 14th March (Staudacher, 1998). The eruption was centred in the middle of the NE Network, this is unfortunate as at least five survey stations of the NE Network are now buried.

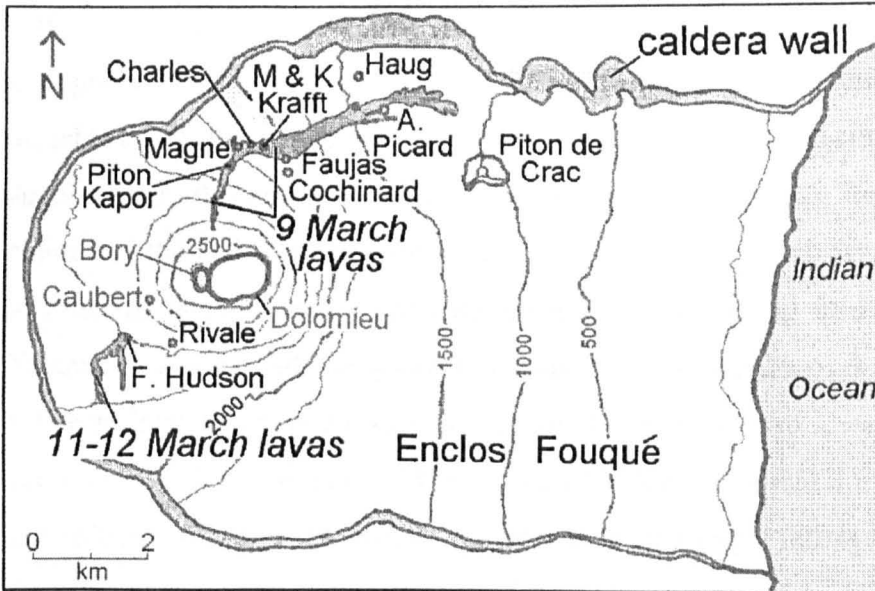


Figure 6-2 The lavas from the March 1998 eruption showing the path of the lava flow and the names of the prominent cones near the flow (From Staudacher, 1998).

6.4 Previous models for the stability of the volcanic edifice

The stability of the Piton de la Fournaise edifice is questioned due to the following evidence: (i) soft sloping material of Piton des Neiges that lies under the edifice, (ii) east-facing collapse structures to the west of l'Enclos Fouqué, (iii) active rift-zones oriented along the lines of previous collapse, (iv) a young slump feature within the Grand Brûlé; (v), off-shore deposits which were once part of the sub-aerial island (Lénat *et al.*, 1989a).

Development of the shield volcano on an underlying, sloping topography causes asymmetrical development. A simple, isolated shield volcano will develop a

symmetrical gravity-dominated stress field, characterised by three rift zones, roughly 120° apart (Carracedo, 1994). Piton de la Fournaise however, has growth on the flanks of Piton des Neiges, the underlying slope expedites the gravitational pull of the eastern sector of the edifice seawards. Stress disequilibrium due to the asymmetrical loading and gravitational stress is characterised by the development of (i) décollement faults along lines of reduced stress, and (ii) volcanic rift-zones. The décollement faults form parallel to maximum gradient of a sloping flank of the edifice, the edifice may then slide down the underlying slope as a single block or as a fragmented pile, the rift-zones often form shear zones at the edge of this unstable block. Labazuy (1996) modelled the sliding edifice as a cone of sand on a ductile layer, the model formed transverse faults coupled to the gliding plane oblique to the main direction of extension. This inherent instability is exacerbated as Piton de la Fournaise is not only situated on the sloping flanks of Piton des Neiges but also on underlying debris avalanche and slump deposits. The boundary between these sedimentary deposits and the fresh lavas form a weak layer and a likely sliding plane. Basaltic edifices frequently develop within a cycle of growth and collapse, consequently future instability is more likely if this cycle is observed. East-facing headwalls of previous collapses can be found to the west of the l'Enclos Fouque, these are formed as a result of either catastrophic or piecemeal lateral collapse. Therefore the interpretations of these features suggests that collapse has occurred in the past and if a similar failure conditions are established then failure may again occur.

Rift-zones (as examined in Section 1.3) can lead to edifice instability and collapse through asymmetrical growth of the edifice and the persistent linear extension of the flank through mechanical and thermal effects.(McGuire 1996). Piton de la Fournaise has three active rifts, illustrated in Figure 6-1, the morphology of the edifice has caused the eastern (seaward) rift-zones to be the most active. These rifts trend in a similar orientation to the aforementioned collapse structures. The volcanic rift-zones are the focus for potential flank failure; the relationship between magma emplacement in the rift-zones and flank mobility has been

determined through ground deformation monitoring and is discussed in Section 6.8.

A further piece of evidence in support of collapse is the slump section in the lower part of the Grand Brûlé called the Grandes Pentes. The Grandes Pentes (see Figure 6-1) is currently the most easterly slump block of the volcano (Duffield *et al.* 1982; Labazuy, 1996). Duffield *et al.* (1982) speculate that this feature is analogous to the Hilina Pali in Hawaii, proposing that the normal fault scarps are a product of continuous down-slumping, bounded by the active rift-zones (see Appendix I). Large fault-divided blocks also suggest the existence of subsided lava flows within the Grand Brûlé area (Lénat *et al.*, 1989a).

A side-scan sonar undertaken in 1989 reveals 500km³ of mass wasting deposits comprising sub-aerial fragmented lava off-shore from the Grand Brûlé. These off-shore deposits suggest that the source of the numerous slumps and debris avalanches is greater than the size of the current caldera would indicate this implies that either; (i) the edifice before the collapse was probably very much larger than the edifice today or (ii) some of the collapse deposits are from the collapses of earlier edifices. The scars visible on Piton de la Fournaise only can account for 60km³, suggesting that there are buried scars which account for the missing material. At the distal part of the deposits there is a compressive zone as the sliding blocks are buttressed against the seafloor, there is no major buttressing feature on the island (eastern side). The youngest materials to come from the Grand Brûlé are less than ten thousand years old.

From the evidence outlined above it is proposed that the Piton de la Fournaise edifice will undergo collapse in the future. It is unclear however what the conditions necessary for this collapse are and when they will be in place. The interpretation of recent eruptive events and new ground deformation data provide information on the relationship between fresh magma and the edifice.

Piton de la Fournaise is 2637m high and made up of successive lava flows and sheaves of dykes, it has developed on sediment layers consisting of hylaclastics and collapse deposits on the southern slopes of the Piton des Neiges edifice. This soft layer is recorded from 200m to 700m beneath the edifice (Rançon *et al.*, 1989) providing the possible 'ductile layer' discussed above. Lénat *et al.* (1989a) noted that there is always more recorded ground deformation and seismicity on the eastern and central areas rather than the western flank, this confirms the eastward alleviation of built-up stresses. The mechanism which instigates this is suggested by Lénat *et al.* (1989a) to be gravity-sliding, and by Duffield *et al.* (1982) to be a magma pressure exceeding of the rock strength, causing lateral dilation of the rift-zones to the less buttressed east, the same as in Hawaii, (Appendix A).

Observations of recent eruptions (1985-6 and 1998) have identified right and left lateral *en echelon* fissures on the eastern flank that indicate preferential eastward extension (Lénat *et al.*, 1989b). The current stability of the edifice depends upon the set of conditions necessary for eastward collapse. Eruptive fissures from flank eruptions that occurred between 1980 and 1990 developed either *en echelon* faulting or lateral eastward displacement. This indicates that the mechanical extension from shallow dyke intrusion is influenced by the broader east-west stress regime acting over the eastern flank. However, Hirn (*pers com*) interprets seismic data from eruptions in the 1980s to represent passive intrusive sheets, suggesting that passive eruptions occur on the flanks via open fissures rather than forceful propagating along the rift-zone. This would suggest that the EW extension occurs prior to magma intrusion and is thus not caused by magma-related stresses. Necessain *et al.* (1996) also link magmatic activity with eastward displacement of the eastern flank, although they attribute the eastward movement to a release of accumulated stresses in the summit rather than ascending magma from depth. Labazuy (1996) agrees speculating that the mechanism is mechanical and thermal changes induced by the magma intrusions, Labazuy, however, argues that the accumulated stresses are periodically released in large-scale events similar to those in Hawaii (Moore *et al.*, 1994), rather than released during eruption events.

These issues are examined through the analysis of ground deformation in order to investigate the inter-eruptive displacements (if any) and in the event of a fresh magma intrusion, the role of fresh magma-related stresses. It is accepted that collapse has occurred in the past, but as mentioned earlier, it is not known if the conditions for collapse to occur again are met. If the main trigger is magma intrusion in the rift-zones then analysis of ground deformation over the rift-zones provide important information. In this study the following specific ground deformation effects will be assessed: (i) slow creep with no magmatic intrusion (highlighting the importance of E-W gravitational stresses), (ii) eastward displacement during a magmatic event, (iii) slow creep before or after an intrusive event (indicating gravitational sliding).

6.5 The ground deformation monitoring of the volcano

The Piton de la Fournaise Volcano Observatory was established in 1979 after the eruption in 1977 which occurred outside the l'Enclos Fouqué; it was constructed in the style of the Hawaiian Volcano Observatory. The main objectives of the observatory are to; (i) monitor the geophysical and geochemical activity of the volcano in order to evaluate volcanic hazards, (ii) provide predictions and warnings to public officials, and (iii) undertake research with the Institute de Physique de Globe de Paris (IPGP) (Toutain, 1990). At the present time the observatory monitors seismicity with a seismic network including two digital three-component short period seismometers, differential magnetism, ground deformation and geochemical changes. Most of the instruments are automatic and telemeter information directly to the observatory and the IPGP, France. The ground deformation monitoring comprises automated and non-automated components. The automated monitoring includes: a six point electronic tilt array; an automatic EDM and one extensometer. The non-automated monitoring includes: a geodetic network; a levelling network and a 19 station dry-tilt network. The geodetic network monitors line length changes between survey

stations on the rim of the craters and the rim of the l'Enclos Fouqué depression, see Figure 6-3.

The following objectives were established in order to fulfil the general aims of the study and to answer the specific site-related questions listed in Section 1.2; (i) measure rift-related ground deformation; (ii) investigate the relationship between significant ground deformation on the eastern flank and seismicity within the rift-zones; (iii) evaluate the use of GPS over the EDM/theodolite. The two ground deformation networks monitored within this study were set-up in December 1993 on the NE and SE rift-zones, see Figure 6-3.

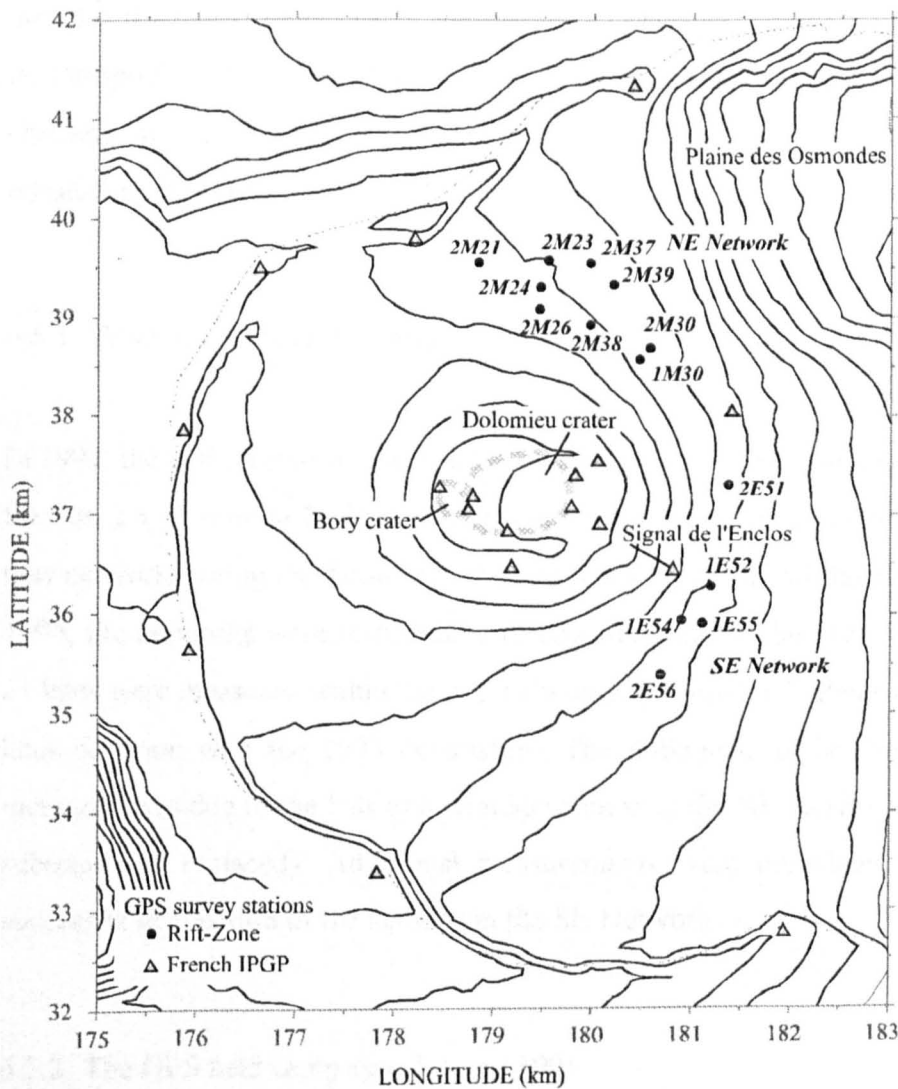


Figure 6-3 The NE, SE and IPGP Ground Deformation Networks in l'Enclos Fouqué, (contour intervals = 100m, the central cone contour = 2500m).

The network on the NE network contains 10 stations, the central part of the network is a well braced quadrilateral with good redundancy (including one French survey station). The extremities of the network are however weaker relying too much on too few stations.

The network on the SE rift-zone contains six stations and although it does not fully span the rift-zone it covers the large fissures on the eastern part of the rift. There were a few problems experienced in setting up the networks; (i) the flanks of the volcano are frequently immersed in cloud concealing the topography (this impedes the measurement using the Electronic Distance Meter); (ii) the difficulty in transporting the measuring equipment over the shelly pahoehoe and (iii), climbing up to elevated cones to achieve line-of-sight proved problematic and time consuming. The network was not fully completed during the first campaign.

6.5.1 Total station field campaign: 1993-4

In 1993, the initial network was established following the methodology outlined in Section 2.3. A total of 21 lines were occupied between the 16 stations of the two new networks, using the Total Station comprising an EDM and theodolite. In May 1994, the networks were re-occupied to complete the baseline networks, in total 21 lines were measured within the two networks, unfortunately there were only 16 lines common with the 1993 occupation. The difference in the lines that were measured was due to the loss of a strategic station in the NE Network (which was subsequently replaced). Additional measurements were completed due to the successful occupation of the stations in the SE Network.

6.5.2 The GPS field campaign: January 1995

A static survey was conducted using three single frequency (ASHTECH™) GPS receivers, as they are single frequency receivers the ionospheric delay can not be calculated. This necessitates the positioning of the reference receivers close to the rover receiver within the networks as to limit the atmospheric differences between the receivers. The receivers were multichannel and carried out code and phase processing. Two receivers acted as reference stations, positioned at opposite ends of the network. They repeatedly measured a single baseline to assess the precision of the technique. The third receiver acted as the rover occupying in turn all the remaining stations in the network. The occupation time for each station was a minimum of forty minutes, this enabled the same satellites to be tracked by the three occupied stations simultaneously, thereby permitting the differencing of data, as explained in Section 2.5.2. Each network takes at least three full days to measure.

In 1996, the ten-station network covering the NE rift zone, was extended to eleven stations to incorporate the French geodetic station (1M30). The SE network was modified and now comprises of seven stations. One French benchmark was abandoned (*Signal de l'Enclos*) due to logistical problems and two French new stations (*2E56 and 1M30*) were added to improve the spread of the network over the rift zone and permit direct marrying with the French network.

A new network was established at the coast where the sub-aerial rift zones are at their widest, survey stations were installed adjacent to the French coastal survey stations, (see Figure 6-4). This third network stretches from St. Philippe to St. Rose, across the bottom of the Grand Brûlé, and is located to determine whether detected deformation around the upper fractures is purely localised, or if it extends further down the rifts to the coast.

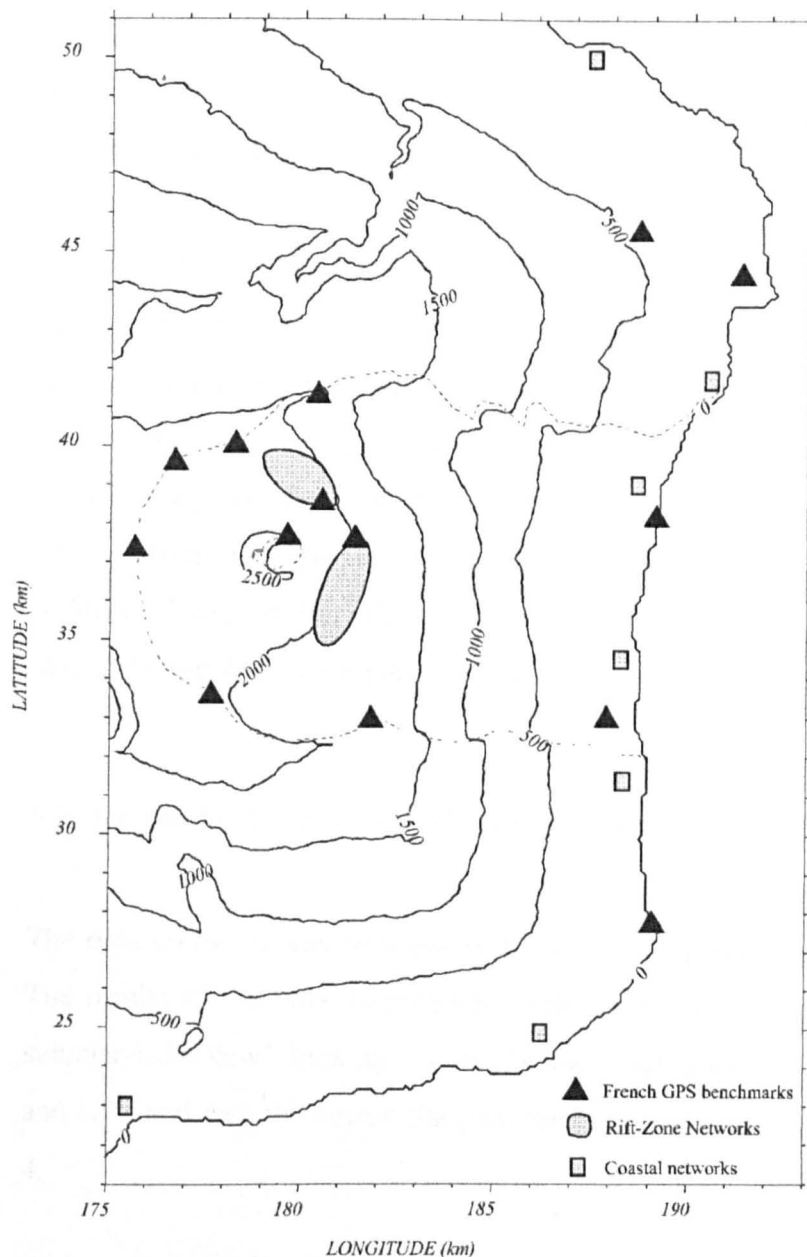


Figure 6-4 The areas covered by the Rift-Zone networks and the survey stations of the Coastal Networks including the principal French GPS benchmarks.

Field operating procedure is explained detail in Section 2.7, at each survey station, the following site information was recorded in a notebook: date, station location, identification codes, antenna height and alignments, software constants, temperature and pressure. Temperature and pressure were recorded as the standard tropospheric model was not suitable for the climate of Réunion, this information was then input into a software model devised for the island (Cosquer

pers com). Post-processing was not undertaken in the field; this was not ideal but unavoidable. To achieve an accuracy comparable to EDM (around 5-10mm), the field GPS data need be processed to remove atmospheric variables, satellite errors and to undertake differential corrections. The post-processing was undertaken using GPPS 5.1 software (ASHTECH™) at the Institut de Physique de Globe de Paris, under the guidance of Pierre Briole. The software required pre-processing steps to be undertaken before the main data processing, these included the manual identification and mending of cycle-slips. The French survey stations in the network were held fixed (to the co-ordinate obtained during the occupation of the whole island) in order to locate the entire network as absolute WGS84 co-ordinates. The precision of the network was derived from internal estimates within the GPPS and AG3D programs to be on average less than 15mm.

6.6 The results of the NE and SE Rift-Zone Networks

The data collected was satisfactory for the initial measurement of the networks. The results of the three occupations undertaken over the period 1993-1995 are summarised below⁴, looking first at the line length changes recorded using EDM and GPS and then the vector changes, the data are listed in Appendix B-3 and B-4.

6.6.1 1993 to 1994; Line length and vector changes.

The line length changes between 1993 and 1994 showed only negligible differences, the repeatability of the measurements are illustrated in Figure 6-5; the line length differences are mostly within the 10mm + 3ppm error established for EDM technique. Only one line length exceeds this limit it is between 2M24 to 2M25. Other measurements to this either of these points do not exceed the measurement limits.

⁴ The data from 1993 was obtained from S. Saunders and W. J. McGuire.

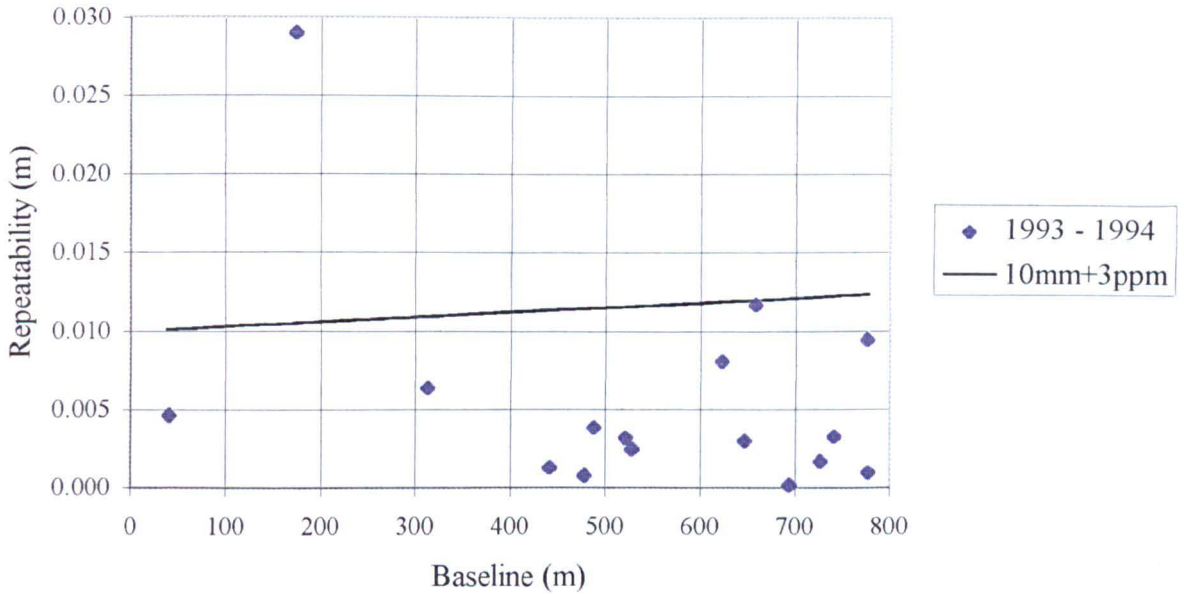


Figure 6-5 Variations in the measurement of lines between survey stations from 1993 to 1994

Figure 6-6 shows the horizontal vector displacements between 1993 and 1994. If the magnitude of the survey station velocities are compared with the line length changes in Figure 6-5, then it is apparent that the magnitudes of the vector displacements are disproportionately large. This is attributable to the method used to transform the EDM data into co-ordinates and therefore the magnitude of change must not be considered significant. There are no coherent block movements of survey station displacement within the network, although it is noted that all the displacements are either NNE or SSW.

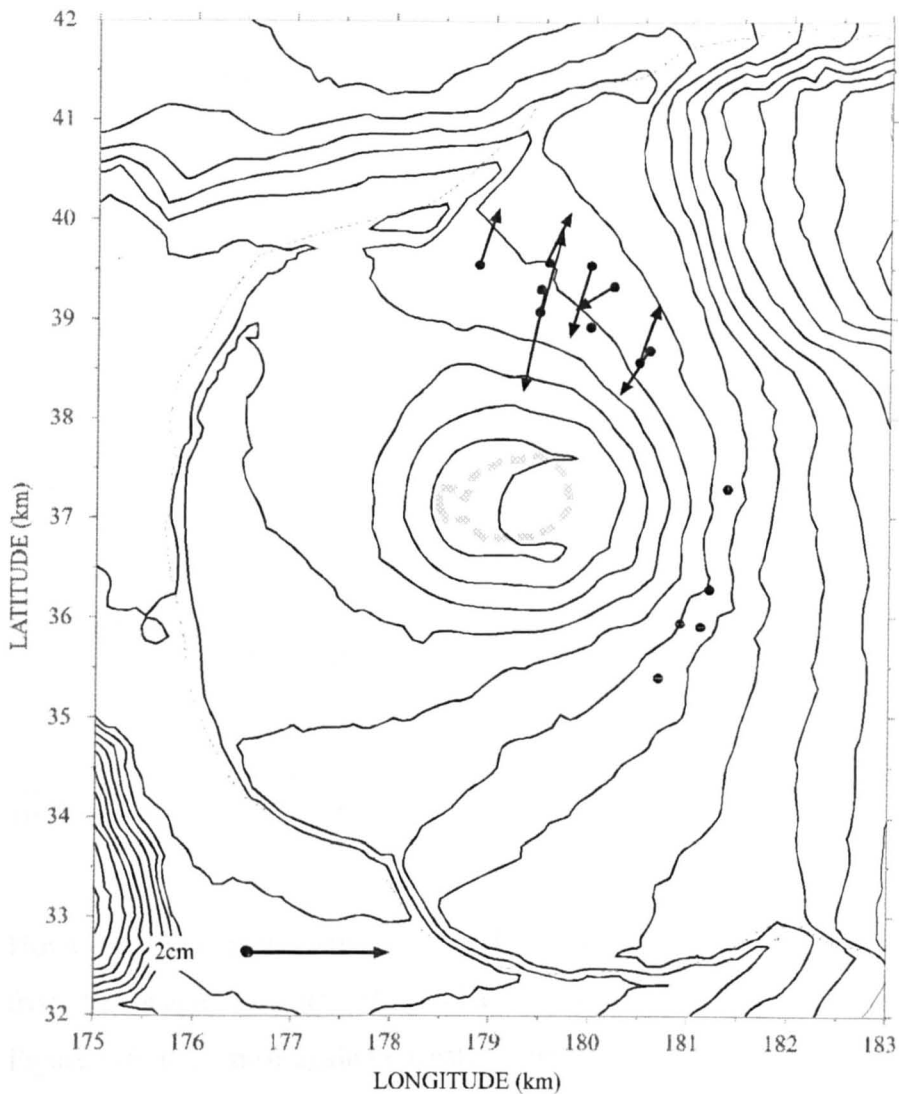


Figure 6-6 Vector displacements from 1993 to 1994 (for key and station numbers see Figure 6-3).

6.6.2 1994 to 1995; line length and vector changes.

The line lengths measured in 1995 verify a problem with survey station 2M25. Four of the EDM readings in the survey indicated a line length extension of 4-6m, as all of these readings were to a 2M25 it is not thought that the deformation relates to a shallow intrusion. No other survey stations appear to be displaced and it is assumed that the nail or the lava on which the nail is situated has become unsteady. As a result this survey station was removed from the network. The data-

set without these outliers indicates the true spread of the data, three lines exceed the estimate of equipment and user error illustrated in Figure 6-7 as sigma or $10\text{mm}+3\text{ppm}$. These fall just above the line and represent only very small changes.

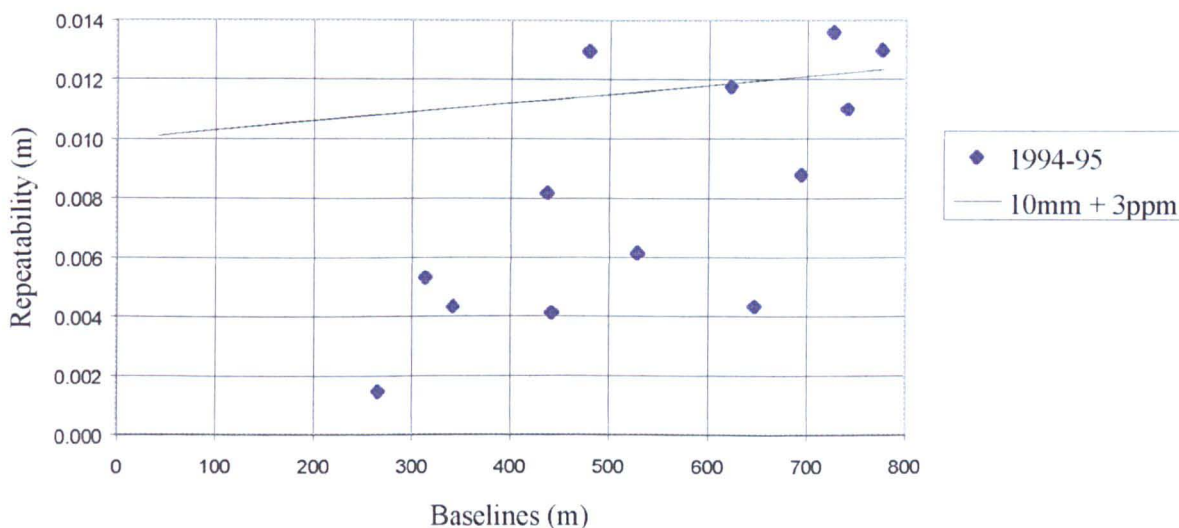


Figure 6-7 The different measurement of lines between survey stations from 1994 to 1995 (excluding 2M25).

However, the changes are very small and no tangible conclusion can be drawn from this single data-set. The horizontal vector displacements are illustrated in Figure 6-8, they must again be treated with caution due to the errors added by the EDM to co-ordinate transformation. They do not show any significant deformation. Some of the deformation patterns are however similar to those recorded between 1993 to 1994. This is probably a reflection of the shared 1994 data-set rather than any significant phenomena. If however, the patterns do reflect real changes then they are too small to be magmatic and may be due to unstable the shelly pahoehoe which covers this whole area.

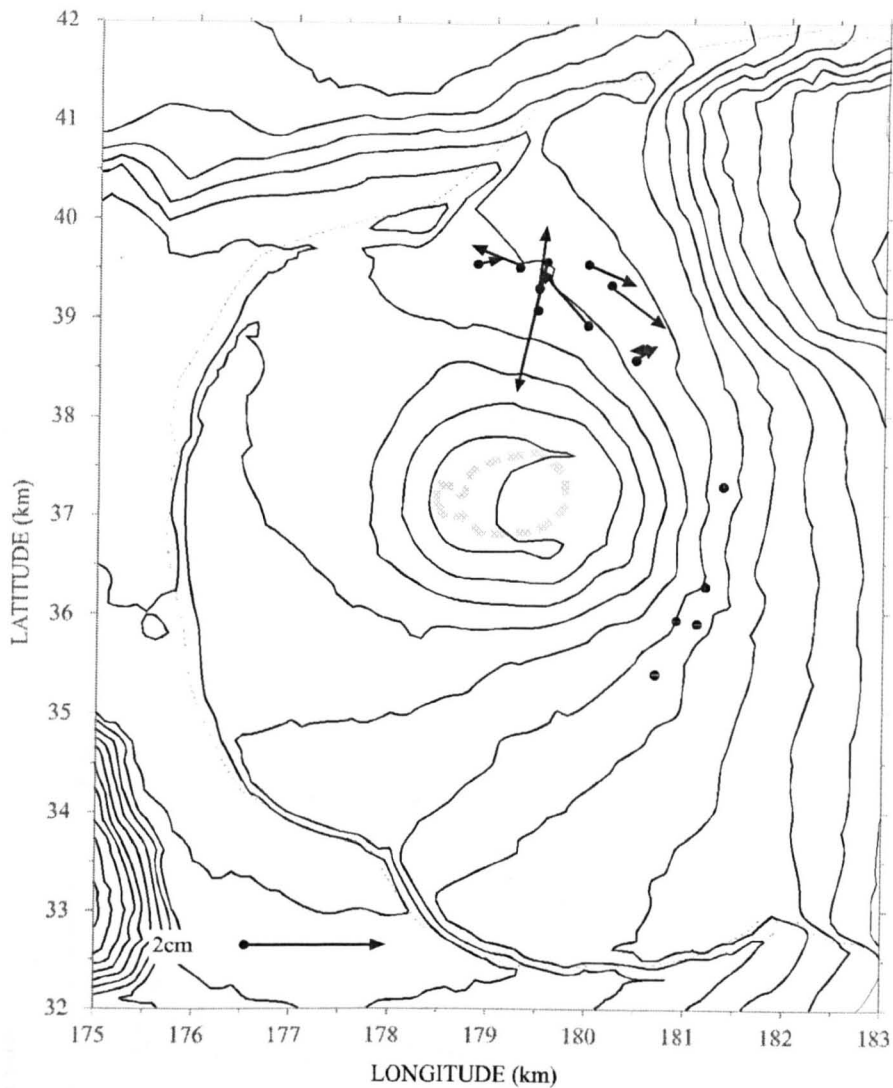


Figure 6-8 Vector displacements from 1994 to 1995 (for key and station numbers see Figure 6-3).

6.6.3 1993 to 1995; EDM vs. GPS & total vector displacement within the study

In 1995, the introduction of the GPS technique facilitated a comparison between the accuracy of the two techniques. On first observation the two measurement sets show much lower changes than the annual changes on Etna (Section 5.10) during its inter-eruptive period, this comparison will be examined further in Chapter Eight. After the processing of GPS data in 1995, the set of co-ordinates obtained in WGS84 was transformed into grid co-ordinates. These grid co-ordinates were

then used to translate the EDM line lengths and vertical angles into grid coordinates using AG3D (Ruegg & Bougault 1982) (see Section 3.2).

The horizontal vector displacements are illustrated in Figure 6-9. Changes do appear to be substantial but due to the very minor changes in line length they are not considered significant but rather a reflection of the transition from EDM to GPS. One of the lines from the SE Network shows extension through out the period from 1993 to 1995 and although this is not considered significant the changes have been noted and continuation of the patterns during any future measurements will be recorded.

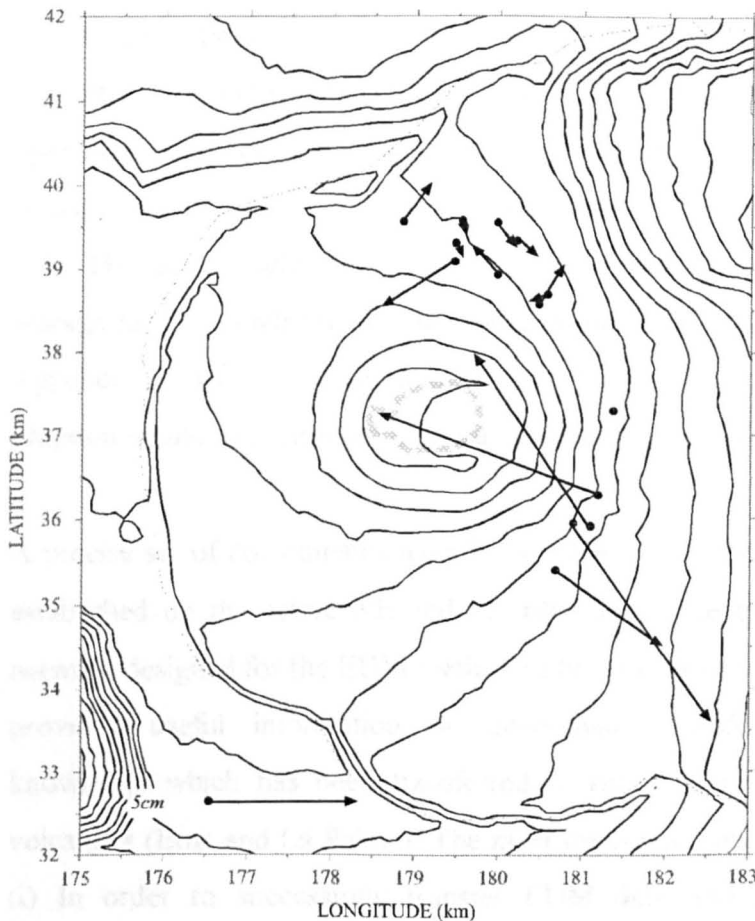


Figure 6-9 Vector displacements between 1993-1995 (for key and station numbers see Figure 6-3).

The vector changes do not show any coherent groupings of adjacent survey stations which could indicate significant deformation. There is also no eastward

velocity of the survey stations that would have indicated a continuous eastward movement over the eastern flank. There was also no extension of fractures or fissures within the rift-zones over this period, although this may be due to the highly fractured shallow pahoehoe surface.

6.7 Discussion of results

To summarise, the results indicate that there has been no significant deformation during the period 1993-5. It is thus proposed that rift-related displacements are either (i) too small to be recorded during the time period, (ii) absent during the inter-eruptive period, or (iii) absent during this particular inter-eruptive period. The inactivity confirms the lack of a permanent shallow magma reservoir or an open system. In contrast the open system at Etna produces a much higher level of background deformation (this will be discussed further in Chapter Eight, Section 8.3). The lack of deformation also negates the possibility of a shallow rift-zone storage facility, similar to the one beneath the rift-zones of Kilauea, Hawaii (see Appendix I). The solidification and compaction of such a reservoir after the last eruption would have resulted in more significant ground deformation.

A precise set of co-ordinates have been collected for the two geodetic networks established on the active NE and SE rift zones. The experience of adapting a network designed for the EDM method to be monitored with the GPS method has provided useful information on co-ordinate transformation and provided knowledge which has been transferred to rift zone networks on other active volcanoes (Etna and La Palma). The most important methodological findings are: (i) In order to successfully transfer EDM data into grid co-ordinates both horizontal and vertical angles are required. (ii) a large dense network of survey stations over a very unstable area permits the loss of a few survey stations due to both the fragility of the terrain and eruptions. (iii) very compact networks however can be totally destroyed by eruptions, sufficient survey stations should be located beyond the study area in order to constrain any such destructive events. Although

the data collected did not indicate any significant ground deformation is has nevertheless produced an inter-eruptive data set.

6.8 The ground deformation results of the March 1998 eruption

The March 1998 eruption was briefly described in Section 6.3. The eruption was preceded by measurable ground tilt around the summit craters, although the GPS survey stations were only measured after the eruption had stopped. The results are illustrated in Figure 6-10. The survey stations that show 42 and 34 centimetres of horizontal displacement are the remains of the Rift-Zone GPS network (stations 2M26 and 1M30 see Figure 6-3). Data reveal that there is a definite eastward displacement of measured survey stations, the largest movements are nearest to the fissure openings.

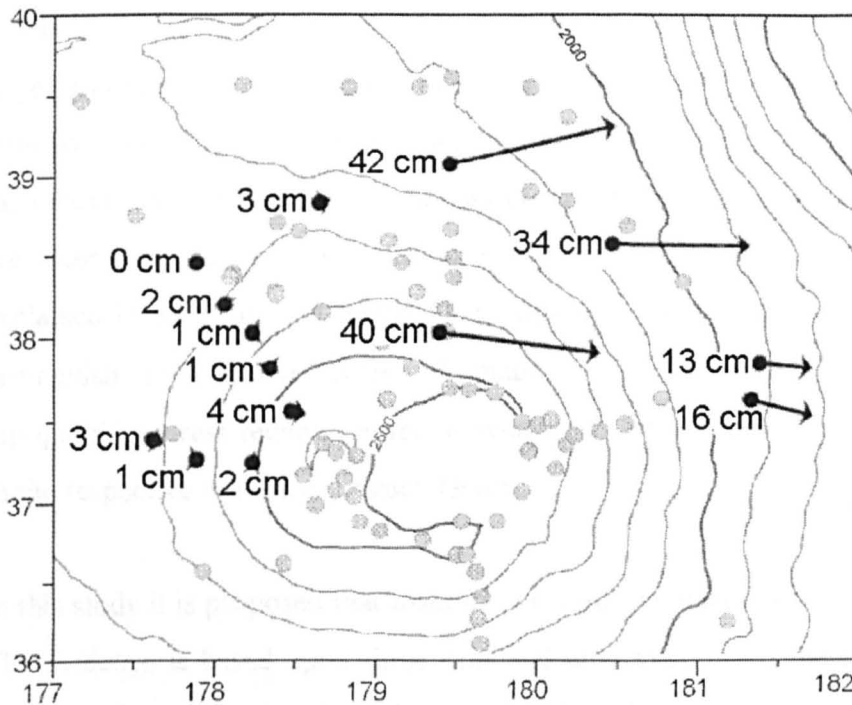


Figure 6-10 Horizontal ground deformation vectors (GPS) from the March 1998 eruption of Piton de la Fournaise, the filled circles represent (EDM & GPS) survey stations (from Staudacher, 1998). For the location of the eruption see Figure 6-2 and for the survey stations refer to Figure 6-3.

The survey stations to the west of the fissure to not appear to be influenced by the eruption. This data provides strong evidence for co-eruptive eastward

displacement. The stations further from the site reveal less deformation, this may be due to the accommodation of strain within shallow fractures. The data should be compared with measurements of the coastal stations in order to examine the extent of the easterly displacements.

6.9 Implications of the ground deformation data to edifice instability.

The relatively long inter-eruptive period from 1993-1996 permits the author to speculate on the current stability of the ridge and to assess the role of gravitational stresses on the eastern flank without the influence of magmatic stresses. The eruption in 1998 provides data to test the hypothesis developed for the mobile eastern flank.

Before the present state of stability can be determined, the evidence of past instability needs to be clarified, (this was examined in detail in Section 6.4). The huge landslide deposits suggest that past collapses have occurred in an E-SE direction from Piton de la Fournaise; this is verified by the huge landslide scar of the Grand Brûlé. The two main factors contributing to the instability of the area are *magmatic* and *gravitational stresses*. The mechanics of these forces is explained in detail in the Chapter One. Although it is a highly subjective task to distinguish the relative roles of magmatic, gravitational and local (e.g. topographic) stress regimes, eruptive events and inter-eruptive periods give clues to the respective influences of each factor.

In this study it is proposed that *instability is strongly linked to magmatic activity*. The evidence is based upon three principal observations; (i) there is no distinct ground deformation, geophysical or geochemical changes nor significant seismicity during the inter-eruptive periods, (only just before the 1996 intrusive event and the 1998 eruptive event); (ii) immediately before the August 1985, November 1986 and February 1988 eruptions, deep seismicity was recorded beneath the eastern flank, (separate from the shallow summit swarms) (Hirn, *pers com*; Delorme *et al.*, 1989); (iii) eastward displacement (in the form of *en echelon*

fracturing and survey station displacement) occurs during eruptions but not the inter-eruptive periods. All this evidence will be discussed and evaluated in more detail.

Most of the activity (eruptive and seismic) occurs in the eastern part of the l'Enclos Fouqué predominately in the NE and SE rift-zones. Although the rift-zones of Piton de la Fournaise are not topographically distinct ridges, they are easily identifiable by numerous cinder cones and recent lava flows. The lack of a distinct ridge topography suggests that the dykes do not propagate along the rifts due to the ridge morphology (as it is not very well defined). Therefore other factors must be important. There is extensive ground cracking on the east side of the l'Enclos Fouqué, especially within the SE rift-zone, the source of this ground cracking may be wholly or in part due to gravitational sliding. The ground deformation data revealed no significant displacement of these cracks during the inter-eruptive period.

Summit eruptions are a result of the ascent of magma into the shallow storage area and the summit craters, the excess magma pressure can then cause the propagation of a dyke into the flank. However, there must be a set of conditions which induce the dykes to be propagated into the NE and SE Rift-Zones. Some of the possible reasons behind this were examined in Section 1.3. For Piton de la Fournaise, whether the intrusion of magma forces the propagation of magma into the flank or if the transport is facilitated by the eastward sliding of the eastern flank, needs to be ascertained. The ascent of magma into the summit area causes seismicity at depth beneath the flank, (notably in the Plaine des Osmondes) this indicates brittle failure at depth due to gravitational strain or forceful magma ascent. However, if the only force effecting the magma was magmatic stresses then the fissures would open with no right or left lateral slip. The fissures associated with the last eruptions (1984-6, 1997-8) on Piton de la Fournaise have been either *en echelon* (E-W extension) or exhibit lateral slip indicating eastward movement of the sector between the rift-zones. This suggests a combination of magma and gravitational stresses.

If deformation occurs before the actual eruption of magma, then the forces affecting the stability occur as a result of the magma at depth rather than mechanical displacement at the surface. Deep influences of magma are most likely be due to increasing pore fluid pressures reducing the cohesion of the flank. However, there is little deformation recorded before the intrusive event, but such measurements are rarely taken immediately prior to the eruption or intrusion. Further interpretation of the evidence found in recent literature strongly confirms that the gravitational stresses are very influential (but apparently only in combination with magmatic stresses) and it is these stresses which pre-determine the propagation of the dykes rather than the magma-related stresses at the dyke tips.

In conclusion, a simplistic conceptual model of the stress regime is derived from the limited available data. The eruption fissures propagate into the weakest part of the edifice, the rift-zones. During inter-eruptive intervals there is no rift-related movements or gravity sliding, suggesting that during this time the minimum compressive stress is vertical. However this switches to horizontal during the ascent of magma into the shallow storage area, reducing the rock strength within the rift-zones, thus facilitating the propagation of fissures along the rift-zones. The less buttressed flank on the top of the soft Piton des Neiges sediments accommodates the stresses through the formation of *en echelon* faults facilitating eastward displacement.

A more complex model involves the concept of a subsurface wedge. The magmatic trigger may have a mechanical impact on a wedge into the eastern flank. In Hawaii, Clague and Denlinger (1994) have developed a model which suggests that an olivine *mush* develops at the base of the magma reservoir, and slides due the force of gravity down the slope of the edifice base (on that case on the underlying flank of Mauna Loa) causing wedge effect which precipitates flank mobility. A similar model was also suggested by Clague and Denlinger (1994) to apply for Piton de la Fournaise, Rousset *et al.* (1989) located dunite beneath the Grand Brûlé which may form part of the olivine wedge. This argument suggests

that eruptive flank fissures form due to the impact of deep magma intrusion on a wedge (comprised of the olivine mush) which pushes the flank eastward thus opening the rift-zones facilitating the shallow propagation of magma.

6.10 Summary

The Rift-Zone Networks were successfully established to an accuracy of 10-20mm (although part of the NE Network was destroyed during the latest eruption). The results indicate that there was no significant inter-eruptive deformation and that the flank is stable during the 1993-1996 inter-eruptive period. In answer to the question asked at the start of the chapter (p174), the hypothesis that the magmatic stresses control the stability of the eastern flank is accepted although the EW extensional stresses (maybe caused by the sliding unbuttressed flank) are also thought to play some part, but as yet undetermined. This hypothesis was conveniently tested by the 1998 eruption during which eastward dislocation was observed through; (i) lateral displacement of GPS survey stations in the order of 10-40cm (measured by the Piton de la Fournaise Observatory) and (ii) by the formation of an echelon fissures in the NE Rift-Zone. The study concludes that the edifice of Piton de la Fournaise is only stable during inter-eruptive periods and that given the unresolved relationships between shallow morphology, magma-related stresses and pore fluid pressures it can not be confidently stated that the flank will remain stable during the future emplacement of magma.

7. LA PALMA

Cumbre Vieja volcano on La Palma is less active than both Mt. Etna and Piton de la Fournaise having had only two eruptions this century. There are however, common geological concepts to be addressed, such as evidence of past landslides, the persistent intrusion of dykes into a rift-zone and eruptions of predominately basaltic products. During the 1949 eruption a major fault developed at the apex of the rift-zone ridge, it was displaced by four metres and is interpreted to form the headwall of a slump four kilometres long. It may be the initial stage in broadscale flank failure and the stability of the ridge in relation to eruptive activity needs to be ascertained. Monitoring ground deformation at La Palma is particularly important since any reactivation of this fault will be identified by changes in the ground surface spanning and in the area adjacent to the fault. The site-related question listed in Section 1.2 asks; *Is the steep-sided rift-zone of the Cumbre Vieja volcano on La Palma stable during the current inter-eruptive period, and what is the likely outcome of a fresh dyke emplacement?* These questions will be addressed through the establishment and monitoring of a new ground deformation network. The installation of this network was completed in two parts; a small network was established over the surface traces of the 1949 fault, and later this was expanded to cover the whole of the southern part of the island. The results of this chapter have been presented at conferences and public meetings, and submitted for publication¹.

¹Moss J. L. (1997) Using GPS to monitor the Cumbre Vieja volcano. *La Palma Astronomical Observatory Seminar Series*, Santa Cruz de la Palma. April 1997. Public meeting.

Moss J. L. (1997) Ground deformation monitoring of the Cumbre Vieja Volcano, Canary Islands. *Abstract volume, Proceedings of the International workshop on Immature Oceanic Island Volcanoes.*

Moss J. L. McGuire W. J., Page D. (1998) Ground deformation monitoring of a potential landslide at La Palma, Canary islands. 1998 submitted to *Journal of Volcanological and Geothermal Research* July 1998.

McGuire W. J. & Moss J. L. (1997) Monitoring active volcanoes. *Abstract volume, Proceedings of the Internat. workshop on Immature Oceanic Island Volcanoes, Sept.*

7.1 Introduction

The Canary Islands are located above a hotspot on the Atlantic oceanic plate close to the African continental plate. The sediment series suggests that the oldest island Fuerteventura is approximately 20-30Ma B.P. (Carracedo *et al.*, 1997a). The formation of the Canarian archipelago by an asthenospheric plume has been argued by numerous authors (Anguita & Hernán, 1975; Férand *et al.*, 1986; Carracedo, 1996). The models broadly agree that Canarian hotspot is the locus for an ascending mantle plume; the convected material spreads out under the plate raising temperatures and causing crustal uplift. Initial hotspot volcanism extended along the NE margin of the continental plate to form Fuerteventura and Lanzarote; the slow eastward movement of the oceanic plate over the hotspot then proceeded to produce the sequence of seven islands, see Figure 7-1. Carracedo *et al* (1997a) traced the path of the hotspot through the activity of each island to reveal that periods of activity on one island coincides with a period of inactivity on an adjacent island (for example the exchange of activity between La Palma and El Hierro). This is thought to be a result of the accommodation of stresses within a limited area due to the ascent of magma.

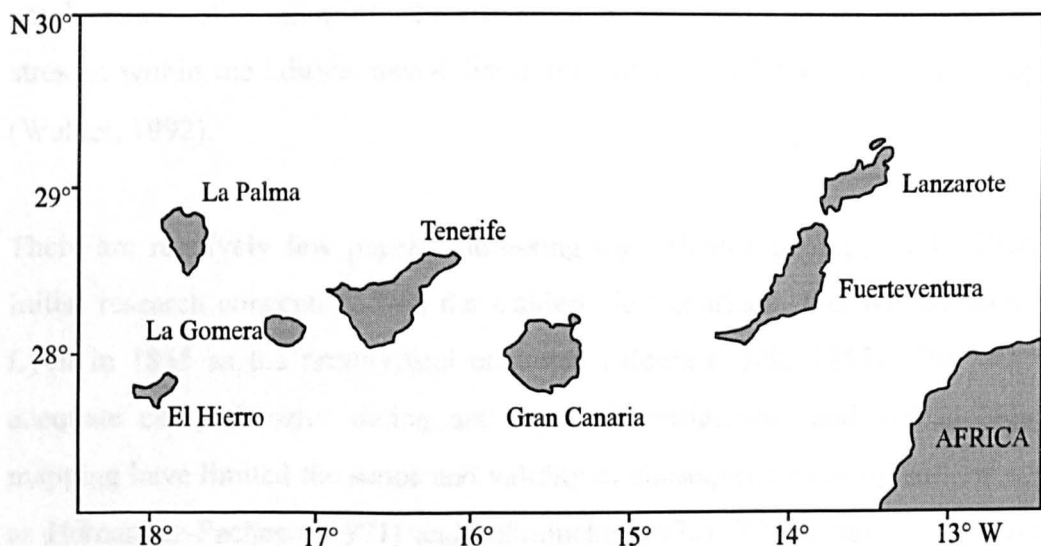


Figure 7-1 Location map of the Canary Islands in the Atlantic ocean, 200km west of Africa.

The volcanoes evolve in a pattern similar to one recognised in Hawaii (Walker, 1990), which is characterised by shield growth followed by a period of inactivity and subsequent strong erosion succeeded by a further post-erosional stage of activity, labelled the *gap stage* (Carracedo *et al.* 1997a). The islands can be divided into two groups according to age and activity. The first group includes Lanzarote, Fuerteventura and Gran Canaria which are all older than 12ma and currently in the rejuvenated stage of volcanism and La Gomera which is in the gap stage. The second group includes Tenerife, La Palma and El Hierro, they are all younger than 7.5ma and are in the initial shield-building stage (Carracedo *et al.*, 1997a)..

There is evidence of persistent flank collapse in the Canary Islands; Tenerife, El Hierro, La Palma and Gran Canaria have all undergone flank collapses. This is evident by the huge off-shore deposits of blocky volcanic debris and the wide depressions on the islands caused by the displacement of material (Holcomb & Searle, 1991; Carracedo 1994; Masson *et al.*, 1997; Schmincke *et al.*, 1997). Tenerife and El Hierro have well defined rift-zones at the head of large amphitheatre shaped depressions facing the off-shore deposits. Persistent emplacement of magma into the rift-zones is thought to adjust the balance of stresses within the edifice, destabilising the unbuttressed flank causing collapse (Walker, 1992).

There are relatively few papers addressing the volcanic geology of La Palma. Initial research concentrated on the Caldera de Taburiente this was defined by Lyell in 1855 as the prototypical erosional caldera (Lyell, 1855). The lack of adequate comprehensive dating and detailed stratigraphic and volcanological mapping have limited the scope and validity of subsequent work by authors such as Hernandez-Pacheco (1971) and Schmincke (1976). The review of La Palma geology below, concentrates on recent papers which use accurate dating techniques and relate to detailed mapping and interpretation of the geology of the island. Many of the findings of these studies were presented at the International Workshop in Immature Oceanic Islands, La Palma 1997.

7.2 The geology of La Palma

La Palma is the second youngest of the Canary islands (28°N 17°W) and is situated at the western end of the archipelago. It measures 45km by 30km wide and consists of three subaerial volcanoes: Taburiente-Cumbre Nueva, Bejenado and Cumbre Vieja (Figure 7-2). The highest point on the island at 2426m is the top of the Taburiente volcano, and the highest point on the Cumbre Vieja is at Deseada (1979m). La Palma is located on 160Ma oceanic crust south-west of a transform fault located at 29°N 19°W (Guillou *et al.*, 1997).

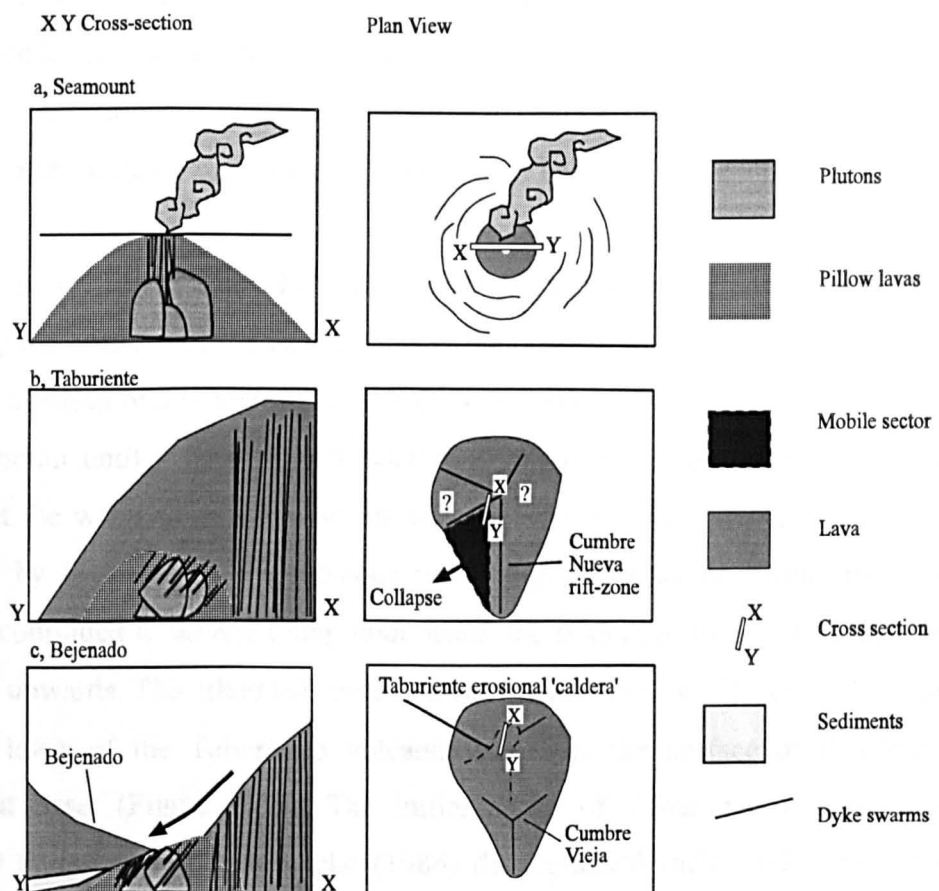


Figure 7-2 Sketch to illustrate the evolution of the island of La Palma, after Staudigel and Schmincke (1984); Carracedo *et al.* (1997c) & Ancochea *et al.* (1994).

This is the closest regional tectonic fault to the island and there is no evidence that it affects the volcanology or stability of the island. The island comprises two

principal geological units: (i) the submarine and plutonic basement complex, and (ii) the overlying subaerial lavas. The submarine series is exposed in the Caldera de Taburiente, tilted 50° on an azimuth of 230° radial to the eroded centre. The plutonic base of the seamount series is exposed in the centre and the pillow lavas are exposed at the edge of the eroded centre of Taburiente, suggesting that the intruded magma uplifted the seamount, see Figure 7-2b. The Taburiente volcano was subsequently formed on top of this tilted substrate.

Watts and Masson (1995) measured up to 2500m of subsidence on Tenerife by looking at submarine canyons which were formed subaerially. This phenomenon is not seen in La Palma where mapping beach shoreface deposits and ancient tuff rings shows that there has been no vertical change in the location of these deposits, indicating no uplift or subsidence on La Palma (*Day pers com*).

The recent work by Staudigel & Schmincke (1984) and Carracedo *et al.* (1994) outlining the creation of the island concurs that growth of the island commenced with the creation of a seamount. The eruption of pillow lavas fed by dykes raised the seamount until it breached the surface of the ocean (see Figure 7-2a). The action of the water caused intense erosion of lavas and generated volcanoclastic deposits by hydrovolcanic explosions producing a distinct unconformity. The magma continued to ascend rising underneath the seamount forcing it to tilt and be lifted upwards. This tilted substrate is incised with swarms of feeder dykes that fed the lavas of the Taburiente volcano that layer the surface of this tilted seamount base. (Figure 7-2b). The initial shape of Taburiente is unknown, however Staudigel and Schmincke (1984) distinguished radial dykes and two clusters of dykes that could be rift-zones, oriented N63°E and N06°E. Carracedo *et al.* (1997) contests this, suggesting a possible triple rift system oriented NS, NW and NE (see Figure 7-2b). Ancochea *et al.* (1994) found four possible collapse deposits around the volcano suggesting that the volcano developed through a combination of growth and collapse phases. This concept of growth and collapse is backed up by recent offshore surveys which have found ten potential landslide deposits around the island (Masson *pers com*), although older

layers may be buried beneath the visible deposits. The volcano underwent a reorganisation of the stress regime favouring dyke emplacement in the north-south rift, the Cumbre Nueva (there is no clear indication for the reasons for this). The preferential, persistent intrusion of dykes into the rift continued until the west flank of the Cumbre Nueva ridge catastrophically collapsed (in approximately $566\pm 5\text{ka}$, (Guillou *et al.*, 1997)). The landslide collapsed along a strike-slip fault. The northern boundary of which is located within the Barranco de Las Angustias (above the present level of exposure) (Figure 7-2b). The collapse involved an estimated volume of $180\text{-}200\text{km}^3$ (Wijbrans *et al.*, 1997; Carracedo *et al.*, 1997). Activity then migrated to the base of the now collapsed Cumbre Nueva ridge, forming the Bejenado volcano. It is not known how long the edifice was active but could have been any time between the collapse of the Cumbre Nueva ($566\pm 5\text{ka}$) and the growth of the Cumbre Vieja ($125\pm 3\text{ka}$) (Guillou *et al.*, 1997) (see Figure 7-2c). However, there may have been a period of quiescence (after the Bejenado activity) before the growth of the currently active Cumbre Vieja volcano on the southern flank of Taburiente (Figure 7-2c).

7.3 The Cumbre Vieja Volcano

The Cumbre Vieja has a current sub-aerial area of 220km^2 and an estimated volume of 125km^3 (Carracedo *et al.*, 1997d). The volcano grew on the side of a ridge formed by the collapse of the Taburiente-Cumbre Nueva rift-zone about 125ka B.P. Until the youthful-looking cones located on the Bejenado are dated, the time lapse between the demise of the Bejenado and the growth of the Cumbre Vieja will remain unclear. Cumbre Vieja is argued to have originally developed as a triple-rift volcano with rift-zones trending NE, NW and N-S. They are identified from cone distribution (Carracedo *et al.*, 1994) and the morphology of elongate vent systems and dykes (Day *et al.*, 1997); although counter arguments protest that there is no overall triple rift pattern (Stüdigel *pers. com*). There is no evidence for a central crater complex or a central conduit feeder system.

Intense eruptive activity occurred between 125 and 80ka BP and was followed by a quieter erosional period between 80 and 20ka BP, this erosional period is identified in the coastal stratigraphy (Carracedo *et al.* 1997c). From 20ka to 7ka BP activity re-commenced along all three rifts. It is speculated that around this time a reorganisation of the plumbing system occurred, which led to the abandonment of the NE and NW rifts and the subsequent preferential and persistent utilisation of the N-S rift, possible mechanisms that may have caused this are examined in Section 7.10. This N-S rift has developed through successive eruptions to form a steep sided, high aspect, topographic ridge with slopes of 16-20°, development of the single rift-zone ridge increased the gravitational loading and slope gradient of the Cumbre Vieja volcano. Reorganisation of the rift system was interpreted by Carracedo and co-workers (Carracedo *et al.*, (1997c) to be due to the stress regime generated along the topographic ridge (Fiske & Jackson, 1972; McGuire & Pullen, 1989). Carracedo *et al.* (1997c) reaffirmed the N-S orientation of the principal stress by the alignment of the feeder dykes beneath elongated cones on the rift, this model follows the assumption that the dykes propagate perpendicular to the minimum compressive stress.

The ridge is made up of lavas and pyroclasts, the lavas are alkaline basalts, basanites, trachybasalts and tephrites, these are incised by a number of Phonolite domes. Evidence, derived from the historic eruptions examined below, suggests that the steep western flank of the volcano has developed a number of faults and therefore may be unstable and liable to collapse.

7.4 The historical activity of the Cumbre Vieja volcano

There have been six recorded eruptions since 1500AD noted in historical documents, and two others that are suspected to have occurred in sub-historical time, see Figure 7-3. The eruptions of 1585, 1712 and 1949 are characteristically similar, involving the opening of west-north-west (WNW) trending arrays of right stepping, east-west trending *en echelon* fissures on the western flank. The departure from the north-south trend to the E-W orientation of the *en echelon*

patterns is argued by Day (*pers com*) to be due to the reorientation of ascending NW-SE rift dykes to the principal N-S trend. Day (*pers com*) speculates that the triple rift pattern is still dominant below the 6-10km deep reservoir system (identified by Kluegel *et al.*, 1997) but is separated from the shallow surface by a detachment fault. Day's model appears to assume that the dominant N-S trend is a function of a shallow stress regime probably caused by the topography of the edifice.

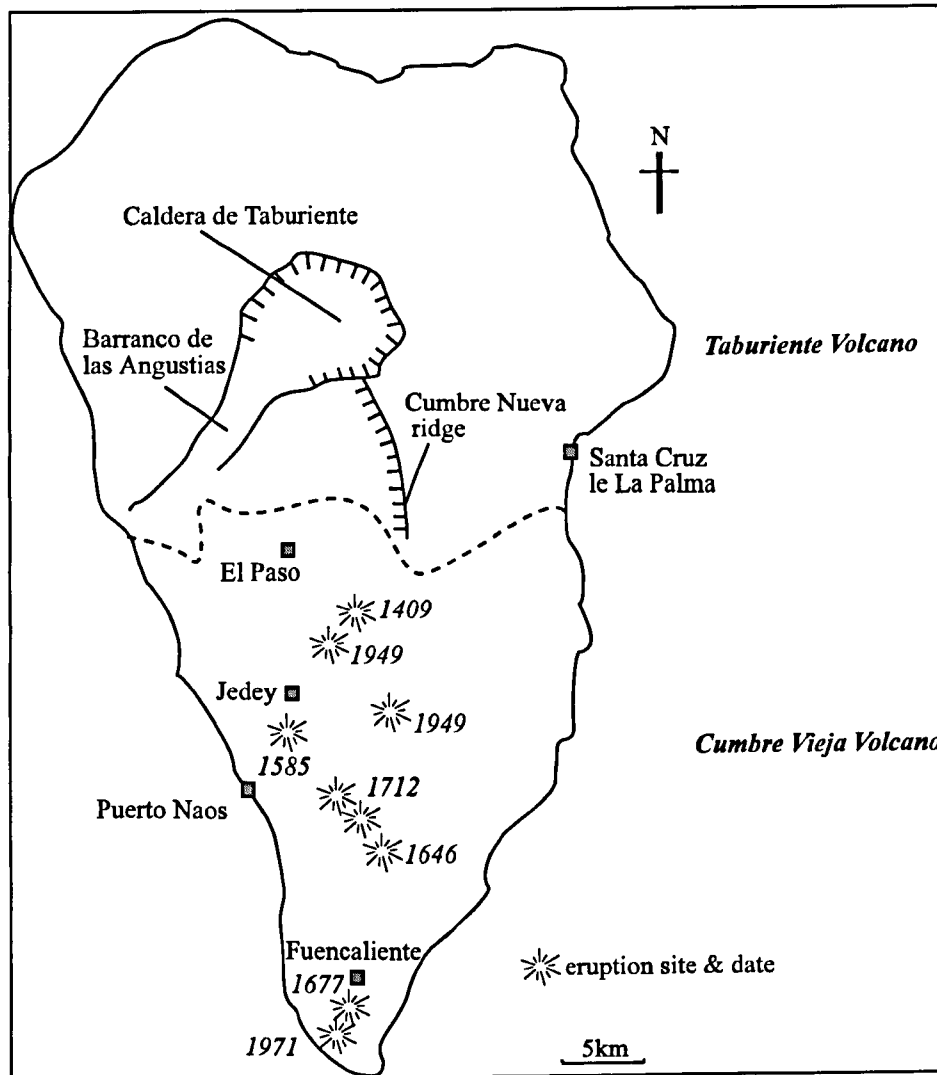


Figure 7-3 A simplified sketchmap of the historic eruption sites

Another interpretation could be that changes in the gravitational stress regime of the edifice caused the re-organisation of the rift-zones, however, the volume of exposed cones in the NE and NE Rift-Zones suggests that there has not been enough lava produced from eruptions to increase gravitational stresses. If there

had been a large amount of erupted material then this may have increased the gravitational loading of the edifice, changing the local stress regime by aligning the maximum compressive stress to the vertical. This interpretation establishes that in the absence of major topographic changes, another factor must have modified the stress regime, and in light of the available evidence Day's model is accepted.

The 1949 eruption began on the apex of the ridge and is thought to have instigated an aborted slump of a section of the western flank of Cumbre Vieja along the detachment fault proposed by Carracedo *et al.* (1997b). The eruption was preceded by felt seismicity which may have started as early as thirteen years before (Klugel *et al.*, 1997), intensifying during the final three months immediately prior to the eruption. This is contested by Day (*pers com*) whose interpretation of original documentation (Martin San Gil, 1960) indicated that there were just two discrete seismic events in 1936 and 1939 and that these were probably attributable to non-eruptive dyke emplacement. If believed however, the seismicity noted by Klugel *et al.* (1997) prior to the eruption in 1949 indicates that there was either magma ascent and/or deep fracturing occurring for up to 13 years prior to the eruption. Klugel *et al.* (1997) interpret this to be the ascent of xenolith rich magma into the 7-11km storage area just above the Moho (situated at around 13-15km depth in the Canary Islands (Mangas *et al.*, 1997)). Ironically, the second interpretation of the precursive seismicity by Day (*pers com*) that there were just two discrete episodes of seismicity strongly confirms the proposal of Klugel and co-workers that there has been no constant replenishment of the shallow magma reservoir with fresh magma, because xenoliths of varied contact times are not observed.

The 1949 eruption began on June 24th and lasted until July 6th, with the primary eruption site (Duraznero) located on the crest of the Cumbre Vieja ridge at an altitude of about 1800m (Figure 7-4). The initial eruption produced predominately lithic breccias and juvenile spatter (Day *et al.* 1997). From July 1st to July 2nd a surface rupture emerged oriented at 345° adjacent to the eruption

site, this was not accompanied by any changes in activity. On July 8th a 600m *en echelon* fissure system opened at San Juan, 2.5km to the north-west of Duraznero, producing scoria, lapilli and aa flows. The fissure collapsed but continued to produce lava flows which eventually entered the sea forming a lava delta. The Duraznero and San Juan eruptions (up to the time of the fissure collapse) emitted products interpreted to be from the same source (Day *et al.*, 1997), however, the later part of the San Juan eruption and a subsequent reactivation at Duraznero produced a second chemically-different set of products (Day *et al.*, 1997). In the middle of July there was a phreatic eruption at the Hoya Negro that produced explosive material indicating that this eruptive phase was due to cooling heat source. The second phase at Duraznero began on July 30th forming an elongate north-south fissure (of a different orientation to the surface rupture), the effusion rate was high forming fire fountains and lava flows.

The timing of the eruption and the switching of eruption sites represents the interruption of the magma feeding system during its course. This is verified by the two distinct types of magma from the early and late stages of the eruption. Activity commenced with a dyke fed eruption at Duraznero, during this phase a fault opened adjacent to the site, however, it did not display any features such as escaping gases or heat that would have connected it to the continuing activity. Eruption then ceased at this site to restart two days after at San Juan 2.5km away. One interpretation is that the development of the detachment surface into a fault that breached the ground surface disconnected the magma supply at depth so that the activity lasted for only a few more days. The ascending magma was thus forced to seek a new least-effort path to the surface through the Western Flank and the fissure system at San Juan collapsed as the magma supply withdrew. The new pulse of magma (the second batch) could not follow the same route to the surface via San Juan as the fault now became 'fixed' and the original least-effort route to the surface prevailed, thus returning activity to Duraznero.

A few weeks before the start of the 1971 eruption seismicity was felt over the southern part of the island, the initial eruption site was located in the south of the

island along the N-S rift-zone. The eruption produced numerous scoria and spatter cones and basaltic lava flows, these flows were directed eastwards and southwards by the topography of the flank creating significant lava platforms. No surface fault ruptures were recorded, Carracedo *et al.* (1997c) suggested from this that, low ridge eruptions are unlikely to cause slumping along the detachment surface. Kluegel *et al.* (1997) assessed the ascent of magma into the Cumbre Vieja volcano through the analysis of xenolith fragments. Xenoliths collected at the eruption site had a magma contact time that indicated that they had been stored within a sill prior to the 1949 eruption, a new resurgence of magma into the storage area would have emitted the stored magma during the latter eruption. The fragments indicated that the xenoliths has been exposed to either magma or an olivine mush for a long time; with temperature and pressure constraints indicating that the contact lasted from years to decades at a depth of between 7 and 11km. Klügel and co-workers argue that magma ascended in many stages carrying peridotite xenoliths to a shallow reservoir of dykes and sills.

Hansteen *et al.* (1997) has suggested, due to the nature of the xenoliths at La Palma that shallow mush zones as opposed to the deep ones proposed for Hawaii (Denlinger, 1996) and Piton de la Fournaise (Rousset *et al.*, 1989) make up part of the magma reservoir. The intense seismicity experienced three months prior to the eruption could indicate propagation of shallow dykes from the storage area towards the surface. From the xenolith settling rates the calculated transfer time for peridotites from the shallow reservoir to the surface is very rapid; around 2-4 days. During the eruption the sills are depleted and the xenoliths from the bottom of the reservoir are erupted during the end of the eruption. Hansteen *et al.* (1997) analysed individual xenoliths to infer the pressure ranges experienced during formation in order to estimate the depth. Two distinct ranges were found: 100Mpa and 200-350Mpa, these depths related to storage around the Moho and at shallower levels of 7-11km concurring with Klügel *et al.* (1997).

7.5 The objectives of the baseline ground deformation network

The steep gradient and high-aspect-ratio of the Cumbre Vieja ridge coupled with the prospect of future magma intrusion suggests that large-scale sector failure, as seen earlier in the history of La Palma and at other Canary Islands, could be instigated by the evolution and collapse of this volcanic ridge. The potentially unstable sector is around 20km long and up to 10km wide. The northern boundary of the potential slip zone is located in the vicinity of the San Juan fissures and the Jedey vents, where in 1949 *en echelon* fissures opened perpendicular to the N-S alignment of the rift. These fissure eruptions were fed by dykes trending 90° from the N-S trend. The southern boundary is at the tip of the island where further dykes were re-oriented 40° from the principal N-S trend to feed the 1677 eruption and also in the vicinity of the latest eruption in 1971 (Day *pers com*). The 1949 eruption at the summit of the ridge, generated normal faults along north-south fissures parallel to the rift-zone, which are downthrown to the west with displacements of up to four metres. Future dyke intrusion could cause further westward displacement, culminating in piecemeal or wholesale failure of the western flank of the ridge. The island of La Palma does not have, at the time of writing, any real-time continuous monitoring. In recent years a single seismometer has been used to record background seismicity, however, due to persistent vandalism and technical problems this has not been continuous. From the limited data set collected and the perceptions of the islanders it can be confidently stated that there has been no significant seismic events since the last eruption in 1971. Jiménez *et al.*, (1994) completed a GPS survey, installing benchmarks in the southern part of the island to constrain their microgravity results, these however are not thought to have been re-occupied. Unfortunately the benchmarks they installed are tribrach-specific and are not compatible with currently used apparatus.

The arcuate normal faults indicate that the area of potential collapse is a broadly curving sector. The deformation analysis aims to determine if the 1949 fault is stable or undergoing aseismic fault creep. The existence of creep would allow the

definition of the distal boundaries of the fault and to determine if the creep is localised to the 1949 fault or if it is uniform over the whole of the unstable sector. A ground deformation network was set up to detect precursory tumescence and surface faulting as well as broadscale uplift or subsidence. Installation of a ground deformation network compliments the seismometer to provide the initial stage of baseline monitoring of the island.

The establishment of the ground deformation monitoring program facilitated analysis of the stability of the ridge, ascertaining the level of inter-eruptive ground deformation that occurred on the island between 1994 and 1998. In the event of a future intrusion of magma or the dislocation of the western flank the deviation from the background levels can be accurately assessed. During future eruptions (if the island has not collapsed) each dyke emplacement event within the network would be measured, the dyke dimensions determined, and the movement during the events analysed and interpreted. Deformation of the whole island can also record the current rates of either uplift or subsidence. Researchers working on the island (McGuire *pers com*; Klügel *pers com*, 1997) speculate that large scale uplift over the whole island could occur prior to an eruption.

The network was established in two stages: firstly an initial small network covering active faults and secondly the expansion to form a broad-scale network encompassing the southern part of the island below the Caldera de Taburiente. The project was conducted in these two stages due to the unavailability of Global Positioning System (GPS) hardware at the start of the project and the requirement of a minimum of three occupations over the fissured area of the ridge to assess the activity of the faults.

7.5.1 Stage One: The ridge network

In October 1994 a baseline ground deformation network was established in the central area of the Cumbre Vieja ridge affected by the 1949 faulting, in order to

assess if aseismic creep was occurring during the current inter-eruptive period. If creep continues between eruptive events then failure could not necessarily be linked to magmatic activity and the stability of the western flank could be determined by other topographic and gravitational factors, such as over-steepened slopes and water saturation. This would have a major implication for the hazard evaluation of the island as failure could occur during inter-eruptive events. The stations were established along the crest of the ridge on elevated cones to allow for clear line of sight between stations.

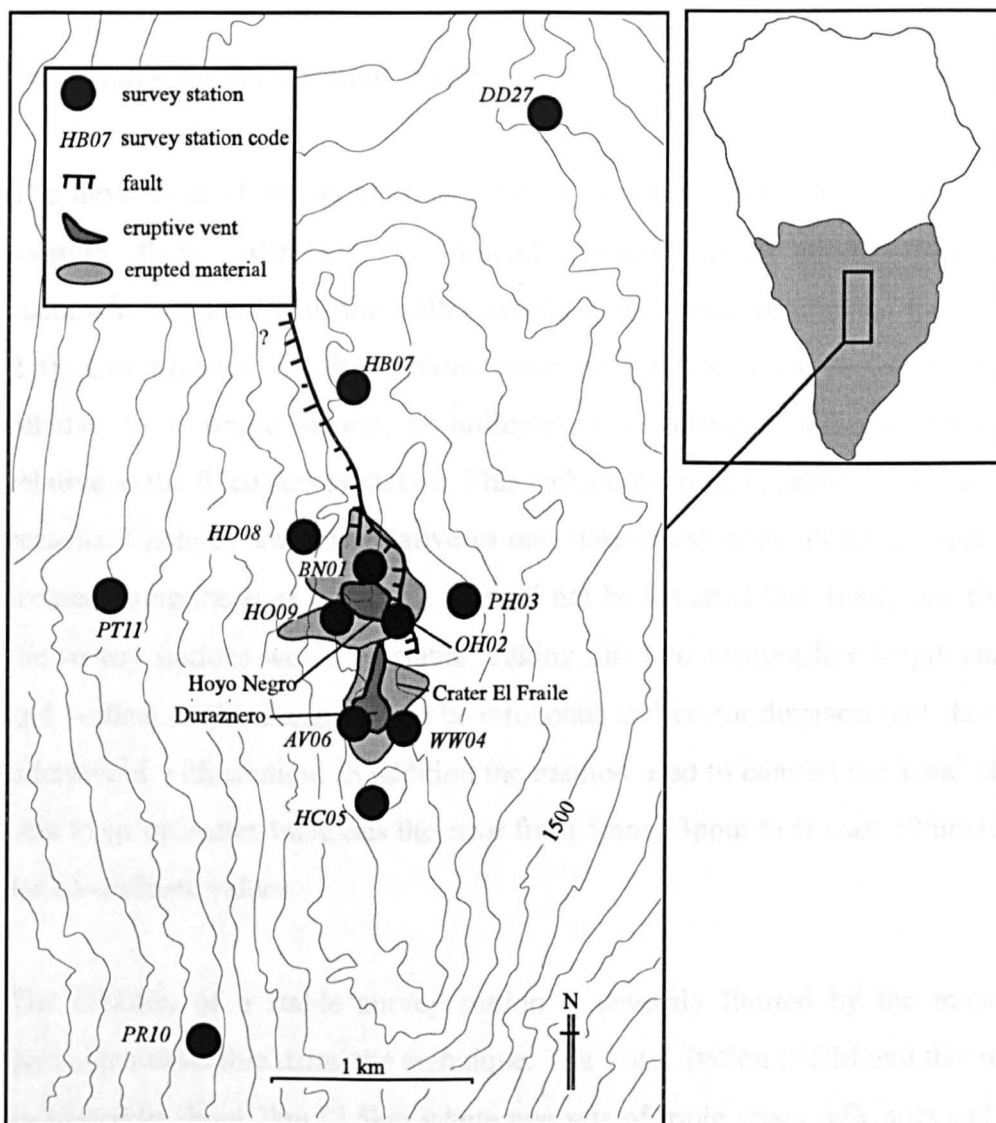


Figure 7-4 The ridge network established in 1994 showing the proximity to the features of the 1949 eruption. (Source Carracedo *et al.* 1997d)

The array of stations forms a well-braced network with 22 measurable vectors, comprising 11 benchmarks and incorporating 2 Spanish triangulation pillars. During the first set of measurements, a Total Station incorporating Electronic Distance Measurement (EDM) and a theodolite was used to measure the slope distance and vertical angle between survey stations.

The field application of this method is accurate to $5\text{mm} \pm 5\text{ppm}$, see Section 2.4. Figure 7.4 shows the nine ridge survey stations on the network (pr10 and pt11 are 2.5km off the ridge to the west, illustrated in Figure 7-5).

Transition from Total Station to GPS

The next stage of the monitoring program sought to monitor the whole of the western flank. Although the baseline ground deformation network was successfully established, the EDM technique has many limitations (see Section 2.4). Co-ordinates for the stations were devised on a contracted framework relative to a single station, co-ordinate vector changes indicate movements relative to the fixed survey station. This technique proved unsatisfactory for many reasons. Changes are only relative to one station and since all the stations were located along the apex of the rift it could not be assumed that at any one time all the survey stations would be stable. Taking this into account line length changes and vertical angle changes could be erroneous and vector displacement should be interpreted with caution. In addition the method used to convert the Total Station data to co-ordinates increases the error from $5\text{mm} \pm 3\text{ppm}$ to at least $10\text{mm} \pm 3\text{ppm}$ for co-ordinate values.

The location of a stable survey station is severely limited by the maximum distance measurable using the technique. The Total Station (EDM and theodolite) is limited to about 2km (2.5km where two sets of triple prism reflectors and fully charged batteries are used). There are no clear stable line-of-sight locations to install survey stations off the ridge, the distances are too great and the line of sight is restricted by numerous trees. The area is also limited due to the weather.

Although the average temperature is around 20°C, the island is affected (especially between November and March) by strong winds which develop into storms on the top of the ridge. Even gentle north-easterly winds form low clouds over the ridge, providing a problem with visibility prohibiting the use of the Total Station as the signals are blocked. Another major problem is the size of the potentially unstable western flank. To cover this area using EDM would be logistically unacceptable in terms of the number of survey stations needed and the time it would take to occupy the sites.

Due to these factors another technique was sought which is not limited by line-of-sight, distance and the weather. Due to the successful transition to using the Global Positioning System on Etna (Chapter 5) Piton de la Fournaise (Chapter 6), this technique was applied on La Palma. This enabled forward planning of survey station sites and since the weather ceased to provide a problem in obscuring line-of-sight daily occupation plans could be devised.

7.5.2 Stage Two: The Western Flank Network

The baseline network encompasses the whole western flank of the Cumbre Vieja ridge providing tight clusters of survey stations around the northern and southern boundaries and at the apex where the 1949 fault is situated see Figure 7-5. Preliminary positioning of the survey stations was completed using the geological map (Carracedo *et al.*, 1997d), a road map and consultation with Simon Day. The network is divided into three levels of application, firstly a broad network of survey pillars measurable accurate only to 10mm. Pillars provide an accessible rapid assessment of the flank, location from the nearest road requires brief station descriptions and this network can be measured in one day. Occupation of the pillar survey stations should be conducted annually to determine if the island is undergoing any broadscale inflation or deflation. The group comprises three pillars, one located within the flank at Jedey (je13), and two located at the top of

the ridge at Nambroque (ph03) and El Duraznero (hc05), the co-ordinates are known to (estimated) 10mm. The next group of survey stations is the main flank network, comprising 26 survey stations. The ridge part of the network comprises the nine survey stations spanning the 1949 fault installed in October 1994.

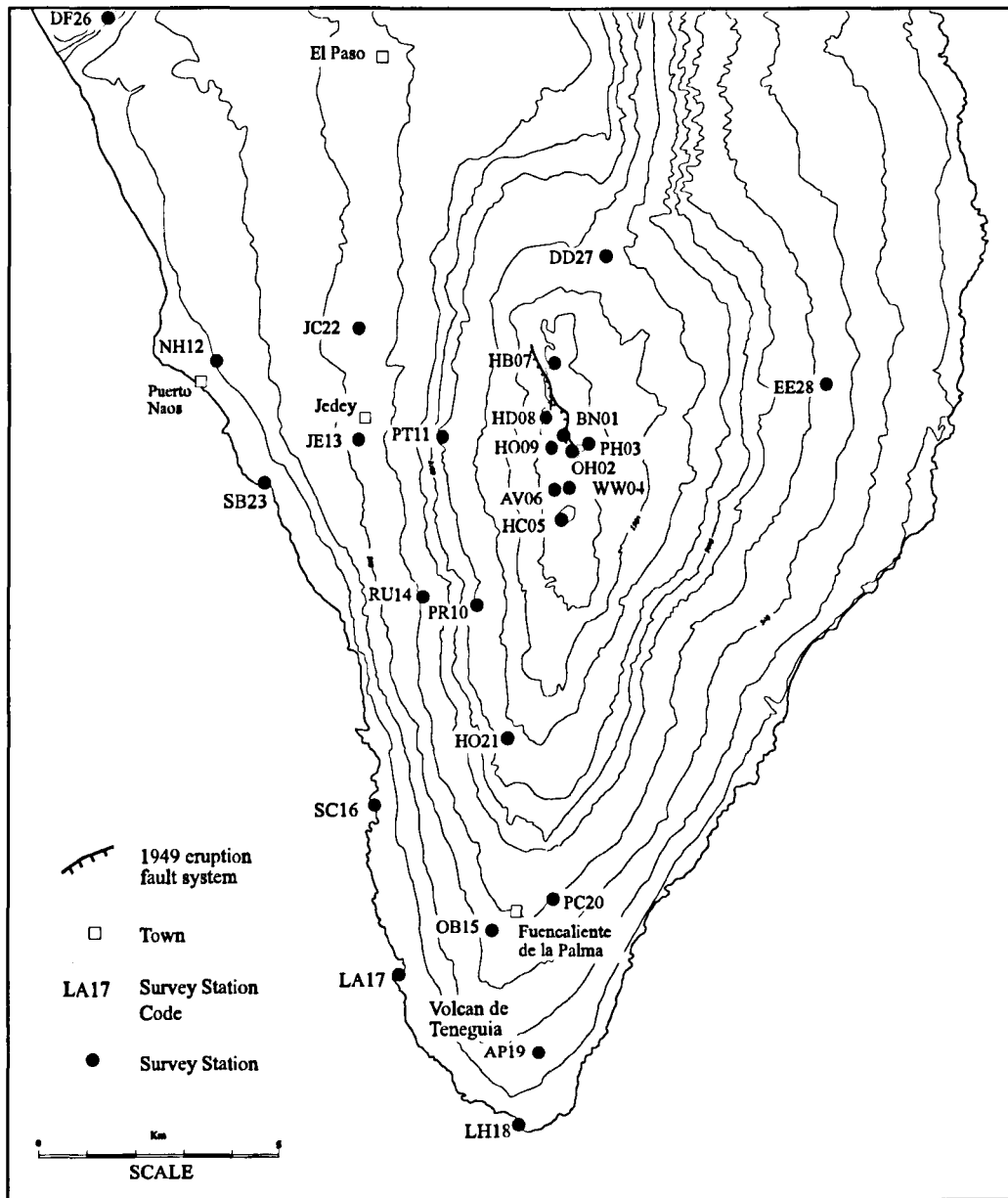


Figure 7-5 The Western Flank Network showing the survey stations and principal towns. (Source Carracedo *et al.* 1997d)

Survey stations situated around the probable southern boundary of the fault are positioned to establish the alignment of the principle stress and to determine if local topographic or underlying influences are causing the least-effort path to be diverted normal to the axis. Three survey stations were established five km apart

spanning the sub-historic lavas situated on the SW coastline of the island. The dense network of stations are positioned to detect rift-related movements and off-rift dyke propagation.

7.6 Measuring the ridge network (using the Total Station and GPS), 1994-97

In 1994 and 1996 the ridge network was occupied using a Total Station. The set-up and measurement was completed within two weeks. In 1994 20 lines of the possible 22 within the network were measured, two lines over 1.9km were omitted as they were obscured by poor weather. In 1996 21 lines were measured, once again the missing measurement was unobtainable due to persistent cloud. Temperature and pressure readings are taken at the end of each line and incorporated into the data processing. In 1997 eight stations were measured in order to compare the EDM measurements with GPS readings taken at the same time.

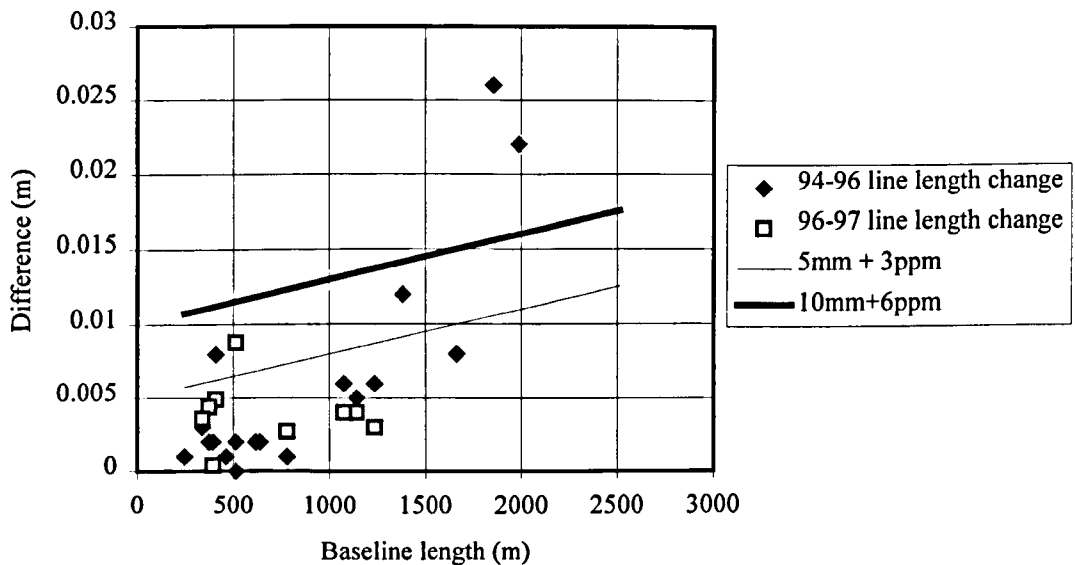


Figure 7-6 The changes in line length plotted against the $5\text{mm} \pm 3\text{ppm}$ error estimate; all the data-sets are obtained using EDM.

The results from the EDM surveys indicate that the baseline distance changes between the survey stations range from 4-10mm; with changes of 8-10mm over

long lines with large height differences and for lines measured to pillars. The estimated error for the EDM method is σ ($5\text{mm} \pm 5\text{ppm}$) for a single survey and 2σ for comparisons between two surveys. Figure 7-6 shows the differences measured between common lines using the total station from October 1994 to March 1997. The data listed in Appendix B.6 shows the line lengths and co-ordinates measured during the program, it can be seen that measuring vertical angles produces a greater error. As these are used to obtain grid co-ordinates to compare temporal vector changes vector comparisons for baselines showing negligible or insignificant changes can be misleading. Comparison over time provides a more accurate picture, when trends manifest in a single comparison remain evident. Figure 7.6 represents the repeatability of measuring a single vector in different surveys. The difference (in baseline length) between one year and the next is plotted against the baseline length. The two vectors above this line indicate either negligible movements or error, these are vectors from station ph03 to stations bn01 and oh02. Station ph03 is a pillar it can be assumed that the errors result from inaccurate set-up (other measurements to this station are below σ).

Figure 7-7 shows the vector movements of the ridge network between October 1994 and March 1996 (for the locations of the survey stations relative to the 1949 fault refer to Figure 7-4) The numbers indicate the EDM station code (to compare with the GPS code see Appendix C). The vectors are generated from the EDM data using a set of reference grid co-ordinates derived in 1997 using GPS. This method of co-ordinate generation adds error ellipses of around 10-15mm. The co-ordinate changes therefore appear larger than expected given the changes in line length, as indicated in Figure 7-6. The vector plot highlights that the magnitude of the displacements is within the error estimate.

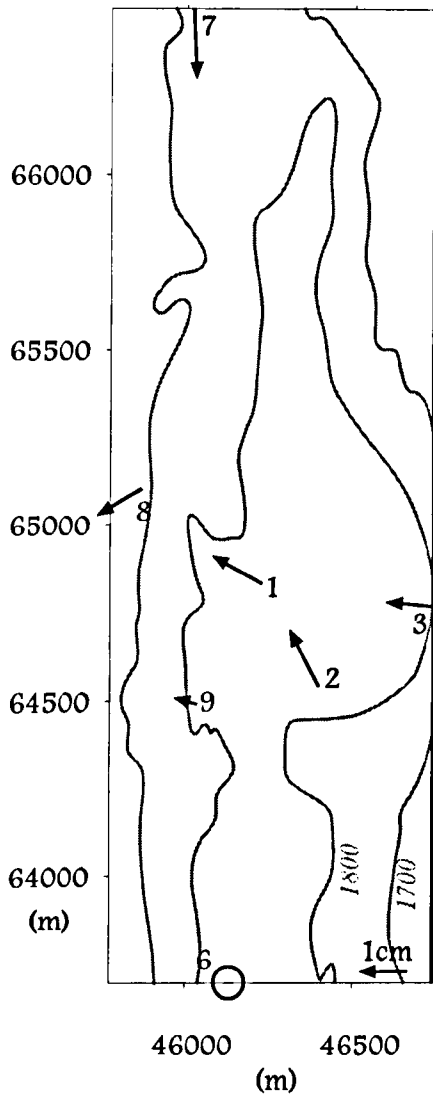


Figure 7-7 Vector changes between 1994 and 1996, with approximate height contours. (Source Carracedo *et al.* 1997d)

Vectors represent co-ordinate changes that are of an insignificant magnitude to represent shallow sub-surface magma movements, the patterns of vector displacement are compared over time to distinguish the coherent displacement of individual or groups of survey stations. Expected displacement values for shallow dyke intrusion are in the magnitude of 500mm and above, and the values for deeper magmatic or tectonic influences are 25mm and above. These values are estimated from the amount of displacement recorded during the 1949 eruption and the background values recorded at Mount Etna when magma is rising in the system (Section 5.10). Aseismic creep is estimated to be between 0.8-1.5mm and can only be detected by analysing data-sets over a number of years (Rasà *et al.*, 1996). However, evidence of such long term movement can also be detected in

the surrounding geomorphology or man-made structures, but this has not been recorded at the Cumbre Vieja.

7.7 The GPS network, 1997

In 1997, the GPS network was measured using the rapid static technique outlined in Section 2.6, with two GPS receivers. A single station was occupied for ten hours to obtain a single point position enabling the station to be used as a fixed reference point. The position was processed using UNIX based GYPSY software. The single point calculation was suggested to be more accurate than linking the network to the fixed station at Maspalomas in Gran Canaria (Blewitt *pers com*). One receiver was positioned at the reference point (nh12) and the other was moved between adjacent survey stations. The distance between the receiver and the rover is limited to 10km, however, once a survey station is occupied by the rover receiver then it becomes capable of being used as the reference. Increasing the number of reference points away from the original single point (nh12), permitted the occupation of the whole network. Survey station ww04 on the ridge was not occupied due to strong winds. Two pillars in the southern part of the island were measured (sa24 & sd25) although they were eventually abandoned as the bases were not very stable. Most of the survey stations were measured at least twice in order to obtain a good co-ordinate and to permit network adjustment. It was not possible to process the data in the field due to limited computer capability, so all the post-processing was completed after the field work.

Post-processing was carried out using GYPSY and PRISM software (ASHTECH™); the processing techniques applied by the software are explained in Section 2.5. The single point position was obtained for nh12 using the UNIX based GYPSY software, this position was kept fixed. The rest of the survey points were processed from this fixed position. During the initial processing run it became apparent that despite long occupation times there was not sufficient data to fix every rover survey station. This was (in a few cases) probably due to tree

canopy above or adjacent to the survey station causing cycle-slips although other observations between the reference and the rover failed without obvious reason. As the most of the survey stations were occupied at least twice very few were totally lost. Co-ordinates were not obtained for stations pt11 and sc16, these will be obtained during the next survey. The southern part of the network had very large errors (~5-cm) so this half was re-processing using a single point position fix (again obtained using GYPSY) for ob15, the southern survey stations processed from this position. The northern and southern parts of the network were network adjusted together using SNAP (ASHTECH™), and the common survey station je13, was held fixed. The adjusted network comprised 39 vectors although the problems fixing the co-ordinates produced a few open-ended baselines since the unfixed baselines were omitted.

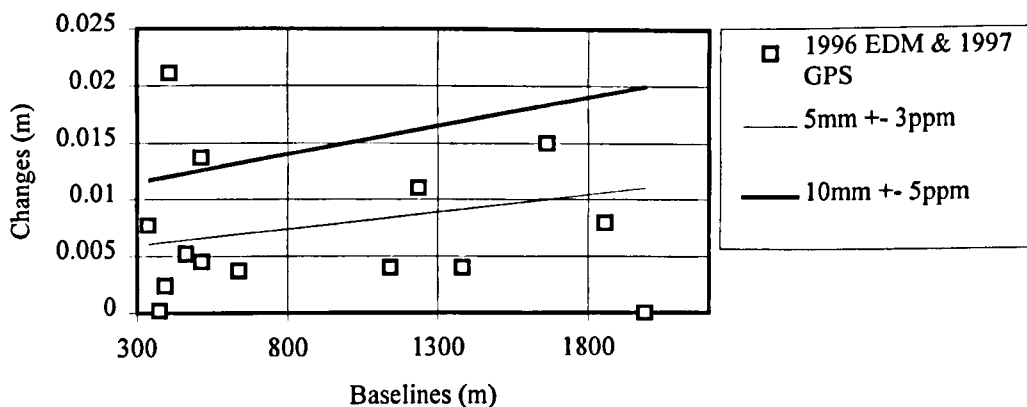


Figure 7-8 Line length differences between 1996 EDM data and 1997 GPS data.

The differences in the two techniques are illustrated in Figure 7-6 and Figure 7-8, this reveals that the data-set combining the two techniques produce a poorer repeatability than when just EDM data-sets are compared. The average horizontal error ellipse for the GPS data are 0.723cm (major) and 0.486cm (minor), the average vertical error ellipse represents a lower accuracy at 1.58cm (major) and 0.533 (minor). The poorer accuracy of vertical positioning is expected when undertaking rapid static GPS. These are only estimates of error but they do confer with Figure 7.9.

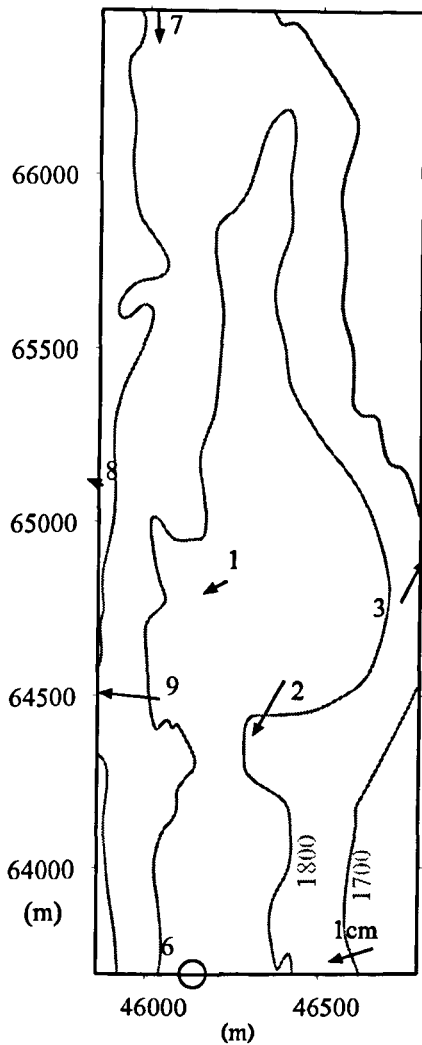


Figure 7-9 The vector differences between 1996 and 1997 with approximate height contours. (Source Carracedo *et al.* 1997d)

The vectors changes between 1996 and 1997 (Figure 7-9) are within the 10-15mm error ellipse for the conversion of EDM data to co-ordinates. The vector changes do not indicate the same co-ordinate pattern observed between 1994 and 1996, but survey stations hd08, bn01, oh02 and ho09 do however show a continued westward displacement. The coherent nature of the co-ordinate velocity does suggests that there is a common mechanism. This will be discussed further in Section 7.8.

Inconsistent displacement of ph03 verifies the westward block displacement of most of the other stations since it is to the east of both the ridge and the 1949 fault. Actual baseline length measurements also adhere to this pattern suggesting that the coherency is not a product of the transformation between EDM data and co-ordinates in 1996. Survey station hb07 has been consistently displaced towards the south, as this survey station is situated on a south-facing slope then the cause of this displacement is most likely slope creep.

7.8 Results and interpretation

The results indicate that there was no measured significant ground deformation on the island between 1994 and 1997. This absence of notable ground deformation at the apex of the ridge suggests that at present this surface

representation of the fault is no longer active. This implies that there is no flank-wide coherent movement along the detachment fault and that there has been no intrusion of magma into the centre of the ridge. The small coherent pattern of movements are at present too small to be confidently considered significant. The most likely causes of this movements are displacement caused by the load of material on the downthrown block. It is too pre-mature to assess the relationship between these movements and the faulted area, if there is no active relationship then the fault must therefore be solely activated by magmatic intrusion causing the detachment fault to breach the surface. At this stage the results must be examined with caution. The vector changes recorded are all within the error ellipses of the data collection and processing techniques.

Nevertheless there are patterns emerging, Figure 7-10 shows that between 1994 and 1997 vector displacement has been consistently from the east to the west for the majority of the stations on the ridge. These changes can not be explained by the nature of the survey station monumentation (the differing aspects of the slopes near which the stations are installed argues against this). If surface creep is causing the coherent displacements then annual re-occupation will indicate the nature and rate of creep of the stations. Fault related displacements (determined by analysing displacements each side of the fault), indicates that survey stations each side of the 1949 are displaced to the west. The uncertain stability of the western flank requires a further occupation of the network, to ascertain if the displacements could be evidence of slow deformation. Further field campaigns are required to constrain the long term deformation patterns.

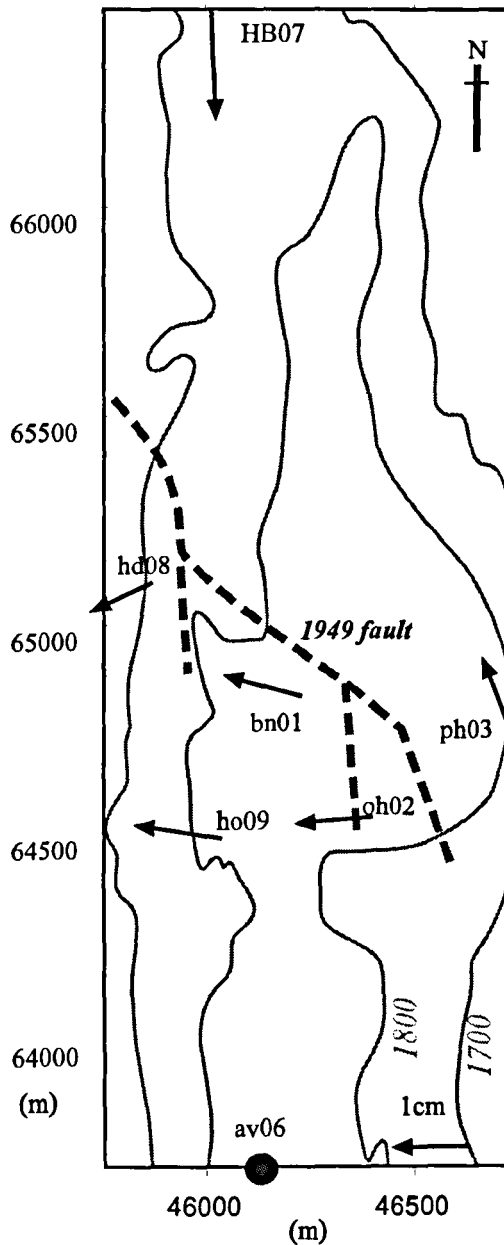


Figure 7-10 Vector changes between 1994 and 1997 showing the position of the 1949 fault. (Source Carracedo *et al.* 1997d)

The results between 1994 and 1997 reveal an interesting pattern of potentially significant coherent data. A further occupation of the network using GPS was required in order to determine if the patterns are maintained. The continued occupation of the network has been funded by the Civil Authorities of The Canary Islands.

7.8.1 Additional data: the 1998 re-occupation

The aim of the 1998 campaign was to re-occupy the whole of the ground deformation network to ascertain the current stability of the western flank and to check for precursory signs of activity. The occupation was undertaken using two dual frequency GPS receivers, these use a combination of code and phase processing to obtain accuracies of $10\text{mm}\pm 2\text{ppm}$.

During the field-processing the known reference was obtained by a static GPS computation from one days occupation. In order to asses if the co-ordinates of the network had changed from 1997 the final results were processed using one station from 1997 as fixed (the co-ordinate is assumed not to have changed). The choice of the fixed survey station was determined by the result which produced the least errors or network adjustment irregularity (nh12). On the first day the stations which were to be used as reference stations within the campaign were occupied and fixed. Due to the time constraints of the survey these key survey stations were only fixed from the single base preventing internal checking using loop misclosures. Accuracy and precision of the technique was instead ascertained using the internal software checks and comparison of the co-ordinates with the previous years data. Data illustrated in Figure 7-11 did not reveal any significant displacements. It could be argued that groups of survey stations display coherent patterns such as jc22, sb23& je13 and la17, ap19 & lh18. These patterns may indicate localised movements although there appears to be no relation between these small movements and the detachment surface. Despite these interesting displacements the results indicate that there are no significant changes over the network. Within the limited time period of the research the surveys will only detect deformation patterns over 5mm due to the accuracy limitations of the methods used. Examination of the western flank over a number of years will determine with a higher degree of certainty that there is no creep. The patterns identified between 1994 and 1997 do not appear to be maintained in the 1998 survey, this suggests that either the westward pattern of displacement did not

reflect real movements suggesting that the pattern was coincidental or that the creep is periodic.

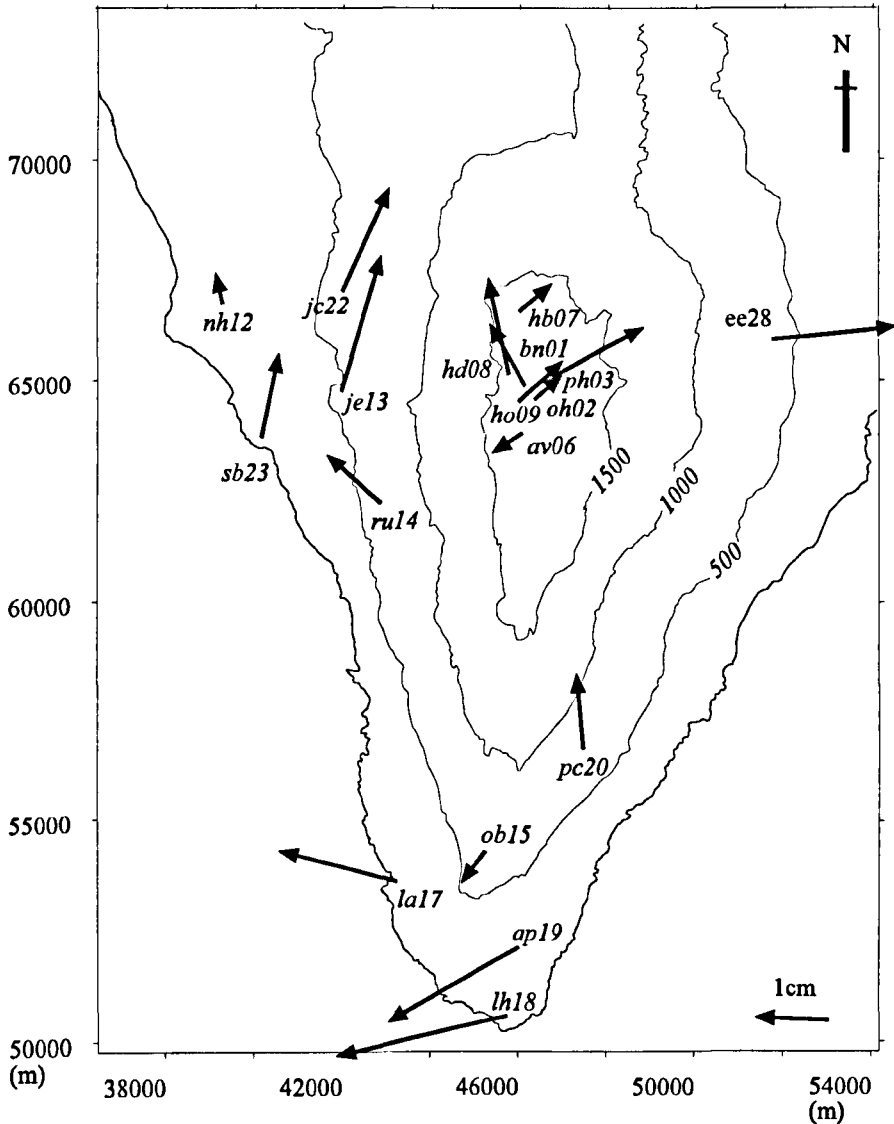


Figure 7-11 Co-ordinate velocity between 1997-8 with an approximate contour outline showing the locations of the survey stations. (Source Carracedo *et al.* 1997d).

In summary, this research can thus conclude that between October 1994 and September 1998, the 1949 fault remained stable and that there was no survey station displacement detected, which could be interpreted as deformation precursory to eruptive activity. The network has, however only been measured twice using the GPS technique any the long term patterns concerning changes in elevation of the survey stations can not be ascertained yet. The recommendation

is to continue to monitor the network periodically in order to maintain the analysis of creep over the network and to examine vertical changes, the constant threat of future activity highlights the importance of the on-going monitoring program.

7.9 Modelling magma intrusion

If the surface deformation had been verified in 1998 then the most likely causes would be surface creep or displacement caused by the load of material on the downthrown block (of the western mobile sector). The results of this research reveal that the fault must therefore be activated by magmatic intrusion. In order to estimate the relationship between the intruding dyke and the edifice; finite element modelling is used. The principles of finite element modelling and the mechanical parameters used in the sequence of tests are examined in Section 3.5. The exact variables applied in the model reflect known workable ratios between the rock strength and magma pressure, this is largely because in the absence of accurate data on the strength and elasticity of the La Palma rocks and sediments. It is understood that this is not ideal but it is unavoidable given the constraints of the both the time available and the software. The geometric model of La Palma is devised from the geological map the cross sections showing dip of the detachment fault were used as a basis of the geometry (Carracedo *et al.*, 1997).

Figure 7-12 shows the basic geometric cross-section model, the Cumbre Vieja is growing on top of the older volcano and on the left (western) side a thin layer of sediments represent the collapse material of the Cumbre Nueva rift. The detachment surface is represented by a arcuate void about 2km long between the sediment layer and the overlying Cumbre Vieja. The mechanical properties of all the models are listed in Table 7-1.

Variable	Cumbre Vieja (N/m ²)	Sediments (N/m ²)	Cumbre Nueva (N/m ²)
Young's Modulus	5.e+10	1.e+8	2.e+10
Poisson's ration	0.25	0.004	0.01
Dyke opening pressure	2.e+8	2.e+8	2.e+8

Table 7-1 Physical parameters for the finite element model illustrated in Figure 7-12

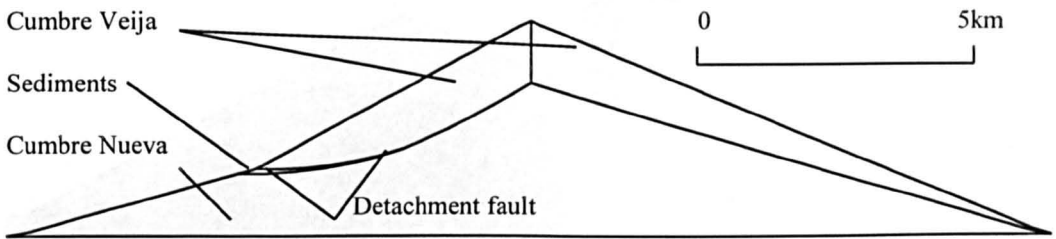


Figure 7-12 The basic geometric model of the southern part of the island of La Palma

The next step was to introduce the propagating dyke into the basic geometric model. Figure 7-13 shows the Mohr stress concentration around the intruding dyke; the higher the value of the Mohr stress the greater the chance of brittle failure. As the dyke propagates a uniform stress field develops but does not as yet reach the surface.

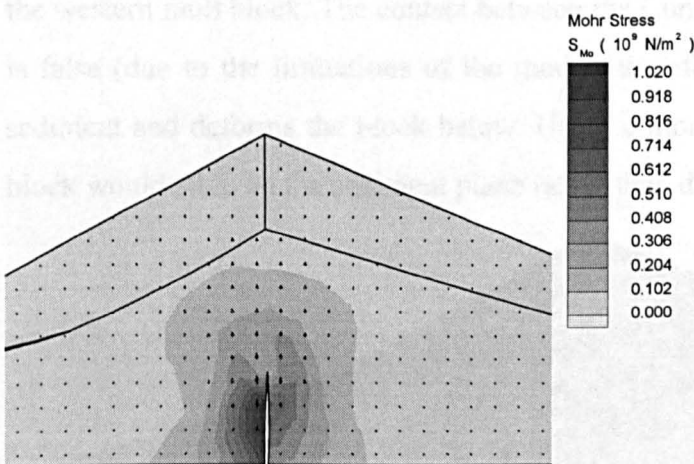


Figure 7-13 The Mohr stress value of the start of the dyke emplacement into the N-S rift-zone.

Figure 7-14 shows the relationship between the stress field and the dyke as it becomes larger nearing the surface; the Mohr stress field indicates the stress

build-up at the top of the detachment fault. At this stage the detachment fault may begin to move, repeated intrusions or storage at depth would increase the likelihood of flank failure.

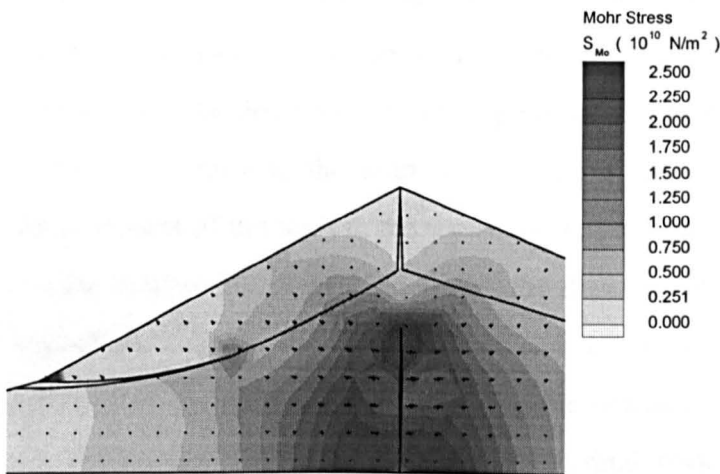


Figure 7-14 The Mohr stress field around the dyke as it propagates towards the surface.

The final stage of dyke emplacement is illustrated in Figure 7-15 (with the darker shades representing the area of greatest displacement). The vectors illustrate the direction of movement. The model is severely limited since only elastic deformation can be modelled but it shows the influence of the intruding dyke on the western fault block. The contact between the Cumbre Vieja and the sediments is false (due to the limitations of the model) therefore the block sinks into the sediment and deforms the block below. Using a more sophisticated software the block would slide on the sediment plane rather than deforming into it.

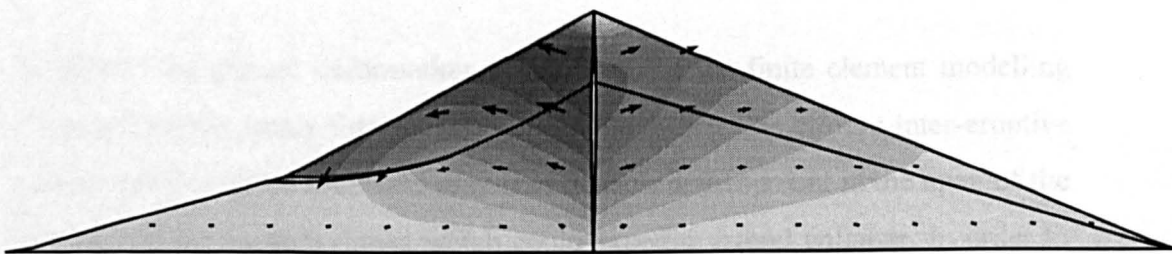


Figure 7-15 The displacement of the edifice due to the dyke reaching the surface.

The depth of sediment layer determines the stability of the overlying block, and the height of the detachment 'void' determines if the stresses dissipate equally between the western and eastern flanks of the edifice. The model showing a high

detachment surface shows little surface deformation as the stresses are halted by the void confirming the observations of Carracedo *et al.* (1997c), who maintained that the propagating dykes were disconnected from influencing stresses at shallow levels. From the modelling it can be concluded that during the early stages of the ascent of a narrow dyke, the central section below the ridge would be the first to be deformed by the magma, which would also induce high pre fluid pressures or activate the fault at the apex of the ridge. This may explain the development of the fault at the top of the ridge during the 1949 eruptive episode. As the narrow dykes were emplaced the detachment fault was affected near the top of the ridge at the first point of contact. As the stresses increase the area effected by the dyke widens increasing the stresses on the flanks of the volcano and begins to effect the lower flanks. In the final model the role of the detachment fault in separating the stress patterns from depth with the shallow surface is illustrated, and explains the re-organisation of the dyke orientation at the surface as proposed earlier by Day. This model argues that the 1949 summit eruptions were fed by very narrow feeder dykes, probably vertical or sub-vertical, the observation that only the upper ridge was effected by faulting is explained by the narrow stress field around the thin feeder system. A more extensive feeder system or shallow storage would have effected the lower regions of the western flank causing a more broadscale activation of the fault.

7.10 A model for the structural evolution of La Palma

Results of the ground deformation monitoring and the finite element modelling discussed above, imply that the island is stable during this current inter-eruptive period and that future eruptions may lead to fault development at the apex of the ridge or on the western flanks which could expedite lateral collapse. In order to understand the role of ground deformation in the stability of the edifice, the theory of the structural evolution of La Palma must be discussed further with respect to the results of the study.

Evolution of volcanism at La Palma has centred on two elements; construction and destruction. Growth and re-organisation of rift-zones have contributed to the construction of the island while erosion and sector collapses have modified the shape of the island through destruction of the developing form. The growth cycle of the Canary Island volcanoes is to a lesser extent repeated throughout the growth of each shield, it is observed by the volcanoes which are in the initial stage of shield building, they develop through a sequence of growth, collapse, erosion with periods of lesser activity. The relationship between these opposing factors controls the nature and operation of volcanism on the island. This section will attempt to construct a model of the island and to argue the ideas of magma transport and storage promoted by Carracedo *et al.*, (1997c).

As previously discussed, the Taburiente volcano developed on a tilted seamount, the associated dykes are either radial or confined to discrete rift-zones, with lava flows dipping away from the centre of Taburiente. This observation suggests that there was a central feeder system. However, a similar old central vent complex Piton des Neiges on Réunion Island (see Section 6.2) has been eroded into Cirques and displays little evidence of a central vent complex. If the Taburiente edifice initially developed radial dykes, then edifice itself must have been a large symmetrical form. This bulk may then have (due to the gravitational stress) formed the triple rift system. Therefore it can be proposed that Taburiente grew as a central vent volcano until gravitational stresses facilitated the formation of rift-zones at either 120° angles on the flanks or in the oblique patterns suggested by Stüdigel & Schminke (1984) and Ancochea *et al.* (1994). The Taburiente volcano originally developed a triple branched rift-system that then switched to preferential persistent dyke emplacement in the N-S rift (the Cumbre Nueva). The Cumbre Vieja rift system also became reorganised favouring the north-south rift similar to the Taburiente suggesting that there could be common influences. There is no evidence for an underlying ridge beneath the Cumbre Nueva, the re-organisation of the rift-zones that occurred forming the Cumbre Nueva rift-zone most likely was a result of a change in sub-surface magma transport and storage

or the gradual construction of a ridge that started a self-perpetuating cycle of growth (Fiske & Jackson, 1972).

The Cumbre Vieja volcano developed on the N-S ridge that resulted from the collapse of the Cumbre Nueva rift. The N-S ridge of the underlying Cumbre Nueva may have prompted the propagation of north-south dykes into the new Cumbre Vieja edifice. However due to the similar re-organisation of the rift-zones in the Taburiente volcano a change in the sub-surface transport and storage of magma may have again occurred. The initial Cumbre Vieja dykes would have facilitated the persistent parallel emplacement of dykes due to two factors; (i) the cooling dykes provide thermally-favourable pathways, and (ii) the weaker walls of the dykes cause the least effort path for propagation (Walker, 1990). This N-S orientation was thus carried through from the old volcano to the new volcano. Bejenado did not develop rift-zones when it grew within the collapse scar although possibly would have, given time to develop, produced rift-zones perpendicular to the slope as seen at Kilauea, Hawaii due to the buttressing effect. This is recorded at many other volcanoes such as at Fogo, where the rift-zones are developed such that the seaward movement of the sector, between the rift-zones, is perpendicular to an underlying collapse scar of the island (Day *in press*); and on Réunion where the younger Piton de la Fournaise grew in an old collapse scar the slopes of Piton des Neiges, facilitating a similar arrangement of rift-zones.

Figure 7-16 illustrates the model of the development of rift-zones through buttressing of an older edifice. The buttressed model depicts the development of rift-zones by illustrating the orientation of the rift-zones on the younger volcano. This indicates that it is improbable that the Cumbre Vieja rift-zones grew as a result of buttressing by Taburiente in the same manner as occurs at Kilauea and Piton de la Fournaise, and that the rift-zone location is unlikely to cause instability. The Cumbre Vieja grew on a pre-existing ridge (See Figure 7-16, single rift), Kilauea and Piton de la Fournaise grew in collapse scars on the flanks of the older volcanoes.

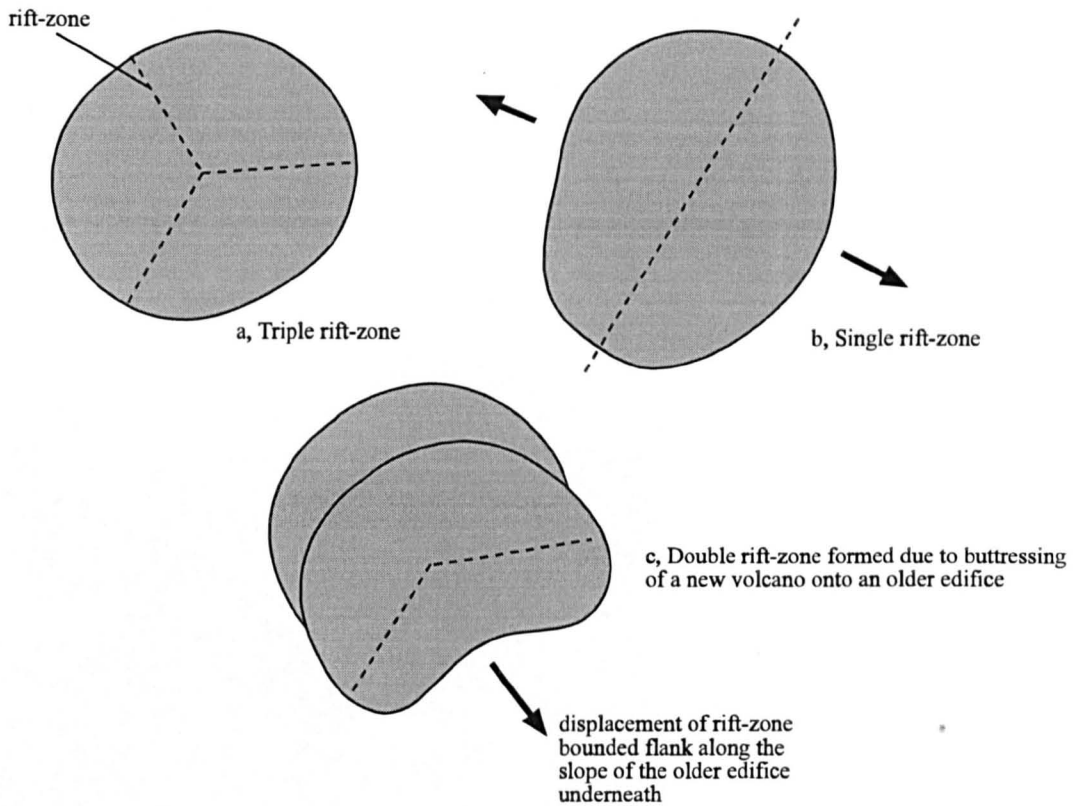


Figure 7-16A sketch combining separate volcanoes onto the same base to show the role of buttressing on the creation of unstable rift-zone-bounded sectors; the grey dashed lines represent the rift-zones.

There is no evidence from the oceanic explorations around the Canary Islands (Holcomb & Searle, 1991) for the existence of any major regional stress trends. There must be a predominant stress regime, such that the horizontal stresses are greater or weaker than the vertical stresses. For the formation of a coherent triple branched rift-zone to grow over time, there must be regional or local stress regime governing the persistent parallel propagation of dykes. In light of this assumption, it is proposed that the maximum compressive stress was vertical during the primary stage of growth (when the triple rift-zone array developed), facilitating the emplacement of dykes in the spreading rift-zones. This is assumed due to two factors: (i) As the edifice grew up the spine of the Cumbre Nueva ridge the resultant buttressing (of the underlying ridge) increased the relative contribution of N-S compressive stresses until the direction of maximum compressive stress became N-S. (ii) The extension of the rift due to persistent N-

S dyke emplacement caused the E-W compressive stress to become less than the N-S compressive stress. This would have caused the system to self-perpetuate as a N-S maximum compressive stress facilitates preferential use of the N-S rift over the N-W and N-E rifts as seen in Figure 7-17.

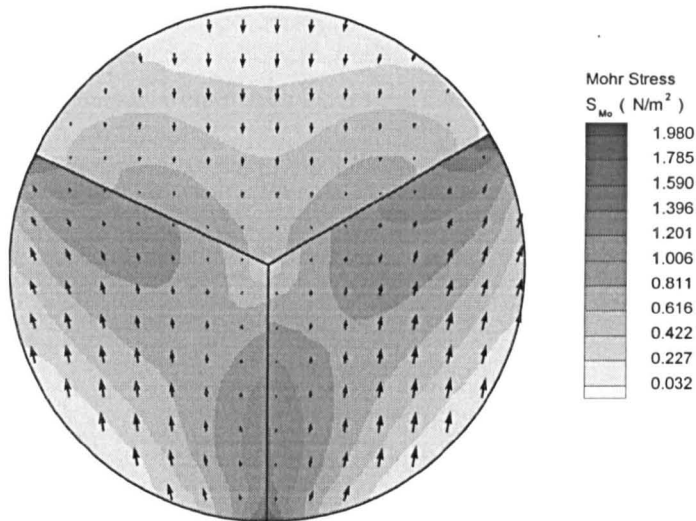


Figure 7-17 The Mohr stress values for a simplistic triple-rift array undergoing N-S compression (where N-S is down the page), the dark areas indicate increased strain and the arrows illustrate the compressive stresses.

Figure 7-17 illustrates the areas most susceptible to brittle failure, the higher the Mohr stress indicated the greater potential for failure suggesting that the most favourable route for magma eruption is N-S. This indicates that a switch in the stress regime (making the maximum compressive stress N-S) would effectively cease activity on the NW and NE rift-zones due to the resultant compression that would form in the shear zones. This would create a *least effort path* for future emplacement at the base of the island, explaining the southward propagation of the fault. This model is founded on the following assumptions, (i) there is an overriding stress regime for a new volcanic edifice, (ii) the feeder dykes are predominately N-S, and (iii) the material underneath the Cumbre Vieja ridge forms a topographic ridge. Although (i) is unknown, recent work agrees that most of the feeder dykes are oriented N-S (Klugel *et al.*, 1997) and that the remains of the Cumbre Nueva ridge form a topographic high beneath the Cumbre Vieja. The current activity of the Cumbre Vieja is on the N-S rift-zone and along the western flank of the ridge (See Section 7.3). The fissures on the western flank reflect the

re-orientation of the NW magma ascent from depth into the N-S trend due to the existence of a detachment fault under the western flank of the edifice. At present the predominant measured orientation of dykes in the rift-zone is N-S, however, past activity along the NW and NE rifts permits these pathways to be still considered potentially active since the contact between the dyke and the wall rock is weaker providing a potential pathway along the higher bulk density of the dyke swarm (Walker, 1992).

Magma ascending along the NW rift would reach the detachment fault and be cut off from the magma source, re-alignment to the topographically controlled N-S trend would produce oblique fissures on the western flank. Day (*pers com*) suggests that this local realignment of the least effort path justifies the formation of the *en echelon* fissures of the western flank. The recent increase in the number of fissure eruptions on the western flank, may be due to a change in the plumbing system at depth favouring the NW path of ascent, or it may be due to local stress changes within the shallow edifice caused by the growth of the detachment fault. The detachment fault is probably a consequence of the Cumbre Vieja edifice growing on the fault scarp of a past collapse. The Cumbre Nueva fault scarp forms a steep ridge covered with sediments on the western flank, this western boundary between the sediments and the Cumbre Vieja lavas will be weaker than the eastern flank boundary on the other side of the ridge. Loading from the growth of the edifice with the increasing confining pressure with depth has caused the creation of the detachment fault.

7.10.1 Surmised eruption scenarios

The 1949 eruption produced a fault with up to four metres of westward normal displacement along the top of the Cumbre Vieja ridge, future dyke emplacement could lead to the collapse of the ridge along the detachment fault. The 1949 fault is just a surface expression of the detachment fault; collapse could occur at other points high on the ridge as the fault propagates to the surface. The first recorded signs of impending activity are seismicity (Martin San Gil, 1960) and surface fault development and growth as seen in 1949; there have also been reports of

springs drying and the intoxication of small animals. Carracedo *et al.* (1997b) imply that it would be unlikely for an eruption low down on the ridge to instigate a flank collapse. However, an eruption near the top of the ridge could either cause an aborted collapse (like in 1949) or a giant lateral collapse (similar to the Cumbre Nueva). The hazard implications for these scenarios are immense, any eruption has the potential to lead to the loss of life and livelihood, but a flank collapse would cause devastation and propel a tsunami to the western coast of the United States (McGuire & Moss, 1997). An aborted collapse would also produce intense seismic damage to buildings and the island's infrastructure. Figure 7-18 illustrates a simplification of the landslide hazard potential from future eruptions on the island. Indicating that the greatest hazards are from eruptions high in the ridge that could potentially cause a giant lateral collapse.

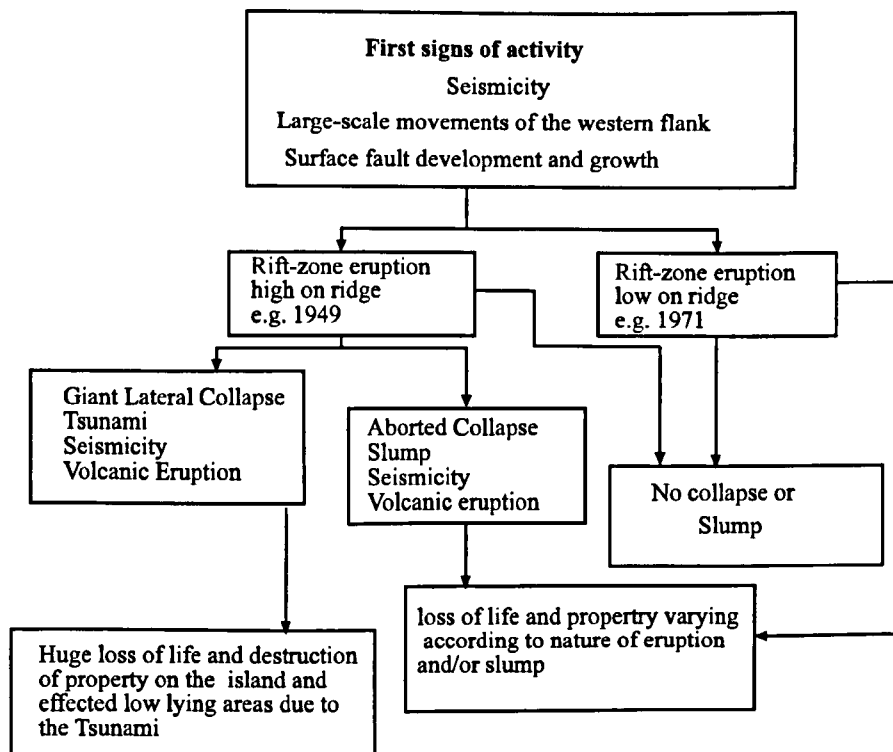


Figure 7-18 The hazard potential from landslides on the Cumbre Vieja volcano, after Carracedo *et al.* (1997b).

7.11 Conclusions and Summary

Successful establishment of the ground deformation network using firstly EDM then GPS has provided ground deformation data for the period spanning October

1994 to September 1998. The initial set-up of the ridge network used EDM with a theodolite, this was satisfactory to measure the small ridge network but it was unfeasible to expand the network off the ridge to cover the western flank. The Western Flank Network was thus established using GPS in 1997 over the western flank from the Barranco de las Angustias to the tip of the island. Data from all the surveys displayed a good repeatability between surveys (of <10mm) permitting the confident conclusion that no significant deformation had occurred. The 'insignificant data' (under 10mm) did however form coherent patterns between 1994 and 1997 which suggested slow westward displacement of the 1949 fault at the apex of the ridge. However a re-occupation in 1998, undertaken to test this observation did not find an extension of this pattern, suggesting that the displacement was either restricted to the period between 1994 and 1997 or that the pattern was coincidental. FE modelling illustrated the deformation associated with an intruding dyke, found that the increased strain (and likely failure) was concentrated near the apex of the ridge, further intrusion to the surface effected the whole of the western flank. It is proposed that the 1949 intrusion caused the fault to develop and had further intrusions occurred, broadening the effected area then the western flank could have failed along the detachment fault. Collapse of the Cumbre Vieja is inevitable, it is part of the evolutionary cycle of Oceanic shield volcanoes, the style of collapse is however pre-determined by the underlying topography and the ascent of magma.

8. CONCLUSIONS

8.1 An evaluation of the methodology

The study collected ground deformation data from a number of networks positioned over active rift-zones and tectonic faults to an accuracy of approximately 5-12mm. An evaluation of the methodology is undertaken in order to establish the validity of the results. Evaluation criteria determine the strengths and weaknesses of the study design and its impact on the analysis of the results. For a discussion of the data see Section 8.3.

The main limitation of the methodology was the limited time-span of the study; during the (approximate) three years of the monitoring program, there were no flank eruptions on any of the three selected volcanoes. However, this was anticipated and the absence of an eruptive event on the rift-zones and the lack of substantial ground displacement provides valuable insight into inter-eruptive edifice stability in the absence of a fresh intrusion or eruption of magma. Although the applicability of this monitoring program to monitor a flank eruption was not determined, studies previously undertaken on Etna suggest that this research project followed the most effective procedure (McGuire & Pullen, 1989; Murray, 1994; Murray & Sergeant, 1994; Nunnari & Puglisi, 1994). The study has produced new data-sets for each of the selected volcanoes, the EDM data were transformed into grid co-ordinates and the GPS data were presented in both WGS84 and grid co-ordinates. Line-length data and the co-ordinates are listed in Appendix B.

The advantages and disadvantages of surveying using GPS compared with an EDM and a theodolite were outlined at the outset of the study (Section 2.8). New findings in the application of these techniques in this study have revealed further advantages and disadvantages that were not addressed by the instrument manufacturers or previous authors: this new information is summarised below:

- (i) *Geological features* in the area under investigation are the primary considerations when installing a new GPS network (in a rural unpopulated area) on a volcano. This is because the technique does not require line-of-sight between survey stations and has a maximum baseline length of 23km. However, since the optimum baseline length when undertaking rapid static GPS is less than ten kilometres, additional base-stations are positioned in the centre of a network to act as a 'brace' and linking the extremities of a large network.
- (ii) *Meteorological conditions* hampered the use of GPS despite the fact that GPS is sold as an all weather technique. High winds had a direct effect, producing antenna vibrations on Etna and Cumbre Vieja. Although the GPS is not affected by rain and cloud conditions, persistent low cloud on Piton de la Fournaise halted the use of both EDM and GPS due to the dangers of navigating across the lava fields and on Etna lightening storms frequently drove the surveying team from the summit for many days.
- (iii) *Urban GPS networks* were very difficult to install due to the problems of multipath, a poor sky-view from the receiver to the satellite and new developments (new houses and roads adjacent to or on top of survey stations). As explained in Section 2.6, multipath is the unexpected reflection of satellite signals off metal surfaces (this modifies the range from the receiver to the satellite). Problems arise from survey stations that are adjacent to reflective objects including chain link fences, pylons, metal gates and buildings. To achieve a satisfactory accuracy (away from areas of multipath) a good sky view is required, which is often difficult in urban areas.
- (iv) *Methodological constraints* are an important consideration when establishing and measuring an EDM network. The geometry of the network must be a well braced quadrilateral of inter-visible survey stations that are less than two and a half kilometres apart with sufficient redundancy to obtain co-ordinate positions to the required accuracy. This presented two issues: (1) The

necessary use of elevated areas to install survey stations, for example, the establishment of the network on Piton de la Fournaise necessitated the installation of a number of survey stations on the top of dangerously steep cones. (2) It is not possible to locate new survey stations in areas that do not have line-of-sight to a station in the network, for example on La Palma it was not possible to locate stations to obtain baselines from the top of the Cumbre Vieja ridge to the bottom due to distance and tree cover.

These new findings revealed that EDM and GPS excel over each other in different locations and under different conditions. While the wide, open, rural areas are suitable to be measured using GPS, urban areas or places with many metal obstructions such as chain link fences, pose a problem for obtaining accurate GPS data in areas which necessitate a 'small dense network'. Future network occupations, especially on the Timpe faults (where there are buildings and high cliffs) would be best measured with the latest Total Stations that combine high precision GPS with an EDM and a theodolite (Trimble™).

The changing patterns of deformation on active rift-zones required the application of a rapid, cheap and accurate survey marker; so the main form of new survey marker installed were steel nails and fixed discs. Although pillars are recommended for most high precision surveys (Frei & Schubernigg, 1992; Hofmann-Wellenhof *et al.* 1997 pp159) the changing, often destructive, nature of the volcano and the number of survey stations required to span a wide unstable area must be taken into account. It is not logistically desirable or economically viable to install a network of 20-30 pillars in an unstable area, especially if many are likely to be destroyed by the process under investigation. Experience gained through this study suggests that the best method to use for new networks is to install a broad well-spaced network of a large number of survey stations over the study area. When specific areas show signs of sudden or gradual deformation then new survey stations are installed to intensify the network to better constrain the ground surface changes. *This new method of measuring ground deformation on dynamic areas may be transferred to other unstable phenomena such as active*

landslides, anthropogenic ground disturbance (e.g. disused mines) or coastal erosion.

The baseline data sets were successfully established on the selected volcanoes. The Piton de la Fournaise network has been taken over by the Piton de la Fournaise Volcano Observatory. The Etna network is now being measured (in part) by groups from Newcastle University and Brunel University. The Cumbre Vieja network is still being monitored by the author in association with Cheltenham and Gloucester College of Higher Education and The Benfield Grieg Hazard Research Centre at University College London with funding from the Benfield Grieg Hazard Research Centre and the Spanish Civil Authorities, and there are plans to expand the network to cover the whole island and link with GPS survey stations on the other Canary Islands.

8.2 The principal findings of the study

As rift-zones develop in a volcanic edifice, the persistent intrusion and emission of magma produces disproportionately loaded flanks or ridges which in time form steep gravitationally unstable flanks. The role of rift-zones is therefore crucial as they facilitate this asymmetrical development of the edifice. The resulting strain imbalance caused by continually distending rift-zones and flank growth is equalised by the displacement of the seaward flank through either slow creep or periodic slope failure.

Investigation of ground deformation on three active volcanoes; Etna, Piton de la Fournaise, and the Cumbre Vieja, has developed a new understanding of the nature and operation of these rift-zone systems. Identification of the relationships between magma, edifice morphology (both surface and mass) and underlying regional fault systems have furthered the understanding of inter-eruptive behaviour. Despite the highly active nature of both Etna and Piton de la Fournaise, only Etna experienced eruptive activity *during* the monitoring program (and this was only from the central craters rather than on the flanks). The absence of a flank

eruption has, however, provided a very valuable 'window' through which to study non-magmatic deformation. For each selected volcano, specific questions have addressed the most important factors that control rift-zone development, instability and slope failure. In order to examine the results of the entire study the final question draws these conditions together to ask; *Are the relationships between gravitational, magmatic and tectonic stresses similar for all the case-study sites and how do the different morphologies affect deformation patterns?*

Each of the three volcanoes has at least one rift-zone that lies at the head of a recognised unstable sector of the edifice. The continued emplacement of magma 'behind' this sector may ultimately lead to further collapse. This investigation has used ground surface displacements to record and analyse the relationship between the rift and the flank in order to determine the influences or combination of influences which that may expedite failure. An important finding of the study has been that despite the existence of features that are thought to be gravitationally unstable, without the input of magmatic stresses the edifices appear stable. The next section will thus address the similarities between the selected sites and specific results relating to the presence of magma and the paucity of significant deformation.

8.3 Are the relationships between gravitational, magmatic and tectonic stresses similar for all the case-study sites ?

This answer to the above question is perplexing. Firstly, as previously mentioned there has not been an interaction of magma with gravitational and tectonic stresses on each selected volcano. So the following conclusive statements, that have already been explained in the previous chapters, are made to clarify the observed and perceived relationships noted within the study:

- (i) Piton de la Fournaise did not erupt during the monitoring programme between 1993-1996. A fissure eruption in 1998 destroyed most of the survey stations, but revealed magma-related deformation in the form of eastward

displacement of the area adjacent to the rift-zone thus linking the fresh magmatic intrusion to seaward gravitational displacement.

- (ii) Cumbre Vieja did not experience any significant ground deformation, although, coherent but statistically insignificant <10mm patterns were detected between 1994 and 1997 that suggested seaward displacement of the material around the 1949 fault. This pattern was, however, not maintained during a 1998 occupation of the network, leading to the conclusion that the network area is stable.
- (iii) Etna undergoes small but continuous deformation as a result of the open magma system. Two distinct deformation patterns emerged: the possible rift-related deformation around the area of the 1989 fault on the southern wall of the Valle del Bove and distinct shallow block movements in the upper south-eastern flank, that are interpreted to be a result of either deep regional tectonic fault displacements or shallow topographically-induced stresses.

Interpretation of the data suggests that the presence or absence of magma appears to denote the existence of significant (or almost significant) deformation. The affects on the edifice from the intrusion of magma may be either thermal, mechanical or from secondary influences such as changes in pore fluid pressures. Mount Etna and Piton de la Fournaise experienced magma-related deformation due to the resurgence and eruption of magma, but the specific affects of pore fluid pressure increases or rift-distension are not discernible from the analysis of the ground deformation data.

The slight deformation measured on the upper flanks of Mt. Etna was most likely caused by the re-filling of the central conduits with magma, however, the patterns manifest in this deformation reflect the prevailing tectonic stresses. The tectonic influence may be divided into two facets: (1) local topographic influences, and (2) deep seated regional tectonic activity. The displacement of coherent blocks in the shallow surface (originally identified by McGuire & Pullen, 1989 and re-defined in Section 5.7) is attributable to either one, or a combination, of these influences. The shallow blocks are divided into two distinct eastern and western groups. The

eastward displacement of the easterly groups has long been associated with the instability of the edge of the Valle del Bove cliff (*local topographic affect*). McGuire & Pullen (1989) interpreted this eastward displacement of the area adjacent to the cliff to be due to the persistent emplacement of dykes behind the cliff wall. This, however, does not explain the westward displacement of the western group of survey stations (Figures 5.6 & 5.10). A new model is proposed, in which the east-west dilation of this set of blocks is a result of an underlying SE oriented tectonic fault (*deep seated regional tectonic activity*). The fault displacement is inherited from depth via the shallow blocks and activity along this deep fault produces flank eruptions on the SE flank of Etna. Stewart *et al.* (1997) propose that the Timpe accommodate rift-related stresses and that without this accommodation rift-zones would lock. The findings of this study suggest that the seismic correlation (Section 4.3) between the East Flank Faults and the rift-zones is due to *a common source* and that it is the deep tectonic fault displacements that are accommodated by the Timpe Faults producing periodic displacements and creep. One conclusion from earlier works is agreed, the easterly displacement of the Upper South-Eastern Flank is threatening the stability of the Valle del Bove cliff.

The significant displacements on Piton de la Fournaise during the 1998 eruption display the interaction between magmatic and gravitational stresses. After a relatively long (five year) inter-eruptive period during which there was no significant deformation, there was a summit eruption which culminated in the propagation of a dyke into the northern flank. Unfortunately, only two of the rift-zone survey stations were reoccupied (by the Piton de la Fournaise Volcano Observatory). The eruption fissures formed in an *en echelon* pattern that inferred lateral displacement to the east: the survey stations (including other French EDM & GPS stations) east of the fissures were displaced to the east. The results outlined in Chapter 6 infer that the deformation that occurred is a combination of the magmatic stresses and the inherent gravitational instabilities within the eastern flank. Like Etna, Piton de la Fournaise displays magmatic deformation that takes on a pattern attributable to another influence, in this case gravitational instability.

8.4 *How do the different edifice morphologies affect deformation patterns?*

If there is evidence of a previous collapse from a volcanic edifice then it is likely that failure will occur again if the same conditions are manifest. A steep-sided edifice which is already over-loaded with lava flows is likely to collapse in the event of an intrusion of magma behind the slope. However, Day (1996) maintains that the slope angle is unimportant if the edifice is permeable or strongly fractured as this facilitates edifice destabilisation due to high pore fluid pressures.

As discussed in Chapter Seven, the 1949 eruption of the Cumbre Vieja caused a 4m displacement of a fault on the western flank of the edifice, which strongly suggested that the edifice was not stable and that the flank could fail catastrophically during the next eruption high on the flank. The Cumbre Vieja ridge is approximately 2km tall and 15km wide, its steep sides suggest that dilation of the rift-zone could lead to flank failure. Coherent displacement around the 1949 fault measured between 1994 and 1997 indicated that the 1949 fault running along a section of the top of the ridge may not be stable (although his argument was later rejected due to the lack of coherency of the 1998 data-set). Had long-term slow creep been detected, the flank could not be considered stable and it would have been labelled a non-magmatic slow moving landslide, which would have had major implications for hazard assessment of the whole island. However, in the absence of magma, and despite the steep flanks, at the end of the monitoring program it was concluded that the edifice is stable during the inter-ruptive period. Although the volcano may collapse during the next eruption, the fault is not creeping and therefore not liable to collapse *before* the next magmatic intrusion.

Piton de la Fournaise, however, has relatively shallow slopes and the rift-zones do not form ridges. The ground deformation was only measured adjacent to the fissures during the 1998 eruption, and it is therefore not possible to verify how much of the eastern flank was displaced. It is unlikely that the shallow slope would

catastrophically fail during a dyke intrusion at the present time due to the lack of gravitational loading. However, the composition of the edifice may override the morphological influences. It was speculated that the flank may be underlain by a soft olivine wedge which is destabilising the flank from beneath, although this would be exacerbated by a steeper external slope, the shallow morphology could still be prone to failure. The morphology of Etna is very complex, as explained in Section 8.1, although the edifice has relatively shallow slopes, the surface morphology of the Upper South-Eastern Flank has major implications on stability since the steep cliff of the Valle del Bove is liable to collapse if a dyke is emplaced just behind and parallel to the cliff. The results from the monitoring of the Lower Eastern Flank Networks revealed a slight eastward displacement of all of the survey stations. It may thus be proposed that the edifice, although generally stable, is undergoing slow moving eastward creep, most probably as a result of the underlying tilted substrate.

As stressed at the start of the section, the presence of a past collapse indicates that future failure is likely. The identification of some of the relationships between magma intrusion and the composition and stability of the edifice creates a model of edifice stability for the present time.

8.5 Further research

Although the networks were set-up to be measured over a long period, this short *window* has revealed many interesting results and produced a great number of questions. The work on Etna has not conclusively established how stable the volcano is and can only produce speculation on the complexity of the potential eruption and slope failure triggers. It is recommended that more detailed work is continued on the SE network coupled with an examination of the NE rift-zone and its relationship with the Pernicana fault, preferably during a flank eruption. The combination of ground deformation analysis with other geophysical techniques should be undertaken to maximise the potential value of the data, particularly in identifying the possible SE fault under the SE flank. The latest eruption of Piton

de la Fournaise will be examined in detail by the Piton de la Fournaise Observatory, and will hopefully reveal the displacement of the eastern flank and constrain the limits of the east flank displacement. The finite element modelling was limited by the simplistic Quickfield™ software. Although the results were satisfactory, a more detailed three dimensional package would increase the flexibility of the simulations and allow more material parameters to be incorporated.

The research undertaken in this study is designed to be continued through long-term monitoring in the future. This is especially important in La Palma since although the Cumbre Vieja is at present stable, the *next* intrusive event high on the ridge may cause either a massive aborted collapse or a catastrophic lateral failure of the western flank.

A. KILAUEA VOLCANO, HAWAII

Swanson *et al.* (1976 p35) stated that “any oceanic shield volcano that grows on the flank of an earlier shield in the absence of a dominant tectonic stress system should behave similarly to Kilauea”. Although the volcanoes selected in the study are not all oceanic shield volcanoes it is valuable to draw comparisons with Kilauea due to these structural and volcanological similarities. The basic structure and eruptive patterns of Kilauea are briefly summarised to substantiate comparative ideas and theories.

All three case study volcanoes within this research are similar to Kilauea volcano, since they are all predominately basaltic edifices with recognised rift-zones at the head of an unstable flank. Like Etna and Piton de la Fournaise the structure is buttressed on the non-seaward side and the rift-zones that bisect the summit region delimit the mobile seaward flank.

Kilauea is situated on the largest most easterly island in the Hawaiian archipelago, the edifice is buttressed to the west as it is growing on the flank of an older volcano, Mauna Loa (see Figure A-1). Kilauea does not form a large cone, instead, due to; (i) the buttressing affect of Mauna Loa, and (ii) the persistent intrusion of dykes into the linear east and south-west rift-zones, it forms a low shield. The edifice is comprised of cones, pit craters, and fissures, it is approximately 80km long and 30km wide, elongated in a NE orientation. Kilauea is thought to be the most active volcano in the world, erupting almost every year from either the summit or the East and South-West Rift-Zones. The latest eruption commenced in 1983 from the East Rift-Zone and is still in progress at the time of writing. The edifice is predominately basaltic forming a broad shield with shallow slopes (10-25°) (Walker, 1990). The shallow slopes are a result of the following factors; (i) high lava discharge rate spreading the emitted products far from the vent, often via lava tubes, (iii) rift-zone eruptions that do not build a

central cone but instead a low linear ridge that is widened by injection of magma into rift-zones, (iv), persistent subsidence of summit area. (Walker, 1990).

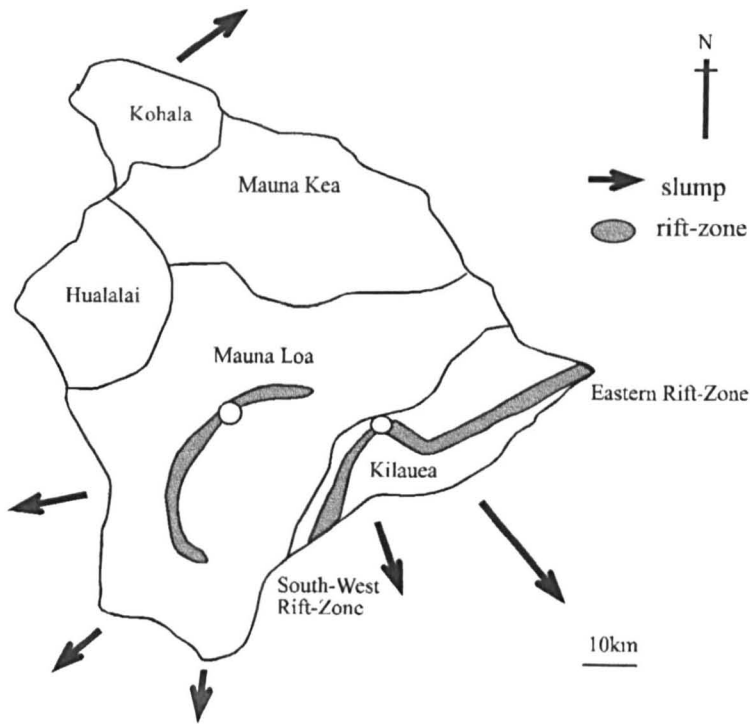


Figure A-1 The Big Island of Hawaii showing the relative surface areas of the volcanoes; the central vents of Mauna Loa and Kilauea are indicated by a white circle and the shaded areas are their active rift-zones.

Six main structural divisions of Kilauea were identified by Swanson *et al.* (1976); (i) summit area containing the main collapsed calderas; Halamaumau and Kilauea Iki, (ii) East Rift-Zone, 5km wide ridge characterised by recent lava flows, vents, fractures, and pit craters, (iii) South-West Rift-Zone, 4km wide rift characterised by cones, vents and large fractures, (iv) Koae fault system, E-NE trending, 3km wide array of fractures connecting the two rift-zones, (v) South flank, the seaward flank bounded by the rift-zones, containing the Hilina Fault System, (vi) North flank, bounded by the East Rift-Zone and the summit area, characterised by E-NE dipping lava flows. The two distinct fault systems, the Koae and Hilina are characterised by large fractures (1-3m wide) and frequent seismic activity. The rift-zones are well-defined, a positive Bouger gravity anomaly (Kinoshita *et al.*, 1963 in Swanson *et al.*, 1976) and a fast seismic velocity (Hill, 1969 in Swanson

et al., 1976) provide geophysical evidence confirming that the rifts contain hundreds to thousands of intruded dykes (Swanson *et al.*, 1976).

The magma ascends in the central conduit system into shallow storage reservoirs beneath the summit, the magma supply rate, estimated from recent eruptions is thought to be around $9 \pm 3 \times 10^6 \text{ m}^3$ (Swanson *et al.*, 1972; Dzurisin *et al.*, 1980; Duffield, *et al.*, 1982). The shallow storage areas are maintained by neutral buoyancy (Walker, 1990; Ryan, 1987). Distinct inflation and deflation cycles are revealed by ground deformation, the co-seismic inflation commences as the magma propagates within fractures at depth entering the shallow magma reservoir. Ground cracks form to accommodate this expansion. The pressure is released (from the expanding magma reservoir) through either a summit eruption or the lateral transfer of magma into a rift-zone reservoir which often culminates in a flank eruptions. A lack of earthquakes during the transfer of magma from the summit magma reservoirs into the East Rift-Zone reflects the relatively open transport system between the two areas. Local deformation occurs around the eruption site, as either a radial uplift or if the eruption occurs in a rift, an axial graben forms along the ridge. The persistent intrusion of magma into the rift-zones is thought to facilitate the lateral sliding of the South Flank of the volcano. The South Flank and the SW Rift-Zone are coherently displaced as a single slump block.

Seismological evidence reveals a correlation between eruptive events, the distribution & timing of earthquakes and movement of the slump block (Swanson *et al.*, 1976). Most of the earthquakes which occur beneath Kilauea are either below the summit related to the ascend of magma, or at shallow depths beneath the South Flank usually towards the end of or after an eruption. The focal mechanisms of these South Flank Earthquakes indicate a maximum stress axis oriented SE either horizontal or plunging seaward (Endo 1971 in Swanson *et al.*, 1976). This observation suggests that the persistent intrusion of dykes into the Eastern Rift-Zone facilitate the seaward slumping of the edifice (Swanson *et al.*, 1976). However, the instability of the seaward flank is most likely a combination

of theories; (i) the seaward flank may be propelled by gravitational sliding, resulting from the growing mass of the edifice due to the frequent eruptions, and (ii) similar to Piton de la Fournaise, the downward motion of the mobile flank is expedited along the slopes of the underlying edifice. Recent petrological evidence however, suggests an additional complex mechanism. A model proposes that olivine crystals, that have sunk to the bottom of the magma reservoir, accumulate forming an *olivine mush* (this has a similar rheology to a glacier). The mush advances under the force of gravity to become a 'pushing' wedge under the South Flank, forcing the seaward sliding of the south flank (Clague & Denlinger, 1994). The last major movement of the south flank was in 1975 when a 7.2 magnitude earthquake within the Hilina fault system caused 3.5m of vertical displacement and 8m horizontal displacement (Hawaiian Volcano Observatory Monthly Reports, 1970-1976), in addition to these periodic releases of strain, slow continuous creep occurs along the length of the South Flank (Denlinger *pers com*). Moore *et al.*, (1989) reveal off-shore landslide deposits from slump and debris avalanche deposits (see Figure A-1), suggesting that collapse is an important part of the development of the Hawaiian Islands.

B. GROUND DEFORMATION DATA

B.1 Etna: Cartesian WGS84 co-ordinates and error ellipses for the Upper and Lower Eastern Flank networks

Etna 1994 derived from EDM data

Station	X	Y	Major axis (cm)	Minor axis (cm)
e4	50780.32	57642.07	10.4	6
e5	50880.77	57184.08	8.1	7.1
e6	50488.25	57018.66	7.8	6.8
e7	50633.46	56649.58	12.7	6
e8	49588.42	57329.36	7.7	6.2
e10	50085.49	56760.5	8.2	7.9
e11	49496.36	56560.98	9.9	7.6
e12	49224.03	56292.58	8.2	0
e18	51232.08	54655.11	13	3.6
e29	51974.85	54178.28	3.3	3
e31	50901.4	56857.1	11.4	7.1
e39	50081.94	57875.5	0	0
e48	50575.28	55658.31	3.7	3.4
e49	52250.69	53495.51	10.7	3.2
e50	52932.74	53624.69	13.1	6.8
e51	51641.69	54941.15	9.5	5.5
e52	52539.9	54302.15	9.7	5.2
e54	51975.93	54767.3	18.3	8.1
e56	50474.46	53390.68	23	9.4

Etna 1995 derived from EDM data

Station	X	Y	Major axis (cm)	Minor axis (cm)
e16	49328.19	54483.52	0	0
e18	51232.05	54655.1	3.7	3.1
e19	51350.23	55164.98	4	3.4
e29	51974.8	54178.29	4.7	2.9
e36	51358.43	55213.13	4.1	3.5
e48	50575.24	55658.35	3.6	3.3
e49	52250.66	53495.54	4.2	1.9
e51	51641.66	54941.14	3.9	3.6
e52	52539.84	54302.17	4.9	0
e54	51975.92	54767.34	21.7	3.2
e56	50474.43	53390.66	4	3.1
e4	50780.29	57642.09	4.9	2.9
e5	50880.74	57184.1	3.8	2.8
e6	50488.24	57018.65	3.9	2.8
e7	50633.45	56649.59	3.2	0
e8	49588.38	57329.3	3.3	2.9
e10	50085.49	56760.48	4.3	3.6

e11	49496.38	56560.94	6.2	3.7
e37	50781.6	57642.75	4.9	2.9
e39	50081.88	57875.48	3.8	1.2
e42	49848.68	58071.33	0	0

Etna 1996 *Leica* GPS data (68% error ellipses in m)

Station	x	y	z	Major axis	Minor axis	Height
c3	4877795.050	1323721.891	3877617.603	0.0158	0.0136	0.0226
c4	4877975.978	1323580.579	3877438.387	0.0154	0.0127	0.0207
e10	4880922.126	1307927.670	3883225.670	0.0073	0.0046	0.0085
e11	4881140.594	1307376.040	3883026.103	0.0068	0.0055	0.0091
e12	4881306.290	1307138.409	3882762.845	0.0083	0.0052	0.0094
e13	4881255.661	1306882.938	3882935.583	0.0102	0.0056	0.0118
e14	4881691.318	1307038.400	3881956.139	0.0085	0.0075	0.0144
e15	4882109.726	1306690.437	3881356.648	0.0208	0.0113	0.0204
e16	4882091.192	1307456.647	3881125.102	0.0077	0.0055	0.0085
e17	4881472.478	1305797.726	3882574.672	0.0129	0.0126	0.0278
e18	4881495.724	1309268.815	3881259.996	0.0034	0.0027	0.0049
e19	4881278.367	1309249.376	3881859.118	0.0135	0.0089	0.0185
e26	4880419.132	1306600.989	3884883.538	0.0142	0.012	0.0327
e29	4881403.814	1310013.348	3880737.453	0.0096	0.0077	0.0196
e3	4880855.746	1307395.051	3883788.941	0.0046	0.004	0.0074
e31	4880645.388	1308698.585	3883295.420	0.0058	0.0047	0.0086
e32	4880865.634	1309255.124	3882120.698	0.0080	0.0068	0.0133
e33	4880041.090	1309811.801	3882357.247	0.0083	0.0057	0.0113
e37	4880297.143	1308481.262	3883985.411	0.0047	0.0036	0.0064
e39	4880466.317	1307801.882	3884270.235	0.0138	0.0082	0.0149
e39gp	4880467.451	1307803.629	3884268.568	0.0071	0.0054	0.0118
e42	4880436.487	1307552.357	3884445.741	0.0061	0.0049	0.0075
e48	4881431.530	1308571.478	3882341.110	0.0075	0.0073	0.0132
e49	4881557.963	1310340.221	3880054.765	0.005	0.0039	0.0083
e5	4880497.700	1308637.647	3883586.432	0.0095	0.0081	0.0202
e51	4881276.193	1309634.224	3881530.838	0.0129	0.0077	0.0171
e52	4881202.785	1310544.656	3880850.289	0.0096	0.0061	0.0127
e53	4881099.282	1310699.477	3880910.999	0.0153	0.0083	0.0221
e54	4881208.186	1309962.115	3881325.880	0.0031	0.0023	0.0044
e56	4882239.532	1308683.448	3880099.579	0.0057	0.0047	0.0081
e6	4880700.364	1308285.411	3883458.106	0.011	0.0079	0.0158
e61	4881910.707	1310101.559	3879650.789	0.0048	0.0041	0.0093
e63	4881249.606	1310964.106	3880111.743	0.004	0.0034	0.0057
e65	4881320.947	1307878.491	3882513.835	0.0105	0.0089	0.0147
e66	4877509.302	1316724.404	3881493.195	0.0088	0.007	0.0152
e67	4883076.310	1306112.313	3879626.962	0.0051	0.004	0.0088
e7	4880831.525	1308470.934	3883126.440	0.0072	0.0053	0.0109
f1	4871291.273	1325373.189	3885024.855	0.016	0.0141	0.0314
f2	4869511.201	1319179.412	3890092.901	0.0118	0.01	0.016
m2	4876289.375	1319815.116	3881273.457	0.0118	0.0101	0.0173

m4	4875821.155	1320341.284	3881424.629	0.0162	0.0131	0.02
v4	4871746.596	1317458.575	3888425.027	0.021	0.0169	0.0321
v5	4872057.578	1317426.955	3888088.532	0.008	0.0068	0.0133

Etna 1997 *Leica* GPS data (68 % error ellipses in m)

Station	x	y	z	Major axis	Minor axis	Height
c1	4877968.892	1323525.364	3877450.054	0.0266	0.0154	0.031
c2	4877867.547	1323605.838	3877534.868	0.0224	0.0143	0.0274
c3	4877795.075	1323706.143	3877602.608	0.0192	0.0118	0.0239
c4	4877975.989	1323564.845	3877423.404	0.0193	0.0121	0.024
c5	4877828.603	1323700.999	3877558.212	0.0222	0.015	0.0344
c6	4877807.006	1323724.721	3877577.015	0.0343	0.023	0.0693
e10	4880922.197	1307911.914	3883210.72	0.0068	0.0056	0.0107
e11	4881140.659	1307360.267	3883011.159	0.0101	0.0085	0.019
e12	4881306.4	1307122.658	3882747.923	0.0063	0.0058	0.0102
e13	4881255.73	1306867.181	3882920.634	0.0096	0.0085	0.0183
e15	4882109.774	1306674.671	3881341.65	0.0147	0.0097	0.0183
e16	4882091.272	1307440.884	3881110.148	0.016	0.0142	0.0271
e18	4881495.814	1309253.071	3881245.074	0.0094	0.0068	0.0139
e19	4881278.43	1309233.631	3881844.156	0.0074	0.0049	0.0116
e29	4881403.836	1309997.585	3880722.474	0.0132	0.011	0.0342
e31	4880645.446	1308682.83	3883280.471	0.0083	0.0058	0.0121
e32	4880865.789	1309239.385	3882105.796	0.0185	0.0116	0.0353
e33	4880041.09	1309796.018	3882342.244	0.024	0.0182	0.0338
e37	4880297.214	1308465.5	3883970.472	0.0077	0.0063	0.0108
e42	4880436.631	1307536.54	3884430.776	0.0354	0.0195	0.0555
e48	4881431.59	1308555.708	3882326.146	0.0066	0.0051	0.009
e49	4881558.047	1310324.469	3880039.843	0.0083	0.008	0.0145
e5	4880497.771	1308621.883	3883571.486	0.0084	0.0069	0.0157
e51	4881276.191	1309618.472	3881515.859	0.0084	0.0064	0.0144
e52	4881202.845	1310528.891	3880835.317	0.0153	0.0119	0.0229
e54	4881208.274	1309946.377	3881310.94	0.0206	0.0117	0.0227
e56	4882239.601	1308667.699	3880084.635	0.0052	0.0046	0.0094
e6	4880700.428	1308269.644	3883443.162	0.0095	0.0064	0.0115
e61	4881910.786	1310085.804	3879635.853	0.0076	0.0063	0.0114
e63	4881249.658	1310948.346	3880096.788	0.0041	0.0031	0.0067
e65	4881321.011	1307862.733	3882498.882	0.0107	0.008	0.0116
e66	4877509.376	1316708.656	3881478.269	0.0144	0.009	0.0176
e68	4880447.301	1307810.005	3884262.62	0.0116	0.0082	0.0133
e69	4882130.133	1308477.578	3880260.34	0.0074	0.0049	0.0103
e7	4880831.62	1308455.176	3883111.507	0.0063	0.0051	0.0088
e8	4880855.965	1307379.185	3883773.944	0.0088	0.0072	0.017
f1	4871291.227	1325357.425	3885009.84	0.0169	0.0119	0.0286
f2	4869511.196	1319163.652	3890077.967	0.0209	0.0165	0.0304
m2	4876289.494	1319799.458	3881258.441	0.0261	0.0178	0.0268
m4	4875821.159	1320325.535	3881409.657	0.0147	0.0095	0.0191
v4	4871746.616	1317442.845	3888410.102	0.0165	0.0105	0.0213

v5	4872057.693	1317411.234	3888073.584	0.0198	0.0123	0.0275
----	-------------	-------------	-------------	--------	--------	--------

B.2 EDM line-length changes over the Upper South-Eastern Flank Network

From	To	Previous measurement Date		1994	1994b	1995	1995b	1996	1997
8	10			778.041	778.044	778.049		778.052	778.043
8	11			814.491	814.494	814.496		814.507	814.493
12	11			391.44		391.440		391.444	391.445
12	13			312.518		312.514		312.517	312.514
14	12	1993	899.458			899.457		899.457	899.684
14	13			1083.186		1083.172		1083.179	1083.348
15	13			1805.389		1805.412			1805.435
15	12	1993	1680.335			1680.345		1680.351	1680.382
15	17	1992	1639.01			1639.054		1639.085	
16	15	1993	800.624			800.630		800.646	800.631
16	56	1993	1605.825			1605.83		1605.847	1605.849
17	13	1992	1163.964			1163.98		1164.024	
18	48			1288.083		1288.082		1288.102	1288.1
19	48			966.523		966.551			
36	48			949.569		949.569			
48	31			1242.915		1242.922		1242.934	1242.945
48	7			993.391		993.398		993.408	993.409
48	10			1206.798		1206.815		1206.826	1206.823
48	11			1408.136		1408.154		1408.166	1408.172
48	13			1798.712		1798.731		1798.748	1798.749
48	15			2228.731		2228.758		2228.773	2228.784
18	19			550.49		550.491			
18	51			505.037		505.043		505.047	505.053
18	29	1993	914.219			914.214		914.236	914.244
19	36			48.864		48.863			
19	51			380.25		380.249			
29	49			772.43		772.424		772.445	772.407
51	49			1660.27		1660.261		1660.306	1660.265
52	29			579.167		579.164		579.166	579.154
52	49			894.857		894.851	894.882	894.876	894.839
53	52			195.884		195.879		195.878	
54	51			392.596		392.603		392.613	392.605
54	52			752.025		752.018		752.044	752.033
62	49					698.052			
4	39			754.834	754.841	754.829	754.835		
4	5			472.739		472.764			
5	39			1080.293	1080.299	1080.291	1080.301	1080.313	
6	5			426.155		426.150			426.156
6	31			447.433	447.434	447.428		447.440	447.45
6	7			402.024		402.017			402.035
6	10			480.811	480.808	480.807		480.815	480.815

6	39	1993	973.719			973.709	973.716	973.721	
7	5			592.296		592.299		592.305	592.31
7	39			1374.484		1374.492		1374.509	
8	5			1308.887	1308.889	1308.9	1308.897	1308.913	1308.902
8	31			1409.593		1409.605			1409.612
8	7			1263.709	1263.727	1263.717		1263.732	1263.72
8	6			962.446	962.447	962.451		962.464	962.449
10	39	1993	1146.577			1146.591	1146.603		
10	11			625.974	625.970	625.970		625.980	625.988
31	39			1336.537		1336.54	1336.551	1336.566	
37	5	1993	473.124			473.131		473.142	473.148
37	39	1993	755.848			755.825		755.845	
39	42			306.519		306.552		306.520	
39	60					621.698			
39	8			740.8	740.806	740.813	740.82	740.817	
39	64					1374.499	1374.499		
42	60			329.406		329.412			
42	8			794.907		794.918		794.927	
60	8			1055.773		1055.732			
16	48	1993	1776.681		1776.672	1776.678			1776.702
16	18			1912.225		1912.236		1912.259	1912.283
56	61					1523.324		1523.344	1523.337
56	49			1792.013		1792.018		1792.05	1792.041
56	18			1497.454		1497.464		1497.489	1497.489
56	29			1695.233		1695.233		1695.27	1695.27
61	49					587.000			587.015
63	52					850.629		850.636	

Line-length data from EDM and GPS data for the Lower Eastern Flank Networks

Network		1992		1993		1994		1995		1996		1997
From-to		August EDM	April EDM	July EDM	October EDM	October EDM	July EDM	July GPS	June-EDM	June GPS	July GPS	
Macchia												
m2	m1	55.602	55.590	55.596	55.597		~		~			
m2	m5	383.312	383.333	383.328	383.308		383.322		~			
m2	m3	435.221	435.140	435.235	435.215	~	~		~			
m2	m4	720.330	720.351	720.343	720.329		720.350	720.385	720.341	720.371		
m1	m3	405.223	404.966	405.233	405.233	~	~		~			
m1	m5	376.557	376.556	376.568	376.565	~	~		~			
m1	m4	702.445	702.457	702.460	702.459	~	~		702.797			
m1	m6	1072.54	1072.55	1072.550	1072.554	~	~		~			
m2	m6		1040.72	1040.704	1040.700		1040.707		~			
m7	m6								~			
m7	m5								~			
m7	m4								~			
m7	m1								~			
m2	m7								443.869			
m8	m7								414.267			

m2	m8								55.496		
Carruba											
c1	c2	293.510	293.520	293.514	293.526	293.515	293.530		293.531		293.541
c1	c3	141.057	141.086	141.221	141.069	141.059	~		141.075		141.074
c1	c4	183.842	184.635	184.649	184.643	~	~		~		
c1	c5	33.825	33.823	33.848	33.803	33.722	33.818		33.810		
c2	c5	286.476	286.477	286.467	286.451	286.460	286.462		~		286.474
c2	c1	293.518	293.523	293.522		~	~		~		293.541
c2	c3	154.728	154.742	154.749		~	~		~		154.727
c2	c4	117.566	116.687	116.690	116.653	~	~		~		
c5	c4					~	~		~		
c1	c7							55.865		55.867	
c1	c6						291.238	291.373	291.233	291.243	291.225
c7	c5						37.180		37.185		37.179
c7	c6						241.746		241.747		241.736
c7	c2								249.449		249.453
Trecastagni											
t3	t1					45.638	45.654		45.652		
t3	t2					49.927	49.934		49.931		
t4	t2					50.265	50.270		50.265		
t4	t1					47.330	47.330		47.329		
Vena											
v2	v1					39.104			39.108		
v2	v3					55.154			55.159		
v2	v4					109.768			~		
v3	v4					89.167			~		
v1	v4					140.641			~		
v1	v3					93.905			93.902		
v4	v5										

B.3 Piton de la Fournaise Cartesian WGS84 co-ordinates and error ellipses.

Piton de la Fournaise 1993 derived from EDM data (error ellipses in m)

Station	x	y	z	major axis	minor axis	Height
2 E51	3349637.728	4916530.237	-2297267.257	0.0001	0.0001	0.0001
2 E52	3349599.763	4916151.032	-2298226.576	0.0001	0.0001	0.0016
2 E53	3349914.375	4916188.592	-2298043.229	0.0028	0.0019	0.0016
2 E54	3349777.547	4915886.235	-2298543.623	0.0053	0.0032	0.0026
2 E55	3349565.179	4915949.147	-2298549.86	0.006	0.0024	0.0026
2 E56	3349817.017	4915573.224	-2299039.687	0.0147	0.0075	0.0033
2M21	3352299.575	4915942.88	-2295244.442	0.0001	0.0001	0.0001
2M22	3351727.755	4916335.347	-2295197.041	0.0001	0.0001	0.0017
2M24	3351679.253	4916231.489	-2295491.847	0.0032	0.0048	0.0017
2M25	3351686.912	4916185.051	-2295655.131	0.003	0.0034	0.0503
2M26	3351701.821	4916159.903	-2295690.96	0.0029	0.003	0.002
2M27	3351932.799	4916180.856	-2295267.151	0.0015	0.0022	0.002
2M30	3350651.037	4916593.442	-2296014.673	0.0102	0.0142	0.0028

2M37	3351323.404	4916514.226	-2295221.187	0.0021	0.0077	0.002
2M38	3351231.247	4916378.591	-2295822.852	0.0072	0.008	0.0025
2M39	3351092.164	4916595.021	-2295418.193	0.0042	0.0102	0.0025

Piton de la Fournaise 1994 co-ordinates derived from EDM data (error ellipses in m)

Station	x	y	z	major axis	minor axis	Height
2M21	3352299.575	4915942.880	-2295244.442	0.0001	0.0001	0.0001
2M22	3351932.779	4916180.866	-2295267.216	0.0017	0.0037	0.0001
2M23	3351727.754	4916335.348	-2295197.040	0.0017	0.004	0.0001
2M24	3351679.252	4916231.498	-2295491.827	0.0022	0.004	0.0001
2M25	3351686.905	4916185.042	-2295655.130	0.0024	0.0036	0.0001
2M26	3351701.828	4916159.902	-2295690.953	0.0034	0.0037	0.0001
2M30	3350651.034	4916593.449	-2296014.661	0.0001	0.0001	0.0001
2M37	3351323.403	4916514.235	-2295221.171	0.0025	0.0034	0.0001
2M38	3351231.242	4916378.598	-2295822.844	0.0024	0.0035	0.0001
2M39	3351092.159	4916595.029	-2295418.184	0.0036	0.0031	0.0001

Piton de la Fournaise 1995 co-ordinates ASHTECH™ GPS

Station	x	y	z	Stations fixed during adjustment
2E52	3349599.662	4916151.017	-2298226.578	
2E54	3349778.017	4915886.842	-2298543.849	
2E55	3349565.051	4915949.033	-2298549.858	
2E56	3349816.987	4915573.115	-2299039.618	
2E51	3349637.728	4916530.236	-2297267.257	
1F20	3350202.265	4915254.53	-2299292.532	Fixed
2M21	3352299.575	4915942.879	-2295244.441	
2M22	3351932.767	4916180.867	-2295267.216	
2M23	3351727.737	4916335.334	-2295197.01	
2M24	3351679.221	4916231.456	-2295491.814	
2M25	3351684.919	4916179.032	-2295658.651	
2M26	3351701.83	4916159.978	-2295690.953	Fixed
2M27	3351932.808	4916180.958	-2295267.23	
1M30	3350717.696	4916506.654	-2296123.629	Fixed
2M30	3350650.929	4916593.306	-2296014.59	
2M37	3351323.35	4916514.149	-2295221.127	
2M38	3351231.182	4916378.527	-2295822.813	
2M39	3351092.075	4916594.895	-2295418.114	

B.4 Piton de la Fournaise EDM and GPS line-length measurements, 1993-95

Survey station		1993	1994	1995
From	To	Dec. EDM	May EDM	Jan. GPS
2M21	A2	437.8069		
2M21	2M23	695.1652	695.1654	695.1742
2M21	2M24	727.5287	727.5270	727.5406

2M21	2M26	777.0374	777.0279	777.0409
2M21	2M25	776.3190	776.3200	777.9068
2M24	2M25	169.9293	169.9583	174.9721
2M24	A2	342.5456		
2M25	A2	459.3539		
2M25	2M38	522.7032	522.7064	522.1351
2M25	2M37	654.8318	654.8435	659.1382
2M24	2M37	528.9818	528.9843	528.9904
2M38	2M37	623.6109	623.6190	623.6308
2M38	2M30	647.7651	647.7621	647.7664
2M25	2M23	483.8415	483.8454	489.2605
2M25	A2	459.3548		
2M23	A2	266.1325		
2M23	2M37	442.8103	442.8116	442.8157
2M39	2M37	314.3428	314.3492	314.3439
2M39	2M38	479.5147	479.5155	479.5285
2M39	2M30	741.8785	741.8752	741.8862
2M24	2M22		342.4800	342.4757
2M25	2M22		459.2827	463.3068
2M25	2M22		459.2827	
2M23	2M22		266.1304	266.1319
2M25	2M26	46.2432	46.2385	41.1396
1M21	1M22		437.8338	437.8420
1M21	1M30			1895.5691
2M24	1M30			1182.9921
2M26	1M30			1129.5678
1M21	2M30			1932.4118
1M30	2M38			
1M38	1M21			1290.6458
1M21	1M30			1895.5608
1M22	1M30			1521.8340
1M23	1M30			1381.3574
1M30	1M21			1895.5550
1M30	2M39			803.5510
2M37	1M21			1131.3318
2M37	1M30			1086.9122
2M39	1M21			1383.2298

B.5 Cumbre Vieja Cartesian WGS84 co-ordinates and error ellipses.

Cumbre Vieja 1994-5 ridge grid co-ordinates

Station	1994				1995			
	x	y	major axis	minor axis	x	y	major axis	minor axis
Bn01	46230.25	64829.05	1	0.2	46230.26	64829.04	24.2	7.3
oh02	46399.96	64539.1	0.9	0.2	46399.97	64539.09	24.6	7.1
ph03	46737.36	64768.94	1	0.3	46737.37	64768.94	24.4	8.2
av06	46133.82	63691.41	0	0	46133.82	63691.41	0	0
hb07	46020.62	66476.44	0.6	0	46020.62	66476.46	13.8	0
hd08	45871.78	65102.6	1.6	0.6	45871.79	65102.6	23.7	13.4

ho09	46037.58	64489.06	1	0.4	46037.58	64489.06	25.8	8.2
------	----------	----------	---	-----	----------	----------	------	-----

Cumbre Vieja 1997 ASHTECH™ GPS (error ellipses in m)

Station	x	y	z	mmajor axis	minor axis	Height
ap19	5341525.246	-1719130.629	3022404.893	0.014	0.001	0.0324
av06	5337688.109	-1717805.956	3033400.353	0.0041	0.004	0.0107
bn01	5337208.182	-1717550.556	3034404.766	0.015	0.009	0.0237
ee28	5337283.184	-1711753.083	3034746.982	0.0055	0.005	0.0132
hb07	5336314.015	-1717483.663	3035806.389	0.0058	0.005	0.0154
hd08	5336890.359	-1717825.054	3034597.229	0.007	0.005	0.0134
ho09	5337270.289	-1717772.886	3034086.722	0.0095	0.008	0.0255
jc22	5333837.917	-1720873.841	3035716.855	0.007	0.005	0.014
je13	5334917.294	-1721250.77	3033727.843	0	0	0
la17	5339847.516	-1721478.319	3023598.577	0.0097	0.008	0.0228
lh18	5341978.901	-1719565.036	3020967.984	0.0091	0.005	0.0154
nh12	5332824.838	-1723398.328	3035291.778	0.0028	0.002	0.0069
ob15	5340704.264	-1719667.42	3024473.878	0.0042	0.003	0.0096
oh02	5337421.064	-1717440.623	3034166.608	0.0047	0.004	0.0108
pc20	5340371.44	-1717228.947	3026646.123	0.0107	0.007	0.0204
ph03	5337413.287	-1717083.666	3034364.923	0.0094	0.007	0.0206
ru14	5336428.294	-1720713.873	3031525.005	0.0048	0.004	0.0113
sb23	5334287.113	-1723008.223	3032525.691	0.0036	0.003	0.0092

Cumbre Vieja 1998 using Leica™ (error ellipses in m)

Station	x	y	z	major axis	minor axis	Height
ab24	5338907.788	-1714791.352	3030350.284	0.0256	0.0232	0.026
ap19	5341525.233	-1719130.681	3022404.947	0.0209	0.0187	0.027
as30	5335020.088	-1720754.211	3033915.519	0.0142	0.0119	0.022
av06	5337688.070	-1717805.928	3033400.344	0.0077	0.0061	0.01
bn01	5337208.129	-1717550.529	3034404.765	0.0071	0.0054	0.009
ee28	5337283.185	-1711753.128	3034747.054	0.0241	0.0212	0.022
hb07	5336313.979	-1717483.635	3035806.392	0.0062	0.0046	0.007
hd08	5336890.319	-1717825.031	3034597.244	0.0077	0.0066	0.011
ho09	5337270.258	-1717772.852	3034086.726	0.0072	0.0059	0.01
jc22	5333837.938	-1720873.838	3035716.878	0.0101	0.0088	0.015
je13	5334917.352	-1721250.772	3033727.890	0.0157	0.0092	0.022
la17	5339847.512	-1721478.359	3023598.655	0.0195	0.0166	0.02
lh18	5341978.870	-1719565.060	3020968.020	0.0266	0.0215	0.038
nh12	5332824.837	-1723398.327	3035291.776	0.0077	0.0055	0.009
ob15	5340704.268	-1719667.446	3024473.949	0.0183	0.0156	0.017
oh02	5337421.021	-1717440.590	3034166.602	0.0065	0.005	0.008
pc20	5340371.442	-1717228.985	3026646.220	0.0204	0.0175	0.022
ph03	5337413.385	-1717083.664	3034365.006	0.0074	0.0062	0.011
pt11	5336117.438	-1719436.650	3033897.222	0.0151	0.0142	0.022
ru14	5336428.309	-1720713.874	3031525.003	0.0094	0.0069	0.012
sb23	5334287.116	-1723008.209	3032525.695	0.0098	0.0077	0.014
sc16	5337519.549	-1721669.880	3027600.763	0.021	0.0187	0.027

sv29	5332243.139	-1717357.948	3040964.740	0.0163	0.0107	0.02
ww04	5337742.404	-1717576.553	3033468.007	0.0075	0.0062	0.01

B.6 Cumbre Vieja EDM line length measurements (m)

Survey stations		1994	1996	1997	1997	1998
From	To	EDM	EDM	EDM	GPS	GPS
pt10	av06	2374.665	2513.083		2513.056	
ho09	pr11		2033.017			2033.01
hb07	ho09	1988.788	1988.81		1988.81	1988.81
hb07	oh02	1978.944			1978.962	1978.966
hd08	pr11		1919.572			1919.555
hb07	ph03	1856.382	1856.408		1856.4	1856.412
hb07	bn01	1663.875	1663.883		1663.898	1663.892
hb07	hd08	1382.297	1382.309		1382.313	1382.302
av06	ph03	1235.976	1235.982	1235.979	1235.971	1235.998
av06	bn01	1142.106	1142.101	1142.097	1142.105	1142.118
ww04	ph03	1075.063	1075.069	1075.073		1075.082
ww04	oh02	780.889	780.89	780.8927		780.902
hd08	ho09	638.497	638.499		638.5027	638.517
ww04	hc05	616.574	616.572			
hc05	hc05	514.266	514.266		514.2615	
bn01	ph03	511.525	511.523	511.5318	511.5093	511.542
hd08	bn01	461.949	461.95		461.9552	461.954
oh02	ph03	408.434	408.442	408.4371	408.4209	408.435
ho09	bn01	392.988	392.986	392.9864	392.9884	392.9837
ho09	oh02	373.513	373.515	373.5106	373.5152	373.507
bn01	oh02	337.826	337.829	337.8254	337.8331	337.8213
av06	ww04	245.244	245.245			245.242

APPENDIX C

STATION DESCRIPTIONS

The survey station descriptions are a rough guide to their locations, it is recommended that a handheld GPS receiver is used to locate the survey nails. Full detailed descriptions are freely available from the author.

C.1 The survey station descriptions from the Upper Eastern flank network of Etna.

Station ID	Name	X	Y	Z	type	date	location
e10	Flo	4880922.126	1307927.670	3883225.669	green disc	1981	040° from abandoned funivia, 136° from e8, on a pahoehoe flow within a collapsed lava tube
e11	XX	4881140.594	1307376.040	3883026.102	green disc	1981	From the abandoned funivia walk out across the lava following the same contour to the first outcrop
e12	Second	4881306.290	1307138.408	3882762.845	green disc	1981	West from XX slightly downslope on the next outcrop
e13	Lava Cave	4881255.661	1306882.938	3882935.582	green disc	1981	West from Second 318°, outcrop with cave, marker 2m SW from cave, 3m SE from cairn
e14	Lava peak	4881691.318	1307038.400	3881956.138	green disc	1981	Downslope from Second towards Monte Nero, an aa flow & 'grassy' area, marker on lower of two outcrops
e15	Monte Nero	4882109.726	1306690.437	3881356.648	green disc	1981	South side of rim of Monte Nero cone, approach from Lava Peak
e16	Car Park	4882091.192	1307456.646	3881125.102	green disc	1981	Halfway up road on 'clear' area south of road, cross aa flow disc near the cairn
e17	Far out	4881472.477	1305797.726	3882574.671	green disc	1981	South & down from Lava Cave, furthest edge of ash slope, where slope levels out
e18	Bad	4881495.723	1309268.814	3881259.995	green disc	1981	Downslope from Better on a flat green area near a cairn
e19	Better	4881278.366	1309249.375	3881859.118	green disc	1981	Downslope from Montagnola along the southern wall of the Valle del Bove, green patch on ridge up from the rim, near a cairn
e26	IC12	4880419.132	1306600.988	3884883.538	green disc	1971	Along the summit road past TDF, by the new road

APPENDIX C

STATION DESCRIPTIONS

e29	Path	4881403.813	1310013.347	3880737.452	green disc	1981	Halfway along the path from Ladybird to the road in a rock at the crest of a hill
e31	Bloody Brilliant	4880645.387	1308698.585	3883295.420	nail	1987	The lookout point for the Valle del Bove, second fence post from the right, 15m from the cliff on the right on a small raised slab
e32	Bloody Awful	4880865.634	1309255.123	3882120.698	nail	1987	Descend the ash slope from Montagnola into the Valle del Bove right past the first buttress and stop at the next, the nail is on the buttress
e33	Volcan's crease	4880041.090	1309811.800	3882357.246	nail	1987	Descend from Bloody awkward to the pahoehoe flow at the bottom, walk north across the flow towards the 1993 vent (may be dead since 1999?)
e37	Ruegg's Nail	4880297.143	1308481.261	3883985.410	large headed nail	?	Near the Belvedere shrine, towards the cliff from the Belvedere green disc
e39	GPS Bob	4880466.316	1307801.881	3884270.235	small square pin	1987	Roof of the Torre del Filosifo (TDF) south-west corner by fixed GPS, 3 rd strip of roofing in 1m from edge, 5mm square pin
e39gps	GPS	4880467.451	1307803.629	3884268.568	fixed GPS		SW corner of TDF roof, screw-thread mount
e42	Ashley's chunks	4880436.486	1307552.356	3884445.740	nail	1987	Up from road towards observatory vent, cross the aa flow to the right to the highest point, 334° to Observatory vent, 194° to MFS, 128° to TDF
e48	Montagnola	4881431.530	1308571.478	3882341.109	rusty rod	1993	Near the top by the aerials, measure 190cm from triple pole, 99cm from rusty pole, 130cm from x-shaped spike
e49	Climbing wall	4881557.962	1310340.221	3880054.764	nail	1993 (Sept.)	Lava levee above Zaffarana road by wall, walk across to second levee walk up ridge 5-10m
e5	First	4880497.699	1308637.647	3883586.431	green disc	1981	2m east of the highest point of an outcrop, on a flat ground level slab

APPENDIX C

STATION DESCRIPTIONS

e51	Spiny	4881276.193	1309634.224	3881530.837	nail	1993	Walk along rim of VDB past Better & a metal hoop onto, long green area, nail just down a stepped area with small bare patches, by a cairn & stick
e52	Ladybird	4881202.785	1310544.656	3880850.289	nail	1993	Walk down & along from Fracture past man-made circular structures, head SE towards 1792 cone keep on the flat, on black flat pahoehoe flow
e53	Seaview	4881099.282	1310699.476	3880910.998	nail	1993	From Ladybird walk seawards along ridge towards levee, 3m north of distinct pointy rock (193m-e52)
e54	Fracture	4881208.185	1309962.115	3881325.880	nail	1993	Walk down from Spiny along edge of rim, cross distinct 1989 fracture trace, stop by cracked slab of rock in the rim, nail 2m back in slab
e56	Silvestri Inferiori	4882239.531	1308683.447	3880099.578	green disc	1993	Southern rim of Silvestri Inferiori cone on concrete mound (tourist view point)
e6	Inter	4880700.363	1308285.410	3883458.106	green disc	1981	In a rock within a small group of boulders in the ash slope below TDF
e61	Indestructible	4881910.707	1310101.559	3879650.789	nail	1995	By entrance, walk back up road 15m then cross flow to right to furthest 'crag', nail in aa flow
e63	Yellow Bird	4881249.605	1310964.105	3880111.742	nail	1996	(near old Tesco's) on flat pahoehoe flow over barriers, small (3mm) vesicle filled with yellow paint, centre on middle of main blob
e65	Jo's arrow	4881320.947	1307878.490	3882513.834	corner of 90° spike	1996	concrete block near 1985 hornitos, metal 90° spike points NNE towards Belvedere, centre over the outer corner or tip of the point (arrow)
e66	Hot Concrete	4877509.301	1316724.404	3881493.194	nail	1996	Quarry road from Milo
e67	Serre la Nave	4883076.310	1306112.313	3879626.961	GPS Screw	?	A screw mounted in a block on concrete in the grounds of the astronomical observatory
e7	Cisternazza	4880831.525	1308470.933	3883126.439	green disc	1981	In the middle of a large boulder in front of the Cisternazza pit by the road
e8	Monte Frumento Supino	4880855.745	1307395.050	3883788.941	disc in stone cross	1981	In a cross etched in a slab of rock, 2m south of the windbreak on the top of Monte Frumento Supino (MFS)

C.2 Survey stations of the Lower Eastern flank networks, for locations see Figure C-1

Station ID	new ID	Name	X	Y	Z	type	date	location
c1	c3	WB	4877795.066	1323721.918	3877617.594	nail	1992	For Carruba survey stations see Figure C.1 Near small lay-by on left after town of Carruba, red mark on wall
c2		Blackberry	4877968.883	1323541.138	3877465.04	nail	1992	In a driveway of a house up a hill beyond nursery, by wall on right just before the gate.
c3		nursery	4877867.538	1323621.613	3877549.854	nail	1992	By furthest wall of the entrance to the nursery, 1m out from wall
c4		aga				nail	1992	DEAD
c5		swallow	4877828.603	1323716.777	3877573.206	nail in wall	1992	In high wall opposite WB, first nail you come to along the wall.
c6	c4	way-hey	4877975.988	1323580.623	3877438.387	nail	1995	turn right out from under the tunnel past the house and stop by the fence, nail in road close to wall
c7		spelky palms	4877806.913	1323740.469	3877591.927	nail in wall	1995	In the high wall further along from swallow
f1		Fondacello	4871291.272	1325373.189	3885024.855	nail	1996	North of the town of Fondacello along the coast road, past the last 'shops' on the right stop by first houses on the left, stop by first gate, nail in pavement 1.5m south of a lamppost .
f2		Piedimonte	4869511.201	1319179.412	3890092.901	nail	1996	West of Piedimonte over the rail tracks, stop by octagonal house, nail 2m in from the road in the left end of the driveway entrance.
m1		minty				nail	1992	See Macchia survey stations, Figure C-1. On the top of the cliff, one furthest downhill
m2		apex	4876289.374	1319815.116	3881273.457	nail	1992	higher nail at the viewpoint at the top of the cliff

APPENDIX C

STATION DESCRIPTIONS

m3		brush				nail	1992	dead
m4		lemon	4875821.154	1320341.283	3881424.628	nail	1992	in the middle of a gateway just after a small shed before the water-tank
m5		lay-by				nail	1992	in a lay-by at the base of the viewpoint, near the middle (often has 'stuff' dumped on it)
m6		doggy				nail	1992	near a gateway with two stone dogs, by the pylons down from the viewpoint.
v1		Rachel				nail	1994	See Vena survey stations, Figure C-1., near a small hole in the wall
v2	v4	fanta	4871746.596	1317458.575	3888425.027	nail	1994	just before the bend where the wall is kinked
v3		oak tree				nail	1994	dead - on a stone under an oak tree 4m NW of break in white line
v4		vine				nail	1994	along the road by the 'broken house' by a telephone post and a lemon grove
v5	v5	orange gate	4872057.577	1317426.954	3888088.531	nail	1995	further along the Vena road by a large orange gate before the breaks in the road.
t1		Guinness				nail	1994	Trecastagni survey stations see Figure C-1.
t2		sweaty				nail	1994	
t3		dead bird				nail	1994	
t4		motorbike				nail	1994	

APPENDIX C

STATION DESCRIPTIONS

C.3 The survey stations of the Piton de la Fournaise Rift-Zone Network

The terrain around the survey stations and the path through the network has been greatly altered by the 1998 eruption in the middle of the network. The station locations are thus brief and only should be used to distinguish the stations, the GPS (handheld) should be used to locate the nails in the future.

Station ID	old ID	Name	X	Y	Z	type	year	Location
2M21	A1	Burn	3352299.575	4915942.879	-2295244.441	Nail	1993	head eastward along the path away from the crater path, nail is on the first raised lava slabs in the rift-zone.
2M22	A2	Aussie	3351932.767	4916180.867	-2295267.216	Nail	1993	dead?
2M23	A3	Frazzle	3351727.737	4916335.334	-2295197.01	Nail	1994	dead -covered in lava in 1998
2M24	A4	Cocked leg	3351679.221	4916231.456	-2295491.814	Nail	1993	dead -covered in lava in 1998
2M25	A5	Not nodger	3351684.919	4916179.032	-2295658.651	Nail	1993	abandoned
2M26	A6	Patrick's tripod	3351701.83	4916159.978	-2295690.953	French Nail	1993	up from the path near the magnetic stations
2M27	2	Dead Aussie	3351932.808	4916180.958	-2295267.23		1993	dead
2M37	A7	Big Grey Bit	3351323.35	4916514.149	-2295221.127	Nail	1993	dead -covered in lava in 1998
2M38	A8	Walnut	3351231.182	4916378.527	-2295822.813	Nail	1993	up from the path on a pahoehoe slab within a lava levee
2M39	A9	Faujas	3351092.075	4916594.895	-2295418.114	Nail	1993	dead -covered in lava in 1998
2M30	A10	Blister	3350650.929	4916593.306	-2296014.59	Nail	1993	after Cochard (left) north of the path 20m on a raised pahoehoe slab
1M30		Cordemoy	3350717.696	4916506.654	-2296123.629	GPS Nail	1992	on a near a lava tube on a flat slab near the edge of a lava levee
1F20		Chateau Fort	3350202.265	4915254.53	-2299292.532	GPS Pillar	1993	East of the Dolomieu crater
2 E51	B11	Chod	3349637.728	4916530.236	-2297267.257	Nail	1993	just before the surface fractures in a lava levee up from the path
2 E52	B12	Crack	3349599.662	4916151.017	-2298226.578	Nail	1993	past the large (50-100cm) surface fractures down from the path
2 E53	B13	Signal				Fr. Nail	1993	On the Signal de l'Enclos cone

APPENDIX C

STATION DESCRIPTIONS

2 E54	B14	Silver	3349778.017	4915886.842	-2298543.849	Nail	1993	On a silvery pahoehoe slab down from the path
2 E55	B15	Square	3349565.051	4915949.033	-2298549.858	Nail	1993	up from silver at the top of the lava levee
2 E56	B16	Dog	3349816.987	4915573.115	-2299039.618	Nail	1993	500m along the path from Silver at the base of a small cone on the right of the path
COASTAL NETWORK								
2A44		Blowhole	3345639.669	4911043.386	-2309480.628	Nail	1994	north of St. Philippe stop in a lay-by near a rocky outcrop by the seam where the sea blows up through a natural hole
2A45		Restauration	3341261.467	4916482.974	-2304490.513	Nail	1994	In a carpark by a restaurant
2A43		Cyclone Vert	3342643.258	4913696.081	-2308241.136	Nail	1994	In the centre of the Grand Brule by the lay-by near the information post
2G21		Virgin	3342872.732	4920170.005	-2294163.675	Nail	1994	Near a shrine in a carpark
2A55		Moustic	3346656.096	4922093.384	-2284409.448	Nail	1993	near the natural swimming pool, on the top of the cliff
1A60		BelAir	3341969.292	4922879.051	-2290010.324	GPS Nail	1993	By the top of a hill near to the French benchmark

C.4 The survey station descriptions from the Cumbre Vieja Network.

Station ID	old ID	Name	X	Y	Z	type	year	Location
bn01	1	black hole	5348300.03	-1959934.924	3040705.563	nail	1994	Top of the ridge, 20m from the north rim of the Hoya Negro 1.5m right of the path on a patch of grey indurated ash in the middle of a cross made of stones.
oh02	2	overhang	5348485.192	-1959750.430	3040450.791	nail	1994	Top of the ridge, on the south rim of the Hoya Negro, on the highest point of the rim, nail in a triangular rock 5m from edge.
ph03	3	pillar the hun	5348483.244	-1959383.892	3040652.864	pillar	1994	Pillar on top of Nambroque
ww04	4	windy whatsit	5337742.404	-1717576.553	3033468.007	nail	1994	nail in boulder over looking Crater Fraile in cinders on the opposite side of the ridge to Atlantic view, small cairn
hc05	5	hooded	5349035.388	-1960009.825	3039256.291	pillar	1994	<i>Dead - pillar collapsed</i>

APPENDIX C

STATION DESCRIPTIONS

av06	6	chuff Atlantic view	5348792.514	-1960039.360	3039705.668	rod	1994	top of the western rim of Duraznero on a promontory marked by tape
hb07	7	howling Barquita	5347479.339	-1960163.254	3042153.258	rod	1994	top of southern rim of Barquita from the road up the zig-zag path to the top, along the path past the tree for 25 paces, rod is 1m up from path by large cairn & wind break.
hd08	8	hound	5348064.433	-1960324.523	3040945.875	nail	1994	from the bottom of the barranco that goes under the bridge (as you ascend to the top of the ridge) walk west up through the pine woods then head south towards a forked tree along the ridge (Hierro is further along the ridge)
ho09	9	Hierro	5348396.941	-1960144.165	3040406.7	rod	1994	western rim of the Hoya Negro opposite overhang (oh02) on slight promontory
pr10	10	P.I.R.S	5348650.203	-1962332.142	3038735.628	nail	1994	at the P.I.R.S building (near to ru14) walk ~50m down the lava ridges 20-30m to the right of the fence the nail is on a flat aa lava flow couple of m west of the highest point
pt11	11	the pits	5336117.438	-1719436.650	3033897.222	two nuts on a piece of studding	1994	on the western rim of the large craters above Jedey (stop along the forest track by the two large pits with few trees) walk down the right of the pits following the ridge, down the lava flows and along a narrow ridge, the rod is 188cm from forked tree & a narrow path to the left.
nh12		its no holiday	5345294.897	-1967441.947	3042389.378	nail	1994	nail (temp base station nail) in rock by lay-by garden, 11 rocks up from the corner (with table & benches(by a large pink flowery bush
je13		Jedey	1147043.307	-1957412.594	-6241631.91	pillar	1994	Pillar at Jedey on top of the hill
ru14		rustling bushes	5348511.057	-1963465.080	3038387.438	nail	1994	first lay-by on the right after the Jedey barranco, right of a flat rock in the middle of the lay-by, 17 paces from the south end.
ob15		orange blob	5352877.012	-1960960.227	3031366.06	rod	1994	on a hill on the right before the San Antonio car park, between the boulders on top of the hill, 19cm from orange

APPENDIX C

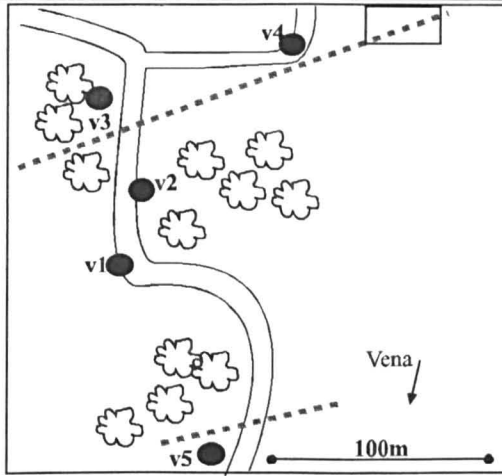
STATION DESCRIPTIONS

								(lichen) boulder, 36cm from opposite rock, 6mm diameter rod.
sc16		sea cave	5337519.549	-1721669.880	3027600.763	nail	1994	along from Puerto Rico, just after a small house on the left, the nail is 15 paces from the white line in the middle of the road by to the back and left of the lay-by
la17		Larga	5352561.575	-1963116.265	3030798.445	nail	1994	In the small fishing hamlet of Larga by the beach-bar, the nail is in a, flat stone just in the edge of the beach, by the wall about 5m in from the ramp. MEASURE AT LOW TIDE
lh18		lighthouse	5354693.613	-1960430.672	3028159.044	nail	1994	By the old lighthouse on the southern tip of the island, on a flat slab of pahoehoe in front of the cliff
ap19		apricot	5354077.436	-1960132.664	3029507.422	nail	1994	(west of island - just) by a small wall on the road up from the lighthouse towards Fuencaliente, 1m before the start of the wall
pc20		pine cone	5352452.503	-1958550.814	3033491.397	nail	1994	(west of island) along the west road away from Fuencaliente, stop by dirt track to the right and small house on the left. The nail is on the small ridge on the seaward side of the road.
ho21		Hoopoe	5351806.784	-1960936.604	3033435.886	stone pillar	1994	on the upper road of the rift-zone up from Fuencaliente by a view point to the left open towards the sea after a drive up through the woods, the mark is a hole in the top of a small concrete pillar.
jc22		junction	5346000.758	-1964493.944	3042638.065	nail	1994	at the junction of the roads to Jedey (south) - Puerto Naos and El Paso, there is a house with a track cutting off the junction, the nail is in a pahoehoe slab 10m within the junction.
sb23		sea banana	5346941.239	-1966550.573	3039720.185	nail	1994	down the hill from Fuencaliente back along the road towards the north as far as possible, on entering the banana groves turn left at a small house with a green door to reach a cliff above the sea, stop and walk west towards a small platform on the left overhanging the cliff slightly

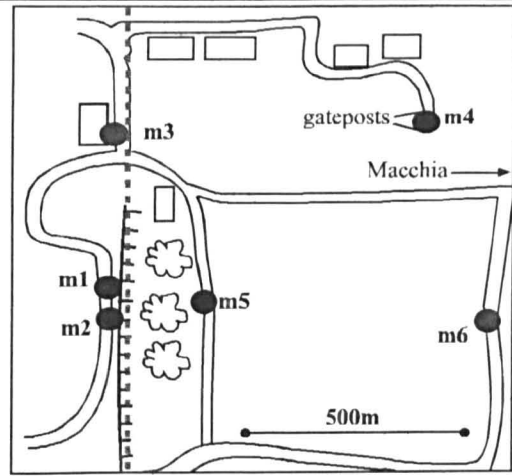
APPENDIX C

STATION DESCRIPTIONS

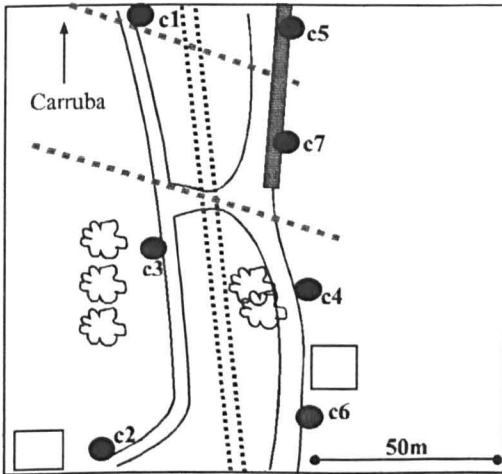
ab24		aniseed	5338907.788	-1714791.352	3030350.284	nail	1998	(west of island) along the western road (heading N) just past the 'Guanche' caves, stop by a pull in on the left with a house above on the hill, there is a distinctive outcrop on the right, the nail is just down from the highest point.
dd27		delias dyno-rod	5346658.615	-1959291.564	3044194.439	rod	1994	dead
ee28		east of eden	5349487.341	-1953912.324	3041685.123	nail	1994	(west of island) along the western road (heading N) past aniseed, the nail is just on the right in a small pull-in (break in white line in road) nail 4m up track on the right
sv29		santa claus valley	5332243.139	-1717357.948	3040964.740	nail	1998	from El Paso, turn left immediately before the visitor centre drive from about 1km until you see a small road to the right by a big tree, stop and climb back onto the rock field overlooking the road, the nail is slightly west of the highest point on a flat rock.
as30		alpine scalectrix	5335020.088	-1720754.211	3033915.519	nail	1998	take the road up to the Jedey dome, as you ascend follow the road until you see a right turn which goes up and into the woods (last before road splits under dome) stop just before the road goes into the woods, nail on pahoehoe slab 3m to the right.



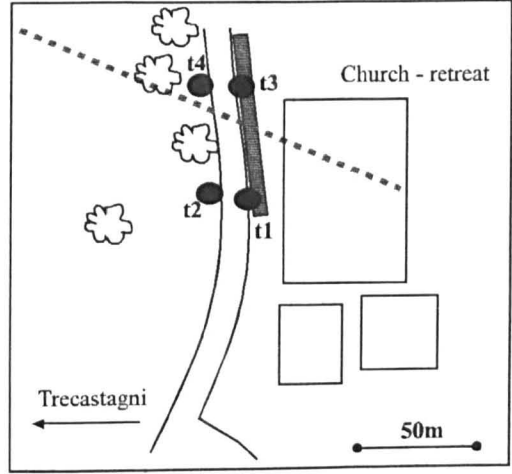
a, Vena



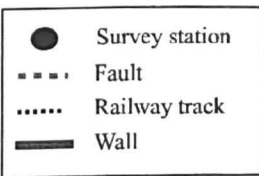
b, Macchia



c, Carruba



d, Trecastagni



Abdel-Monem A., Watkins N. D. and Gast P. W. (1972) Potassium Argon ages, volcano stratigraphy and geomagnetic polarity history of the Canary Islands: Tenerife, La Palma and Hierro. *American Journal of Science*. **272**, 805-825.

Alparone S., Pellicori O., Ursino A., Ferruci F., Gresta S., & Guerra I. (1994) Shallow microseismic swarms and intrusive mechanisms at Mount Etna: 1989-1991. *Acta Vulcanologica*, **4**, 75-79.

Ancochea E., Hernan F., Cendrero A., Cantagrel J.M., Fuster J.M., Ibarrola E. and Coello, J. (1994) Constructive and destructive episodes in the building of a young Oceanic Island, La Palma, Canary Islands, and genesis of the Caldera de Taburiente. *Journal of Volcanology and Geothermal Research* **60**, 243-262.

Anguita F. and Hernán F., (1975) A propagating fracture model versus a hot spot origin for the Canary Islands. *Earth Planet. Sci. Letters*. **27**(1), 11-19.

Armienti P., Innocenti R., Petrini R., Pompilio M., & Villari L. (1989) Petrology & Si-Nd Isotope geochemistry of recent lavas from Mt. Etna bearing on the volcano feeding system. *Journal of Volcanology and Geothermal Research*, **39**, 315-327.

Bachelery P. (1981) *Le Piton de la Fournaise (Ile de la Reunion); etude volcanologique, structurale et petrologique*. Univ. Clermont II, France.

Bachelery P., Lénat J-F., Delorme H., Toutain J-P., Chemineé J-L. (1990) 1930 to 1990 eruptive activity at Piton de la Fournaise volcano: Structural insights on the magma storage and feeding systems. *Preprint*.

Barberi F., and Carapezza M. L., (1996). The problems of volcanic unrest: the Campi Flegrei case history. *Proceedings of the course the mitigation of volcanic hazards, Vulcano, Italy, 1994*. Environment and Climate Programme, European Commission.

Bawden G., W., Donnellan A., Kellogg L., H., Dong D. and Rundle J., B. (1997) Geodetic measurements of horizontal strain near the White fault, Kern County, California. *Journal of Geophysical Research* **102** (B3):4957-4968.

Birch F., (1966) Compressibility; Elastic constants. In *Handbook of Physical Constants*. Memoir 97, ed S. P. Clark, the Geological Society of America. New York.

- Blewitt G. (1997) Basics of the GPS technique: Observation Equations. [In: *Geodetic Applications of GPS*, Swedish Land Survey].
- Bock Y., Abbot R.I., Counselman III C.C., Gourevitch S.A. and King R.W. (1985) Establishment of three-dimensional geodetic control by interferometry with the Global Positioning System. *Journal of Geophysical Research* 90 (B9):7689-7703.
- Bonaccorso A. (1996) Dynamic inversion of ground deformation data for modelling volcanic sources (Etna 1991-93). *Geophysical Research Letters* 23, 451-454.
- Bonaccorso A. and Davis P.M. (1993) Dislocation modelling of the 1989 dike intrusion into the flank of Mount Etna, Sicily. *Journal of Geophysical Research* 98, 4261-4268.
- Bonaccorso A., Verlardita R. and Villari L. (1994) Ground deformation modelling of geodynamic activity associated with the 1991-1993 Etna eruption. *Acta Vulcanologica* 4, 87-96.
- Bonelli Rubino J. M. (1950) *Contribucion al estudio de la erupcion del Nambroque a San Juan (Isla de la Palma)* Madrid, Instituto Geografico y Catastral, 25.
- Borgia A., Garduño V. H., Neri M., Pasquaré G. and Tibaldi A. (1994) Dislocation rate, kinematics and evolution of the system - North0east Rift-Pernicana Fault, Mount Etna, Italy. In *Sea-level change and the stability and activity of coastal and island volcanoes*, Environment Programme Contract EV5V-CT92-0170, Intrim report, Commission of the European Communities, Brussels, 236.
- Bousquet J-C., Lanzafame G. and Paquin C. (1988) Tectonic stresses and volcanism: in-situ stress measurements and neotectonic investigations in the Etna area (Italy). *Tectonophysics* 149 219-231.
- Brantley. and Topinka. (1984) Volcanic Studies at the U.S Geological Survey's David A. Johnston Cascades Volcano Observatory, Vancouver, Washington. *Earthquake Information Bulletin*. 16 (2):79-84.
- Briole P., Nunnari G. and Puglisi G (1990) Ground deformations: GPS and IPGP Tilt data. In *Mt. Etna: the 1989 eruption*. Barberi F., Bertagnini A., Landi P. (eds) 47-53. Pisa: Giardini.
- Briole P., Gaulon R., Nunnari G., Puglisi G. and Ruegg J.C. (1992) Measurements of ground movement on Mount Etna, Sicily: A systematic plan to record different temporal and spatial

components of ground movement associated with active volcanism. In: Gasparini P., Scarpa R. and Aki K. (Eds.) *Volcanic Seismology*, pp. 120-132. Berlin Heidelberg: Springer-Verlag]

Briole P., Bachèlery P., McGuire W.J., Moss J.L., Ruegg J.C. and Sabourault Ph. (1996) Deformation monitoring of Piton de la Fournaise: Evolution of the monitoring techniques and knowledge acquired in the last 5 years. *2nd Workshop on European Laboratory volcanoes*. (In Press)

Briole P., Ruegg J-C., Chemineé J-L., Ammann J., Bachèlery P., Brefort D., Delmond J-C., Kowalski Ph., Sabourault Ph., McGuire W. J., Moss J. L. (1997) Deformation of Piton de la Fournaise: Evolution of the monitoring techniques and knowledge acquired in the last 5 years. IACEI General Assembly, Puerto Rico.

Bruyninx C. and Warnant R. (1995) Detection of ground movements on the Mt. Etna volcano using the Global Positioning System. *Acta Vulcanologica* 7 (1):27-33.

Bulmer M. H. and Guest J. E. (1996) Modified volcanic domes and associated debris aprons on Venus. In *Volcanic instability on Earth and other Planets*. McGuire W. J., Jones A. P. and Neuburg J. (eds) The Geological Society of London.

Burgmann R., Segall P., Lisowski M. and Svarc J. (1997) Postseismic strain following the 1989 Loma Prieta earthquake from GPS and leveling measurements. *Journal of Geophysical Research* 102 (B3):4933-4956.

Burnside C. D., (1991) *Electromagnetic distance measurement*, 3rd edn. London: Blackwell.

Butler R. W. H., Grasso M., & La Manna F. (1992) Origin and deformation of the Neocene-Recent Maghrebian foredeep at the Gala Nappe, SE Sicily. *Journal of the Geological Society, London*. 149, p547-557.

Calvari S., Coltelli M., Neri M., Pompilio M. and Scribano V. (1994) The 1991-1993 Etna eruption: Chronology and lava flow-field evolution. *Acta Vulcanologica* 4 1-14.

Calvari S., Gropelli, G. & Pasquarè G. (1996) The last 100,000 years of Mount Etna's history as inferred from a geological survey of the south-western wall of the Valle del Bove. In: *Etna: 15 years on*. Gravestock P. G., & McGuire W. J. (Eds) ODA/Cheltenham & Gloucester College of Higher Education, 16-19.

Carracedo J. C. (1994) The Canary Islands: an example of structural control on the growth of large oceanic-island volcanoes. *Journal of Volcanological and Geothermal Research*. 60.

Carracedo J. C. (1996) A simple model for the genesis of large gravitational landslide hazards in the Canary Islands. In: *Volcano instability on the Earth and other planets*. McGuire W. J., Jones A. P. and Neuberg J. (eds) Geological Society London.

Carracedo J. C. (1997) Late (Quaternary) shield-stage volcanism in La Palma and El Hierro, Canary Islands. *Proceedings of the International workshop on Immature Oceanic Island Volcanoes, La Palma*. Abstract, 61 p.

Carracedo J. C., Day S., Guillou H., Rodriguez Badiola E., Canas J. A. and Pérez Torrado J. F. (1997a) Geochronological, structural and morphological constraints on the genesis and evolution of the Canary Islands. *Proceedings of the International workshop on Immature Oceanic Island Volcanoes, La Palma*. Abstract.

Carracedo J.C., Day S.J. and Guillou, H. (1997b) The Cumbre Nueva collapse and Cumbre Vieja volcano. In: Estacion Volcanologia de Canarias and the Depto. de fisica-Geologia, U.d., Grand Canaria, (Ed.) *Excursion Guidebook*, pp. 1-28.

Carracedo, J.C., Day, S.J., Guillou, H. and Gravestock, P. (1997c) The later stages of the volcanic and structural evolution of La Palma, Canary Islands: The Cumbre Nueva giant Collapse and the Cumbre Vieja Volcano. Submitted to *Journal of Volcanology and Geothermal Research*.

Carracedo, J.C., Day, S.J., Guillou, H. and Gravestock, P. (1997d) Spain. Geological colour map (1/33,000) of the Cumbre Vieja Volcano, La Palma, Canary Islands. [1/33000] 1st edn. Canary Islands: Consejo Superior de Investigaciones Cientificas and Cons. Politica Territorial, Gobierno Canarias.

Chester D. K. and Duncan A. M. (1982) The interaction of volcanic in Quaternary times upon the evolution of the Alcantara and Simento rivers, Mount Etna, Sicily. *Catena*, 9, 319-342.

Chester D.K., Duncan A.M., Guest J.E. and Kilburn C.R.J. (1985) *Mt Etna: the anatomy of a volcano*. London: Chapman and Hall.

Chevallier L. & Bachèlery P., (1981) Evolution structurale du volcan actif du Piton de la Fournaise, Ile de la Réunion, Ocean Indien Occidental. *Bulletin of Volcanology*. 44 (4): pp723-741.

Chevallier L. & Verwoerd W.J. (1988) A numerical model for the mechanical behavior of intraplate volcanoes. *Journal of Geophysical Research* **93** (B5):4182-4198.

Clague D. A. and Denlinger R. (1994) Role of Olivine cumulates in destabilizing the flanks of Hawaiian volcanoes. *Bulletin of Volcanology*, **56**, 425-434.

Clocchiatti R., Joron J. J., and Treuil M. (1988) The role of selective alkali contamination in the evolution of recent historic lavas of Mount Etna. *Journal of Volcanological and Geothermal Research*, **34**, 241-249.

Cocina O., Neri G., Privitera E., and Spampinato S. (1995) Evidences of magma uprise at Mount Etna from hypocenter locations and stress tensor inversion. *Per. Mineral*, **64**, 137-139.

Coltelli M., Garduno V.H., Neri M., Pasquare G. and Pompilio M. (1994) Geology of the northern wall of the Valle del Bove, Mt Etna (Sicily). *Acta Vulcanologica* **5** 55-68.

Condomines M., Tanguy J-C., and Michaud V. (1995) Magma dynamics at Mt Etna: constraints from U-Th-Ra-Pb disequilibria and Sr-isotopes in historical lavas. *EPSL*, **132**, 25-41.

Cristofolini R., Patané G., & Recupero, S. (1982) Morphological evidence for ancient volcanic centres and indications of magma reservoirs underneath Mt. Etna, Sicily. *Geografica Fisica e Dinamica del Quaternario*, **5**, 3-9.

Crook C. N., (1984) Geodetic measurements of horizontal crustal deformation associated with the October 15, 1979 Imperial Valley (California) earthquake. Thesis, *Imperial College of Science and Technology* - **34-7623**.

Davis P.M., Hastie L.M. and Stacey F.D. (1974) Stresses within an active volcano - with particular reference to Kilauea. *Tectonophysics* **22**, 355-362.

Day S.J. (1996) Hydrothermal pore fluid pressure and the stability of porous, permeable volcanoes. In: McGuire W.J., Jones A. P. and Neuberg J. (Eds.) *Volcano Instability on the Earth and Other Planets*, pp. 77-94. London: Geological Society]

Day S. J., Carracedo J. C., Guillou H and Gravestock P. (1998) Recent structural evolution of the Cumbre Vieja volcano, La Palma, Canary Islands: volcanic rift zone reconfiguration as a precursor to volcano flank instability. Submitted to *Journal of Volcanology and Geothermal Research*, July 1998.

- Dclancy P., T., Fiske R., S., Miklius A., Okamura A., T. and Sako M., K. (1990) Deep Magma Body Beneath the Summit and Rift Zones of Kilauea Volcano, Hawaii. *Science* **247** 1265-1372.
- Delorme H., Delarue J-F. and Bachèlery P. (1989) Reports from the Observatoire Volcanologique du Piton de la Fournaise. *Sean. Bull.* **11** (1-3, 6, 7, 11 & 12):
- Denlinger R., P. and Okubo P. (1997) A huge landslide Structure on Kilauea Volcano, Hawaii. Submitted to *Journal of Geophysical Research*.
- Denlinger R.P. and Okubo P. (1995) Structure of the mobile south flank of Kilauea volcano, Hawaii. *Journal of Geophysical Research* **100**, 24499-24508.
- Dieterich J. (1988) Growth and persistence of Hawaiian Volcanic Rift Zones. *Journal of Geophysical Research* **93**, 4258-4270.
- Dieterich J. and Decker R.W. (1975) Finite element modelling of surface deformation associated with volcanism. *Journal of Geophysical Research* **80** (29):4094-4102.
- Dikau R., Brunsten D., Schrott L., Ibsen M-L. (eds.) (1997) *Landslide recognition: identification, movement and causes. Report no.1 of the European Commission environment programme, contract number EV5V-CT94-0454*. John Wiley & Sons, Chichester.
- Dixon T., H., Farina F., Mao A., Webb F., Bursik M., Stein R. and Marshall G. (1995) GPS Monitoring Data for active volcanoes available on Internet. *Transactions of the American Geophysical Union*. **76** 2
- Duffield W.A., Stieltjes L. and Varet J.. (1982) Huge Landslide blocks in the growth of Piton de la Fournaise, La Reunion, and Kilauea Volcano, Hawaii. *Journal of Volcanology and Geothermal Research* **12**, 147-160.
- Dzurisin D., Koyanagi R. Y. and English T. (1984) Magma supply and storage at Kilauea volcano, Hawaii. *Journal of Volcanology and Geothermal Research*, **21**, 177-206.
- Elsworth D. and Voight B. (1995) Dike intrusion as a trigger for large earthquakes and the failure of volcano flanks. *Journal of Geophysical Research*

Feraud G, Giannerini G, Camnpredon R. and Stillman C. J. (1985) Geochronology of some Canarian dykes swarms: contribution to the volcano-tectonic evolution of the Archipelago, *Journal of Volcanological and Geothermal Research*. **25**, 29-52.

Ferrucci F., Gaudiosi G., Azzaro R. and Imposa S. (1993) Mt Etna: a model for the 1989 eruption. *Journal of Volcanology and Geothermal Research* **56** 35-56.

Ferrucci F. and Patane D. (1993) Seismic activity accompanying the outbreak of the 1991-1993 eruption of Mt. Etna (Italy). *Journal of Volcanology and Geothermal Research* **57** 125-135.

Fiske R. S. and Jackson E.D. (1972) Orientation and growth of Hawaiian volcanic rifts: the effect of regional structure and gravitational stresses. *Proceedures of the. Royal Society of London. A*. **329** 299-326.

Forgione G., Luongo G., & Romano R. (1989) Mt. Etna (Sicily): Volcanic Hazard Assessment. IACEI Proceedings in Volcanology, 1. *Volcanic Hazards*. Latter J. H., (Ed) Springer - Verlag, Berlin, Heidelberg. 137-150.

Foulger G. R., Bilham R., Morgan J., and Einarsson P. (1987) The Iceland geodetic field campaign 1986. *EOS* **68**, 1801-18.

Frazzetta G. and Villari L. (1981) The feeding of the eruptive activity of Etna volcano. The regional stress field as a constraint to magma uprising and eruption. *Bulletin of Volcanology*, **44**.

Frei E. and Schubernigg M. (1992) GPS surveying techniques using the 'Fast Ambiguity Resolution Approach (FARA)'. 34th Australian Surveyors Congress and the 18th National Surveying Conference at Cairns, Australia, May 23-29.

Gee, J., Staudigel, H., Tauxe, L. and Pick, T. (1993) Magnetization of the La Palma Seamount series: Implications for seamount Paleopoles. *Journal of Geophysical Research* **98**, 11743-11767.

Genrich J., F., Bock Y. and Mason R., G. (1997) Crustal deformation across the Imperial Fault: Results from kinematic GPS surveys and trilateration of a densely spaced, small aperture network. *Journal of Geophysical Research*. **102** (B3):4985-5004.

Gillot P. Y., & Nativel P., (1989) Eruptive history of Piton de la Fournaise volcano, Réunion Island, Indian Ocean. *Journal of Volcanological and Geothermal Research*. **36**, 53-65

Gillot P. Y., Kieffer G., and Romano R (1994) The evolution of Mount Etna in the light of Potassium-argon dating. *Acta Volcanologica*, **5**, 81-88.

Guest J. E. and Duncan A. (1981) Internal plumbing of Etna. *Nature*, **290**, p584-586.

Guest J. E., Chester D. K. and Duncan A. M., (1984) The Valle del Bove, Mount Etna: its origin and relation to the stratigraphy and structure of the volcano. *Journal of Volcanological and Geothermal research*, **21**, 1-23

Guillou H., Carracedo J-C., Day S. J., (1997) Dating of the upper Pleistocene - Holocene volcanic activity of La Palma using the Unspiked K-Ar technique. Submitted to Journal of Volcanological and Geothermal Research.

Grindley G. W. (1973) Structural control of volcanism at Mount Etna. *Philosophical Transactions of the Royal Society of America*. **274**, 165-175.

Hansteen T., Klügel A., and Schmincke H.U. (1997) Magnetic underplating and crustal magma accumulation beneath the Canary Island Archipelago as evidenced by fluid inclusions. *Internat. Workshop on Immature Oceanic Volcanoes*. Sept.

Head J. W. (1996) Volcano instability development: a planetary perspective. In McGuire W.J., Jones A. P. and Neuberg J. (Eds.) Volcano Instability on Earth and other Planets. Geological Society Special Publication No. 110. P1-24.

Hernandez-Pacheco A. (1971) Nota previa sobre el Complejo Basal de la Isla de la Palma (Canarias). *Estud. Geol.* **27**, 255-265.

Hofmann-Wellenhof B., Lichtenegger H., and Collins J., (1997) *Global Positioning System Theory and Practice*. 4th edition, Springer-Verlag Wien, New York.

Holcomb R.T. and Searle R.C. (1991) Large landslides from Oceanic Volcanoes. *Marine Geotechnology* **10**, 19-32.

Iwatsubo and Swanson (1966) Methods Used to Monitor Deformation of the crater Floor and Lava Dome at Mount St. Helens, Washington: In: Ewert and Swanson (Eds.), Monitoring Volcanoes: Techniques and Strategies Used by the staff of the Cascades Volcano Observatory. *U. S Geological Survey Bulletin*. **223**

Kendall M. G. and Stuart A. (1965) *The advanced theory in statistics*, Macmillan

Kieffer G. (1985) Evolution structurale et dynamique d'un grand volcan poligenique: stades d'édification et activité actuelle de l'Etna (Sicile). PhD Thesis, Univ of Clermont Ferrand, 497 pp.

Klügel, A., Hansteen, T.H. and Schmincke, H. (1997) Rates of magma ascent and depths of reservoirs beneath La Palma (Canary Islands).

Kokelaar P. and Romagnoli C. (1995) Sector collapse, sedimentation and clast population evolution at an active volcano: Stromboli, Italy. *Bulletin of Volcanology* 57 240-262.

Labazuy Ph. (1996) Recurrent landslides events on the submarine flank of Piton de la Fournaise (Réunion Island). In McGuire W.J., Jones A. P. and Neuberg J. (Eds.) *Volcano Instability on Earth and other Planets*. Geological Society Special Publication No. 110. P1-24

Labaume P., Bousquet J-C. and Lanzafame G. (1990) Early deformations at a submarine compressive front: the Quaternary Catania foredeep south of Mount Etna, Sicily, Italy. *Tectonophysics*, 177, 349-366.

Lanzafame G., Neri M. & Rust D., (1996) Active tectonics affecting the eastern flank of Mount Etna: structural interactions at a regional and local scale. In: *Etna: 15 years on*. Gravestock P. G., & McGuire W. J. (Eds) ODA/Cheltenham & Gloucester College of Higher Education, 22-24.

Latora V., Rapisarda A., & Vinciguerra S. (1996) Microseismicity affecting the low time-clustering properties of the eastern flank of Mount Etna between 1989 and 1994. In: *Etna: 15 years on*. Gravestock P. G., & McGuire W. J. (Eds) ODA/Cheltenham & Gloucester College of Higher Education, 20-22.

Lénat J-F (1989) Patterns of volcanic activity of Piton de la Fournaise (Réunion Island, Indian Ocean). A synthesis based on monitoring data between 1980 and July 1985, and in historic records since 1930. In Latter J. H. (Ed) *Volcanic Hazards, IAVCEI Proceedings in Volcanology*.

Lénat J-F. and Aubert M. (1982) Structure of Piton de la Fournaise volcano (La Reunion Island, Indian Ocean) from magnetic investigations. An illustration of the analysis of magnetic data in a volcanic area. *Journal of Volcanology and Geothermal Research* 12, 361-392.

Lénat J-F., Bachèlery P. (1990) Structure et Fonctionnement de la zone centrale du Piton de la Fournaise. In Lénat J-F. (Ed) *Le Volcanisme de La Réunion Monographie. Centre des recherches Volcanologies*, Clermond Ferrand, 257-296.

Lénat J-F, Bachèlery P., Bonneville A., Tartis P., Cheminee J-L and Delorme H. (1989) The December 4,1983 to February 18,1984 eruption of Piton de la Fournaise (La Reunion, Indian Ocean): Description and Interpretation. *Journal of Volcanology and Geothermal Research* 36 87-112.

Lénat J-F., Vincent P. and Bachèlery P. (1989) The off-shore continuation of an active basaltic volcano: Piton de la Fournaise (Reunion Island, Indian Ocean);structural and geomorphological interpretation from sea beam mapping. *Journal of Volcanology and Geothermal Research* 36, 1-36.

Lentini F., (1982) The geology of the Mt. Etna basement. In Romano R. (eds) *Mount Etna Volcano*. Memorie della Società Geologica Italiana, 23, 7-25.

Levitich B. G. (1971) *Theoretical Statistics, Vol 2: Statistical Physics*. Northern Holland Publishing Company, Amsterdam.

Lister J.R. and Kerr R.C. (1991) Fluid-mechanical models of crack propagation and their application to magma transport in dykes. *Journal of Geophysical Research* 96, 10049-10077.

Lo Giudice E., Patane G., Rasà R. and Romolo R. (1982) The structural framework of Mount Etna. *Mem. Soc. Geol. It.* 23, 125-158.

Lo Giudice E. and Rasà R (1986) The role of the new structural trend on the recent geodynamic evolution of north-eastern Sicily and its volcanic implications in the Etnean area. *Journal of Geodynamics*, 25, 309-330.

Lo Giudice E. and Rasà R. (1992) Very shallow earthquakes and brittle deformation in active volcanic areas: the Etnean region as an example. *Tectonophysics* 202 257-268.

Lyell C. (1855) A manual of elementary geology II. *London*, 1-498.

Mangas J., Clocchiatti R., Pérez Torrado F. C., Massare D. (1997) Peridotite xenoliths, olivine - pyroxene megacrysts and cumulates of the Bandama volcanic complex (Gran Canaria, Canary Islands): genesis in the oceanic lithosphere. *Internat. Workshop on Immature Oceanic Volcanoes*. Sept.

- Martin San Gil (1960) *El Volcan de San Juan*, Madrid 239pp
- Masson D. G., Weaver P., and Watts T. (1997) Debris avalanche deposits on the submarine flanks of the Canary Islands. *Internat. Workshop on Immature Oceanic Volcanoes*, Sept.
- Massonnet D., Briole P. and Arnaud A. (1995) Deflation monitoring of Mount Etna monitored by spaceborne radar interferometry. *Nature* **375**, 567-570.
- McDougall I. (1971) The geochronology and evolution of the young volcanic island of Réunion, Indian Ocean. *Geochimica et Cosmochimica Acta*, **35**, pp261-288.
- McGuire W. J., (1982) Evolution of the Etna volcano: information from the southern wall of the Valle del Bove caldera. *Journal of Volcanology and Geothermal Research*, **13**, 241-271.
- McGuire W. J., (1983) Prehistoric dyke trends on Mt Etna; implications for magma transport and storage. *Bulletin of Volcanology*, **46**.
- McGuire W. J. (1991) Monitoring active volcanoes. *Geology Today*, Sept-Oct. p181-187.
- McGuire W. J. (1995) *Project SEAVOLC: Sea-level change and the stability and activity of coastal and island volcanoes. 2*, Cheltenham: Commission of the European Communities.
- McGuire W.J. (1995a) Piton de la Fournaise - *European Laboratory Volcano; Contribution of the Centre for Volcanic Research*, Cheltenham, UK. E. U. E. U. (1995)
- McGuire W. J. (1995b) Dyke-induced rifting and edifice instability at Mount Etna. 3rd International Dyke Conference, Jerusalem.
- McGuire W. J. (1996) Volcano instability: a review of contemporary themes. In McGuire W.J., Jones A. P. and Neuberg J. (Eds.) *Volcano Instability on Earth and other Planets*. Geological Society Special Publication No. 110. P1-24
- McGuire W. J. (1997) Volcanic Disasters: past, present and future. *Science progress* **80(i)** 83-99.
- McGuire W.J. and Pullen A.D. (1989) Location and orientation of eruptive fissures and feeder dykes at Mount Etna; influence of gravitational and regional tectonic stress regimes. *Journal of Volcanology and Geothermal Research* **38**, 325-344.

McGuire W.J., Pullen A.D. and Saunders S.J. (1990) Recent dyke-induced large scale block movement at Mount Etna and potential slope failure. *Nature* **343**, 357-359.

McGuire W.J., Murray J.B., Pullen A.D. and Saunders S.J. (1991) Ground deformation monitoring at Mt Etna; edifice for dyke emplacement and slope instability. *Journal of the Geological Society* **148** 577-583.

McGuire W. J., Moss J. L., Saunders S. J. Stewart I. S. (1996) Dyke-induced rifting and edifice instability at Mount Etna. In: Gravestock P. and McGuire W.J. (Eds.) *Etna 15 years on*, pp. 64-66. Cheltenham: Cheltenham and Gloucester College of Higher Education]

McGuire W. J., Stewart I. S., & Saunders S. J., (1997) Intra-volcanic rifting at Mount Etna in the context of regional tectonics. *Acta Volcanologica* **9(1/2)** 147-156.

McGuire W. J. & Moss J. L. (1997) Monitoring active volcanoes. *Abstract volume, Proceedings of the International workshop on Immature Oceanic Island Volcanoes*.

McTigue D.F. (1987) Elastic stress and deformation near a finite spherical magma body: Resolution of the point source paradox. *Journal of Geophysical Research* **92** (B12):12931-12940.

Melosh H.J. and Williams C. A. Jr. (1989) Mechanics of Graben formation in crustal rocks: A finite element analysis. *Journal of Geophysical Research* **94** (B10):13961-13973.

Merle O. and Borgia A. (1996) Scaled experiments of volcanic spreading. *Journal of Geophysical Research* **101**, 13805-13817.

Mogi K., (1958) Relations between the eruptions of various volcanoes and the deformations of the ground system around them. *Bulletin of the Earthquake Research Institute*, **36**, pp94-143.

Montalto A., Vinciguerra S., Menza S., & Patané G. (1996) Recent seismicity of Mount Etna: implications for flank instability. In, *Volcano instability on the Earth and Other Planets*. McGuire W. J., Jones A. P. & Neuberg J. (Eds). Geol. Soc. London, Spec. Pub. **110**, 169-177.

Moore J., Normark W., R. and Holcomb R., T. (1994) Giant Hawaiian Landslides. *Annu. Rev. Earth Planet. Sci* **22** 119-144.

- Moss J. L. , Saunders S. J., & McGuire W. J. (1995) The monitoring and interpretation of recent ground movements on active volcanoes. *Poster. Volcanoes in the Quaternary*, The Geological Society of London.
- Moss J. L. (1996) Recent horizontal ground deformation at Mount Etna, Sicily. In: Gravestock P. and McGuire W.J. (Eds.) *Etna 15 years on*, pp. 64-66. Cheltenham: Cheltenham and Gloucester College of Higher Education]
- Moss J.L. & McGuire W. J. (1997) Ground deformation monitoring at Mount Etna: the transition from IR-EDM to GPS. IACEI General Assembly, Puerto Rico.
- Moss J. L. & McGuire W. J. (1997) Ground deformation monitoring at Mount Etna: the transition from IR-EDM to GPS. *VSG-Minsoc 1997 Conference Proceedings*, Cambridge.
- Moss J. L., McGuire W. J. & Gilman J (1997) Under the volcano: measuring deformation on Italy's Mt. Etna. *GPS World*, **8**, (4), 22-33.
- Moss J. L. (1997) Ground deformation monitoring of the Cumbre Vieja Volcano, Canary Islands. *Abstract volume, Proceedings of the International workshop on Immature Oceanic Island Volcanoes*.
- Moss J. L., McGuire W. J. & Page D. (1998) Ground deformation monitoring of a potential landslide at La Palma, Canary Islands. Submitted to *Journal of Volcanological and Geothermal Research* July 1998.
- Mulargia F. and Achilli V., (1991) Is a destructive earthquake imminent in southeastern Sicily?. *Tectonophysics*, **188**, pp399-402.
- Mulargia F., Marzocchi W., Gasperini P., (1992) Statistical identification of physical patterns which accompany eruptive activity on Mt. Etna, Sicily. *Journal of Geothermal and Volcanological Research*, **53**, pp289-296.
- Murray J. B. (1988) The influence of loading by lavas on the siting of volcanic eruption vents on Mt. Etna. *Journal of Volcanological and Geothermal research*, **35**, p121-139.
- Murray J. B. (1990) High-level magma transport at Mount Etna volcano, as deduced from ground deformation measurements. In: *Magma transport and storage*. Ryan (ed). 357-406
- Murray J. B. (1994) Elastic model of the actively intruded dyke feeding the 1991-1993 eruption of Mt. Etna, derived from ground deformation networks. *Acta Vulcanologica*, **4**, p97-99.

Murray J. B. and Guest J. (1982) Vertical ground deformation on Mt. Etna 1975-80. *Geological Society of America Bulletin* **93**. p1160-1175.

Murray J. B. Guest J. E. and Butterworth P. S. (1977) Large ground deformation on Mt Etna Volcano. *Nature*, **266**, 338-40.

Murray J. B. and Pullen A. D. (1984) Three-dimensional model of the feeder conduit of the 1983 eruption of Mt Etna volcano, from ground deformation measurements. *Bulletin of Volcanology*. **47-4** p1145-1163.

Murray J.B., and Sargent P., (1994) GPS joins Etna monitoring programme. *Civil Engineer Surveyor*. November.

Murray J. B., Pullen A. D. and Saunders S. (1995) Ground deformation surveying of active volcanoes. In McGuire W. J., Kilburn C. R. J. and Murray J. (eds) *Monitoring active volcanoes*, pp113-148.

Murray J. B. and Voight B. (1996) Slope instability and eruption prediction on the eastern flank of Mount Etna. In: McGuire W.J., Jones A. P. and Neuberg J. (Eds.) *Volcano instability on the Earth and other planets*, pp. 111-114. London: Geological society]

Nercessian A., Hirn A. and Sapin M. (1991) A correlation between earthquakes and eruptive phases at Mt Etna: an example and past occurrences. *Geophys. J. Int* **105** 131-138.

Nercessain A., (1996) Internal Structure of Piton de la Fournaise volcano from seismic wave propagation and earthquake distribution. *Journal of Volcanological and geothermal Research* **70** 123-143.

Nunnari G. and Puglisi G. (1994) Ground deformation studies during the 1991-93 Etna eruption using GPS data. *Acta Vulcanologica* **4**, 101-107.

Nunnari G. and Puglisi G. (1994) The global positioning system as a useful technique for measuring ground deformations in volcanic areas. *Journal of Volcanology and Geothermal Research* **61** 267-280.

Nunnari G. and Puglisi G. (1996) GPS - Monitoring from space. In *Monitoring active volcanoes*. McGuire W. J., Kilburn C. R. J. and Murray J. B. (eds) UCL Press, London.

- Okada Y. (1985) Surface deformation due to shear and tensile faults in a half-space. *Bulletin of the Seismological Society of America* **75** (4):1135-1154.
- Okamura A.T., Dvorak J.J. and Koyanagi R.Y. (1996) Surface deformation during dyke propagation. Hawaiiin Volcano Observatory Report.
- Patané D., Privitera E., Ferrucci F. and Gresta S. (1996) Seismic activity leading to the 1991-1993 eruption of Mt. Etna and its tectonic implications. *Acta Vulcanologica* **4**, 47-55.
- Pollard D. D. and Muller O. H. (1976) The effect of gradients in regional stress and magma pressure on the form of sheet intrusions in cross section. *Journal of Geophysical Research* **81** (5):975-984.
- Pollard D. D., Delany P. T., Duffield W. A., Endo E. T. and Okamura A.T. (1993) Surface deformation in volcanic rift zones. *Tectonophysics* **94** 541-584.
- Pullen A.D. (1995) Project SEAVOLC: Sea-level change and the stability and activity of coastal and island volcanoes: Finite element modelling. 2, Cheltenham: Commission of the European Communities.
- Rancon J. P., Lerebour P. and Auge T. (1989) The Grand Brûlé exploration drilling: new data on the deep framework of the Piton de la Fournaise volcano. Part 1:lithostratigraphic units and volcano-structural implications. *Journal of Volcanology and Geothermal Research* **36**, 113-127.
- Rasà R., Azzaro R. and Leonardi O. (1996) Aseismic creep on faults and flank instability at Mount Etna volcano, Sicily. In: McGuire W.J., Jones A. P. and Neuberg J. (Eds.) *Volcano instability on the Earth and other planets*, pp. 179-192. London: Geological Society.
- Richards M., A., Duncan R., A. and Courtillot V., E. (1989) Flood basalts and Hot-spot Tracks: Plume Heads and Tails. *Science* **246** 103-107.
- Rittman A. (1973) Structure and evolution of Mt. Etna. Ph. *Trans. R.Soc.London. A.* **274**, 5-16.
- Rousset D., Bonneville A. and Lénat J-F. (1996) Detailed gravity study of the offshore structure of Piton de la Fournaise volcano, Reunion Island. *Bulletin of Volcanological Research.* **49**, 713-722.

Rousset D., Lesquer A., Bonneville A. and Lénat J-F. (1989) Complete gravity study of Piton de la Fournaise volcano, Reunion Island. *Journal of Volcanology and Geothermal Research* **36**, 37-52.

Rubin K. & Garcia M. (1994-1998) Global Volcanism Reports, Smithsonian Insitute.

Ruegg J-C., & Bougault C., (1992) *Programme de Compensation AG3D*. Institut du Globe de Physique du Paris.

Rust D. & Neri M. (1996) The boundaries of large-scale collapse on the flanks of Mount Etna, Sicily. In: McGuire W.J., Jones A. P. and Neuberg J. (Eds.) *Volcano instability on the Earth and other planets*, pp. 193-208. London: Geological Society]

Ryan M.P. (1987) Neutral Buoyancy and the mechanical evolution of magmatic systems. In: Mysen B. O. (Ed.) *Magmatic Processes: Physicochemical Principles*, pp. 259-287. The Geochemical Society]

Rymer H., Murray J.B., Brown G.C., Ferrucci F. and McGuire W.J. (1993) Mechanisms of magma eruption and emplacement at Mt Etna between 1989 and 1992. *Nature* **361** 439-441.

Rymer H., and Tryggvasson E. (1993) Gravity and elevation changes at Askja, Iceland. *Bulletin of Volcanology*. **55**, 362-371.

Sanderson T.J.O., Berrino G., Corrado G. and Grimaldi M. (1982) Ground deformation and gravity changes accompanying the March 1981 eruption of Mount Etna. *Journal of Volcanology and Geothermal Research* **16** 299-315.

Sapin M. (1996) Stress failure & fluid flow deduced from earthquakes accompanying eruptions at Piton de la Fournaise volcano. *Journal of Geophysical Research*, **70**, 145-167.

Saunders S.J. (1996). Ground deformation on Mt. Etna 1981-1995. Unpublished thesis.

Schmincke H. U. (1976) The geology of the canary Islands. In: G. Kunkel (ed) *Biogeography and Ecology of the Canary Islands*. Jungk, The Hague, 67-184.

Sharpe A. D. L., Davis P. M. and Gray F. (1980) A low velocity zone beneath Mt. Etna and magma storage. *Nature*, vol **287**.

Shaw H. R. (1980) The fracture mechanisms of magma transport from the mantle to the surface. In: R. B. Hargraves (ed) *Physics of Magmatic Processes*. Princeton University Press, Princeton, N-J.

Shimada S., Fujinawa Y., Sekiguchi S., Ohmi S., Eguchi T. and Okada Y. (1989) Detection of a volcanic fracture opening in Japan using Global positioning system measurements. *Letters to nature*

Siebert L. (1984) Large Volcanic debris avalanches: characteristics of source areas, deposits, and associated eruptions. *Journal of Volcanology and Geothermal Research*. **22** 163-197.

Sigmundsson F. (1996) Crustal deformation of Volcanoes. *Proceedings of the course the mitigation of volcanic hazards, Vulcano, Italy, 1994*. Environment and Climate Programme, European Commission.

Smalley R. F. Jr, Chatelain J. L., Turcotte D. L. and Pevcot R (1987) A fractal approach to the clustering of earthquakes: applications to the seismicity of the New Hebrides. *Bulletin of Seism. Soc. Amer.*, **77** (4), 1368-1381.

Staudacher T. (1998) *Global Volcanism Reports*, Smithsonian Institute.

Staudigel, H. and Schmincke H. U. (1984) The Pliocene Seamount Series of La Palma, Canary Islands. *Journal of Geophysical Research*, **89**, B13, 11195-11215.

Staudigel, H., Feraud, G. and Giannerini, G., . (1986) The history of intrusive activity on the Island of La Palma (Canary Islands). *Journal of Volcanology and Geothermal Research* **27**, 299-322.

Staudigel, H. and Schmincke, H., . (1997) The Pliocene Seamount series of La Palma/Canary Islands. *Journal of Geophysical Research* **89**, 11195-11215.

Stieltjes L. and Moutou P. (1989) A statistical and probabilistic study of the historic activity of Piton de la Fournaise, Réunion Island, Indian Ocean. *Journal of Volcanological and Geothermal research*, **36**, 67-86

Stephansson O. and Berner H. (1971) The finite element method in tectonic processes. *Phys. Earth Planet. Interiors* **4** 301-321.

Stewart I., McGuire W.J., Vita-Finzi C., Firth C., Holmes R. and Saunders S.J. (1993) Active faulting and neotectonic deformation on the eastern flank of Mount Etna, Sicily. *Z. Geomorph. N. F.* **94**, 73-94.

Stewart I., Cundy A., Kershaw S., and Firth C. (1997) Holocene coastal uplift in the Taormina area, northeastern Sicily: implications for the southwestern prolongation of the Calabrian Seismogenic belt. *Journal of Geodynamics*, **24**, 1-4, p37-50.

Swanson D. A., Duffield W. S. and Fiske R. S. (1976) Displacement of the south flank of Kilauea Volcano: the result of forceful intrusion of magma into the Rift Zones. *US Geological Survey Professional Paper*, **963**

Tanguy J.C. and Kieffer G. (1976) The 1974 eruption of Mount Etna. *Bulletin of Volcanological Research*. **40-4** 239-252.

Tanguy J. C. and Clocchiatti R. (1984) The Etnean lavas, 1977-1983. Petrology and mineralogy. *Bulletin of Volcanology*. **47**, 879-894.

Tilling, R.I., Heliker, C., and Wright, T.L., 1987, Eruptions of Hawaiian volcanoes: past, present, and future: *U.S. Geological Survey series of general-interest publications*, **54 p.**

Tortorici L., Monaco C., Tansi C. and Cocina O. (1995) Recent and active tectonics in the Calabrian arc (Southern Italy). *Tectonophysics*, **243**, 37-55.

Toutin J. P., Aloupogiannis P., Delorme H., Person A., Blanc Ph., Robaye G., (1990) Vapor deposition of trace elements from degassed basaltic lava, Piton de la Fournaise. *Journal of Volcanological and Geothermal Research*. **40**, pp 257.

Tryggvasson E (1994) Observed ground deformation at Hekla, Iceland, prior to and during the eruptions of 1970, 1980-81 and 1991, *Bulletin of Volcanology*.

Upton B. G. J., & Wadsworth W. J., (1970) Intra-volcanic intrusions of Réunion. *Geological Journal Special Issue*, **2**, p141-156.

Vincent P. M & Kieffer G. (1978) Hypothèse sur la structure et l'évolution de Piton de la Fournaise (Ile de la Réunion) après les éruptions de 1977. *6ème Réunion Annuelle des Sciences de la Terre*, Orsay (Soc. Géol. France Ed.), **407**

Wadge G. (1976) Deformation of Mount Etna, 1971-74. *Journal of Volcanology and Geothermal Research* **1**, 237-263.

Wadge G. and Guest J. E. (1981) Steady-state magma discharge at Mount Etna 1971-1981. *Nature*, **294**, 548-550.

Wahab A., (ed) (1989) Rock mechanics as a guide for efficient utilization of natural resources: Proceedings of the 30th U.S. symposium. Rotterdam: Balkema.

Walker G. P. L. (1990) Geology and Volcanology of the Hawaiian islands. *Pacific Science*, **44**, 315-347.

Walker G., P., L., Eyre P., R., Spengler S., R., Knight M., D. and Kennedy K. (1992) Congruent dyke-widths in large basaltic volcanoes. In: Baer and Heimann, (Eds.) *Physics and Chemistry of dykes*, pp. 35-40. Rotterdam: Balkema.

Walker G.P.L. (1995) "Coherent intrusion complexes" in large basaltic volcanoes - a new structural model. *Journal of Volcanology and Geothermal Research* **50**, 41-54.

Walker, G.P.L. (1990) Geology and Volcanology of the Hawaiian Islands. *Pacific Science* **44**, 315-347.

Watts A. B. and Masson D. G. (1995) A giant landslide on the north flank of Tenerife, Canary Islands, *Journal of Geophysical Research*, **100**, 24487-24498.

Wells D. E., Beck N., Delikaraoglou D., Kleusberg A., Krawiwsky E. J., Lachapelle G., Langley R. B., Nakiboglu M., Schwarz K. P., Tranquilla J. M., Vanicek P. (1986) *Guide to GPS Positioning*. Canadian GPS associates, Fredericton, N. B., Canada.

White R. S., and McKenzie D. (1989) Magmatism at rift-zones: the generation of volcanic continental margins and flood basalts. *Journal of Geophysical Research*, **94**, B6, 7685-7729.

Wijbrans J., Tauxe L. and Staudigel H. (1997) Eruptive chronology and palcomagnetism of the Taburiente volcano, La Palma. *Internat. Workshop on Immature Oceanic Volcanoes*. Sept.

Wilson L. and Head J. W. (1981) Ascent and eruption of basaltic magma on the Earth and Moon. *Journal of Geophysical Research*, **86**, 2971-3001.

Zlotnicki J., Ruegg J-C., Bachèlery P. and Blum P.A. (1990) Eruptive mechanism of Piton de la Fournaise volcano associated with the December 4, 1983, and January 18, 1984 eruptions from ground deformation monitoring and photogrammetric surveys. *Journal of Volcanology and Geothermal Research* **40**, 197-217.

Zumberge J., F., Heflin M., B., Jefferson D., C., Watkins M., M. and Webb F., H. (1997) Precise point positioning for the efficient and robust analysis of GPS data from large networks. *Journal of Geophysical Research* 102 (B3):5005-5018.